

EXPLORING THE COORDINATION CHEMISTRY OF *N, N, N', N'*-TETRAKIS(2-HYDROXYETHYL)ETHYLENEDIAMINE IN POLYNUCLEAR MANGANESE CLUSTER CHEMISTRY

By

ARPITA SAHA

A DISSERTATION PRESENTED TO THE GRADUATE SCHOOL
OF THE UNIVERSITY OF FLORIDA IN PARTIAL FULFILLMENT
OF THE REQUIREMENTS FOR THE DEGREE OF
DOCTOR OF PHILOSOPHY

UNIVERSITY OF FLORIDA

2011

© 2011 Arpita Saha

“To my parents and Subhro”

ACKNOWLEDGMENTS

It feels like a life time achievement to reach to the final stage of writing my dissertation thesis. This is my own journey, but I could never see the end of this long, winding road without the help of some people. I take this opportunity to thank them.

I express my deep gratitude to my doctoral supervisor Dr. George Christou for his excellent guidance, assistance and patience during the course of my graduate studies. His golden advice to ask the question 'Why' is my first lesson to become an independent thinker and a chemist. Not only the insightful discussions, I immensely value all his suggestions, criticism to improve my oral and written communication skills in a scientific community, which in turn made me a strong and confident person. Above all he introduced me to the edteH_4 chemistry which is the soul of this dissertation and I sincerely acknowledge his faith in me. This is an honor and privilege to be a part of the Christou group and I will carry the pride lifelong.

I would like to thank my committee member Dr. Daniel R. Talham for his encouragement and kind words throughout my graduate career. I extend my sincere gratitude to Dr. Mark Meisel, Dr. Ronald Castellano and Dr. Leslie J. Murray for serving as my committee. I greatly appreciate all the scientific discussions with Dr. Daniel R Talham, Dr. Mark Miesel and Dr. Stephen Hill who helped me to become a physical chemist. I acknowledge gratefulness to all my collaborators, especially Dr. Wolfgang Wernsderfer for micro-SQUID measurements, Dr. Oliver Waldmann for INS measurements, and Dr. Artëm E. Masunov and Shrubu for the DFT calculations. I deeply thank to Dr. Khalil A. Abboud for all the X-ray crystal structure analyses throughout my graduate study. I express my deep thankfulness to Dr. Sabyasachi

Sarkar, my undergraduate research advisor, who strongly motivated and supported my decision to continue higher studies in the United States.

I will never forget all my colleagues, especially Rashmi, Antonio, Taketo, Shreya, Tu, Andy, Lynn, Annalease, Amber and Mike for all the fun times, help and understanding. Special thanks to Mike and Matthew to proofread my thesis. I want to thank Alice, Maribel and De’Neka for helping me out with many official works in day to day life. Needless to mention the warm friendships from Debapriya, Swati, Ruma, June, Jaya, Smita, Srishti, Marie and Anna for making my entire stay in Florida so memorable. Special thanks to Dola Kaki, Shampa Kaki and Seba Masi for their motherly support in a foreign land. While I’m away from my family it means a lot to me.

Words are not enough to convey my forever indebtedness to my parents (Mr. Supriya K. Saha and Mrs. Kalyani Saha) for their unending love, faith and encouragement. I am also thankful to my father-in-law (Mr. Subhrangshu N. Saha) and mother-in-law (Mrs. Aloka Saha) and my sisters (Didi and Daisy di) & their families for the love and support.

Finally, I express my indebtedness to my beloved husband Dr. Subhrajit Saha for his unconditional love, support, motivation, trust, advice, zeal and strong sense of humor that brings fresh air to all my good and bad times. He is my greatest critic who motivates me to continue exploring myself and delivering the best in me. I couldn’t possibly be so composed and confident without him and I thank him for believing in me and making me feel so special. My acknowledgement is incomplete without mentioning blessings of the almighty and the invisible presence is behind my existence and strength. I, therefore, humbly express my deepest gratitude by all my life.

TABLE OF CONTENTS

	<u>page</u>
ACKNOWLEDGMENTS.....	4
LIST OF TABLES.....	9
LIST OF FIGURES.....	11
LIST OF ABBREVIATIONS.....	17
ABSTRACT.....	18
CHAPTER	
1 GENERAL INTRODUCTION.....	20
2 SYNTHESIS, STRUCTURE AND ELECTROCHEMICAL AND MAGNETOCHEMICAL PROPERTIES OF A FAMILY OF Mn ₁₂ COMPLEXES CONTAINING THE ANION OF N,N,N',N'-TETRAKIS(2-HYDROXYETHYL) ETHYLENEDIAMINE.....	34
Experimental Section.....	35
Syntheses.....	35
X-ray Crystallography.....	37
Physical Measurements.....	39
Results and Discussion.....	39
Syntheses.....	39
Description of Structures.....	41
Structure of [Mn ₁₂ O ₄ (OMe) ₂ (edte) ₄ (N ₃) ₈](ClO ₄)(N ₃) (2-1).....	41
Structure of [Mn ₁₂ O ₄ (OH)(edte) ₄ (N ₃) ₉] (2-2).....	42
Structure of [Mn ₁₂ O ₄ (OH)(edte) ₄ (N ₃) ₉](ClO ₄)(N ₃) (2-3).....	43
Electrochemistry.....	45
Magnetochemistry.....	46
Dc magnetic susceptibility studies of 2-1, 2-2 and 2-3.....	46
Alternating current (ac) magnetic susceptibility studies for 2-1, 2-2 and 2-3.....	48
Magnetization hysteresis studies below 1.8 K for 2-1.....	49
Concluding Remarks.....	50
3 EXPERIMENTAL AND COMPUTATIONAL STUDIES OF A NEW Mn ₉ SINGLE- MOLECULE MAGNET WITH A HALF-INTEGER SPIN OF S = 21/2.....	69
Experimental Section.....	71
Synthesis.....	71
X-ray Crystallography.....	71
Physical Measurements.....	72

Computational Details	74
Results and Discussion.....	74
Syntheses.....	74
Description of the Structure $[\text{Mn}_9\text{O}_3(\text{OMe})(\text{O}_2\text{CBu}^\dagger)_7(\text{edte})(\text{edteH})_2(\text{N}_3)_2]$	75
Magnetochemistry	77
Dc magnetic susceptibility studies of 3-1	77
Alternating current (ac) magnetic susceptibility studies of 3-1	78
Single-crystal hysteresis studies for 3-1 below 1.8K.....	81
Electrochemistry.....	83
Inelastic Neutron Scattering (INS)	84
Density Functional Theory.....	87
Determination of ground spin state of 3-1	89
Heisenberg exchange constant in Mn_9 system	89
Bonding analysis.....	91
Concluding Remarks	91
4 A RICHNESS OF NEW MIXED-VALENT Mn and Mn/Ca CLUSTERS FROM THE USE OF <i>N, N, N', N'</i> -TETRAKIS(2- HYDROXYETHYL)ETHYLENEDIAMINE: Mn_3 , Mn_4 , Mn_6 , Mn_{10} , Mn_{20} AND $\text{Mn}_{18}\text{Ca}_2$	111
Experimental Section.....	112
Syntheses.....	112
X-ray Crystallography	116
Physical Measurements	120
Result and Discussion	120
Syntheses.....	120
Description of Structures	125
Structure of $[\text{Mn}_3(\text{O}_2\text{CMe})_2(\text{edteH}_2)_2](\text{O}_2\text{CMe})$ (4-1).....	125
Structure of $[\text{Mn}_3(\text{O}_2\text{CMe})_2(\text{edteH}_2)_2](\text{ClO}_4)$ (4-2).....	126
Structure of $[\text{Mn}_4(\text{edteH}_2)_2(\text{hmp})_2\text{Cl}_2][\text{Mn}^{\text{II}}\text{Cl}_4]$ (4-3).....	127
Structure of $[\text{Mn}_6\text{O}_2(\text{O}_2\text{CBu}^\dagger)_6(\text{edteH})_2(\text{N}_3)_2]$ (4-4)	128
Structure of $\text{Na}_2[\text{Mn}_{10}\text{O}_4(\text{OMe})_2(\text{O}_2\text{CEt})_6(\text{edte})_2(\text{N}_3)_6]$ (4-5).....	129
Structure of $(\text{NEt}_4)_2[\text{Mn}_{10}\text{O}_4(\text{OH})_2(\text{O}_2\text{CEt})_6(\text{edte})_2(\text{N}_3)_6]$ (4-6)	130
Structure of $[\text{Mn}_{20}\text{O}_8(\text{OH})_6(\text{O}_2\text{CEt})_6(\text{edte})_4(\text{edteH})_2](\text{ClO}_4)_4$ (4-7)	130
Structure of $[\text{Ca}_2\text{Mn}_{18}\text{O}_8(\text{OH})_5(\text{O}_2\text{CBu}^\dagger)_{4.5}(\text{edte})_5(\text{NO}_3)_{3.5}](\text{O}_2\text{CBu}^\dagger)_{0.5}(\text{NO}_3)_{0.5}$ (4-8) ..	132
Magnetochemistry	133
Dc and ac magnetic susceptibility studies of 4-1 and 4-2	133
Dc and ac magnetic susceptibility studies of 4-3.....	137
Dc and ac magnetic susceptibility studies of 4-4.....	139
Dc and ac magnetic susceptibility studies of 4-5 and 4-6	141
Dc and ac magnetic susceptibility studies of 4-7.....	142
Dc and ac magnetic susceptibility studies of 4-8.....	143
Concluding Remarks	144

5	A FAMILY OF RARE FUSED DOUBLE-CUBANE Mn_4Ln_2 ($Ln = Gd, Tb, Dy, Ho$) AND Mn_4Y_2 COMPLEXES CONTAINING SINGLE-MOLECULE MAGNET	177
	Experimental Section	179
	Syntheses.....	179
	X-ray Crystallography	180
	Physical Measurements	181
	Results and Discussion.....	182
	Syntheses.....	182
	Description of Structure $Mn_4Gd_2O_2(O_2CBu^t)_6(edteH_2)_2(NO_3)_2$	184
	Magnetochemistry	185
	Dc magnetic susceptibility studies	185
	Alternating current (ac) magnetic susceptibility studies	189
	Single-crystal hysteresis studies of 5-2 below 1.8 K.	190
	Concluding Remarks	191

APPENDIX

A	BOND DISTANCES AND ANGLES.....	203
B	LIST OF COMPOUNDS.....	213
C	ELECTROCHEMICAL REVERSIBLE PROCESSES.....	214
D	DFT CALCULATIONS	216
E	VAN VLECK EQUATIONS.....	217
	LIST OF REFERENCES	228
	BIOGRAPHICAL SKETCH.....	243

LIST OF TABLES

<u>Table</u>	<u>page</u>
2-1 Crystallographic data for 2-1 , 2-2 and 2-3	52
2-2 Bond-valence sums for the Mn atoms of complex 2-1 , 2-2 and 2-3^a	53
2-3 Bond-valence sums for the O atoms of complex 2-1^a	53
2-4 Bond-valence sums for the O atoms of complex 2-2^a	53
2-5 Bond-valence sums for the O atoms of complex 2-3^a	54
2-6 Structural types and ground state <i>S</i> values for known Mn ₁₂ clusters.....	54
3-1 Crystallographic data for 3-1 ·4MeCN	93
3-2 BVS calculations for the Mn atoms of complex 3-1^a	93
3-3 BVS calculations for the O atoms of complex 3-1^a	94
3-4 Fitting parameters for plots of χ' vs. angular frequency and χ'' vs. angular frequency for complex 3-1	94
3-5 Computational calculation scheme for seven Heisenberg exchange constants in Mn ₉ complex (3-1).	95
3-6 The distance between Mn _i and Mn _j , Heisenberg exchange constants for two adjacent metal centers and calculated and ideal spin coupling	96
3-7 Löwdin Population analysis for spin densities of complex 3-1	96
4-1 Crystallographic data for 4-1 ·4CH ₂ Cl ₂ , 4-2 ·MeCN, and 4-3	146
4-2 Crystallographic data for 4-4 , 4-5 ·2MeCN and 4-6 ·2MeCN	147
4-3 Crystallographic data for 4-7 and 4-8	148
4-4 Bond-valence sums for the Mn atoms of complexes 4-1 , 4-2^a	148
4-5 Bond-valence sums for the Mn atoms of complexes 4-3 , 4-4^a	149
4-6 Bond-valence sums for the Mn atoms of complexes 4-5 , 4-6^a	149
4-7 Bond-valence sums for the Mn atoms of complex 4-7 and 4-8^a	149
4-8 Bond-valence sums for the O atoms of complexes 4-1 and 4-2^a	150

4-9	Bond-valence sums for the O atoms of complexes 4-3 and 4-4^a	150
4-10	Bond-valence sums for the O atoms of complexes 4-5 and 4-6^a	151
4-11	Bond-valence sums for the O atoms of complex 4-7^a	151
4-12	Bond-valence sums for the O atoms of complex 4-8^a	152
5-1	Crystallographic data for 5-1·3MeCN and 5-2·0.5MeCN	192
5-2	Bond-valence sums for the O atoms of complex 5-1^a	192
5-3	Bond-valence sums for the Mn atoms of complex 5-1 and 5-2^a	192
5-4	Magnetic data summarized from the dc measurements	193
A-1	Selected interatomic distances (Å) and angles (deg) for 2-1·MeCN	203
A-2	Selected interatomic distances (Å) and angles (deg) for 2-2·3MeCN	203
A-3	Selected interatomic distances (Å) and angles (deg) for 2-3·MeCN	204
A-4	Selected interatomic distances (Å) and angles (deg) for 3-1·4MeCN	204
A-5	Selected interatomic distances (Å) and angles (deg) for 4-1·4CH₂Cl₂ and 4-2·MeCN ,	205
A-6	Selected interatomic distances (Å) and angles (deg) for 4-3 and 4-4	205
A-7	Selected interatomic distances (Å) and angles (deg) for 4-5·2MeCN	206
A-8	Selected interatomic distances (Å) and angles (deg) for 4-6·2MeCN	207
A-9	Selected interatomic distances (Å) and angles (deg) for 4-7·x(Solv)	207
A-10	Selected interatomic distances (Å) and angles (deg) for 4-8·5MeCN	209
A-11	Selected interatomic distances (Å) and angles (deg) for 5-1·3MeCN	211
A-12	Selected interatomic distances (Å) and angles (deg) for 5-2·0.5MeCN	211
D-1	Spin of nine Mn atoms are shown in column S1 to S9 indicating different spin orientations.	216

LIST OF FIGURES

<u>Figure</u>	<u>page</u>
1-1 Representation of magnetic field lines of flux (A) for a diamagnetic substance in a magnetic field and (B) for a paramagnetic substance in a magnetic field	29
1-2 Magnetic dipole arrangements in different types of materials.....	29
1-3 Typical hysteresis loop of a magnet, where M is magnetization, H is the applied magnetic field and M_s is the saturation value of the magnetization	29
1-4 Representation of the $[\text{Mn}^{\text{III}}_8\text{Mn}^{\text{IV}}_4(\mu_3\text{-O}^{2-})_{12}]^{16+}$ core (A) and the $[\text{Mn}_{12}\text{O}_{12}(\text{O}_2\text{CMe})_{16}(\text{H}_2\text{O})_4]$ complex	30
1-5 Representative plots of the potential energy barrier for an SMM.....	30
1-6 Magnetization hysteresis loops for a typical $[\text{Mn}_{12}\text{O}_{12}(\text{O}_2\text{CR})_{16}(\text{H}_2\text{O})_4]$ complex	31
1-7 Schematic representation of the change in energy of m_s sublevels as the magnetic field is swept from zero to a non-zero value.....	31
1-8 Representative examples of pyridyl alcohols, pyridyl oximes and non-pyridyl oxime ligands.....	32
1-9 Representative examples of non-pyridyl alcohols.....	33
1-10 <i>N,N,N',N'</i> -tetrakis(2-hydroxyethyl) ethylenediamine	33
2-1 Labeled representation (A) and a stereopair (B) of complex 2-1	56
2-2 Labeled representation (A) and a stereopair (B) of complex 2-2	57
2-3 Labeled representation (A) and a stereopair (B) of complex 2-3	58
2-4 The core of 2-1 (A), 2-2 (B), 2-3 (C) viewed along the c axis..	59
2-5 The core of 2-1 (A), 2-2 (B), and 2-3 (C) viewed along the b axis..	60
2-6 Coordination mode of edte^{4-} found in complexes 2-1 to 2-3	60
2-7 A full CV diagram of complex 2-1	61
2-8 A full DPV diagram for complex 2-1	61
2-9 The CV diagram at the indicated scan rates for the reduction wave of 2-1	62

2-10	Plots of cathodic (●) and anodic (▼) peak current dependence vs. square-root of scan rate ($v^{1/2}$) for -0.24 V (A) and -0.47 V (B) for complex 2-1	62
2-11	Plot of $\chi_M T$ vs. T for complexes 2-1 (●), 2-2 ·6H ₂ O·2MeCN(▼) and 2-3 ·2MeCN(■).....	63
2-12	Plots of reduced magnetization ($M/N\mu_B$) vs. H/T for complexes 2-1 (A), 2-2 (B) and 2-3 (C).....	63
2-13	Plot of reduced magnetization ($M/N\mu_B$) vs. H/T for complex 2-3	64
2-14	Two-dimensional contour plot for the rms error surface vs. D and g for the reduced magnetization fit for complex 2-3	64
2-15	Plots of in-phase χ_M' (as $\chi_M' T$) vs. T and out-of-phase χ_M'' vs. T ac signals for complex 2-1	65
2-16	Plots of in-phase χ_M' (as $\chi_M' T$) vs. T and out-of-phase χ_M'' vs. T ac signals for complex 2-2	66
2-17	Plots of in-phase χ_M' (as $\chi_M' T$) vs. T and out-of-phase χ_M'' vs. T ac signals for complex 2-3	67
2-18	Magnetization (M) vs. dc field scans for a single-crystal of complex 2-1	68
3-1	A partially labeled representation and a stereopair of complex 3-1	97
3-2	The core of complex 3-1 (A) and the core with an emphasis on the triangular sub units (B).....	98
3-3	The coordination modes of edte ⁴⁻ and edteH ³⁻ found in complex 3-1	98
3-4	Plot of $\chi_M T$ vs. T for complex 3-1	99
3-5	Plot of reduced magnetization ($M/N\mu_B$) vs. H/T for complex 3-1 (A) 2D contour plot for the rms error surface vs. D and g for complex 3-1 (B).....	99
3-6	Plots of in-phase χ_M' (as $\chi_M' T$) vs. T and out-of-phase χ_M'' vs. T ac signals for complex 3-1	100
3-7	Plot of the $\ln(1/\tau)$, vs. $1/T$ for complex 3-1 (A). Arrhenius plot obtained from the magnetization vs. time decay study for complex 3-1 (B).	101
3-8	Plots of the in-phase (χ') vs. angular frequency (A), out-of-phase (χ'') vs. angular frequency (A) and χ'' vs. χ' (B) at 3.0 K for complex 3-1	102
3-9	Argand plots of χ'' vs. χ' for complex 3-1 at the indicated temperatures (A). The change in α with temperature in the Argand plot for complex 3-1 (B).....	103

3-10	Magnetization (M) vs. dc field hysteresis loops for a single crystal of 3-1 ·4MeCN Magnetization vs. time decay data for complex 3-1 (C).....	104
3-11	A full CV diagram at 100 mV/s (A) and full DPV diagram for complex 3-1	105
3-12	The CV diagram at 50 - 500 mV/s (A). Plot of cathodic (◆) and anodic (▲) peak current dependence vs. square-root of scan rate ($v^{1/2}$) (B).	106
3-13	INS spectra of 3-1 recorded with an incoming neutron wavelength of 6.5 Å at the indicated temperatures.	107
3-14	INS spectra of 3-1 recorded with wavelength 7.5 Å.....	107
3-15	S(Q,E) plot of the INS spectrum of 3-1 measured with wavelength 7.5 Å.	108
3-16	INS spectra of 3-1 measured with wavelength 3.2 Å. (A) S(Q,E) plots at 1.5 K. (B)	108
3-17	(A) Comparison of the experimental and (lines) INS spectra recorded with wavelength 7.5 Å. (B) Calculated energy spectrum of 3-1	109
3-18	Depiction of the spin alignments in the $S = 21/2$ ground state of complex 3-1	110
4-1	Labeled representation of the cation of complex 4-1 (A). A section of the 1D polymeric chain (B) of complex 4-1	153
4-2	Labeled representation of the cation of complex 4-2	154
4-3	Labeled representation of the cation of complex 4-3	154
4-4	The core of complex 4-3 (A). A section of the 1D polymeric chains of complex 4-3	155
4-5	The labeled representation of complex 4-4 (A). a stereoview (B) and the core (C) of complex 4-4	156
4-6	Labeled representation of the part of $(\text{Na}_2\text{Mn}_{10})_\infty$ polymer, 4-5 (A) and a stereopair (B).....	157
4-7	The core of complex 4-5 (A) and a section of the 1D polymeric chain of complex 4-5 (B).	158
4-8	Labeled representation of the cation of complex 4-6 (A) and a stereopair (B)..	159
4-9	Structural representation of the cation of complex 4-7 (A) and a stereopair (B).....	160
4-10	Labeled representation of the core of complex 4-7	161

4-11	Structural representation of the cation of complex 4-8	161
4-12	Structural representation of the stereopair of complex 4-8	162
4-13	Labeled representation of the core of complex 4-8 (A) and a part of the core of complex 4-8 (B).	162
4-14	Coordination modes of edteH_2^{2-} , edteH^{3-} and edte^{4-} in complexes 4-1 to 4-8	163
4-15	Schematic diagram for the linear Mn_3 core for complexes 4-1 and 4-2 with two exchange coupling parameters, J and J'	164
4-16	Plot of χ_M vs. T for complex 4-1 · H_2O	164
4-17	Plot of $\chi_M T$ vs. T for complex 4-2 · H_2O	165
4-18	Plot of all possible energy states for complex 4-1 using the J value, obtained from the fit to the experimental χ_M data.	165
4-19	Plot of all possible energy states for complex 4-2 using the J values, obtained from the fit to the experimental $\chi_M T$ data.	166
4-20	Plot of reduced magnetization ($M/N\mu_B$) vs. H/T for complex 4-2 · H_2O	166
4-21	Two-dimensional contour plot for the rms error surface vs. D and g for the reduced magnetization fit for complex 4-2	167
4-22	Plot of in-phase χ_M' (as $\chi_M' T$) vs. T ac signals at 1000 Hz for complexes 4-1 · H_2O (\blacktriangledown) and 4-2 · H_2O (\bullet).....	167
4-23	Plot of $\chi_M T$ vs. T for complex 4-3	168
4-24	Schematic diagram for a Mn_4 core with two exchange coupling parameters, J_{wb} and J_{bb}	168
4-25	(A) Plot of energies of various spin states vs. the ratio of J_{wb}/J_{bb} for complex 4-3 . (B) Plot of all possible energy states for complex 4-3	169
4-26	The plots of in-phase χ_M' (as $\chi_M' T$) vs. T ac signals for complex 4-3 at the indicated frequencies.	170
4-27	Plot of $\chi_M T$ vs. T for complex 4-4	170
4-28	Plot of reduced magnetization ($M/N\mu_B$) vs. H/T for complex 4-4	171
4-29	Two-dimensional contour plot for the rms error surface vs. D and g for the reduced magnetization fit for complex 4-4	171

4-30	Plot of in-phase χ_M' (as $\chi_M'T$) vs. T ac signals for complex 4-4	172
4-31	Plot of $\chi_M T$ vs. T for complexes 4-5 ·2H ₂ O (●) and 4-6 ·H ₂ O (▼).....	172
4-32	Plot of in-phase χ_M' (as $\chi_M'T$) vs. T ac signals for complexes 4-5 ·2H ₂ O (●) and 4-6 ·H ₂ O (▼) at 1000Hz.	173
4-33	Plot of $\chi_M T$ vs. T for complex 4-7 ·1.5C ₆ H ₁₄	173
4-34	Plot of reduced magnetization ($M/N\mu_B$) vs. H/T for complex 4-7 (A). 2D contour plot for the rms error surface vs. D and g for complex 4-7 (B).	174
4-35	Plots of in-phase χ_M' (as $\chi_M'T$) vs. T and out-of-phase χ_M'' vs. T ac signals for complex 4-7 ·1.5C ₆ H ₁₄	175
4-36	Plots of $\chi_M T$ vs. T (A) and in-phase χ_M' (as $\chi_M'T$) vs. T ac signals for complex 4-8 ·3H ₂ O (B).....	176
5-1	The structure of 5-1	193
5-2	The stereopair of 5-1	194
5-3	The core of 5-1	194
5-4	The coordination mode of edteH ₂ ²⁻ found in 5-1	195
5-5	A partially labeled representation of complex 5-1	195
5-6	A partially labeled structure and a stereopair of complex 5-2	196
5-7	Plot of $\chi_M T$ vs. T for complexes 5-1 to 5-5	197
5-8	Schematic diagram for Mn ₄ core with two exchange coupling parameters, J_{wb} and J_{bb}	197
5-9	Plot of $\chi_M T$ vs. T for complex 5-5	198
5-10	Plot of all possible energy states for complex 5-5 using the J values, obtained from the fit to the experimental $\chi_M T$ data.	198
5-11	Plot of energies of various spin states vs. the ratio of J_{wb}/J_{bb}	199
5-12	Plot of reduced magnetization ($M/N\mu_B$) vs. H/T for complex 5-1	199
5-13	Plots of reduced magnetization ($M/N\mu_B$) vs. H/T for complex 5-5	200
5-14	Plot of in-phase χ_M' (as $\chi_M'T$) vs. T ac signals at 250 Hz for complexes 5-1 to 5-5	200

5-15	Plots of in-phase χ_M' (as $\chi_M'T$) vs. T and out-of-phase χ_M'' vs. T ac signals for complex 5-2	201
5-16	Magnetization (M) vs. dc field hysteresis loops for a single crystal of 5-2	202
C-1	A typical cyclic voltammogram obtained for a reversible one-electron reduction process.	215

LIST OF ABBREVIATIONS

AF	antiferromagnetic
bpy	2, 2' bipyridine
^t Bu	tertiary butyl, -C(CH ₃) ₃
BVS	bond valence sum
CV	cyclic voltammogram
DPV	differential pulse voltammogram
DFT	density functional theory
DMF	<i>N, N'</i> -dimethylformamide
edteH ₄	<i>N, N, N', N'</i> -tetrakis(2-hydroxyethyl)ethylenediamine
Et	Ethyl, -CH ₂ CH ₃
FM	ferromagnetic
hmpH	2-hydroxymethyl pyridine
INS	inelastic neutron scattering
IR	infrared spectroscopy
JT	Jahn-Teller
Me	Methyl, -CH ₃
PS II	photosystem II
QTM	quantum tunneling of magnetization
SMM	single-molecule magnet
SQUID	superconducting quantum interference device
THF	tetrahydrofuran
TIP	temperature independent paramagnetism
ZFS	zero-field splitting

Abstract of Dissertation Presented to the Graduate School
of the University of Florida in Partial Fulfillment of the
Requirements for the Degree of Doctor of Philosophy

DIVERSITY OF STRUCTURAL TYPES IN MANGANESE CLUSTER CHEMISTRY
INCLUDING SINGLE-MOLECULE MAGNETS FROM THE USE OF *N, N, N', N'*-
TETRAKIS(2-HYDROXYETHYL)ETHYLENEDIAMINE

By

Arpita Saha

August 2011

Chair: George Christou
Major: Chemistry

The research focuses on the investigation of new synthetic routes towards the preparation and subsequent characterization of novel multinuclear transition metal/lanthanide complexes that can function as molecular nanomagnets, better known as single-molecule magnets (SMMs). The major compelling property of these metal clusters is that they behave like tiny magnets i.e. they show slow relaxation of magnetization at low temperature. In addition these molecular systems often exhibit quantum properties which make them interesting candidates to use as qubits in quantum computation. In 1993, the first SMM was discovered, $[\text{Mn}_{12}\text{O}_{12}(\text{O}_2\text{CCH}_3)_{16}(\text{H}_2\text{O})_4]$, better known as Mn_{12}Ac , which was a breakthrough in the field of molecular magnetism. In the subsequent years, there has been massive amount of research in this area, and the SMM database has greatly expanded as research groups around the world have made new ones. The synthesis of such polynuclear metal clusters involves the incorporation of multiple metal atoms supported by organic ligands. In this regard, alkoxide-based ligands play a pivotal role since this functionally is an excellent bridging group that fosters higher nuclearity product formation. Such

polydentate ligands have led to the discovery of many interesting 3d clusters, some of which display SMM behavior.

The dissertation is on the investigation of new synthetic methods, combining an alkoxide-based ligand with various carboxylates and azides. In this regard, potentially hexadentate (O,O,O,O,N,N) *N,N,N',N'*-tetrakis(2-hydroxyethyl)ethylenediamine (edteH₄) ligand has been used. Herein, the synthesis, structure and magnetic properties of various nuclearity Mn_x clusters, where x = 3, 4, 6, 9, 10, 12, 18, 20, have been reported. Among them, the electrochemical behavior (cyclic voltammetry and differential pulse voltammetry) and magnetic susceptibilities (using SQUID magnetometer) of Mn₉ and a family of Mn₁₂ SMMs have been studied in detail. Single-crystal hysteresis loops using micro-SQUID apparatus were obtained and further proved the SMM behavior of the same. Mn₉ is a new, rare half-integer spin SMM with a spin barrier of 49 K, the highest in mixed-valent Mn²⁺/Mn³⁺ chemistry. Inelastic neutron scattering (INS) and computational characterization (using Density Functional Theory) were further performed to assess the zero-field splitting and higher order anisotropic parameters, the energy barrier, the spin-ground state, the Heisenberg exchange coupling parameters (*J*) and the bonding criterion in Mn₉ complex. In addition, a family of isostructural heterometallic Mn-Ln clusters using the same ligand with a [Mn^{II}₂Mn^{III}₂Ln^{III}₂] core (Ln = Gd, Tb, Dy, Ho) has been synthesized as well as a [Mn^{II}₂Mn^{III}₂Y^{III}₂] analog with diamagnetic Y³⁺ to assist the magnetic studies by assessing the nature of the Mn...Ln exchange interactions. Among them the Tb analog exhibits frequency-dependent out-of-phase ac susceptibility signals characteristic of SMMs, which was further confirmed by the observation of magnetization hysteresis.

CHAPTER 1 GENERAL INTRODUCTION

The most distinctive aspect of transition metal chemistry is the formation of coordination complexes. These are species that contain metal ions coordinated to molecules and/or anions as ligands. Any ion or molecule with a pair of non bonding electrons can be a ligand e.g. NH_3 , Cl^- and H_2O . Ligands are classified in many ways e.g. charge, size (bulk), the identity of the coordinating atom(s), or the number of electrons donated to the metal (hapticity). Ethylenediamine (en) is an example of a bidentate ligand, since each end contains a pair of non-bonding electrons that can make a covalent bond with a metal ion. En is also a typical example of a chelating ligand. The term “chelate” originates from the Greek word claw that is it grabs the metal in two or more places. The term “ligand” (Latin ligare, to bind) was first proposed in 1916 by Alfred Stock, a German inorganic chemist. He did pioneering research on borohydrides,^{1,2} silicohydrides³ and coordination chemistry, but coordination complexes have been known since the early eighteenth century e.g. Prussian blue and copper vitriol. The real breakthrough in modern coordination chemistry occurred by a Swiss chemist, Alfred Werner who won the Nobel Prize in 1913 for proposing the octahedral configuration of transition metal complexes.⁴ However, it took several years to develop metal-alkoxide chemistry. In early 1950's, Donald C. Bradley, a British inorganic chemist did some ground-breaking research on synthesizing metal-alkoxide e.g. Monomeric zirconium tetra-tert-butoxide, $\text{Zr}(\text{O}^t\text{Bu})_4$.⁵ Since then, the field of inorganic metal-alkoxide chemistry has developed and continued to be an important part of the frontier research that for example, involves exploring complicated polydentate ligands e.g. crown ethers, cryptands, poly-alcohols, Schiff-based ligands and so on designed to

achieve specific purposes. One of the important applications of polydentate ligands of relevance to these is to make polynuclear transition metal complexes, or clusters containing paramagnetic metal ions.

Mimicking the metal sites of biomolecules is one purpose of making oxide-based metal clusters. For example, this synthetic modeling approach can unfold the nature and mechanism of the active site of the water oxidizing complex, a CaMn_4 cluster in photosystem II (PS II)^{6,7} of green plants and cyanobacteria, as well as illuminating the means of assembly of the multinuclear $\text{Fe}^{3+}/\text{O}^{2-}$ core of the iron-storage protein, ferritin^{8,9} which can store up to 4500 iron atoms. In addition, ferritin is also considered a nanosize magnetic particle and has been investigated for its various magnetic properties. Similarly, many 3d and mixed 3d/4f metal clusters often display interesting and sometimes novel magnetic properties, including high ground-state spin values,¹⁰ currently up to $S = 83/2$ and single-molecule magnetism.¹¹⁻¹⁵ These metal based tiny magnets are individual molecules that can act as nanoscale magnetic particles below a certain temperature. The first single-molecule magnet (SMM), $[\text{Mn}_{12}\text{O}_{12}(\text{O}_2\text{CCH}_3)_{16}(\text{H}_2\text{O})_4]$ (better known as Mn_{12}Ac),¹⁶ was discovered in 1993, which was a breakthrough in the field of molecular magnetism. Over the years many research groups have enriched the database by making new SMMs to improve understanding and control over the synthesis and physiochemical properties of these tiny yet powerful magnets.

For understanding the origin of SMMs, knowledge of magnetism is imperative. The fascinating properties and uses of magnets have captivated humans ever since Thales of Miletus (ca. 634 – 546 BC) first described the phenomenon as the attraction of iron

by “lodestone” in the city of Magnesia.¹⁷ Over the last 2500 years, magnetism has played a pivotal role in the development of human civilization. Humans have used magnets for navigation, power production and various other technological applications, while at the same time exploring the origin of the effect. The popularly known lodestone is a magnetized piece of the mineral magnetite (Fe_3O_4), which the Greeks observed after being magnetized, likely by lightning strikes and the earth’s magnetic field. In the modern technological society, magnetic materials are ubiquitous in various industrial and other applications, such as manufacturing of switches, computer hard drives, credit/debit/ATM cards, televisions, audio devices, motors, and highly specialized instruments like medical MRI equipment, among many others. Modern day magnetic materials include magnetic alloys and oxides, particularly ferrites such as MgFe_2O_4 , which can function in transformer cores, and magnetic recording or information storage devices. Today magnetism is a multi-billion dollar annual industry.

The behavior of any magnetic material is dependent on the presence of unpaired electrons and how they interact with each other.¹⁸ To be more precise, any moving electrical charge with spin and orbital angular momentum generates a magnetic field in a system. The quantitative measurement of the magnetic response of a material to an applied magnetic field is known as susceptibility (χ). The magnetic materials are broadly classified into two categories, which are dia- and paramagnetic materials.

Diamagnetism arises from the interaction of paired electrons with a magnetic field whereas paramagnetism comes from the presence of unpaired electrons in the system. A diamagnet with a small negative χ value (-10^{-5} to $-10^{-6} \text{ cm}^3\text{mol}^{-1}$) is slightly repelled by the magnetic field whereas a paramagnet with a small positive χ value (10^{-3} to 10^{-5}) is

attracted towards the applied field (Figure 1-1). Diamagnetic susceptibilities are independent of field and temperature, whereas paramagnetic susceptibilities of individual isolated paramagnets are inversely proportional with temperature, $\chi = C/T$, where C is Curie constant.¹⁹ However, when the spins come within weak interactions with each other, the relationship is modified using the Curie-Weiss expression, $\chi = C/(T - \theta)$ where θ is proportional to the strength of coupling between adjacent spins.

The type of spin-coupling of adjacent spin pairs, further categorizes the paramagnetic materials. For example, ferromagnetic ordering is achieved when the spins are aligned parallel ($\uparrow\uparrow$) and antiferromagnetic ordering is the result of antiparallel ($\uparrow\downarrow$) spin alignment of the spin pair (Figure 1-2). The commonly known ferromagnetic solids are the materials made of iron, cobalt, nickel and several rare earth metals and their alloys.²⁰ Their susceptibilities vary from 50 to 10,000. Ferrimagnets (e.g. magnetite, Fe_3O_4) also arise from antiferromagnetic coupling; however, a net magnetic moment is achieved due to only partial cancellation of unequal spins (Figure 1-2). Ferro- and ferrimagnetic ordering occurs below a critical temperature, T_c and that for antiferromagnets is below the Neel temperature, T_N when the magnetic moments align in small domains. In the absence of an applied field, the magnetization of the different domains orient randomly and cancel out each other to give a net zero magnetization, thermodynamically (entropically) favored, regardless of the nature of interactions. The situation changes in the presence of an external field when all the domains tend to line up in the direction of the field. At a certain field, magnetization saturation is achieved with a net magnetic moment when all the spins are aligned into one giant domain. The system retains the condition unless an external force is provided to overcome the

energy barrier for domain formation. This property is characteristic of any magnet and can be monitored by the magnetization vs. field study commonly known as hysteresis loop measurement (Figure 1-3).¹⁸ The term hysteresis comes from the fact that the molecule can retain its history as long as no additional field is applied. This makes magnetic data storage possible in ferro- and ferrimagnetic materials. Other magnetic ordering phenomena include spin glass, metamagnetic and canted ferro/antiferromagnetic behavior.²¹

Metal and metal-oxide based traditional magnets or molecular magnets with three dimensional arrays of linked interacting molecules are well reviewed and discussed elsewhere.^{19,22,23} The newest addition to this category is SMMs, where magnetism is zero-dimensional. The necessity of finding new magnets can be understood by analyzing the need of modern technology which is to develop miniaturized devices. In information storage, this would lead to a higher capacity to store digital information in a given area. Hence, the essential need for nanoscale magnets of identical size and behavior. The so-called traditional 'top-down' approach for deriving smaller pieces of a magnet from larger chunks is unable to achieve the required demand of nanoscale magnets of both identical size and shape. In this regard, SMMs have drawn significant attention in the field of nanomagnetism because they represent an alternative, 'bottom-up' route to nanoscale magnetic materials. The 'bottom-up' approach has significant control over the size and magnetic properties of the materials by varying the protective organic shell around the metal core, and hence, single-size (monodispersity), crystallinity and true solubility (organic solvents) can be achieved for SMMs. They are unique types of magnets where individual molecules possess a significant barrier (vs.

kT) to magnetization relaxation, and thus exhibit the properties of a magnet below the blocking temperature (T_B). Here the magnetism is intrinsic to the molecule and does not occur from the intermolecular long range ordering as observed in traditional magnets. This interesting magnetic property comes from a combination of a high ground state spin (S) value (i.e. several unpaired electrons) and magnetic anisotropy (negative zero-field parameter, D). Even after the discovery of various SMMs in transition metal chemistry, the aforementioned $Mn_{12}Ac$ (Figure 1-4)²⁴ and other subsequent members of the $[Mn_{12}O_{12}(O_2CR)_{16}(H_2O)_4]$ ($R = Et, Ph, CHCl_2$ etc.) family¹¹ remain the most popular choice for study by chemists and physicists due to their ease of preparation, crystallinity, high S and D values and high molecular and crystallographic symmetry, which simplifies the spin Hamiltonian and reduces the complexity in various theoretical calculations. Structurally, this well explored family consists of an external belt of eight Mn^{3+} ions ($S = 2$) antiferromagnetically coupled to an inner core of four ferromagnetically coupled Mn^{4+} ions ($S = 3/2$, Figure 1-4) to give an $S = 10$ ground state spin.²⁵ The negative zero-field parameter D is responsible for the loss of degeneracy of the associated m_s levels, where $m_s = +10$ and $m_s = -10$ are the lowest in energy. Thus, there exists an energy barrier for the conversion of the 'spin up' to the 'spin down' situation (Figure 1-5). The slow relaxation of the magnetization vector is a result of this energy barrier, calculated as $S^2 |D|$ for an integer spin and $(S^2 - 1/4) |D|$ for a half-integer spin system.¹² This spin barrier is the reason behind the interesting magnetic behavior of these individual molecules, and the barrier results in a hysteresis loop as also observed in traditional magnets (Figure 1-5). The most unique feature of these magnets is not only the capacity of storing information at a molecular level but the

quantum effects which are manifested in the step-like hysteresis loop (Figure 1-6).¹⁹ The observed steps are the result of faster rate of relaxation of the magnetization vector from one side of the potential energy barrier to the other side when there is an accidental degeneracy in the m_s levels (Figure 1-7). The phenomenon is known as the quantum tunneling of magnetization (QTM)²⁶ which indicates the relaxation in an SMM is not just due to the thermal activation barrier. Transverse anisotropy promotes the tunneling through the energy barrier, which can be achieved by the low symmetry components of the crystal field and by a magnetic field generated by magnetic nuclei. This quantum feature in an SMM makes them interesting potential candidates to be used as quantum bits (qubits) in quantum computation.²⁷⁻³² A quantum computer is a device for computation that is based on quantum mechanics such as superposition and entanglement. Information in traditional computer is stored by strings of '0' and '1's called bits. Quantum information uses qubits, where the two distinguishable configurations (bits, 0 & 1) can have superposition or any combination to give coupled states (00, 11, 01, 10).²⁸ The QTM and quantum phase interference observed in an SMM surely make them attractive to be a part of the designing of new quantum information processing system. In order to achieve the dream goal of using SMMs in real world application, extensive research is necessary to synthesize the appropriate systems and a thorough investigation of various synthetic schemes is the key to this success.

The criteria for making nanomaterials at a molecular level depend mainly on the choice of metal ions and the ligands needed to hold several metals together. Manganese has been the transition metal of choice for SMMs mainly due to the

availability of the anisotropic Mn^{3+} ion.^{10,33-45} Large S values of the resulting molecule can result from (a) ferro- or ferrimagnetic spin alignments and/or (b) competing interactions (spin frustration) in certain M_x topologies that prevent (frustrate) the preferred spin alignment. In case (a), ferromagnetic interactions can result from ligands or structural characteristics known to give ferromagnetic coupling between metal centers. In this regard various RCO_2^- ($R = Me, Et$ etc.) groups and end-on azide bridges are known to promote ferromagnetic coupling between bridging metal ions. To facilitate the formation of polynuclear manganese clusters, many researchers have employed alkoxide-based ligands (Figure 1-8 and 1-9), since this functionally is an excellent bridging group that fosters higher nuclearity product formation.⁴⁶⁻⁵² Such polydentate ligands have led to the discovery of many interesting 3d clusters, some of which display SMM behavior. The successful alkoxide-based ligands so far used in making SMMs in 3d cluster chemistry can be broadly classified into four categories such as pyridyl alcohols, non-pyridyl alcohols, pyridyl oximes and non-pyridyl oximes ligands (Figure 1-8 and Figure 1-9).⁵³ Variation of the bulkiness and the electronic properties of the ligands especially near the bridging O atoms, make them quite interesting to study. It is important to note that many of the ligands are comprised of an ethylene amine backbone. These N, O based ligands have proven to be quite useful in linking higher oxidation state Mn^{3+} or Mn^{4+} to make polynuclear metal clusters.

Following the trail of the ongoing research on making polynuclear Mn based metal clusters, work in this thesis has employed the potentially hexadentate (O,O,O,O,N,N) N,N,N',N' -tetrakis(2-hydroxyethyl) ethylenediamine (edteH₄, Figure 1-10) ligand. Once deprotonated the edteH₄ contains four flexible alkoxide arms that can bridge two or

more metal ions and give high nuclearity products.⁵⁴ The following chapters will show how small changes to the reaction conditions affect the product identity in edteH₄ coordination chemistry. Chapter 2 presents the use of simple Mn salts in making a family of Mn₁₂ SMMs. The electrochemical and magnetochemical properties are discussed. Chapter 3 elucidates how a bulky carboxylate can affect the identity and physiochemical properties of the product, which leads to the isolation of Mn₉. The obtained complex is a rare example of new half-integer spin SMM, and various experimental and computational analyses have been performed. Chapter 4 shows the richness and structural variety encountered in Mn_x and Mn/Ca cluster chemistry (where x = 3, 4, 6, 10 and 20) using the same ligand. Chapter 5 brings new flavor by introducing heterometallic Mn-Ln SMMs (Mn₄Ln₂) using the same ligand. Hence, edteH₄ has proved to be a rich source of many unprecedented metal clusters and the following chapters will unfold the story of this polydentate ligand edteH₄ in Mn, Mn-Ca and Mn-Ln cluster chemistry.

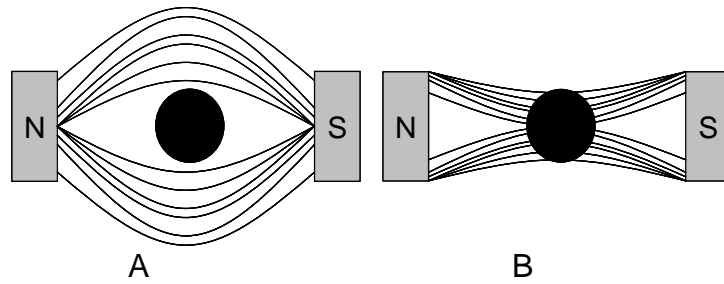


Figure 1-1. Representation of magnetic field lines of flux (A) for a diamagnetic substance in a magnetic field and (B) for a paramagnetic substance in a magnetic field

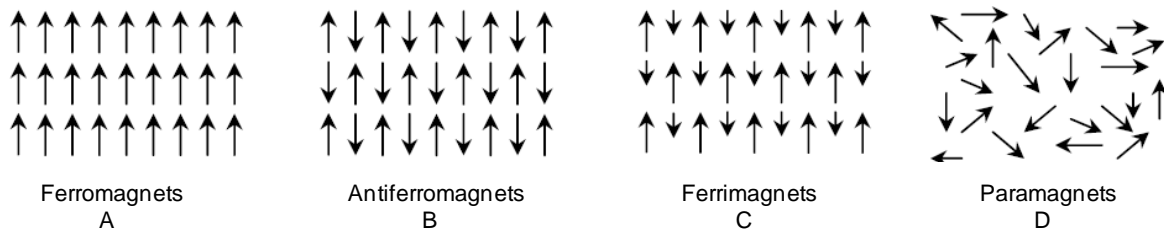


Figure 1-2. Magnetic dipole arrangements in different types of materials. (A) ferromagnetic, (B) ferrimagnetic, (C) antiferromagnetic, and (D) paramagnetic materials

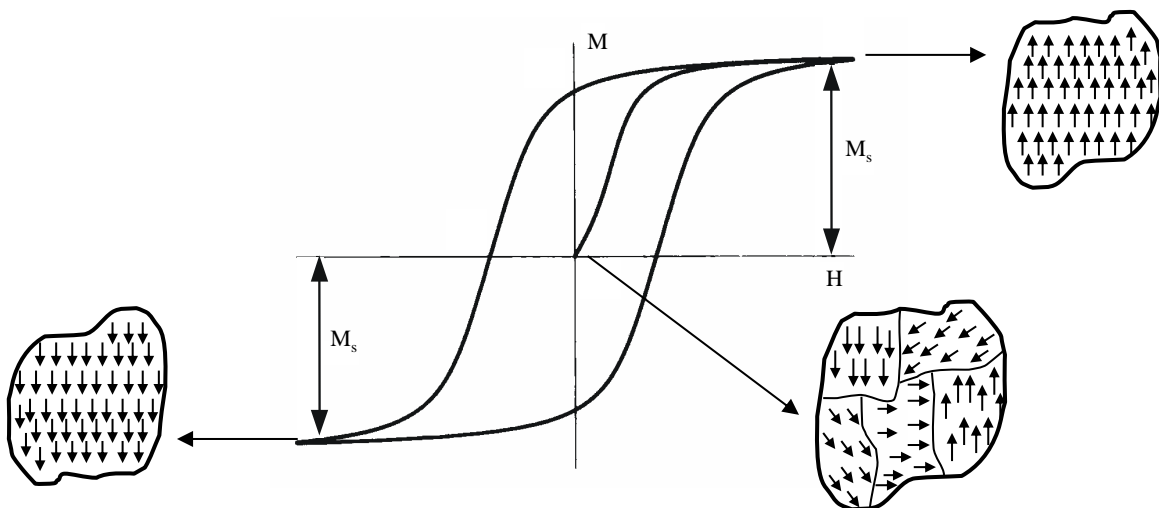


Figure 1-3. Typical hysteresis loop of a magnet, where M is magnetization, H is the applied magnetic field and M_s is the saturation value of the magnetization

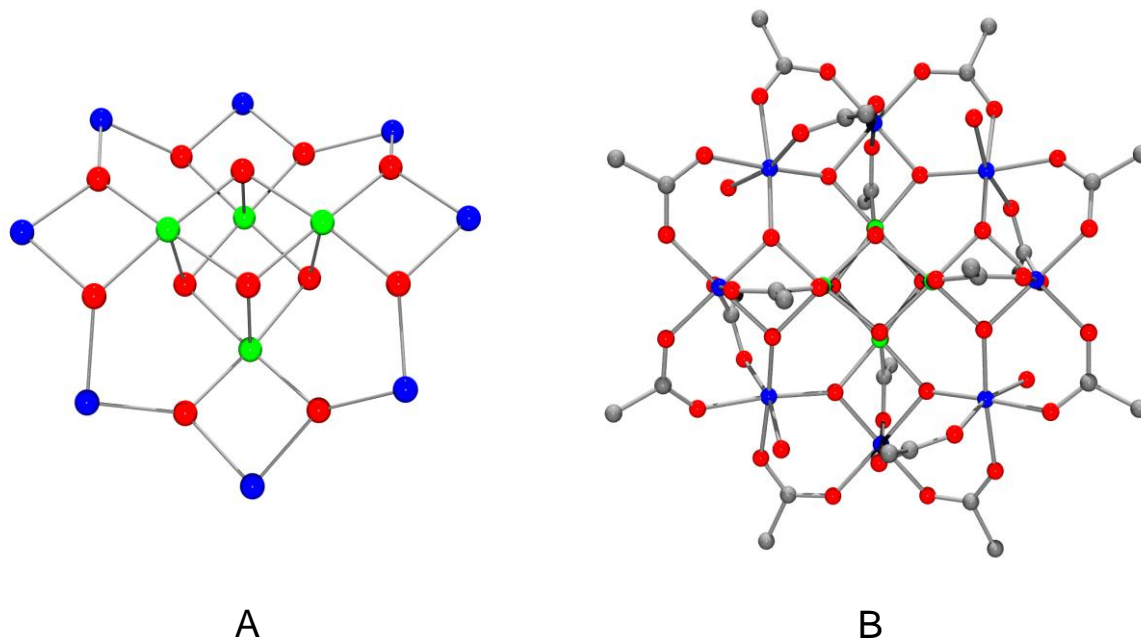


Figure 1-4. Representation of the $[\text{Mn}^{\text{III}}_8\text{Mn}^{\text{IV}}_4(\mu_3\text{-O}^{2-})_{12}]^{16+}$ core (A) and the $[\text{Mn}_{12}\text{O}_{12}(\text{O}_2\text{CMe})_{16}(\text{H}_2\text{O})_4]$ complex with acetates as peripheral ligands (B). Mn⁴⁺ green; Mn³⁺ blue; O red; C gray

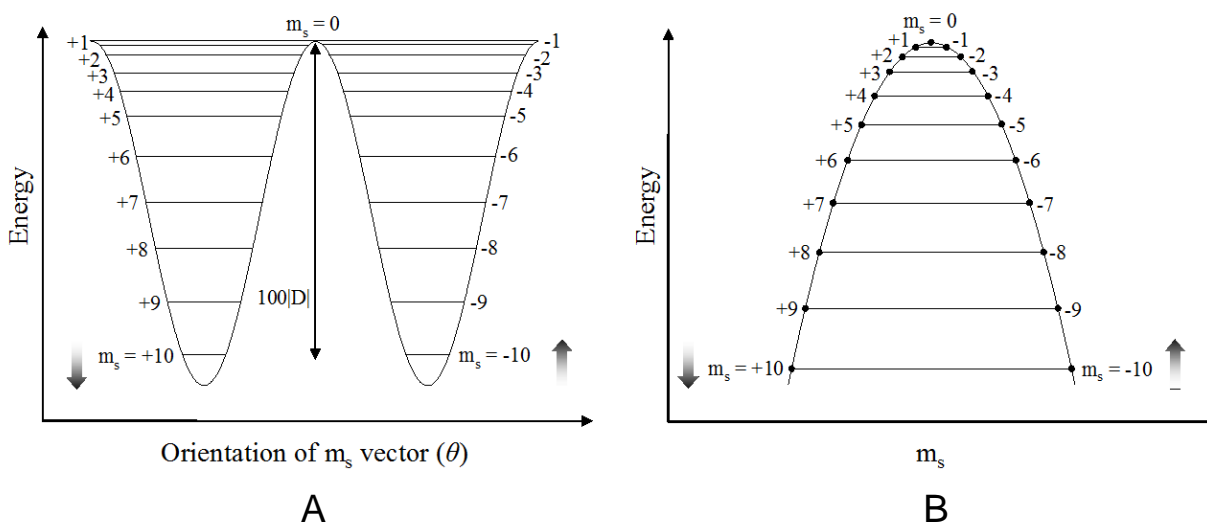


Figure 1-5. Representative plots of the potential energy barrier for an SMM. (A) Plot of the energy versus the m_s sublevel for a Mn_{12} complex with an $S = 10$ ground state, experiencing zero-field splitting, $D\hat{S}_z^2$ and (B) plot of the energy versus the orientation of the m_s vector (θ) along the z axis.

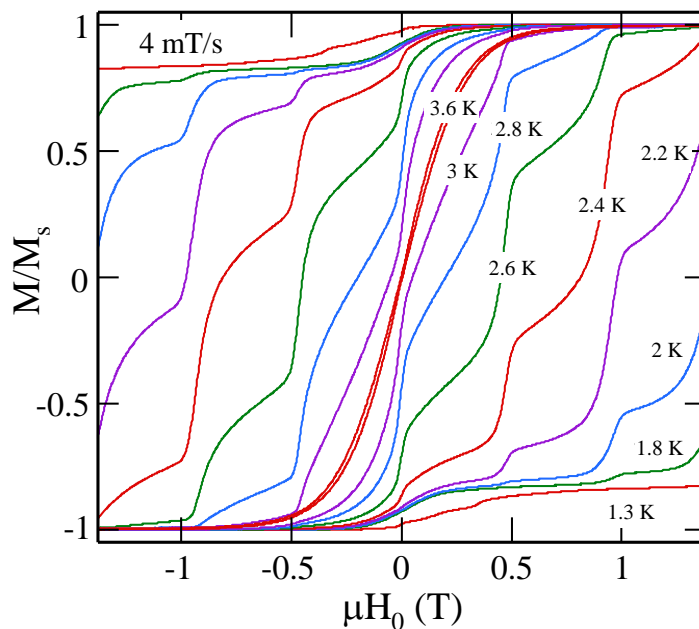


Figure 1-6. Magnetization hysteresis loops for a typical $[\text{Mn}_{12}\text{O}_{12}(\text{O}_2\text{CR})_{16}(\text{H}_2\text{O})_4]$ complex in the 1.3 - 3.6 K temperature range at a 4 mT/s field sweep rate. M is normalized to its saturation value, M_s

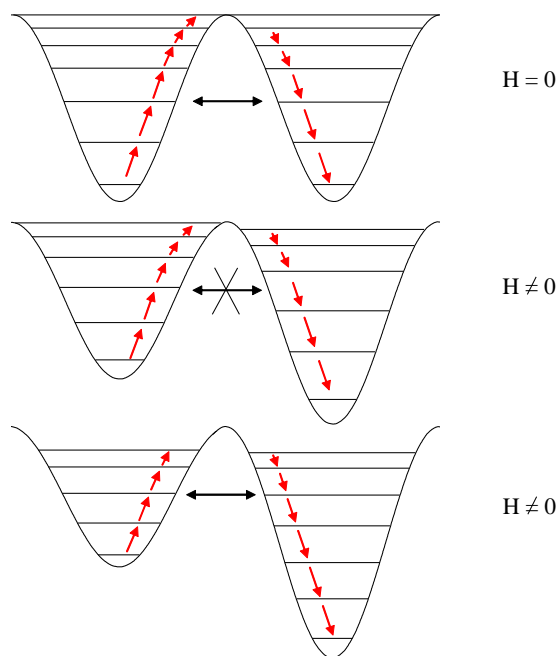
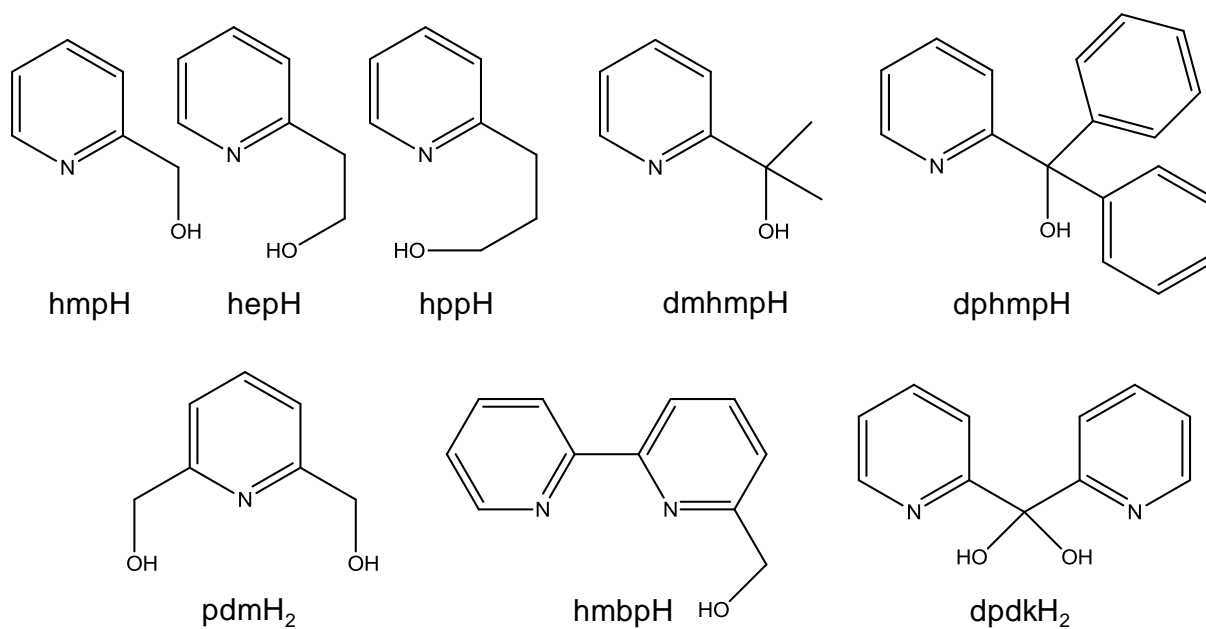
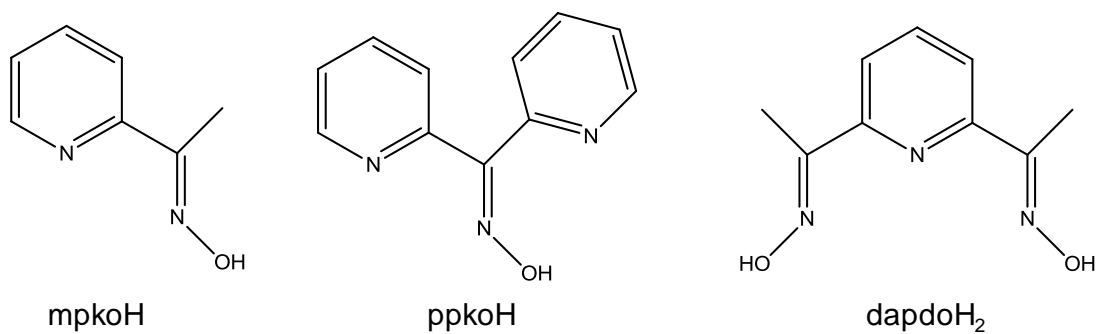


Figure 1-7. Schematic representation of the change in energy of m_s sublevels as the magnetic field is swept from zero to a non-zero value. Resonant magnetization tunneling occurs when the m_s sublevels are aligned between the two halves of the diagram

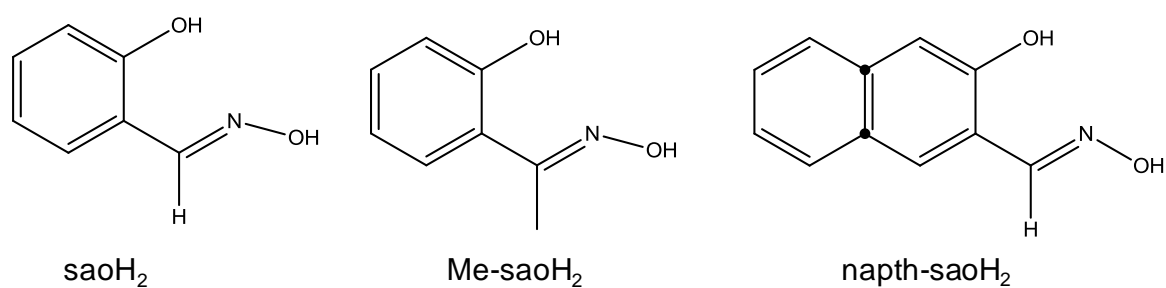
Pyridyl alcohols



Pyridyl-oximes and -dioximes



Non-pyridyl-oximes



Figures 1-8. Representative examples of pyridyl alcohols, pyridyl oximes and non-pyridyl oxime ligands

Non-pyridyl alcohols

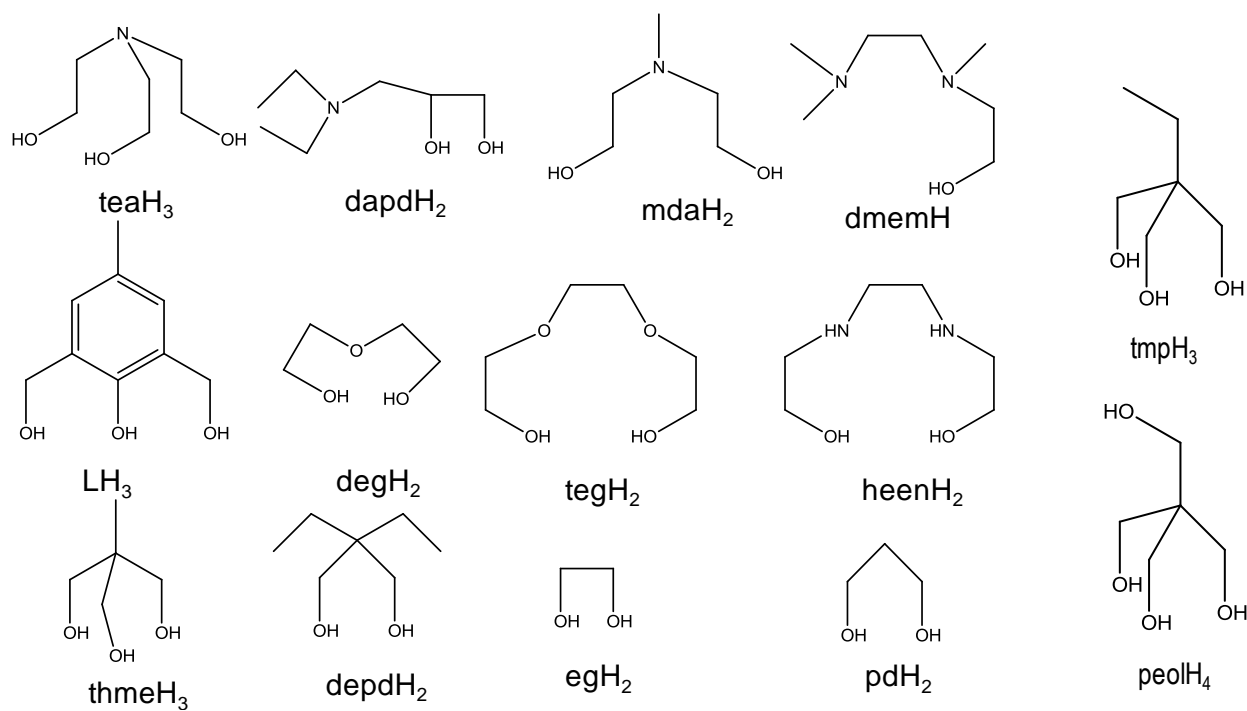


Figure 1-9. Representative examples of non-pyridyl alcohols

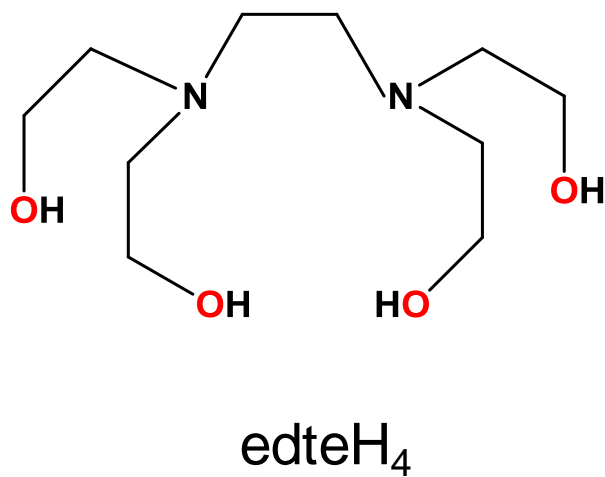


Figure 1-10. *N,N,N',N'*-tetrakis(2-hydroxyethyl) ethylenediamine

CHAPTER 2
SYNTHESIS, STRUCTURE AND ELECTROCHEMICAL AND MAGNETOCHEMICAL
PROPERTIES OF A FAMILY OF Mn_{12} COMPLEXES CONTAINING THE ANION OF
 N,N,N',N' -TETRAKIS(2-HYDROXYETHYL) ETHYLENEDIAMINE

The synthesis of high spin transition metal clusters has become an important sub-discipline of coordination chemistry, especially since the discovery of single-molecule magnets (SMMs)¹¹ in the early nineties. These are individual molecules that possess a significant barrier ($vs kT$) to magnetization relaxation, and thus exhibit the properties of a magnet below their blocking temperature (T_B). The SMM property results from a combination of a high-spin ground state (S) value and an easy-axis type magnetoanisotropy (negative zero-field parameter, D).⁵⁵⁻⁵⁸ Manganese has been the transition metal of choice for SMMs mainly due to the availability of the anisotropic Mn^{3+} (Jahn-Teller distorted ion).^{16,25,26,33} Large S values can result from (a) ferro- or ferrimagnetic spin alignments and/or (b) competing interactions (spin frustration) in certain M_x topologies that prevent (frustrate) the preferred spin alignment. In case (a), ferromagnetic interactions can result from ligands or structural characteristics known to give ferromagnetic coupling between metal centers. One of the best ferromagnetic couplers is the azide (N_3^-) group when it bridges metals in the 1,1-(end-on) fashion.⁵⁹

Following the trail of ongoing research, we have been recently exploring new synthetic methodologies by combining a potentially hexadentate, alcohol-based chelate (O,O,O,O,N,N) N,N,N',N' -tetrakis(2-hydroxyethyl)ethylenediamine (edteH₄, Figure 1-10) with azides. This chelate is comprised of an ethylenediamine backbone with hydroxyethyl arms, which upon deprotonation act as bridging groups to foster formation of high nuclearity clusters. EdteH₄ has been reported by our group to produce Mn_8 , Mn_{12} and Mn_{20} clusters with novel metal topologies.⁶⁰ In addition, edteH₄ has also

produced various Fe_x ($x = 5, 6, 12$)⁵⁴ complexes recently for our group. Previous use of edteH₄ in the literature with other metals has been limited to the preparation of only mononuclear Ca and dinuclear Ba, Cu and V complexes.^{61,62}

It should also be mentioned that during the progress of the ongoing research in our group two Mn₁₂ complexes similar to complexes **2-2** and **2-3** were reported by another research group, Zhou et al.⁶³ However, a thorough study of a much cleaner synthesis and a detailed magnetic study have been performed in our work. For the first time, low temperature hysteresis measurements have been performed for complex **2-1** of this newly found family of Mn₁₂ complexes which differ a lot from the well-explored family of novel $[\text{Mn}_{12}\text{O}_{12}(\text{O}_2\text{CR})_{16}(\text{H}_2\text{O})_4]$ complexes (R = Me, Et etc) known for many years.¹¹

Herein, we report that the use of edteH₄ and azide together in a variety of reactions with manganese salts has resulted in a family of Mn₁₂ SMMs at different oxidation states. The syntheses, crystal structures and electrochemical and magnetic characterization of this Mn₁₂ family will be described.

Experimental Section

Syntheses

All preparations were performed under aerobic conditions using reagents and solvents as received. *Caution! Although no such behavior was observed during the present work, perchlorate and azide salts are potentially explosive; such compounds should be synthesized and used in small quantities, and treated with utmost care at all times.*

[Mn₁₂O₄(OMe)₂(edte)₄(N₃)₈](ClO₄)(N₃) (2-1). To a stirred solution of edteH₄ (0.15 g, 0.64 mmol) and NMe₄OH (0.12 g, 0.64 mmol) in MeCN/MeOH (10/1, v/v) was added

Mn(ClO₄)₂ (0.46 g, 1.28 mmol). The resulting dark-brown solution was stirred for 15 minutes and then NaN₃ (0.08 g, 1.28 mmol) was added to the solution and stirred for further 3 hours. The solution was then filtered and the filtrate left undisturbed at room temperature. After 5 days from slow evaporation, X-ray quality, dark-brown plate-like crystals of **2-1**·MeCN slowly grew in a yield of 30%. The crystals were collected by filtration, washed with Et₂O, and dried in vacuum. Anal. Calc. (found) for **2-1** (solvent-free): C, 23.01 (23.03); H, 3.95 (3.90); N, 22.36 (22.14) %. Selected IR data (cm⁻¹): 2858 (m), 2066 (vs), 1636 (w), 1464 (w), 1337 (w), 1086 (s), 927 (m), 899 (m), 676 (s), 619 (s), 559 (s).

[Mn₁₂O₄(OH)(edte)₄(N₃)₉] (2-2). To a stirred solution of edteH₄ (0.15 g, 0.64 mmol) and NMe₄OH (0.12 g, 0.64 mmol) in MeCN/MeOH (10/1, v/v) was added MnCl₂ (0.25 g, 1.28 mmol). The resulting dark-brown solution was stirred for 15 minutes and then NaN₃ (0.16 g, 2.56 mmol) was added to the solution and stirred for a further 3 hours. The solution was then filtered and the filtrate was layered with diethyl-ether. After 10 days, X-ray quality, dark-brown plate-like crystals of **2-2**·x(solvent) grew in a yield of 13%. The crystals were collected by filtration, washed with Et₂O, and dried in vacuum. Anal. Calc. (found) for **2-2**·6H₂O·2MeCN: C, 23.62 (24.17); H, 4.46 (4.14); N, 23.16 (22.66) %. Selected IR data (cm⁻¹): 2855 (s), 2056 (vs), 1634 (w), 1459 (w), 1336 (w), 1086 (s), 926 (m), 900 (m), 657 (m), 606 (m), 567 (s).

[Mn₁₂O₄(OH)(edte)₄(N₃)₉](ClO₄)(N₃) (2-3). To a stirred solution of edteH₄ (0.15 g, 0.64 mmol) and NEt₃ (0.09 g, 0.64 mmol) in MeCN (10mL) was added Mn(ClO₄)₂ (0.46 g, 1.28 mmol). The resulting dark-brown solution was stirred for 15 minutes and then NaN₃ (0.08 g, 1.28 mmol) was added to the solution and stirred for a further 3 hours.

The solution was then filtered and the filtrate left undisturbed at room temperature. After 7 days from slow evaporation, X-ray quality, dark-brown plate-like crystals of **2-3**·MeCN grew in a yield of 36%. The crystals were collected by filtration, washed with Et₂O, and dried in vacuum. Anal. Calc. (found) for [Mn^{III}₁₂O₄(OH)(edte)₄(N₃)₉](ClO₄)(OH)]·2MeCN: C, 23.53 (23.60); H, 3.95 (3.90); N, 23.07 (23.11) %. Selected IR data (cm⁻¹): 2867 (w), 2066 (m), 1636 (m), 1458 (w), 1089 (vs), 924 (m), 628 (s), 552 (w).

X-ray Crystallography

Data were collected on a Siemens SMART PLATFORM equipped with a CCD area detector and a graphite monochromator utilizing Mo-K α radiation ($\lambda = 0.71073 \text{ \AA}$). Suitable crystals of **2-1**·MeCN, **2-2**·x(solvent) and **2-3**·MeCN were attached to glass fibers using silicone grease and transferred to a goniostat where they were cooled to 173 K for data collection. Cell parameters were refined using up to 8192 reflections. A full sphere of data (1850 frames) was collected using the ω -scan method (0.3° frame width). The first 50 frames were re-measured at the end of data collection to monitor instrument and crystal stability (maximum correction on I was < 1 %). Absorption corrections by integration were applied based on measured indexed crystal faces. The structure was solved by direct methods in *SHELXTL6*, and refined on F^2 using full-matrix least squares. The non-H atoms were treated anisotropically, whereas the hydrogen atoms were placed in ideal, calculated positions and were refined as riding on their respective C atoms.

For **2-1**·MeCN, the asymmetric unit consists of a $\frac{1}{4}$ Mn₁₂ cluster dication, a $\frac{1}{4}$ perchlorate anion, and a $\frac{1}{4}$ azide anion disordered against a $\frac{1}{4}$ acetonitrile. The latter would imply that the acetonitrile or the azide anion should have a 0.5 site occupation factor but because of the disorder, each fragment has a site occupation factor of 0.25.

The perchlorate anion is disordered in its oxygen atoms which were refined in two parts. One of the cluster azides, N6-7-8, is disordered and the latter two were refined in two parts. A total of 282 parameters were included in the final cycle of refinement using 4718 reflections with $I > 2\sigma(I)$ to yield R_1 and wR_2 of 5.06 and 15.97%, respectively.

For **2-2**·x(solvent), the asymmetric unit consists of the Mn_{12} cluster and disordered solvent molecules. Program SQUEEZE,⁶⁴ a part of the PLATON package of crystallographic software, was used to calculate the solvent disorder area and remove its contribution to the overall intensity data. H1, the O18 hydroxyl proton was obtained from a Difference Fourier map and refined as riding on its parent atom. A total of 972 parameters were included in the final cycle of refinement using 6671 reflections with $I > 2\sigma(I)$ to yield R_1 and wR_2 of 5.54 and 12.44%, respectively.

For **2-3**·MeCN, the asymmetric unit consists of a $\frac{1}{4}$ Mn_{12} cluster dication, a $\frac{1}{4}$ perchlorate anion, and a $\frac{1}{4}$ azide anion disordered against a $\frac{1}{4}$ acetonitrile, located on the 2-fold rotation axis. The latter would imply that the acetonitrile or the azide anion should have a 0.5 site occupation factors but because of the disorder, each fragment has a site occupation factor of 0.25. The cluster cation has one azide, N9-10-11, disordered and refined in two parts. There is also a disorder between the N6-7-8 and the O6 hydroxyl group. Due to symmetry, each fragment is assigned a site occupation factor of 0.5. A total of 282 parameters were included in the final cycle of refinement using 3060 reflections with $I > 2\sigma(I)$ to yield R_1 and wR_2 of 5.68 and 16.47%, respectively. The crystallographic data and structure refinement details for the three compounds are listed in Table 2-1.

Physical Measurements

Infrared spectra were recorded in the solid state (KBr pellets) on a Nicolet Nexus 670 FTIR spectrometer in the 400 - 4000 cm^{-1} range. Elemental analyses (C, H and N) were performed by the in-house facilities of the University of Florida, Chemistry Department. Electrochemical studies were performed under argon using a BAS model CV-50W voltammetric analyzer and a standard three-electrode assembly (glassy carbon working, Pt wire auxiliary, and Ag wire reference) with 0.1 M NBU_4PF_6 as supporting electrolyte. Quoted potentials are vs. the ferrocene/ferrocenium couple, used as an internal standard.⁶⁵ Variable-temperature dc and ac magnetic susceptibility data were collected at the University of Florida using a Quantum Design MPMS-XL SQUID susceptometer equipped with a 7 T magnet and operating in the 1.8 - 300 K range. Samples were embedded in solid eicosane to prevent torquing. Magnetization vs. field and temperature data was fit using the program MAGNET.⁶⁶ Pascal's constants were used to estimate the diamagnetic correction, which was subtracted from the experimental susceptibility to give the molar paramagnetic susceptibility (χ_M). Low-temperature (<1.8 K) hysteresis loop and dc relaxation measurements were performed in Grenoble using an array of micro-SQUIDs.⁶⁷ The high sensitivity of this magnetometer allows the study of single crystals of the order of 10 to 500 μm . The field can be applied in any direction by separately driving three orthogonal coils.

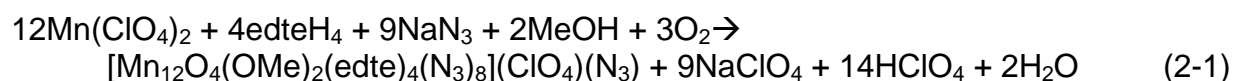
Results and Discussion

Syntheses

Recently, end-on bridging azide groups have proved to be ferromagnetic couplers, and they have been widely employed in manganese cluster chemistry.⁵⁹ In order to make clusters containing Mn^{3+} ions, it is generally necessary to oxidize simple Mn^{2+}

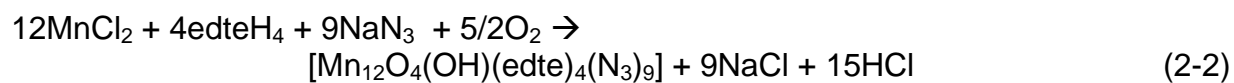
salts. Here, the combination of *N,N,N',N'*-tetrakis(2-hydroxyethyl)ethylenediamine (edteH₄), and azides with various Mn salts has been employed and has afforded three Mn₁₂ complexes which have similar but not identical structures.

The reaction of edteH₄ with Mn(ClO₄)₂, NEt₄OH and NaN₃ in a 1:2:1:2 molar ratio in MeCN/MeOH (10/1, v/v) afforded a reddish-brown solution from which was subsequently obtained the dodecanuclear complex [Mn₁₂O₄(OMe)₂(edte)₄(N₃)₈](ClO₄)(N₃)] (**2-1**) in 30% yield. Its formation is summarized in eq. 2-1, where atmospheric oxygen gas is assumed to provide the oxidizing equivalents.



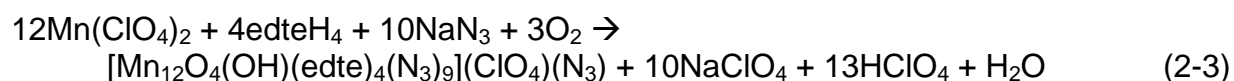
The same product in comparable yield can be obtained by using a Mn(NO₃)₂ as a metal source or different base like LiOH, Et₃N or by varying the amount of NaN₃ or by using NBuⁿ₄N₃ as an azide source. However, the above ratio gives the purest product in the highest yield.

A slight variation in the manganese salt and with a higher amount of NaN₃ resulted in a mixed-valent Mn₁₂ complex with Mn²⁺ and Mn³⁺ ions. The reaction of edteH₄ with MnCl₂, NEt₄OH and NaN₃ in a 1:2:1:4 molar ratio in MeCN/MeOH (10/1, v/v) afforded a reddish-brown solution from which was subsequently obtained the dodecanuclear complex [Mn³⁺₁₀Mn²⁺₂O₄(OH)(edte)₄(N₃)₉] (**2-2**) in 13% yield (eq. 2-2). The same product with a comparable yield was obtained by using a different solvent combination of MeCN/DMF (10/1, v/v). Complex **2-2** contains five bridging azide ligand whereas compound **2-1** contains four (Figure 2-5).



It is important to mention that the above reaction scheme in the absence of azide gives a known Mn₁₂ complex⁶⁰ containing bridging and terminal chlorides. The use of azide promotes preferential binding of azide to high oxidation state Mn ions owing the hard acid – hard base interaction.

When only MeCN was used as the solvent rather than the mixed-solvent, yet another Mn₁₂ complex was isolated. The reaction of edteH₄ with Mn(ClO₄)₂, NEt₄OH and NaN₃ in a 1:2:1:2 molar ratio in MeCN afforded a reddish-brown solution from which was subsequently obtained the dodecanuclear complex [Mn₁₂O₄(OH)(edte)₄(N₃)₉](ClO₄)(N₃) (**2-3**) in 36% yield (eq. 2-3).



It is clear that the described reactions to complex **2-1** to **2-3** are complicated and involve acid-base (water deprotonation to O²⁻/OH⁻ or methanol to OMe⁻) and redox chemistry (Mn²⁺ oxidation) as well as structural rearrangements. It is interesting to note that a slight variation in the identity of the starting materials including Mn salt, base or azide and solvent and their ratio leads to three new Mn₁₂ complexes. Similarity in the reaction scheme has influenced certain structural resemblance results in Mn/O²⁻/edte⁴⁻ ratio as 3:1:1 in all three complexes.

Description of Structures

Structure of [Mn₁₂O₄(OMe)₂(edte)₄(N₃)₈](ClO₄)(N₃) (**2-1**)

A labeled representation and a stereopair of the cation of **2-1** are shown in Figure 2-1 and selected interatomic distances and angles are listed in Table A-1. Complex **2-1** crystallizes in the tetragonal space group P-42₁c with the Mn₁₂ molecule lying on an S₄ symmetry axis and thus only one quarter of this is in the asymmetric unit. The core of **2-**

1 consists of a $[\text{Mn}_{12}(\mu_4\text{-O})_4]^{28+}$ unit (Figure 2-4, A) where each $[\text{Mn}_4(\mu_4\text{-O})]^{10+}$ subunit is connected to a neighboring one by sharing a common Mn^{3+} ion. For the sake of brevity, reference to specific atoms in the following discussion includes their symmetry-related partners. The four $\mu_4\text{-O}^{2-}$ ions (O1) thus serve to connect all twelve Mn atoms. A BVS calculation⁶⁸⁻⁷⁰ for the Mn atoms (Table 2-2) identified Mn1, Mn2 and Mn3 as Mn^{3+} ions. Mn1 and Mn2 are six-coordinate while Mn3 is seven-coordinate. Each edte⁴⁻ group is hexadentate-chelating on Mn3, with each of its deprotonated alkoxide arms bridging to either one (O2, O3, O5) or two (O4) additional Mn atoms. Thus, the edte⁴⁻ groups are overall $\eta^2:\eta^2:\eta^2:\eta^3:\mu_5$ -bridging, as shown in Figure 2-6. The core of **2-1** is additionally bridged by two Mn1-OMe-Mn1 bridges and four end-on azide bridges (Mn1-N3-Mn2), as shown in Figure 2-5, A. Along with the end-on azide bridges, there are four terminal azide groups complete the coordination of Mn2 atom. Charge balance consideration requires 12 Mn^{3+} , 4 O^{2-} , 2 OMe^- , 4 edte⁴⁻, 8 N_3^- , and two additional negative charges from the counter anions. The protonation levels of all O atoms were confirmed in **2-1** by BVS calculations, and the results are listed in Table 2-3. The oxide, MeO^- and edte⁴⁻ oxygen atoms have BVS values of >1.87, confirming them as completely deprotonated, as suggested from their bridging modes.

Structure of $[\text{Mn}_{12}\text{O}_4(\text{OH})(\text{edte})_4(\text{N}_3)_9]$ (**2-2**)

A labeled representation and a stereopair of **2-2** are shown in Figure 2-2 and selected interatomic distances and angles are listed in Table A-2. Complex **2-2** crystallizes in the monoclinic space group $\text{P}2_1/\text{n}$. The core of **2-2** consists of a $[\text{Mn}_{12}(\mu_4\text{-O})_4]^{26+}$ unit (Figure 2-4, B) where each $[\text{Mn}_4(\mu_4\text{-O})]^{n+}$ ($n = 10, 9$) subunit is connected to a neighboring one by sharing a common Mn^{3+} ion. The four $\mu_4\text{-O}^{2-}$ ions (O1) together serve to connect all twelve Mn atoms. BVS calculations for the Mn atoms (Table 2-2)

identified Mn1, Mn3, Mn4, Mn5, Mn6, Mn7, Mn9, Mn10, Mn11 and Mn12 as Mn³⁺ ions, and Mn2 and Mn8 as Mn²⁺ ions. Mn9, Mn3, Mn6, Mn5, Mn2, Mn8, Mn11 and Mn12 are six coordinate while Mn1, Mn4, Mn7 and Mn10 are seven coordinate. Each edte⁴⁻ group is hexadentate-chelating on a Mn³⁺ atom, with each of its deprotonated alkoxide arms bridging to either one or two additional Mn atoms. Thus, the edte⁴⁻ groups are overall $\eta^2:\eta^2:\eta^2:\eta^3:\mu_5$ -bridging, as shown in Figure 2-6. The core of **2-2** also contains one Mn3-OH18-Mn9 and one Mn6-N30-Mn12 bridging units, and four end-on azide bridges as shown in Figure 2-5 (B). Along with the end-on azide bridges, there are four terminal azide groups complete the coordination of Mn2, Mn5, Mn8 and Mn11 atoms. Charge balance consideration and comparison with **2-1** suggests 10 Mn³⁺, 2Mn²⁺, 4O²⁻, 1OH⁻, 4edte⁴⁻ and 9N₃⁻. The protonation levels of all O atoms in **2-2** were confirmed by BVS calculations, and the results are listed in Table 2-4. The oxide and edte⁴⁻ O atoms have BVS values of >1.85, confirming them as completely deprotonated, and BVS value for O18 is 1.01 as expected for OH⁻ group in the complex.

Structure of [Mn₁₂O₄(OH)(edte)₄(N₃)₉](ClO₄)(N₃) (**2-3**)

A labeled representation and a stereopair of the cation of **2-3** is shown in Figure 2-3 and selected interatomic distances and angles are listed in Table A-3. Complex **2-3** crystallizes in the tetragonal space group P-42₁c with the Mn₁₂ molecule lying on an S₄ symmetry axis and thus only one quarter of it is in the asymmetric unit. The core of **2-3** consists of a [Mn₁₂(μ_4 -O)₄]²⁸⁺ unit where each [Mn₄(μ_4 -O)]¹⁰⁺ subunit is connected to a neighboring one by sharing a common Mn³⁺ ion. (Figure 2-4, C). For the sake of brevity, reference to specific atoms in the following discussion includes their symmetry-related partners. The four μ_4 -O²⁻ ions (O1) thus serve to connect all twelve Mn atoms. BVS calculations for the Mn atoms (Table 2-2) identified Mn1, Mn2 and Mn3 as Mn³⁺ ions.

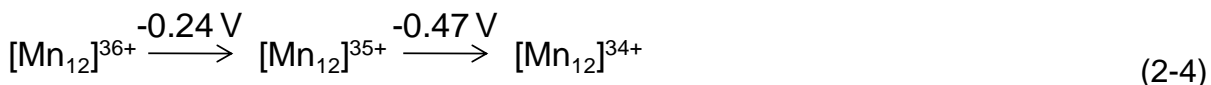
Mn1 and Mn2 are six-coordinate while Mn3 is seven-coordinate. Each edte⁴⁻ group is hexadentate-chelating Mn3, with each of its deprotonated alkoxide arms bridging to either one (O2, O3, O5) or two (O4) additional Mn atoms. Thus, the edte⁴⁻ groups are overall $\eta^2:\eta^2:\eta^2:\eta^3:\mu_5$ -bridging, as shown in Figure 2-6. There is a disorder between the N6-7-8 and the O6 hydroxyl group. The Mn1-O6 bond length of 2.049(9) Å is typical of Mn³⁺-OH⁻ and Mn1-N6 bond length of 2.151(15) Å is also indicative of the presence of Mn³⁺-N moiety in the cluster.⁷¹⁻⁷³ Due to the symmetry, each fragment is assigned a site occupation factor of 0.5. Hence, the molecular formula contains of one Mn1-OH-Mn1 and one Mn1-N6-Mn1 bridging moieties and four end-on azide bridges (Mn1-N3-Mn2) as shown in Figure 2-5 (C). Along with the end-on azide bridges, there are four terminal azide groups complete the coordination of Mn2 atom. Charge balance consideration and comparison with **2-1** suggests 12Mn³⁺, 4O²⁻, 1OH⁻, 4edte⁴⁻, 9N₃⁻ and two additional negative charges come from counteranions. The protonation levels of all O atoms in **2-3** were confirmed by BVS calculations, and the results are listed in Table 2-4. The oxide and edte⁴⁻ O atoms have BVS values of >1.85, confirming them as completely deprotonated, as concluded above from their bridging modes. All the three Mn₁₂ complexes possess similar metal topology however; the difference comes from the number of end-on azides bridges in the core of the complex.

There are many other structural types of Mn₁₂ complexes known in the literature (Table 2-6), the most well-explored being the [Mn₁₂O₁₂(O₂CR)₁₆(H₂O)₄] family, which has been extended over the years to include the 1e⁻, 2e⁻ and 3e⁻ reduced versions of [Mn₁₂]^{z-} family.^{11,74-80} Another Mn₁₂ family was isolated through the reductive aggregation of MnO₄⁻ in MeOH-containing media; this family differs from the previous

one in having a central Mn^{4+}_4 rhombus rather than a Mn^{4+}_4 tetrahedron.^{81,82} The rest of the Mn_{12} complexes cover a wide variety of other structural motifs, including loops, more complicated face-sharing cuboidal units, and wheels amongst others.^{46,83-92}

Electrochemistry

The scan rates for cyclic voltammetry (CV) and differential pulse voltammetry (DPV) were 20-500 mV/s and 20 mV/s respectively. Dry DMF solvent was used, and the concentration of the complex **2-1** was approximately 1 mM and the compound is partially soluble in the electrochemical solvent. Extensive electrochemical studies on the **2-1** have revealed a rich redox chemistry involving more than one peak in reduction processes measured at 100 mV/s (Figure 2-7). Two peaks at -0.24 V and -0.47 V are partially reversible by the usual electrochemical criteria (see Appendix C) suggesting that the Mn_{12} complexes are stable in multiple oxidation levels. The two reduction processes were measured at several scan rates of 20 - 500 mV/s ranges (Figure 2-9). The two observed partially reversible processes can be assigned as the one-electron reduction of Mn^{3+} to corresponding Mn^{2+} ion.⁹³ The isolation of a mixed-valent $\text{Mn}^{\text{II}}/\text{Mn}^{\text{III}}$, complex **2-2** with a similar metal topology suggests the existence of the reduced version of complex **2-1**. The observed CV behavior suggests the electron-transfer series shown in equation 2-4. The reported potentials are vs. ferrocene (ferrocene couple was measured at + 89 mV under the same conditions).



The DPV scans (Figure 2-8) for **2-1** complement the CV measurements. The sharpness of the two peaks at -0.24 and -0.47 V in DPV plot suggests the reversibility of the process. There is another irreversible peak observed at -0.005 V which is likely the

overlap of two oxidation processes. In the latter, a study of the scan rate dependence for the two reduction processes showed a linear dependence of the peak current with square-root of the scan rates ($v^{1/2}$), indicating that the reductions are diffusion-controlled processes (Figure 2-10).

Magnetochemistry

Dc magnetic susceptibility studies of 2-1, 2-2 and 2-3

Solid-state, variable-temperature dc magnetic susceptibility data in a 0.1 T field and in the 5.0 - 300 K range were collected on powdered microcrystalline samples of **2-1**, **2-2**·6H₂O·2MeCN and **2-3**·2MeCN. The obtained data are plotted as $\chi_M T$ vs. T in Figure 2-11. The $\chi_M T$ values of 42.09, 42.44, and 43.19 cm³Kmol⁻¹ are little smaller than the spin-only values ($g = 2$) as expected for non-interacting Mn³⁺₁₂ and Mn³⁺₁₀Mn²⁺₂ mixed-valence situations of **2-1** to **2-3**. The behavior is indicative of predominant antiferromagnetic interactions between the metal ions in the molecule. For all three complexes, $\chi_M T$ values stay fairly constant up to 100 K and decrease smoothly down to 20.31, 19.09 and 17.42 cm³Kmol⁻¹, suggestive of an $S = 6$ spin-ground state for all three of them.

To confirm the above initial estimates of the ground state spin of the three compounds, variable-field (H) and -temperature magnetization (M) data were collected in the 0.1 - 3 T and 1.8 - 10 K ranges. The resulting data for all three complexes are plotted as reduced magnetization ($M/N\mu_B$) vs. H/T , where N is Avogadro's number and μ_B is the Bohr magneton, shown in Figure 2-12. The data were further fitted using the program MAGNET,⁶⁶ by diagonalization of the spin Hamiltonian matrix assuming only the ground state is populated, incorporating axial anisotropy ($D\hat{S}_z^2$) and Zeeman terms,

and employing the full powder average. The corresponding spin Hamiltonian is given by the equation 2-5 where \hat{S}_z is the easy-axis spin operator, g is the Landé g factor, and μ_0 is the vacuum permeability. The last term in eq. 2-5 is the Zeeman energy associated with the applied magnetic field.

$$H = D\hat{S}_z^2 + g\mu_B\mu_0\hat{S}\cdot H \quad (2-5)$$

The best-fit data can be obtained for a certain value of S , g and D . Hence, the fitting verifies the spin-ground state as well as gives an estimation of g and D . However, for all the complexes, attempts to fit the data (using the procedure as above) resulted in poor quality and unreliable fits. The reason could be attributed to the presence of low-lying excited states because (i) the excited states are close enough to the ground state and they have a non-zero Boltzmann population even at the low temperatures used in the magnetization data collection, and/or (ii) even excited states that are more separated from the ground state but have an S value greater than that of the ground-state become populated as their larger M_S levels rapidly decrease in energy in the applied dc magnetic field and approach (or even cross) those of the ground state. Either (or both) of these two effects will lead to poor fits because the fitting program assumes population of only the ground state.⁹⁴⁻⁹⁶ A large density of low-lying excited states is expected for higher nuclearity complexes and the three complexes discussed in this chapter are no exceptions. However, fitting the data for complex **2-3** by fixing $S = 6$ gave a rough estimation of g (1.99) and D (-0.23 cm^{-1}) values. The obtained g value is quite reasonable for a system containing Mn^{3+} ions. One way to avoid the complications and to get a more reliable fitting parameters is to collect the data at lower fields and hence data were collected further in the 0.5 - 0.8 T and 1.8 - 10 K ranges. Due to the

similarity in the magnetic properties as established from the dc magnetic susceptibility studies, the results are mentioned for the complex **2-3** only. The best-fit to the data is shown as the solid lines in Figure 2-13, and was obtained with $S = 6$, $D = -0.27 \text{ cm}^{-1}$, and $g = 1.96$. Fitting with the positive D value gave an unreasonable g value of 2.15 for a system containing all Mn^{3+} ions and is discarded. Alternative fits with $S = 7$ and $S = 5$ gave $g = 1.74$ and $g = 2.39$, respectively. In order to ensure that the true global minimum was obtained and to assess the hardness of the fit, a root-mean-square D vs. g error surface for the fit was generated using the program GRID,⁹⁷ which calculates the relative difference between the experimental $M/N\mu_B$ data and those calculated for various combinations of D and g . This is shown as 2-D contour plot in Figure 2-14. Three local minima are observed. The one at $D = -0.35 \text{ cm}^{-1}$ exhibits the largest error and is hence discarded. Two global minima were obtained for $D = -0.25 \text{ cm}^{-1}$, $g = 1.95$ and $D = -0.30 \text{ cm}^{-1}$, $g = 1.98$. The minima of the other parameter set is shallow, and the fit uncertainties are thus estimated as $D = -0.27(2) \text{ cm}^{-1}$ and $g = 1.96(2)$.

Alternating current (ac) magnetic susceptibility studies for 2-1, 2-2 and 2-3

In an ac magnetic susceptibility experiment, a weak field of 3.5 G, oscillating at a particular frequency (ν) is applied to a sample to probe the magnetization relaxation dynamics. At a higher temperature (above T_b) the magnetization relaxation vector can keep in-phase with the oscillating ac field and the magnetic moment is same as dc susceptibility. The data is plotted as a real part of the ac susceptibility signal which is χ_M' . However, at low enough temperature (below T_b) the thermal energy is lower compared to the barrier of magnetization relaxation and the molecule cannot keep in-phase with the oscillating ac field. As a result the molecule exhibits an out-of-phase ac

susceptibility signal (χ_M''), imaginary part of the real ac signal and the rate at which the magnetization of a molecule relaxes is related to the operating frequency of the ac field. Ac study also plays a pivotal role in assessing the spin ground state of a molecule without the interference of a dc field and these signals for complexes **2-1**, **2-2**·6H₂O·2MeCN and **2-3**·2MeCN at the range of 5 - 1500 Hz frequencies are plotted as $\chi_M'T$ vs. T in Figure 2-15, 2-16 and 2-17 respectively at the temperature spanning over 1.8 - 10 K range. Extrapolation of the plots to 0 K, from temperatures above ~5 K to avoid the effect of weak intermolecular interactions (dipolar and superexchange), gives values of ~ 19.5, ~16.2 and ~17.0 cm³Kmol⁻¹ confirming the presence of an $S = 6$ spin-ground state for all three complexes. The slopes of all the plots decrease rapidly with a decrease in the temperature, revealing the presence of several spin states of larger S values lying very close to the ground state. Frequency-dependent in-phase ac signals are observed below 2.5 K which is concomitant with appearance of ac out-of-phase χ_M'' signals as shown in Figure 2-15, 2-16 and 2-17. However, only tail of the peaks are observed; i.e., the peak maxima lie below 1.8 K, minimum operating temperature of the SQUID magnetometer. This behavior is suggestive of the superparamagnet-like properties of an SMM and single-crystal hysteresis studies were further performed.

Magnetization hysteresis studies below 1.8 K for 2-1

The ac studies strongly suggest an SMM behavior for all three complexes. However, due to the similarity in the dc and ac magnetic susceptibility measurements, the magnetization hysteresis studies were performed for the complex **2-1** only as a representative member of the family. SMM behavior was confirmed by the appearance of hysteresis loops in magnetization vs. dc field scans, measured on a single crystal of

2-1·MeCN using the micro-SQUID apparatus. The applied field was aligned parallel to the easy axis (z axis) of the molecules using the recently reported method.⁶⁷ The temperature-dependence at 0.14 T s⁻¹ and the scan-rate dependence at 0.04 K of the hysteresis loops are shown in Figure 2-18. The coercivities clearly increase with decreasing temperature and increasing scan rate, as expected for the superparamagnet-like behavior of SMMs. The data thus confirm that complex **2-1** is a new addition to the family of SMMs,^{42,98} with a blocking temperature (T_B) of 1.0 K.

However, the hysteresis loops do not show steps characteristic of the quantum tunneling of magnetization (QTM); this behavior is typical for large SMMs, which are more susceptible to step-broadening effects associated with low-lying excited states, intermolecular interactions, and distributions of local environments due to ligand and solvent disorder.^{99,100,101} For **2-1**, the crystal structure shows the presence of disordered solvate molecules in the gaps between molecules and the magnetism data indicates the presence of low-lying excited states in the molecule. Hence, step-broadening effect can be rationalized.

Concluding Remarks

The use of edteH₄ and NaN₃ in the manganese cluster chemistry resulted in a new family of Mn₁₂ complexes with spin-ground state of $S = 6$. After isolating three initial Mn_x complexes of the nuclearity 8, 12 and 20 with edteH₄, this Mn₁₂ family of SMMs adds a new dimension in the study of alkoxide containing polymetallic Mn cluster chemistry. The initial findings bring hope to further scrutinize the system to gain more access to various other nuclearity Mn metal clusters with possible new SMMs. The initial use of azide in this synthetic scheme brings successful incorporation of end-on azides, however, dominant antiferromagnetic interactions are still present in these Mn₁₂

clusters. In the following chapters more use of azide will be studied in the edteH_4 chemistry to tune the magnetic exchange interactions among the Mn ions. Nevertheless, all the complexes show significant barrier of magnetization and display SMM behavior (in-phase and out-of-phase ac magnetic susceptibility signals for all three complexes and hysteresis loops in scans of magnetization vs. dc field for complex **2-1**). Given this success, the use of edteH_4 ligands in Mn cluster chemistry will continue to be investigated.

Table 2-1. Crystallographic data for **2-1**, **2-2** and **2-3**

parameter	2-1 ·MeCN	2-2	2-3 ·MeCN
formula	C ₄₄ H ₈₉ ClMn ₁₂ N ₃₆ O ₂₆	C ₄₀ H ₈₁ Mn ₁₂ N ₃₅ O ₂₁	C ₄₂ H ₈₄ ClMn ₁₂ N ₃₉ O ₂₅
Fw, g mol ⁻¹	2233.24	2047.68	2230.21
crystal system	tetragonal	monoclinic	tetragonal
space group	P-421c	P21/n	P-421c
a, Å	14.2051(6)	11.3888(8)	14.1908(8)
b, Å	14.2051(6)	27.1349(19)	14.1908(8)
c, Å	22.2065(16)	26.1080(18)	22.114(2)
α, β, γ, °	90, 90, 90	90, 91.681(2), 90	90, 90, 90
V, Å ³	4480.9(4)	8064.8(10)	4453.2(6)
Z	2	4	2
T, K	173(2)	173(2)	173(2)
radiation, Å ^a	0.71073	0.71073	0.71073
ρ, g cm ⁻³	1.655	1.788	1.663
μ, mm ⁻¹	1.742	1.897	1.753
R1 ^{b,c}	0.0506	0.0554	0.0568
wR2 ^d	0.1597	0.1244	0.1647

^a Graphite monochromator. ^b $I > 2\sigma(I)$. ^c $R1 = \sum(|F_o| - |F_c|) / \sum|F_o|$. ^d $wR2 = [\sum[w(F_o^2 - F_c^2)^2] / \sum[w(F_o^2)^2]]^{1/2}$, $w = 1/[\sigma^2(F_o^2) + [(ap)^2 + bp]$, where $p = [\max(F_o^2, 0) + 2F_c^2]/3$

Table 2-2. Bond-valence sums for the Mn atoms of complex **2-1**, **2-2** and **2-3**^a

Atom	2-1			2-2			2-3		
	Mn ^{II}	Mn ^{III}	Mn ^{IV}	Mn ^{II}	Mn ^{III}	Mn ^{IV}	Mn ^{II}	Mn ^{III}	Mn ^{IV}
Mn1	3.38	<u>3.14</u>	3.07	3.18	<u>2.96</u>	2.89	3.37	<u>3.13</u>	3.07
Mn2	2.86	<u>2.70</u>	2.63	<u>2.24</u>	2.10	2.05	2.89	<u>2.72</u>	2.65
Mn3	3.15	<u>2.93</u>	2.87	3.44	<u>3.19</u>	3.12	3.18	<u>2.97</u>	2.90
Mn4				3.23	<u>3.01</u>	2.94			
Mn5				3.05	<u>2.87</u>	2.79			
Mn6				3.50	<u>3.27</u>	3.19			
Mn7				3.11	<u>2.89</u>	2.83			
Mn8				<u>2.19</u>	2.05	1.99			
Mn9				3.47	<u>3.22</u>	3.15			
Mn10				3.23	<u>3.01</u>	2.94			
Mn11				2.84	<u>2.67</u>	2.59			
MN12				3.65	<u>3.41</u>	3.33			

^a The underlined value is the one closest to the charge for which it was calculated. The oxidation state of a particular atom can be taken as the nearest whole number to the underlined value

Table 2-3. Bond-valence sums for the O atoms of complex **2-1**^a

Atom	BVS	Assignment	Group
O1	1.89	O ²⁻	O ²⁻
O2	1.93	OR ⁻	edte ⁴⁻
O3	1.97	OR ⁻	edte ⁴⁻
O4	1.87	OR ⁻	edte ⁴⁻
O5	2.07	OR ⁻	edte ⁴⁻
O6	2.40	OR ⁻	OMe ⁻

^aThe BVS values for O atoms of O²⁻, OH⁻ and H₂O groups are typically 1.8-2.0, 1.0-1.2 and 0.2-0.4, respectively, but can be affected somewhat by hydrogen-bonding.

Table 2-4. Bond-valence sums for the O atoms of complex **2-2**^a

Atom	BVS	Assignment	Group
O1	1.98	OR ⁻	edte ⁴⁻
O2	1.85	OR ⁻	edte ⁴⁻
O3	1.97	OR ⁻	edte ⁴⁻
O4	1.92	OR ⁻	edte ⁴⁻
O17	1.91	O ²⁻	O ²⁻
O18	1.01	OH ⁻	OH ⁻

^aSee Table 2-3

Table 2-5. Bond-valence sums for the O atoms of complex **2-3**^a

Atom	BVS	Assignment	Group
O1	1.89	O ²⁻	O ²⁻
O2	1.92	OR ⁻	edte ⁴⁻
O3	1.99	OR ⁻	edte ⁴⁻
O4	1.85	OR ⁻	edte ⁴⁻
O5	2.16	OR ⁻	edte ⁴⁻
O6	0.87	OH ⁻	OH ⁻

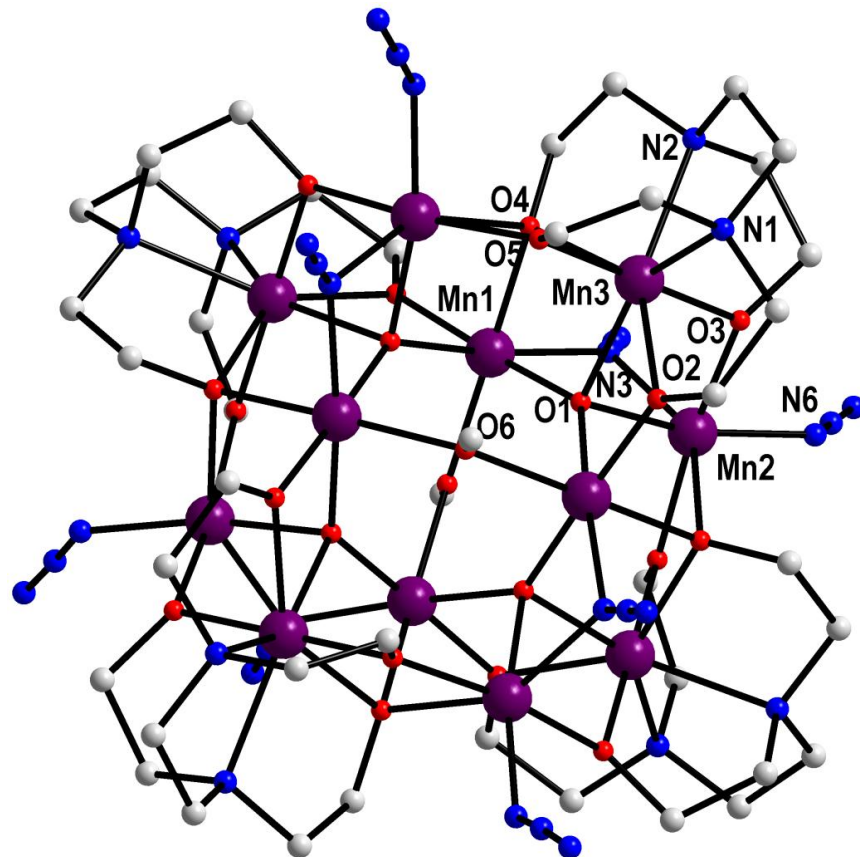
^aSee Table 2-3Table 2-6. Structural types and ground state S values for known Mn₁₂ clusters

Complex ^{a,b}	S	Core	Ref
[Mn ₁₂ O ₁₂ (O ₂ CMe) ₁₆ (H ₂ O) ₄	10	Mn ^{III} ₈ Mn ^{IV} ₄	16
Mn ₁₂ O ₁₂ (O ₂ CCH ₃) ₁₆ (CH ₃ OH) ₄	10	Mn ^{III} ₈ Mn ^{IV} ₄	82
[Mn ₁₂ O ₁₂ (O ₂ CPh) ₁₆ (H ₂ O) ₄	9	Mn ^{III} ₈ Mn ^{IV} ₄	16
[Mn ₁₂ O ₁₂ (O ₂ CEt) ₁₆ (H ₂ O) ₃	9	Mn ^{III} ₈ Mn ^{IV} ₄	74
[Mn ₁₂ O ₁₂ (O ₂ CC ₆ H ₄ -p-Me) ₁₆ (H ₂ O) ₄]	10	Mn ^{III} ₈ Mn ^{IV} ₄	102
[Mn ₁₂ O ₁₂ (O ₂ CCHCl ₂) ₁₆ (H ₂ O) ₄]	10	Mn ^{III} ₈ Mn ^{IV} ₄	103
[Mn ₁₂ O ₁₂ (O ₂ CCHCl ₂) ₈ (O ₂ CCH ₂ Bu ^t) ₈ (H ₂ O) ₃]	10	Mn ^{III} ₈ Mn ^{IV} ₄	103
[Mn ₁₂ O ₁₂ (O ₂ CCHCl ₂) ₈ (O ₂ CEt) ₈ (H ₂ O) ₃]	10	Mn ^{III} ₈ Mn ^{IV} ₄	103
[Mn ₁₂ O ₁₂ (O ₂ CCH ₂ Bu ^t) ₁₆ (H ₂ O) ₄]	10	Mn ^{III} ₈ Mn ^{IV} ₄	104
Mn ₁₂ O ₁₂ (O ₂ CCH ₂ Bu ^t) ₁₆ (CH ₃ OH) ₄	10	Mn ^{III} ₈ Mn ^{IV} ₄	82
[Mn ₁₂ O ₁₂ (O ₂ CCH ₂ Bu ^t) ₁₆ (Bu ^t OH)(H ₂ O) ₃]	10	Mn ^{III} ₈ Mn ^{IV} ₄	105
[Mn ₁₂ O ₁₂ (O ₂ CCH ₂ Bu ^t) ₁₆ (C ₅ H ₁₁ OH) ₄]	10	Mn ^{III} ₈ Mn ^{IV} ₄	105
[Mn ₁₂ O ₁₂ (O ₂ CC ₆ F ₅) ₁₆ (H ₂ O) ₄]	10	Mn ^{III} ₈ Mn ^{IV} ₄	76
Mn ₁₂ O ₁₂ (CH ₂ BrCOO) ₁₆ (H ₂ O) ₄	10	Mn ^{III} ₈ Mn ^{IV} ₄	106
(PPh ₄)[Mn ₁₂ O ₁₂ (O ₂ CEt) ₁₆ (H ₂ O) ₄]	19/2	Mn ^{II} Mn ^{III} ₇ Mn ^{IV} ₄	74
(NPr ⁿ) ₄ [Mn ₁₂ O ₁₂ (O ₂ CPh) ₁₆ (H ₂ O) ₄]	nr	nr	74
(PPh ₄) ₂ [Mn ₁₂ O ₁₂ (O ₂ CPh) ₁₆ (H ₂ O) ₄]	nr	nr	74
(Ph ₃ P) ₂ N[Mn ₁₂ O ₁₂ (O ₂ CPh) ₁₆ (H ₂ O) ₄]	nr	nr	74
(PPh ₄) ₂ [Mn ₁₂ O ₁₂ (O ₂ CCHCl ₂) ₁₆ (H ₂ O) ₄]	19/2	Mn ^{II} Mn ^{III} ₇ Mn ^{IV} ₄	75
(PPh ₄) ₂ [Mn ₁₂ O ₁₂ (O ₂ CCHCl ₂) ₁₆ (H ₂ O) ₄]	10	Mn ^{II} 2Mn ^{III} 6Mn ^{IV} 4	75
(NMe ₄) ₂ [Mn ₁₂ O ₁₂ (O ₂ CC ₆ F ₅) ₁₆ (H ₂ O) ₄]	19/2	Mn ^{II} Mn ^{III} ₇ Mn ^{IV} ₄	76
(NMe ₄) ₂ [Mn ₁₂ O ₁₂ (O ₂ CC ₆ F ₅) ₁₆ (H ₂ O) ₄]	10	Mn ^{II} ₂ Mn ^{III} ₆ Mn ^{IV} ₄	76
(NPr ⁿ) ₄ [Mn ₁₂ O ₁₂ (O ₂ CCHCl ₂) ₁₆ (H ₂ O) ₄]	19/2	Mn ^{II} Mn ^{III} ₇ Mn ^{IV} ₄	107
(NPr ⁿ) ₂ [Mn ₁₂ O ₁₂ (O ₂ CCHCl ₂) ₁₆ (H ₂ O) ₄]	10	Mn ^{II} ₂ Mn ^{III} ₆ Mn ^{IV} ₄	107
(NPr ⁿ) ₃ [Mn ₁₂ O ₁₂ (O ₂ CCHCl ₂) ₁₆ (H ₂ O) ₄]	17/2	Mn ^{II} ₃ Mn ^{III} ₅ Mn ^{IV} ₄	107
[Mn ₁₂ O ₁₂ (Z) ₁₆ (H ₂ O) ₄][PF ₆] ₁₆	10	nr	108
[Fe(C ₅ Me ₅) ₂] _n [Mn ₁₂ O ₁₂ (O ₂ CC ₆ F ₅) ₁₆ (H ₂ O) ₄]	21/2	Mn ^{II} Mn ^{III} ₇ Mn ^{IV} ₄	109
[Mn ₁₂ O ₁₂ (bet) ₁₆ (EtOH) ₄][PF ₆] ₁₄	11	Mn ^{II} ₄ Mn ^{III} ₄ Mn ^{IV} ₄	79
[Mn ₁₂ O ₁₂ (bet) ₁₆ (EtOH) ₃ (H ₂ O)][PF ₆] ₁₃ [OH]	11	Mn ^{II} ₄ Mn ^{III} ₄ Mn ^{IV} ₄	110
(NBu ⁿ) ₄ [Mn ₁₂ O ₁₂ (O ₂ CPh) ₁₆ (OMe) ₂ (H ₂ O) ₂]	6	Mn ^{III} ₈ Mn ^{IV} ₄	81
[Mn ₁₂ O ₁₀ (OMe) ₃ (OH)(O ₂ CC ₆ H ₃ F ₂) ₁₆ (MeOH) ₂]	5	Mn ^{III} ₈ Mn ^{IV} ₄	82
[Mn ₁₂ O ₁₀ (OMe) ₄ (O ₂ -CBu ^t) ₁₆ (MeOH) ₂]	9	Mn ^{III} ₈ Mn ^{IV} ₄	82
[Mn ₁₂ O ₄ (OH) ₂ (PhCOO) ₁₂ (thme) ₄ (py) ₂]	7	Mn ^{II} ₂ Mn ^{III} ₁₀	83
[Mn ₁₂ O ₂ (OMe) ₂ (Hpeol) ₄ (O ₂ CPh ₂) ₁₀ (H ₂ O) ₂]	3	Mn ^{III} ₄ Mn ^{II} ₈	84

[Mn ₁₂ O ₂ (OMe) ₂ (thme) ₄ (OAc) ₁₀ (H ₂ O) ₄]	3	Mn ^{II} ₄ Mn ^{III} ₄ Mn ^{II} ₄	85
[Mn ₁₂ (Adea) ₈ (CH ₃ COO) ₁₄]	7	Mn ^{II} ₆ Mn ^{III} ₆	91
[Mn ₁₂ (dmbshz) ₁₂ (EtOH) ₆]	2	Mn ^{III} ₁₂	92
[Mn ₁₂ (O ₂ CMe) ₁₄ (mda) ₈]	7	Mn ^{II} ₆ Mn ^{III} ₆	46
[Mn ₁₂ O ₄ (OH) ₂ (edte) ₄ Cl ₆ (H ₂ O) ₂]	7	Mn ^{II} ₄ Mn ^{III} ₈	60
[Mn ₁₂ O ₈ Cl ₄ (O ₂ CPh) ₈ (hmp) ₆]	7	Mn ^{II} ₂ Mn ^{III} ₁₀	86
[Mn ₁₂ O ₈ Cl ₄ (O ₂ CPh) ₈ (hep) ₆]	0	Mn ^{II} ₂ Mn ^{III} ₁₀	87
[Mn ₁₂ O ₈ (O ₂ CMe) ₆ (O ₃ PC ₆ H ₉) ₇ (bipy) ₃]	2	Mn ^{III} ₁₂	89
[Mn ₁₂ O ₆ (OH) ₄ (OCH ₃) ₂ (pkO) ₁₂](OH)(ClO ₄) ₃	nr	Mn ^{II} ₄ Mn ^{III} ₆ Mn ^{IV} ₂	90
[Mn ₁₂ O ₇ (OH)(OMe) ₂ (O ₂ CPh) ₁₂ (dmhmp) ₄ (H ₂ O)]	13/2	Mn ^{II} ₃ Mn ^{III} ₉	111

^a Solvate molecules are omitted. ^b Abbreviations: nr = not reported, ZHPF₆ = (4-carboxybenzyl)tributylammonium hexafluorophosphate, bet = betaine, mdaH₂ = *N*-methyl-diethanolamine, hmpH = 2-hydroxymethylpyridine, H₄peol = pentaerythritol, hepH = 2-hydroxyethylpyridine, H₃dmbshz = 2,6-dimethoxybenzoylsalicylhydrazide, Hpko = di-pyridyl ketone oxime, adeaH₂ = *N*-allyl diethanolamine, H₃thme = 1,1,1-tris(hydroxymethyl)-methane, bipy = bipyridine, dmhmpH = 2-(Pyridine-2-yl)propan-2-ol, edteH₄ = *N,N,N',N'*-Tetrakis(2-hydroxyethyl)ethylenediamine

A



B

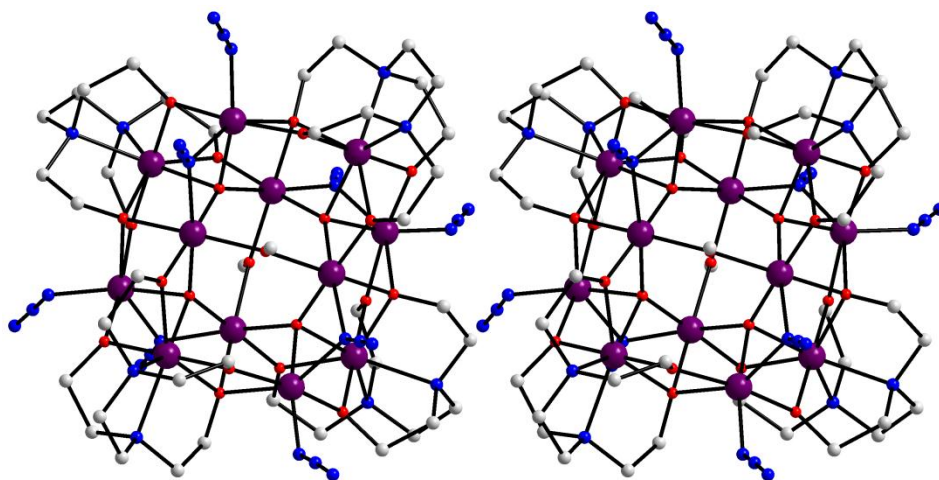
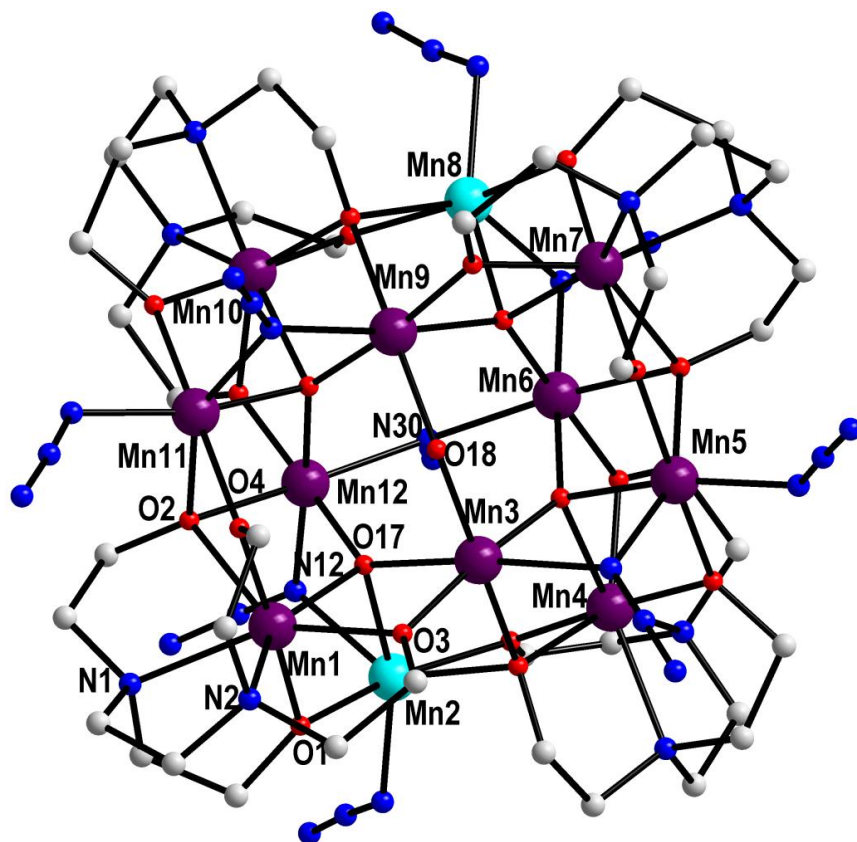


Figure 2-1. Labeled representation (A) and a stereopair (B) of complex **2-1**. Hydrogen atoms have been omitted for clarity. Color code: Mn³⁺, purple; O, red; N, blue; C, light-grey.

A



B

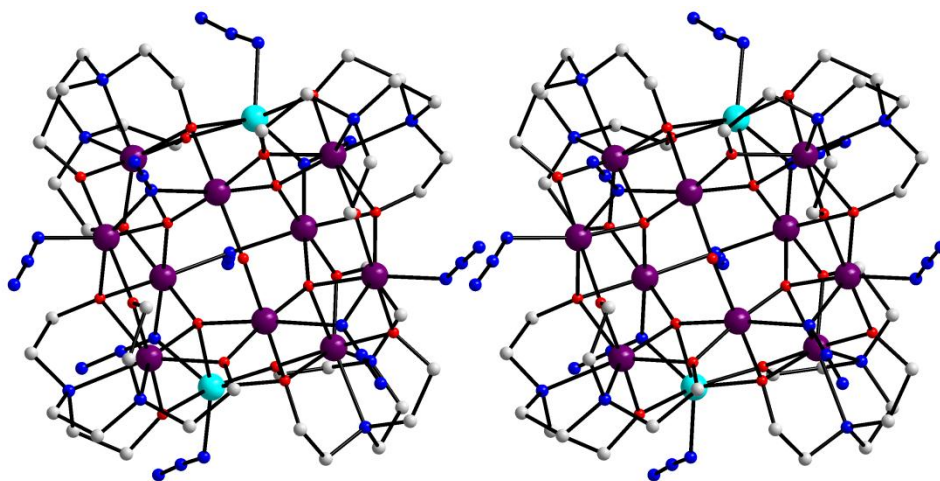
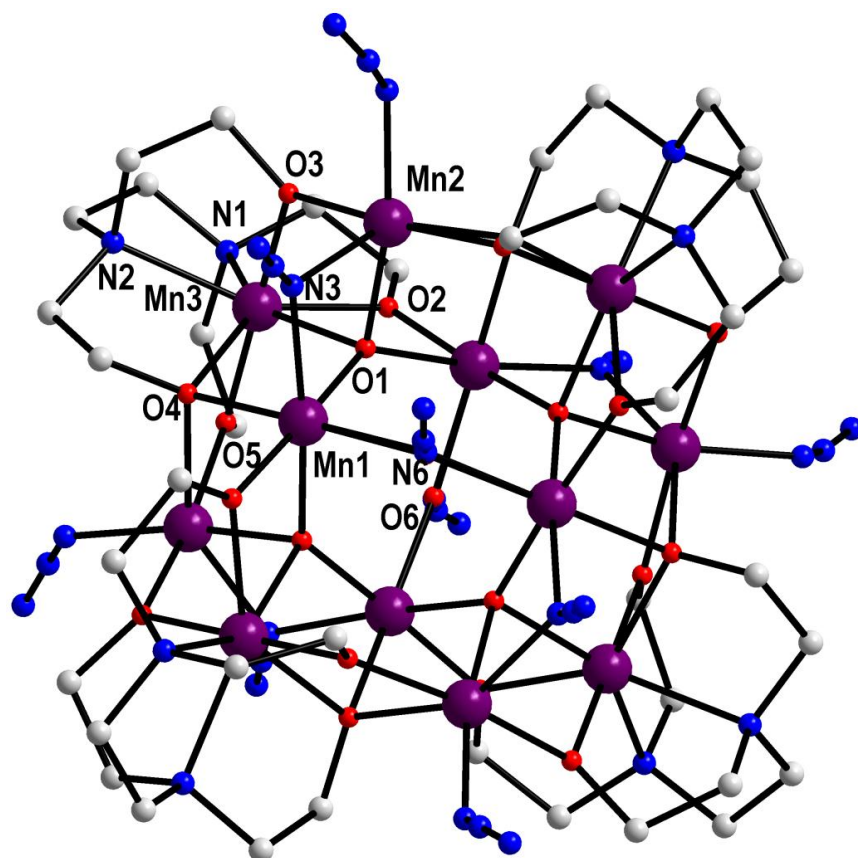


Figure 2-2. Labeled representation (A) and a stereopair (B) of complex **2-2**. Hydrogen atoms have been omitted for clarity. Color code: Mn³⁺, purple; Mn²⁺, cyan; O, red; N, blue; C, light-grey.

A



B

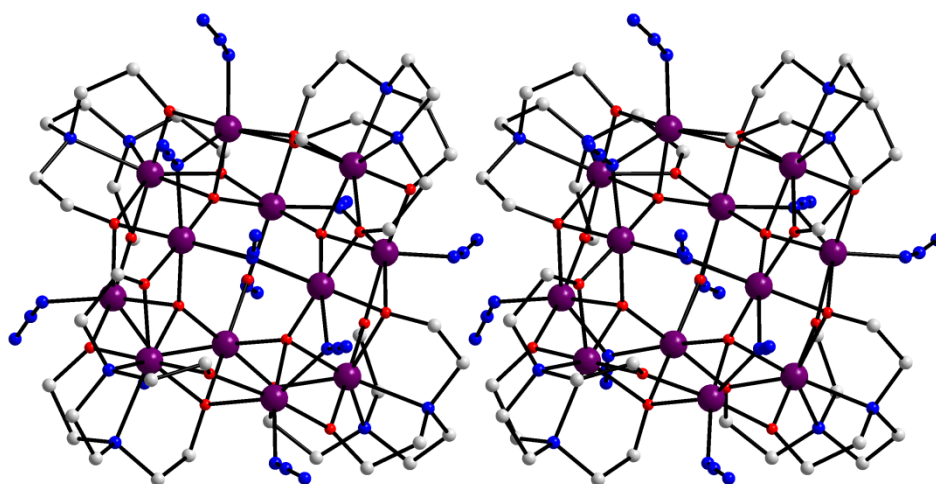
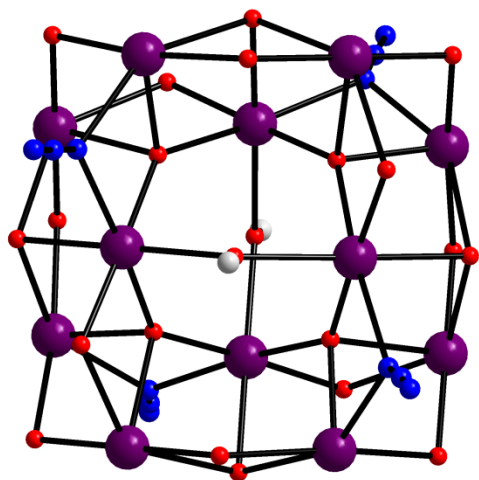
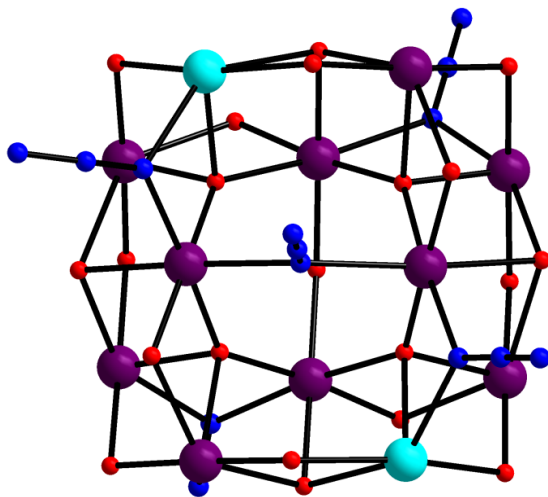


Figure 2-3. Labeled representation (A) and a stereopair (B) of complex 2-3. Hydrogen atoms have been omitted for clarity. Color code: Mn³⁺, purple; O, red; N, blue; C, light-grey.

A



B



C

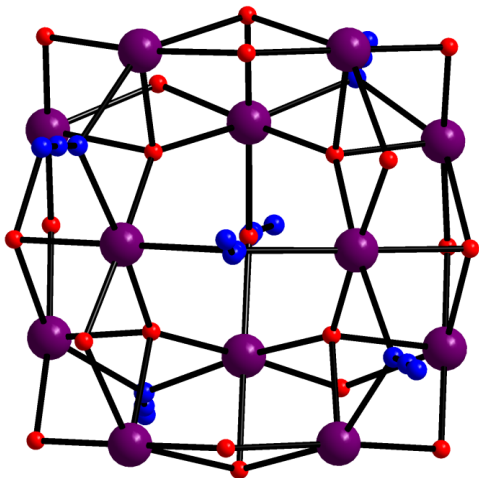


Figure 2-4. The core of **2-1** (A), **2-2** (B), **2-3** (C) viewed along the *c* axis. Color code: Mn^{3+} , purple; Mn^{2+} , cyan; O, red; N, blue; C, light-grey.

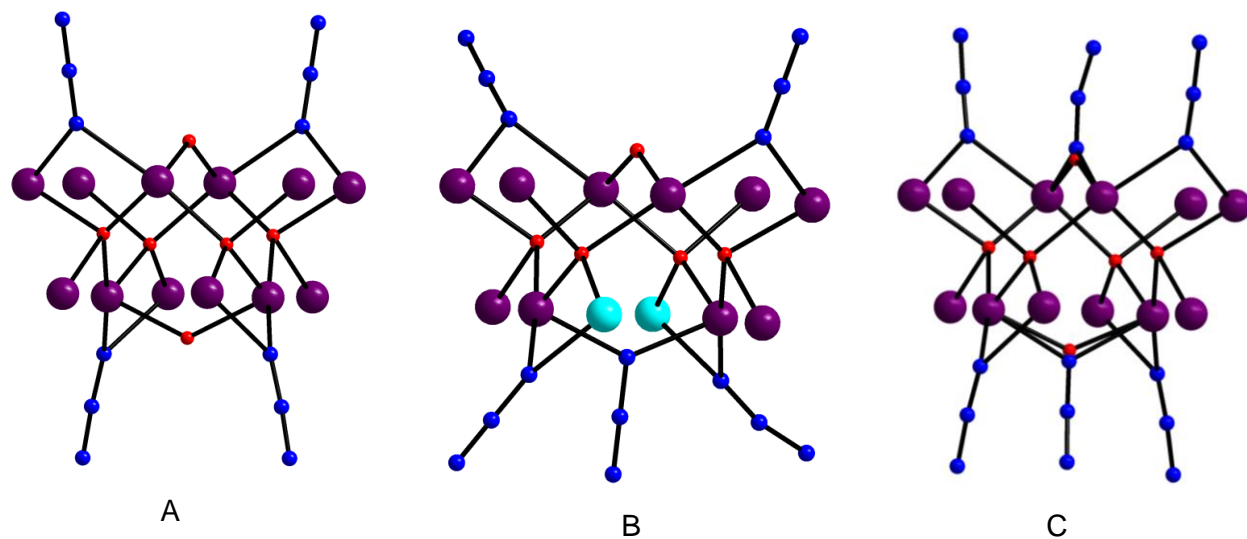


Figure 2-5. The core of **2-1** (A), **2-2** (B), and **2-3** (C) viewed along the b axis. Color code: Mn³⁺, purple; Mn²⁺, cyan; O, red; N, blue; C, light-grey.

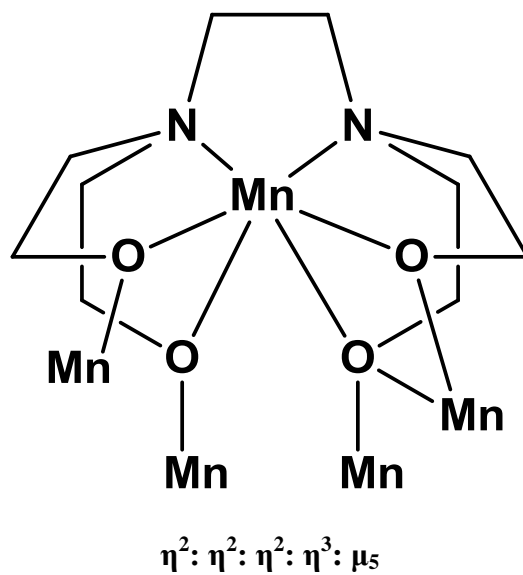


Figure 2-6. Coordination mode of edte⁴⁻ found in complexes **2-1** to **2-3**.

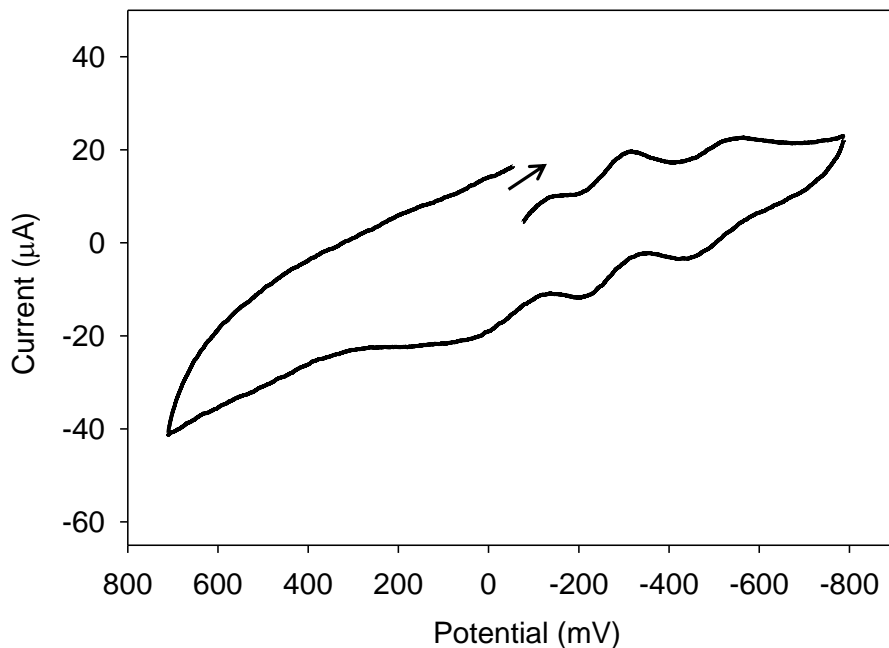


Figure 2-7. A full CV diagram of complex **2-1** at 100 mV/s in DMF containing 0.1 M NBu_4PF_6 as the supporting electrolyte. The indicated potentials are given vs. ferrocene as an internal standard.

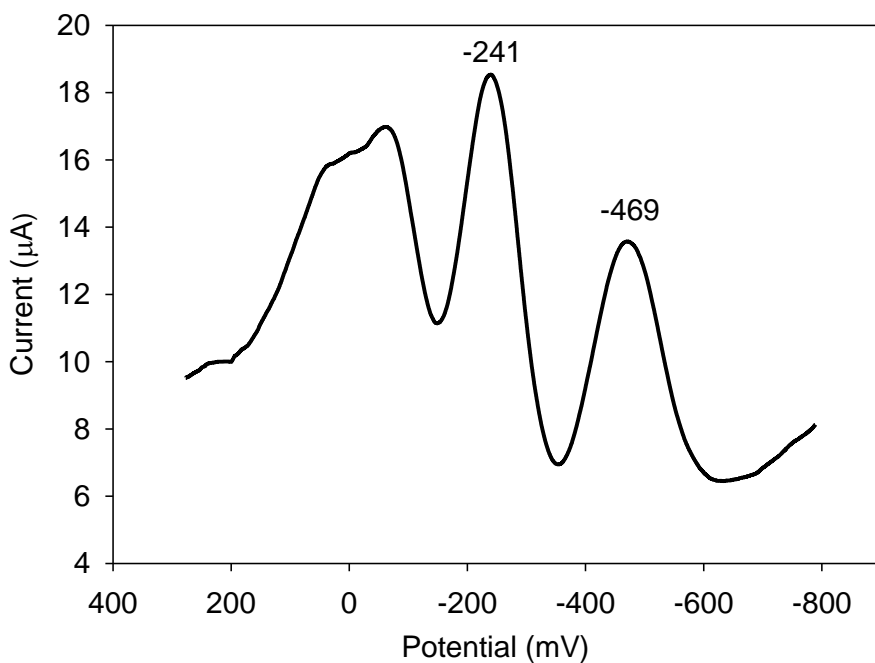


Figure 2-8. A full DPV diagram for complex **2-1** at 20 mV/s. The indicated potentials are given vs. ferrocene as an internal standard.

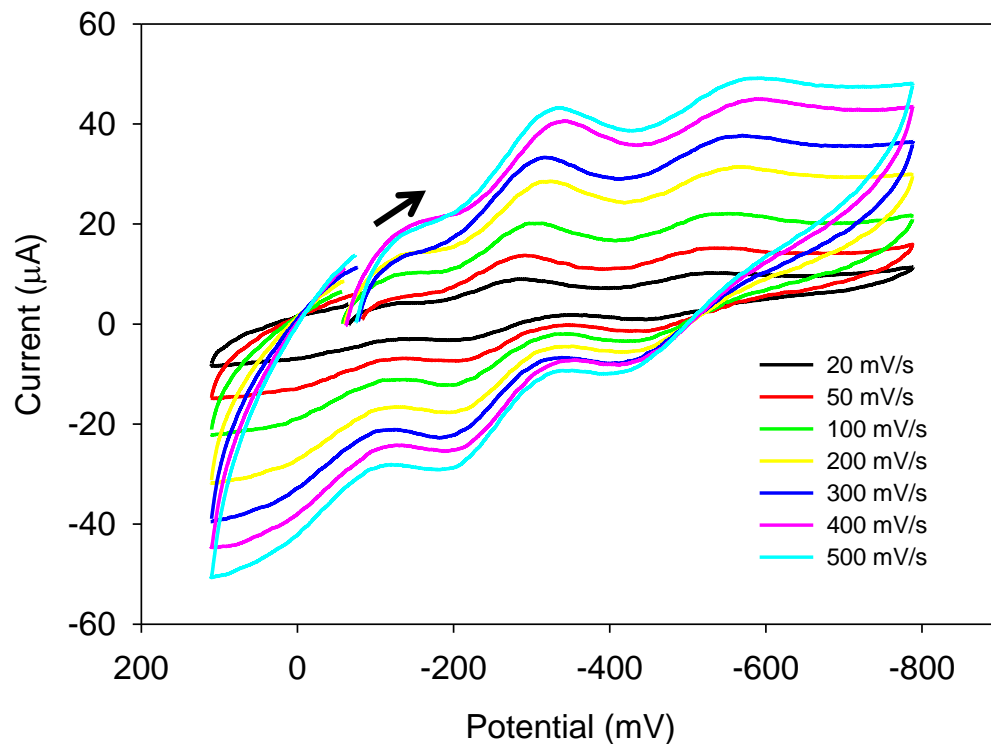


Figure 2-9. The CV diagram at the indicated scan rates for the reduction wave of **2-1**. The indicated potentials are given vs. ferrocene as an internal standard.

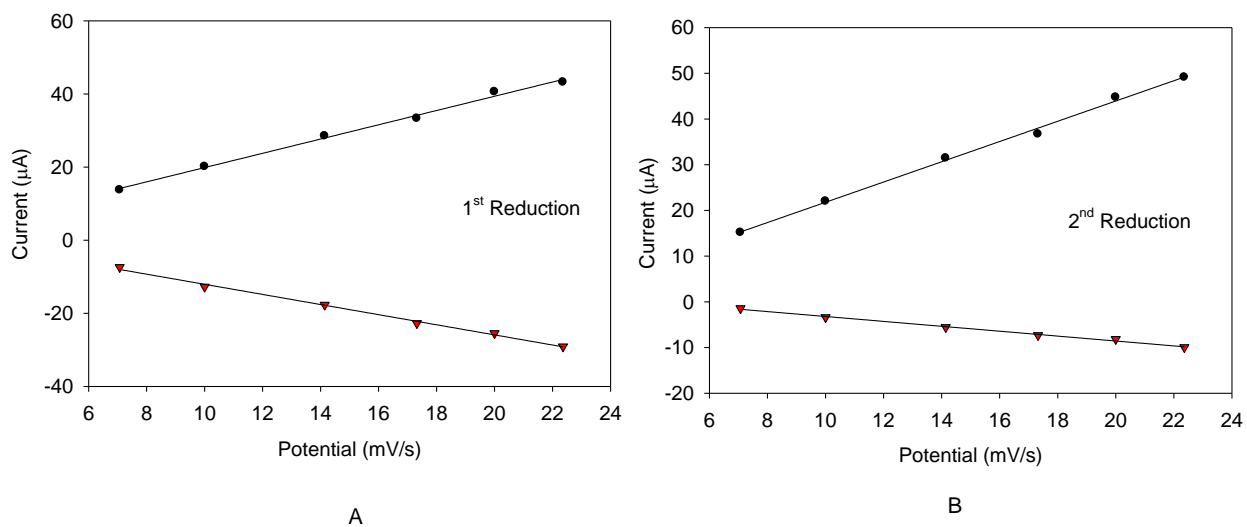


Figure 2-10. Plots of cathodic (●) and anodic (▼) peak current dependence vs. square-root of scan rate ($v^{1/2}$) for -0.24 V (A) and -0.47 V (B) reduction wave for complex **2-1**.

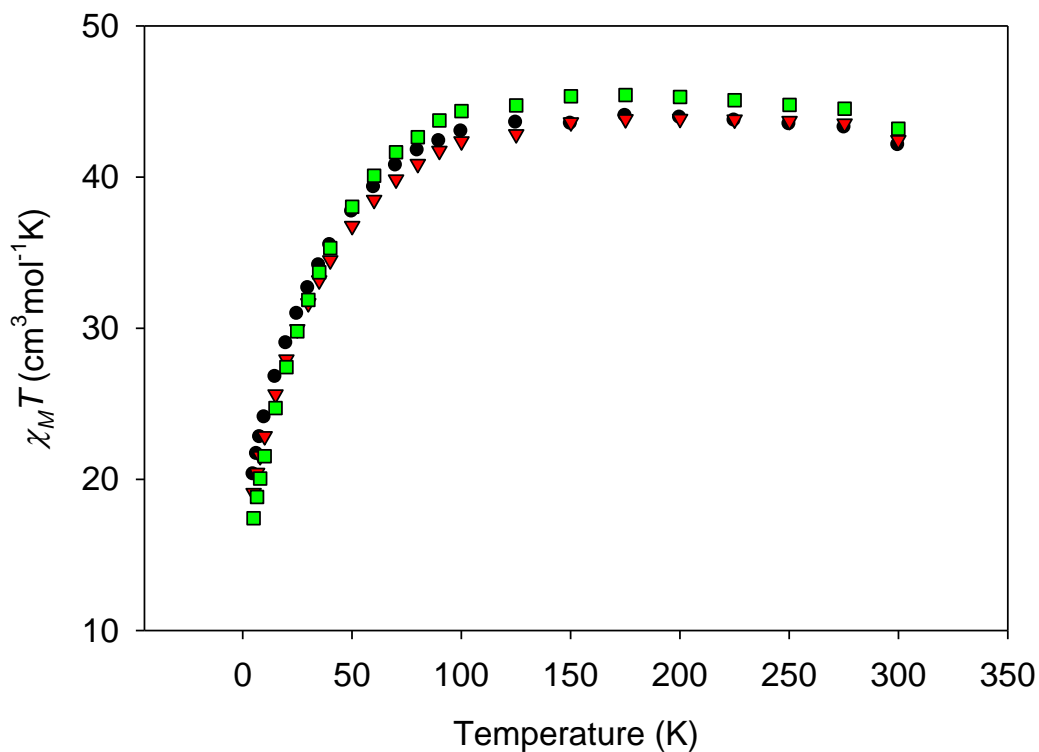


Figure 2-11. Plot of $\chi_M T$ vs. T for complexes **2-1**(●), **2-2**·6H₂O·2MeCN(▼) and **2-3**·2MeCN(■).

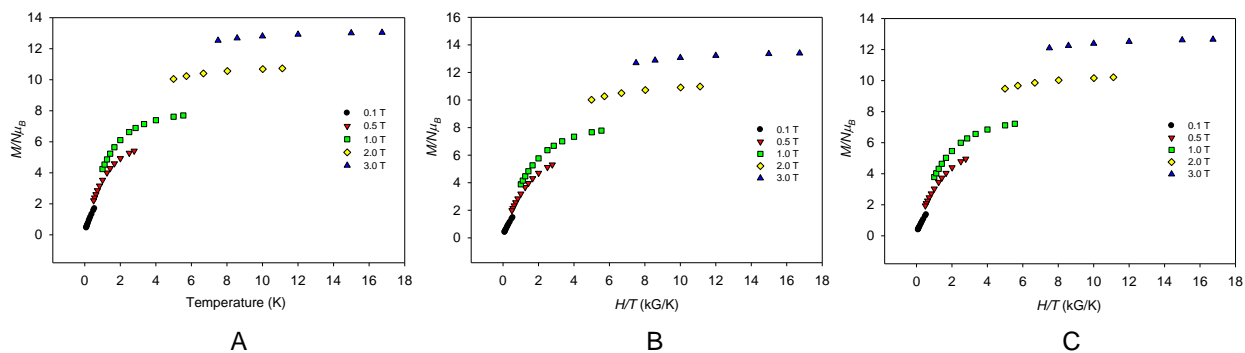


Figure 2-12. Plots of reduced magnetization ($M/N\mu_B$) vs. H/T for complexes **2-1** (A), **2-2** (B) and **2-3** (C) at applied fields of 0.1 - 3.0 T and in the 1.8 - 10 K temperature range.

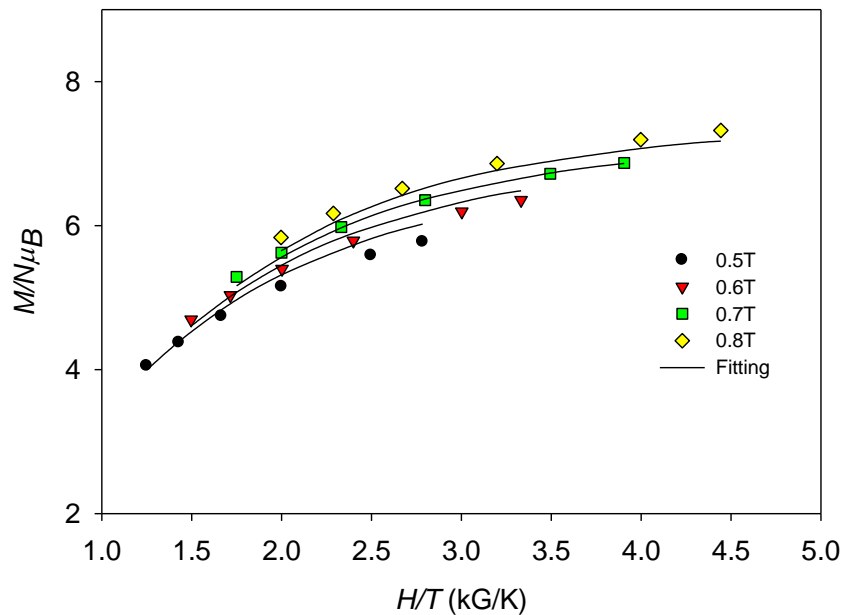


Figure 2-13. Plot of reduced magnetization ($M/N\mu_B$) vs. H/T for complex 2-3 at applied fields of 0.5 - 0.8 T and in the 1.8 - 10 K temperature range. The solid lines are the fit of the data; see the text for the fit parameters.

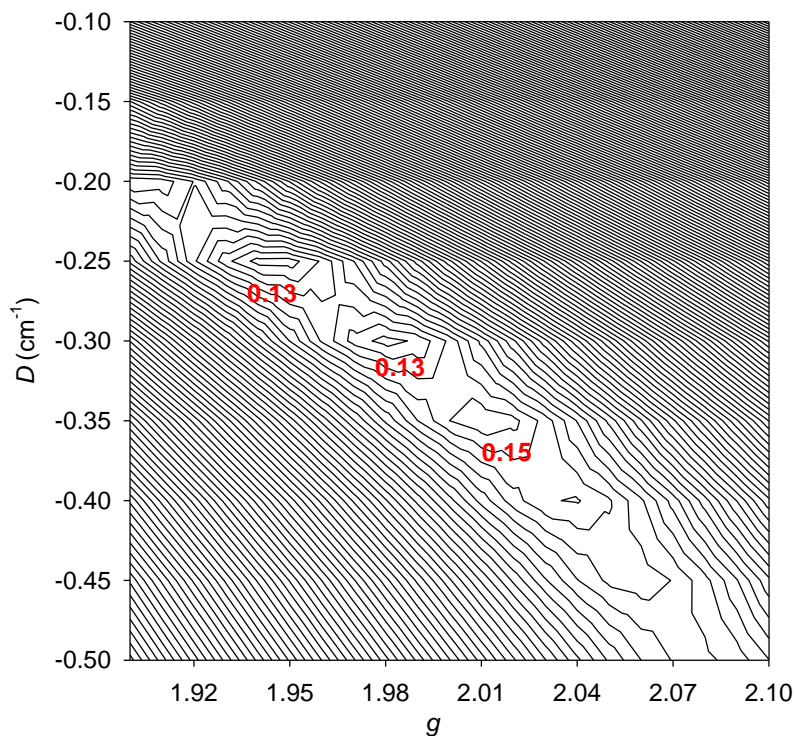


Figure 2-14. Two-dimensional contour plot for the rms error surface vs. D and g for the reduced magnetization fit for complex 2-3.

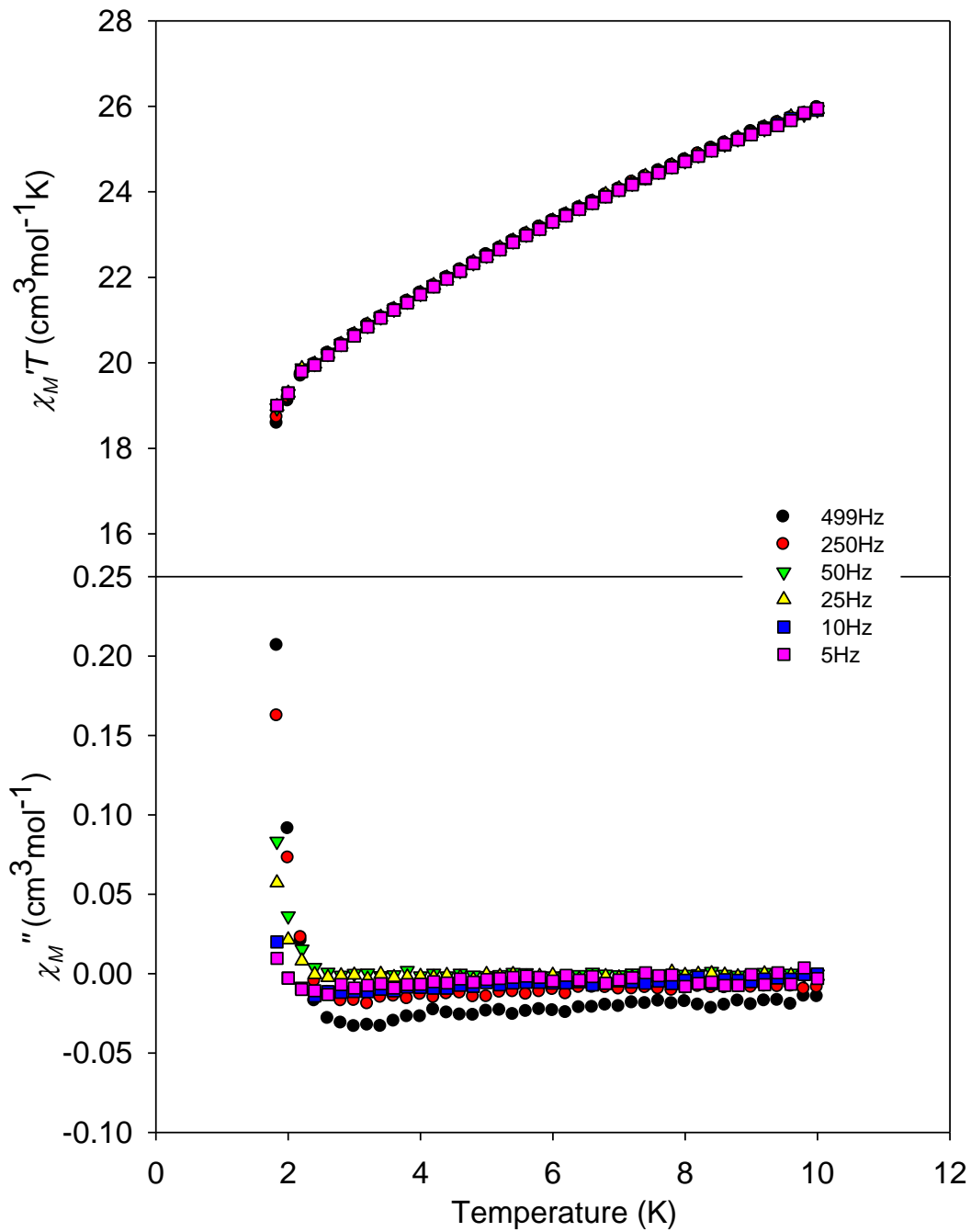


Figure 2-15. Plots of in-phase χ_M' (as $\chi_M'T$) vs. T and out-of-phase χ_M'' vs. T ac signals for complex **2-1** at the indicated frequencies.

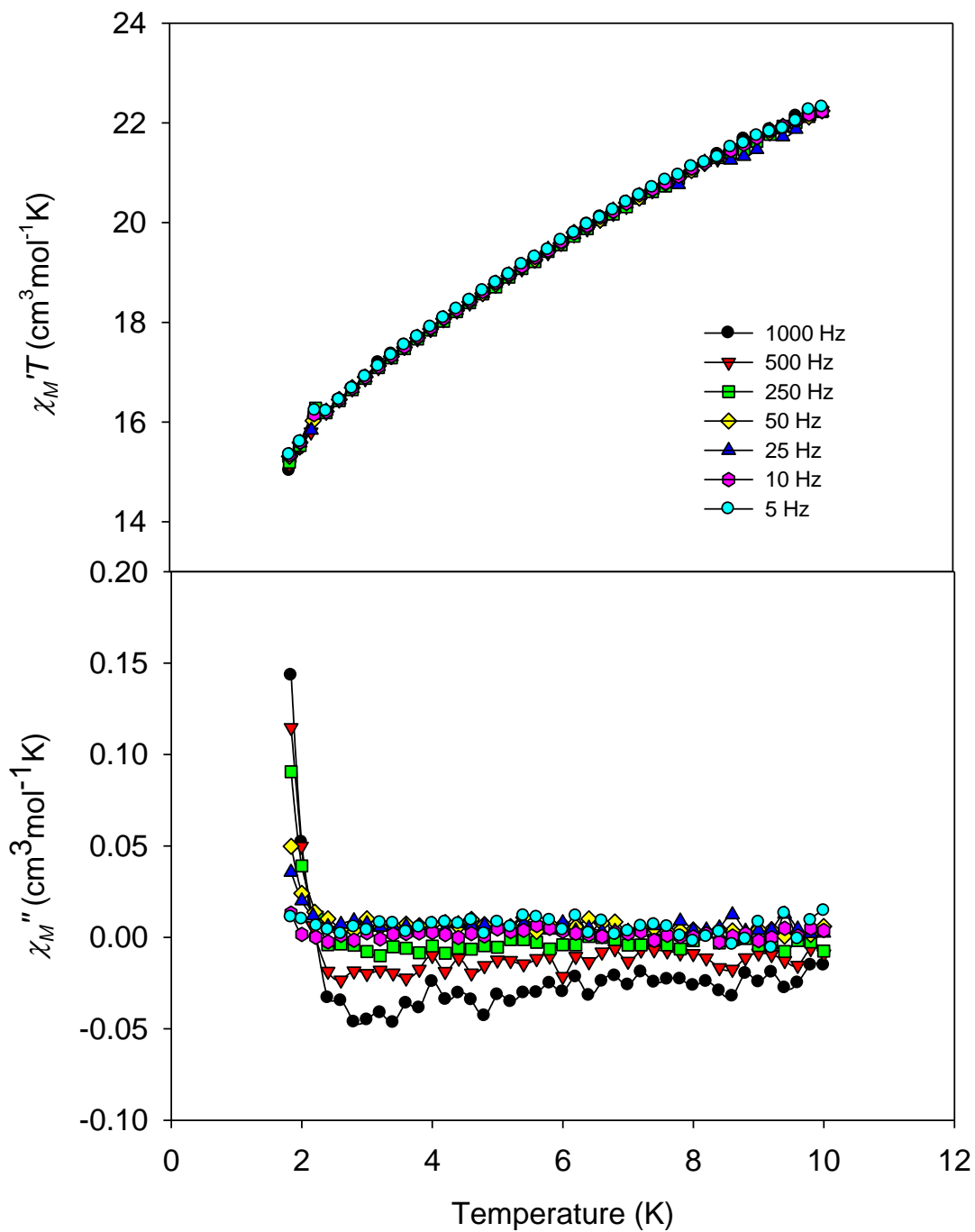


Figure 2-16. Plots of in-phase χ_M' (as $\chi_M' T$) vs. T and out-of-phase χ_M'' vs. T ac signals for complex **2-2** at the indicated frequencies.

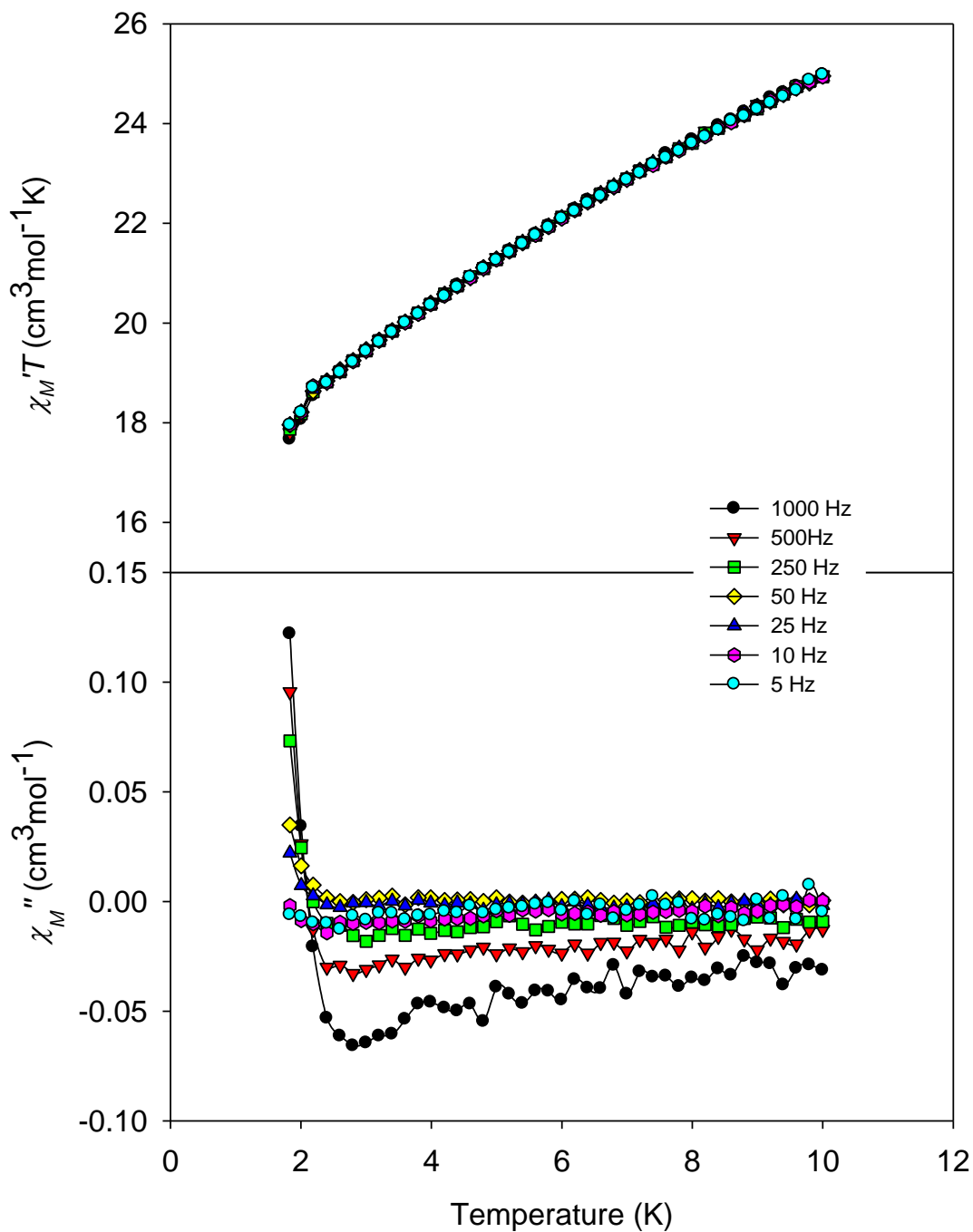
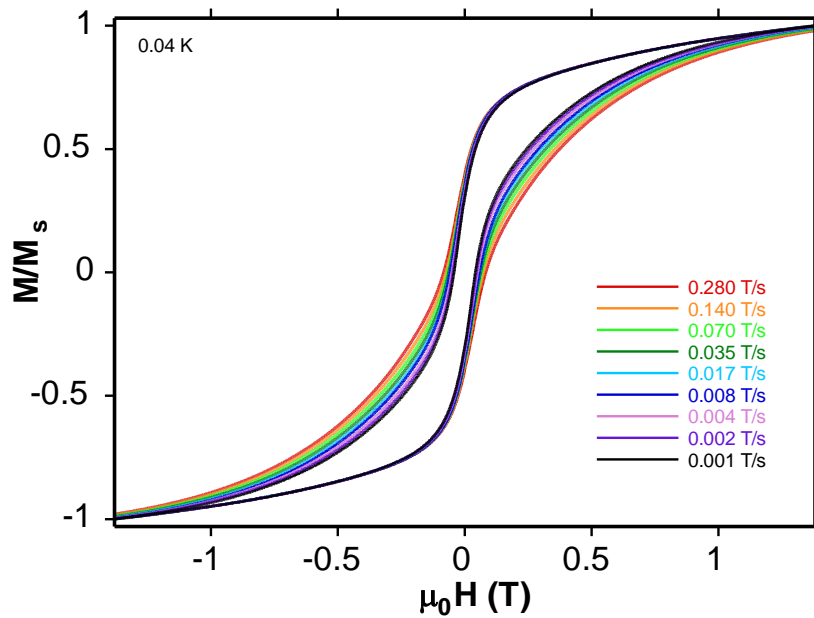


Figure 2-17. Plots of in-phase χ_M' (as $\chi_M' T$) vs. T and out-of-phase χ_M'' vs. T ac signals for complex **2-3** at the indicated frequencies.

A



B

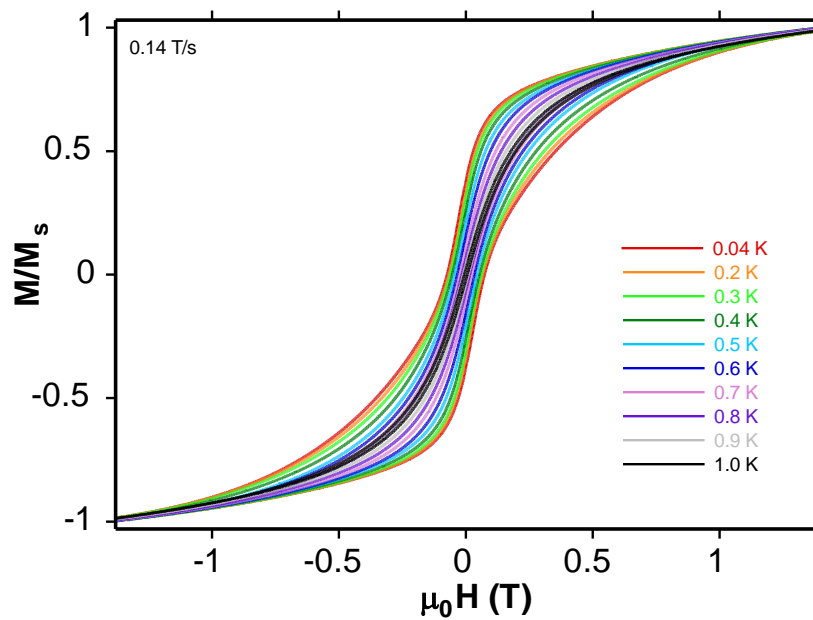


Figure 2-18. Magnetization (M) vs. dc field scans for a single-crystal of complex **2-1** at the indicated field sweep rates (A) and temperatures (B). The magnetization is normalized to its saturation value, M_S .

CHAPTER 3

EXPERIMENTAL AND COMPUTATIONAL STUDIES OF A NEW Mn_9 SINGLE-MOLECULE MAGNET WITH A HALF-INTEGER SPIN OF $S = 21/2$

Single-molecule magnets (SMMs) continue to attract a lot of attention for their potential applications to new technologies such as molecule-based information storage, molecular spintronics, and quantum information processing.^{11,25,30} SMMs represent a molecular approach to nanoscale magnetism, where each individual molecule possesses a significant barrier (vs. kT) to magnetization relaxation, and thus exhibits properties such as magnetic hysteresis below a blocking temperature, T_B .¹² The SMM behavior results from a combination of a high ground-state spin (S) value and an easy-axis type magnetoanisotropy (negative zero-field parameter D), where the latter is the more important parameter for enhancing the SMM property.^{112,113} SMMs also straddle the classical/quantum interface by displaying not only classical magnetic hysteresis but also quantum phase interference¹¹⁴ and quantum tunneling of magnetization (QTM),¹¹⁵⁻¹¹⁷ which makes SMMs potential candidates for use as quantum bits (qubits) in quantum computation.^{28,30} Manganese has been the transition metal of choice to date for SMMs due to its common propensity to yield molecules with large S values, and significant anisotropy from the presence of Jahn-Teller distorted Mn^{3+} ions.³³ Such large S values in Mn_x clusters can result from ferro- or ferrimagnetic spin alignments and/or competing interactions (spin frustration) in certain M_x topologies that prevent (frustrate) the preferred spin alignments. Ferromagnetic interactions can result from ligands or structural characteristics known to give ferromagnetic coupling between metal centers; for example, end-on azide bridges are known to promote ferromagnetic coupling between bridging metal ions.⁵⁹ In addition, to facilitate the formation of polynuclear metal clusters, many researchers have employed alkoxide-based ligands, since this

functionally is an excellent bridging group that fosters formation of higher nuclearity products.^{47-52,118} These synthetic strategies have proved extremely useful in expanding the database of known Mn high-spin molecules and/or SMMs in different directions, including large size (metal nuclearity), very high spin values, and relatively large (vs. kT) anisotropy barriers.^{10,98}

In the present work, we have employed the potentially N,N,O,O,O,O - hexadentate chelate *N,N,N',N'*-tetrakis(2-hydroxyethyl)ethylenediamine (edteH₄) in Mn reactions in the presence of carboxylates and azide as co-ligands. The edteH₄ chelate has been little explored to date in the literature, having been employed in the preparation of mononuclear Ca and dinuclear Ba, Cu and V complexes.^{61,62,119} More recently it began to be investigated in Mn cluster chemistry, and the compounds obtained with it so far have comprised Mn₈, Mn₁₂ and Mn₂₀ clusters with new and interesting metal topologies.⁶⁰ We also reported recently its use in Fe cluster chemistry, where it again proved to be a source of interesting new compounds of various Fe_x ($x = 5, 6, 12$) nuclearities.⁵⁴ We thus concluded we had merely scratched the surface of what it could deliver in polynuclear metal chemistry, believing it had the potential to provide further access to a variety of new structural types with important properties. Herein, we report a new and particularly interesting Mn₉ SMM obtained from edteH₄ that represents a very rare example of a half-integer, high spin SMM, and the results of its detailed study with a wide range of physical (magnetic, electrochemical), spectroscopic (inelastic neutron scattering), and computational (DFT) methods.

Experimental Section

Synthesis

All preparations were performed under aerobic conditions using reagents and solvents as received. $\text{Mn}(\text{O}_2\text{CBu}^t)_2$ was prepared as reported in the literature.¹²⁰

Caution! Although no such behavior was observed during the present work, azide salts are potentially explosive; such compounds should be synthesized and used in small quantities, and treated with utmost care at all times.

$[\text{Mn}_9\text{O}_3(\text{OMe})(\text{O}_2\text{CBu}^t)_7(\text{edte})(\text{edteH})_2(\text{N}_3)_2]$ (3-1). To a stirred solution of edteH_4 (0.20 g, 0.84 mmol) and NEt_3 (0.25 mL, 1.68 mmol) in MeCN/MeOH (20/1, v/v) was added $\text{Mn}(\text{O}_2\text{CBu}^t)_2$ (0.44 g, 1.68 mmol). The resulting dark-brown solution was stirred for 15 minutes under mild heating ($\sim 60^\circ\text{C}$) to dissolve all solids, and then NaN_3 (0.12 g, 1.84 mmol) was added. The solution was stirred for a further 2 hours, filtered, and the filtrate was allowed to slowly evaporate undisturbed at ambient temperature. X-ray quality, dark-brown, plate-like crystals of **3-1**·4MeCN slowly grew over a few days. The crystallographic sample was maintained in contact with mother liquor to prevent damage from exposure to the atmosphere. Otherwise, the crystals were collected by filtration, washed with Et_2O , and dried in vacuum. The yield was 58%. Anal. Calc (Found) for **3-1** (solvent-free): C, 38.40 (38.73); H, 6.25 (6.12); N, 8.14 (7.93) %. Selected IR data (cm^{-1}): 3427 (br), 2957 (s), 2869 (s), 2056 (vs), 1587 (vs), 1482 (m), 1457 (w), 1361 (m), 1289 (w), 1225 (m), 1075 (s), 904 (m), 662 (s), 606 (s), 512 (m), 436 (m).

X-ray Crystallography

Data were collected for **3-1**·4MeCN at 100 K on a Bruker DUO system equipped with an APEX II area detector and a graphite monochromator utilizing $\text{MoK}\alpha$ radiation (λ

= 0.71073 Å). Cell parameters were refined using 9999 reflections. A hemisphere of data was collected using the ω -scan method (0.5° frame width). Absorption corrections by integration were applied based on measured indexed crystal faces. The structure was solved by direct methods in SHELXTL6, and refined on F^2 using full-matrix least squares. The non-H atoms were treated anisotropically, whereas H atoms were placed in calculated positions and refined as riding on their respective C atoms.

Crystallographic parameters are listed in Table 3-1.

The asymmetric unit consists of two chemically equivalent but crystallographically independent Mn_9 clusters, and eight MeCN molecules. The latter were too disordered to be modeled properly, and program SQUEEZE,⁶⁴ a part of the PLATON package of crystallographic software, was used to calculate the solvent disorder area and remove its contribution to the overall intensity data. One cluster has both of its hydroxyl groups disordered, and they were refined in two parts each. The Me groups of $tBuCO_2^-$ on C12 and C42 were also disordered and refined in two parts each. The second cluster has a similar hydroxyl group disorder, but no Me group disorder. For each case of disorder, site occupancy factors were dependently refined. A total of 2103 parameters were included in the final cycle of refinement using 24263 reflections with $I > 2\sigma(I)$ to yield R_1 and wR_2 of 4.74 and 12.45 %, respectively.

Physical Measurements

Infrared spectra were recorded in the solid state (KBr pellets) on a Nicolet Nexus 670 FTIR spectrometer in the 400 - 4000 cm^{-1} range. Elemental analyses (C, H and N) were performed by the in-house facilities of the University of Florida, Chemistry Department. Electrochemical studies were performed in dry *N, N* dimethylformamide (DMF) under argon using a BAS model CV-50W voltammetric analyzer and a standard

three-electrode assembly (glassy carbon working, Pt wire auxiliary, and Ag wire reference) with 0.1 M $\text{NBu}^n_4\text{PF}_6$ as supporting electrolyte. The concentration of **3-1** was ~ 1 mM. The scan rates for cyclic voltammetry (CV) and differential pulse voltammetry (DPV) were 50 - 500 mV/s and 20 mV/s, respectively. Quoted potentials are vs. the ferrocene/ferrocenium couple, used as an internal standard.⁶⁵ Solid-state, variable-temperature dc and ac magnetic susceptibility data were collected on powdered microcrystalline samples of **3-1** at the University of Florida using a Quantum Design MPMS-XL SQUID susceptometer equipped with a 7 T magnet and operating in the 1.8 - 300 K range. Samples were embedded in solid eicosane to prevent torquing. Magnetization vs. field and temperature data were fitted using the program MAGNET.⁶⁶ Pascal's constants were used to estimate the diamagnetic correction, which was subtracted from the experimental susceptibility to give the molar paramagnetic susceptibility (χ_M). Low-temperature (< 1.8 K) hysteresis loop and dc relaxation measurements were performed in Grenoble using an array of micro-SQUIDs.⁶⁷ The field can be applied in any direction by separately driving three orthogonal coils. The applied field was aligned parallel to the easy axis (z axis) of the molecules using a published method.¹²¹ Inelastic neutron scattering (INS) experiments were done at the direct time-of-flight instrument IN5 at the ILL, Grenoble. The powdered, microcrystalline, Mn_9 sample was placed in a double-walled hollow aluminum cylinder (diameter 21 mm, 2 mm cartridge); the sample weight was 2.01 g. The measurements were done at wavelengths of 3.2, 5.0, 6.5, 7.0, 7.5, and 8.0 Å for temperatures in the 1.5 to 40 K range. Only the 3.2, 6.5 and 7.5 Å data are presented here; the resolutions at the elastic line were 310, 41, and 28 μeV . The data were corrected for detector efficiency via a

vanadium standard. The low-angle part of the spectrum is neglected in the analysis, because of the significant instrumental features near the elastic line.

Computational Details

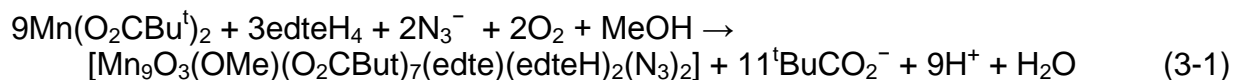
All the reported calculations were performed with the Quantum-ESPRESSO-4.1 program,¹²² using PBE exchange-correlation functional, Vanderbilt ultrasoft pseudopotentials,¹²³ and a plane-wave basis set at the University of Central Florida. The energy cutoffs for the wave functions and charge densities were set at 25 and 250 Ry, respectively. To ensure total energy convergence, all calculations used the spin polarized approach with the Marzari-Vanderbilt¹²⁴ cold smearing (smearing factor 0.0008), and local Thomas-Fermi mixing mode to improve SCF convergence. To calculate the Heisenberg exchange constants, the FM state (multiplicity 38) with all Mn spins parallel, was first optimized. In order to obtain desirable spin states, various different spin-alignments were considered and verified with Löwdin spin densities after SCF convergence. The optimization was previously found to be important for the accuracy of the final results, presumably due to inaccuracies introduced in some of X-ray structures by partial disorder. In the application of the DFT+U method, we simplified rotationally-invariant formulation, implemented by Cococcioni.¹²⁵ The following values of the U parameter were used: 2.10 eV for Mn, 1.00 eV for O and 0.20 eV as previously suggested.¹²⁶

Results and Discussion

Syntheses

The reaction of edteH₄ with Mn(O₂CBu^t)₂, NEt₃ and NaN₃ in a 1:2:2:2.2 molar ratio in MeCN/MeOH (20/1, v/v) afforded a reddish-brown solution from which [Mn₉O₃(OMe)(O₂CBu^t)₇(edte)(edteH)₂(N₃)₂] (**3-1**; Mn²⁺, 8Mn³⁺) was obtained in 58%

isolated yield. The same product was also obtained by using a 1:3 ligand -to- metal ratio; however, the best yield was obtained from the above ratio. The little excess of $t\text{BuCO}_2^-$ helps to facilitate the deprotonation of the edteH₄ ligand along with NEt₃. The formation of **3-1** is summarized in equation 3-1, where atmospheric O₂ gas is assumed to provide the oxidizing equivalents to generate Mn³⁺ from Mn²⁺, and the equation is



balanced accordingly. The specified combination of mixed solvent MeCN/MeOH is crucial to obtain single crystals of **3-1**. Similar microcrystalline products were obtained by changing the second solvent from MeOH to EtOH, DMF, tetrahydrofuran, water or dichloroethane, but the crystal quality was poor. The described procedure in the Experimental Section is the optimized one resulting from an investigation of how various reagent ratios and solvent compositions affected the yield and purity of the obtained complex **3-1**.

Description of the Structure [Mn₉O₃(OMe)(O₂CBu^t)₇(edte)(edteH)₂(N₃)₂]

A partially labeled representation (A) and a stereopair (B) of **3-1** are shown in Figure 3-1, and selected interatomic distances and angles are summarized in Table A-4. Complex **3-1** crystallizes in the monoclinic space group P2₁/n. The compound has apparent C_{2v} symmetry and hence, it can be considered as if two Mn₅ subunits are sharing a common Mn₃(μ₃-OMe) unit (Figure 3-2, A). Each [Mn₅(μ₃-O)(μ₃-OR)(μ-OR)₄] subunit is comprised of a triangular Mn₃(μ₃-O) and a butterfly unit of Mn₄(μ₃-OR)₂ fused together (highlighted by solid lines in Figure 3-2, A). In other words, the core is comprised of a series of fused triangular subunits to give a molecular ladder (Figure 3-2, B). BVS calculations⁶⁸⁻⁷⁰ for the Mn atoms (Table 3-2) identified Mn5 as Mn²⁺ and the

rest are Mn^{3+} ions. Mn1, Mn3, Mn4, Mn6, Mn7, Mn9 are six coordinate while Mn2, Mn5 and Mn8 are seven coordinate. There are two types of ligand bridging modes present in the cluster, singly deprotonated edteH^{3-} and completely deprotonated edte^{4-} group (Figure 3-3). The edte^{4-} group is hexadentate-chelating on Mn5 atom, with each of its deprotonated alkoxide arms bridging to either one (O20, O22) or two (O19, O21) additional Mn atoms. Thus, the edte^{4-} group is overall $\eta^2: \eta^2: \eta^3: \eta^3: \mu^5$ -bridging, as shown in Figure 3-3. The other two edteH^{3-} groups are pentadentate-chelating on Mn2 and Mn8 atoms, with each of its deprotonated alkoxide arms (O15, O17, O18) bridging to one additional Mn atom. Hence, these two edteH^{3-} groups are overall $\eta^2: \eta^2: \eta^3: \mu_4$ -bridging, as shown in Figure 3-3. The peripheral coordination on all Mn^{3+} ions are completed by $\eta^1: \eta^1: \mu$ -bridging ${}^t\text{BuCO}_2^-$ groups. Charge balance consideration requires 8Mn^{3+} , Mn^{2+} , 3O^{2-} , OMe^- , $7{}^t\text{BuCO}_2^-$, edte^{4-} , edteH^{3-} and 2N_3^- . The protonation levels of all O atoms in **3-1** have been determined by BVS calculations, and the results are listed in Table 3-3. The oxides, MeO^- and edte^{4-} O atoms have BVS values of >1.85 , confirming them as completely deprotonated, as concluded above from their bridging modes. There are six significant parallel JT elongations axes (Figure 3-1) present for six, near octahedral Mn^{3+} (Mn1, Mn3, Mn4, Mn6, Mn7, Mn9) ions. The elongated Mn^{3+} -O bonds are $\sim 0.2 - 0.4 \text{ \AA}$ longer than the other Mn^{3+} -O bonds and are being considered as the primary source of anisotropy in the molecule. There are only a few examples of Mn_9 complexes in the literature of structural motifs including molecular cage, and molecular rod.¹²⁷⁻¹³² However, complex **3-1** is structurally unprecedented in the Mn_9 literature.

Magnetochemistry

Dc magnetic susceptibility studies of 3-1

The variable-temperature dc magnetic susceptibility data on compound **3-1** in a 0.1 T field are shown as a $\chi_M T$ vs. T plot in Figure 3-4. The $\chi_M T$ value at 300 K of 25.92 $\text{cm}^3\text{Kmol}^{-1}$ is slightly smaller than the spin-only ($g = 2$) value expected for eight non-interacting Mn^{3+} ions and one Mn^{2+} ion. With decreasing temperature $\chi_M T$ stays fairly constant to ca. 70 K, then increases markedly to a maximum value of 59.41 $\text{cm}^3\text{Kmol}^{-1}$ at ca. 10 K, and then decreases slightly to 58.33 $\text{cm}^3\text{Kmol}^{-1}$ at 5 K, supporting an $S = 21/2$ spin-ground state. The overall behavior of $\chi_M T$ is indicative of predominant ferromagnetic interactions between the metal ions in the molecule. The slight drop in $\chi_M T$ at the lowest temperatures indicates the presence of zero-field splitting and/or intermolecular interactions.

To confirm the above estimates of the ground state spin of 3-1, variable-field (H) and -temperature magnetization (M) data were collected in the 0.1 - 7 T and 1.8 - 10 K ranges. The resulting data are plotted as reduced magnetization ($M/N\mu_B$) vs. H/T , where N is Avogadro's number and μ_B is the Bohr magneton. The data were fit using the program MAGNET,⁶⁶ which is based on diagonalizing the giant-spin Hamiltonian given by equation 3-2, which can be assumed to be valid at low temperatures where only the ground state is thermally populated, and employs a full powder average.

$$H = D\hat{S}_z^2 + g\mu_B\mu_0\hat{S}\cdot H \quad (3-2)$$

The best-fit to the data is shown as the solid lines in Figure 3-5, A and was obtained with $S = 21/2$, $D = -0.37 \text{ cm}^{-1}$, and $g = 2.03$. Fairly good fits were also obtained for $D = 0.35 \text{ cm}^{-1}$ and $g = 1.81$. In order to ensure that the true global minimum had

been located and to assess the robustness of the fit, a root-mean-square D vs. g error surface was generated using the program GRID,⁹⁷ which calculates the relative difference between the experimental $M/N\mu_B$ data and those calculated for various combinations of D and g . This is shown as 2-D contour plot in Figure 3-5, B. Six local minima are observed. The one at $D = 0.35 \text{ cm}^{-1}$ exhibits the largest error and is hence discarded. Among the other five local minima, two global minima were obtained for $D = -0.35 \text{ cm}^{-1}$, $g = 2.00$ and $D = -0.40 \text{ cm}^{-1}$, $g = 2.05$, where the latter is again discarded based on the g value. The minima of the other parameter set is shallow, and the fit uncertainties are thus estimated as $D = -0.37(2) \text{ cm}^{-1}$ and $g = 2.03(2)$. The reduced magnetization fit also provides an alternative spin ground state of $S = 23/2$ with $D = -0.31 \text{ cm}^{-1}$ and $g = 1.85$. Further confirmation of the ground state spin comes from the INS and computational studies.

Alternating current (ac) magnetic susceptibility studies of **3-1**

Ac susceptibilities were measured on microcrystalline samples of **3-1** in a 3.5 G ac field. Frequency-dependent ac susceptibility is an excellent tool to look for slow relaxation of the magnetization vector at low temperature, which is a characteristic feature of an SMM. In addition, the in-phase (χ_M') ac susceptibility signal is invaluable for assessing S without any complications from a dc field, and these signals for complexes **3-1** were measured in the 1.8 - 10 K range at 5 - 1500 Hz. The data are presented as $\chi_M' T$ vs. T in Figure 3-6. Extrapolation of the plots to 0 K, from temperatures above ~5 K to avoid the effect of weak intermolecular interactions (dipolar and superexchange), gives values of $\sim 62 \text{ cm}^3 \text{ K mol}^{-1}$ for **3-1** which confirms the presence of $S = 21/2$ spin-ground state for $g \sim 2.03$. At lower temperature, a frequency-

dependent decrease in $\chi_M' T$ and a concomitant rise in out-of-phase χ_M'' signal were seen (Figure 3-6), which are indicative of a significant barrier to magnetization relaxation. To quantify the effective barrier, construction of an Arrhenius plot is necessary. Ac susceptibility studies at several oscillation frequencies are important tools for determining the true or effective energy barrier (U_{eff}) to magnetization relaxation, because at the χ_M'' peak maxima, the magnetization relaxation rate ($1/\tau$, where τ is the relaxation time) is equal to the angular frequency ($2\pi\nu$) of the oscillating ac field the data can be fitted to Arrhenius equation 3-3. Hence, the plot was constructed and shown in Figure 3-7 (A), and it gave $U_{eff} = 49$ K and $\tau_0 = 3.09 \times 10^{-10}$ s, where τ_0 is the pre-exponential factor. The U_{eff} value of 49 K is the highest yet observed for a high nuclearity $Mn^{2+/3+}$ mixed-valent complex, although still significantly smaller than for the Mn^{3+}_6 (86 K)⁴² and $Mn^{3+/4+}_{12}$ (74 K) complexes.¹⁰⁵

$$1/\tau = (1/\tau_0) \exp(-U_{eff}/kT) \quad (3-3)$$

The upper limit to the energy barrier (U) for a half-integer spin system of $S = 21/2$ and $D = 0.37 \text{ cm}^{-1}$ should be $(S^2 - 1/4)|D|$ which is 59 K and higher than the effective energy barrier (U_{eff}) determined for **3-1**. Thus, U_{eff} is less than U , which is as expected due to the presence of QTM.

For a single relaxation process, as would be expected in a crystalline ensemble of molecules in identical environments with identical barriers, the χ' and χ'' behavior as a function of angular frequency ω ($2\pi\nu$) is given by equations (3-4) and (3-5), respectively, where χ_S ($\chi_{\omega \rightarrow \infty}$) is the adiabatic susceptibility, χ_T ($\chi_{\omega \rightarrow 0}$) is the isothermal susceptibility, and τ is the magnetization relaxation time. For paramagnets obeying the Curie law, the isothermal susceptibility corresponds to the dc susceptibility.

$$\chi'(\omega) = \chi_s + \frac{(\chi_T - \chi_s)}{1 + \omega^2 \tau^2} \quad (3-4)$$

$$\chi''(\omega) = \frac{(\chi_T - \chi_s)\omega\tau}{1 + \omega^2 \tau^2} \quad (3-5)$$

In the case of a distribution of relaxation processes, which results from a distribution of molecular environments in the crystal and an associated range of U_{eff} barrier heights, the expressions for χ' and χ'' are given by equations (3-6) and (3-7), where α gauges the width of the distribution and has a value between 0 and 1.

$$\chi'(\omega) = \chi_s + \frac{(\chi_T - \chi_s)[1 + (\omega\tau)^{1-\alpha} \sin(\alpha\pi/2)]}{1 + 2(\omega\tau)^{1-\alpha} \sin(\alpha\pi/2) + (\omega\tau)^{2(1-\alpha)}} \quad (3-6)$$

$$\chi''(\omega) = \frac{(\chi_T - \chi_s)(\omega\tau)^{1-\alpha} \cos(\alpha\pi/2)}{1 + 2(\omega\tau)^{1-\alpha} \sin(\alpha\pi/2) + (\omega\tau)^{2(1-\alpha)}} \quad (3-7)$$

When $\alpha = 0$, equations (3-6) and (3-7) reduce to equations (3-4) and (3-5), respectively, describing a single relaxation process.

Magnetization relaxation data were collected at several temperatures of 2.0 - 4.2 K on a vacuum dried, microcrystalline sample of **3-1** in a 3.5 G ac field while the oscillating frequencies were in the range of 0.1 to 1500 Hz. The data in the form of $\chi'(\omega)$ and $\chi''(\omega)$ were fitted to see if they followed a single relaxation process or a distribution of single relaxation processes. The data for 3.0 K are presented in Figure 3-8 (A) as χ' vs. ω ($2\pi\nu$) and χ'' vs. ω ($2\pi\nu$). The solid lines result from a least-squares fitting of the data to a single relaxation process, as described by equation 3-4 and 3-5. Better fits were obtained when the data were fitted for a distribution of single relaxation processes (equation 3-6 and 3-7) and are presented in the same figure as dashed lines. A complete list of all the least-squares fitting parameters of the data for the single

relaxation process and the distribution of a single relaxation processes are presented in Table 3-4.

The ac data are also presented as a χ' vs. χ'' plot, which is known as Cole-Cole or Argand plot,^{11,133} as shown in Figure 3-8 (B). The symmetrical shape of the plot suggests that a single type of species is present. The solid line represents a least-squares fit of the data to a single relaxation process as described by equations (3-4) and (3-5) in Figure 3-8. The dashed line represents a fit to a distribution of relaxation processes as described by equations (3-6) and (3-7), yielding the α values 0.329(2) (for χ') and 0.237(2) (for χ''), respectively. The latter fit is clearly superior and indicates a small range of molecular environments. The temperature dependence of the distribution of relaxation processes in the range of 2.0 to 4.2 K is shown in Figure 3-9 (A).

Interestingly, α increases with decreasing temperature causing a wider distribution of relaxation rates at lower temperature (Figure 3-9, B). Such a distribution of molecular environments in Mn_9 molecule would lead to a distribution of ZFS parameter D which affects the potential energy barrier height. A distribution in transverse zero-field interactions could also affect the rate of magnetization quantum tunneling.

Single-crystal hysteresis studies for 3-1 below 1.8K

The ac measurements suggest strongly that **3-1** behaves as an SMM, which was confirmed by the observation of hysteresis loops in magnetization vs. dc field scans, measured on a single crystal of **3-1**·4MeCN using the micro-SQUID apparatus.⁶⁷ The temperature-dependence at 0.14 T s⁻¹ and the scan-rate dependence at 0.04 K of the hysteresis loops are shown in Figure 3-10. The coercivities clearly increase with decreasing temperature and increasing scan rate, as expected for the

superparamagnet-like behavior of SMMs.^{11,19,59} The data thus confirm that complex **3-1** is a new addition to the family of SMMs, with a blocking temperature (T_B) of 2.5 K. The hysteresis loops also clearly show steps at periodic values of applied field due to quantum tunneling of magnetization (QTM), which causes a surge in the relaxation as the M_S levels on the opposite sides of the energy barrier in the $S = 21/2$ double well potential come into resonance at those field positions. The field separation, ΔH , between the steps is proportional to D and is given by equation 3-8.

$$\Delta H = |D|/g\mu_B \quad (3-8)$$

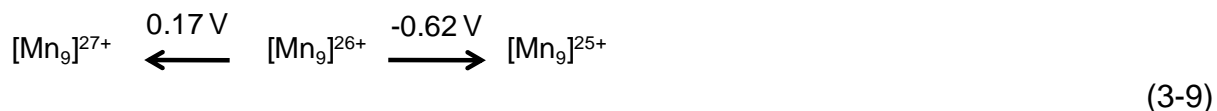
Measurement of the step positions in Figure 3-10 gave an average ΔH of 0.375 T and a resulting $|D|/g\mu_B$ value of 0.17 cm^{-1} (where $D = 0.34 \text{ cm}^{-1}$ for $g = 2.0$), which agrees closely with both the values obtained from the fits to the magnetization data and the INS studies (0.343 cm^{-1} , vide infra). It should be noted that **3-1** has a half-integer spin ground state and hence, it shows no step at zero applied field. The reason behind the suppression of QTM at zero applied field is the spin-parity effect in a half-integer spin system which leads to Kramer's degeneracy whereas QTM is allowed in integer spin system.⁷⁶ However the omission of QTM at zero applied field is less likely due to the fact that it is impossible to ensure absolutely zero external fields. The dipolar fields of neighboring molecules and the hyperfine fields from the ^{55}Mn nuclei ($I = 5/2$, ~ 100% natural abundance) provide a means for QTM to occur at apparently zero applied fields.¹¹⁵ Thus, the expected suppression of QTM for half-integer spin at zero external field is actually quite surprising.

Magnetization vs. time decay data were collected on a single crystal of **3-1**·4MeCN in order to obtain a more quantitative assessment of the magnetization relaxation

dynamics (Figure 3-10, C). The sample's magnetization was first saturated in one direction at ~5 K with a large applied dc field, the temperature was then decreased to a chosen value, and then the field was removed and the magnetization decay monitored with time. The results are shown in Figure 3-10 (C) for the 1.3 - 2.5 K range. From these measurements the Arrhenius plot was constructed and fitted based on equation 3-3 (Figure 3-7, B). These data complement the ac out-of-phase data and confirm the effective energy barrier of 49K, which is the highest in a mixed-valent Mn²⁺/Mn³⁺ system.

Electrochemistry

Electrochemical studies on **3-1** in DMF have revealed a rich redox chemistry involving multiple peaks on the reduction side and one peak in the oxidation side (Figure 3-11, A). Two reduction peaks are irreversible and the peak in oxidation is reversible. The observed CV behavior suggests the electron-transfer series shown in equation 3-9. The reported potentials are vs. ferrocene.



A study of scan rate dependence for the 0.17 V oxidation process has been performed at 50 - 500 mV/s scan rate, which shows reversibility of the peak. The cathodic to anodic peak current separation increases with the scan rate (Figure 3-12, A). In addition, a linear dependence of the peak current with $v^{1/2}$ (v = scan rate) is shown in Figure 3-12 (B) indicating that the oxidation process at the electrode is a diffusion-controlled process. The observed reversible process can be assigned as the one-electron oxidation of Mn²⁺ to corresponding Mn³⁺ ion.⁵² The irreversible processes (-0.62 V and -1.18 V) can be attributed to the reduction of Mn³⁺ to Mn²⁺. The DPV scans

at 20 mV/s for **3-1** are shown in the Figure 3-11 (B). The data obtained from DPV measurement complement the CV data and the peak broadness in DPV study justifies the irreversibility of the reduction peak. The overall result indicates the possibility of isolating a new Mn_9 complex very similar to **3-1** but with all Mn ions in the +3 oxidation state, possibly improving the anisotropy of the molecule by having seven significant JT elongation axes rather than the six JT axes currently seen.

Inelastic Neutron Scattering (INS)

In Figure 3-13 the spectra measured with an incoming neutron wavelength of 6.5 Å are presented. At 1.5 K a strong feature I at ca 0.85 meV and a small feature at ca 0.4 meV, which is marked by an asterisk, are observed. With increasing temperature, feature I decreases and the corresponding anti-Stokes feature I' on the neutron energy-gain side appears. Feature I is hence assigned to a cold transition. The feature at 0.4 meV appears to be temperature-independent between 1.5 and 5.0 K and is not observed on the energy-gain side. It is hence assigned to a spurious feature. With further increasing temperature, hot features ii to v appear between 0.5 and 0.8 meV. In order to observe the peaks with higher resolution, data were recorded with a wavelength of 7.5 Å and are shown in Figures 3-14. At 1.5 K, feature I at 0.847(1) meV is very intense. Its intensity decreases on the neutron energy-loss side and increases on the energy-gain side with increasing temperature, as expected for a cold magnetic transition. With increasing temperature more and more features related to hot magnetic transitions evolve at 0.778(1), 0.706(3), 0.625(4), 0.530(8), 0.41(3), and 0.34(7) meV, which are labeled ii to vii. A feature similar to the one observed in the 6.5 Å data at ca 0.4 meV (marked by the asterisk in Figure 3-13) is not observed in the 7.5 Å data, which confirms our earlier assignment to a spurion. In Figure 3-15, the $S(Q,\omega)$ plot of the 7.5 Å

spectrum measured at 10.0 K is shown, where Q is the momentum transfer. Features I to vi can clearly be observed, which is impressive and demonstrates the high quality of the recorded data. These peaks all show significant intensity over the whole Q range, in particular at the lower Q values, which unambiguously confirms their magnetic origin.¹³⁴⁻

136

Figure 3-16 (A) presents the INS spectra measured with a wavelength of 3.2 Å at the temperatures 1.5 and 40 K. The 1.5 K spectrum shows some peak-like features while the 40 K spectrum is comparatively featureless. Hence, the scattering intensity due to magnetic transitions is apparently swamped out already at 40 K such that these data reflect the lattice contribution. This affords to use them for estimating the lattice contribution at 1.5 K by applying the Bose factor to the 40 K data.¹³⁷⁻¹³⁹ The resulting curve is shown as green dots in Figure 3-16 (A). The measured 1.5 K data can then (approximately) be corrected for the lattice contributions by subtracting from them the Bose-scaled curve, which yields the data shown as blue dots. The Bose-corrected 1.5 K spectrum shows feature I in the tail of the elastic line. At higher energies several further features are observed: feature A at ca. 2.0 meV, feature VIII at ca. 2.7 meV, feature B at ca. 3.1 meV, feature IX at ca. 3.9 meV, and feature C at ca. 4.6 meV. Figure 3-16 (B) shows the $S(Q,\omega)$ plots of the 1.5 K spectrum as is on the left and after the Bose correction on the right, respectively. In the whole energy range a large phononic scattering contribution is observed (left panel), which is well accounted by the Bose correction (right panel). It is noted that a large phononic scattering intensity above energies of 2 meV is commonly observed in non-deuterated samples of molecular nanomagnets. The Q dependence of features VIII and IX suggests a magnetic origin.

For features A, B, and C the situation is less clear, because of their significantly lower intensity. From carefully comparing the 40 K data, the 1.5 K data, and the Bose-corrected 1.5 K data, features A and B seem to appear from an incomplete estimation of the background scattering intensity in the range of 1.5 to 3.5 meV, which is also present at 40 K. This suggests that these features are of phononic origin. Also feature C appears to be of phononic origin. However, while the features I, VIII, and IX are safely assigned as magnetic, the conclusions as regards A, B, and C have to be taken with care in view of the experimental data.

The seven magnetic INS peaks at energies below 1 meV show the typical temperature dependence and picket-fence structure observed in clusters with a zero-field split spin ground-state, which is well separated from higher multiplets, as it is characteristic for SMMs described in the giant spin Hamiltonian approach.^{15,140} From the temperature dependence of these peaks the anisotropy has to be of the easy-axis type, which is consistent with the observation of an out-of-phase magnetization, magnetic hysteresis, and QTM steps. The peaks observed at higher energies correspond then to transitions to higher-lying spin multiplets, and their large energy supports the validity of the giant-spin Hamiltonian picture. However, in view of the many exchange paths and complicated exchange topology, their interpretation is clearly a challenging task, and is not attempted here.

Fitting the energies of the peaks below 1 meV to a rigid spin $S = 21/2$ model with only a second-order easy-axis anisotropy (D term) incorporated did not work well. Hence, higher-order terms^{141,142} were systematically included and the fit results carefully checked for the statistical significance of the terms. Inclusion of a B_4^0 term provided a

nearly perfect description of peaks I and ii, but significant deviations for the lower-lying peaks remained, hence a B_6^0 term had additionally to be added. The best-fit values were $D = -0.343(1) \text{ cm}^{-1}$, $B_4^0 = -0.03(1) \cdot 10^{-4} \text{ cm}^{-1}$, and $B_6^0 = 0.017(2) \cdot 10^{-6} \text{ cm}^{-1}$, which reproduce all seven peaks very well, as shown by the INS simulations presented in Figure 3-17 (A). Some minor discrepancies between experimental and simulated peak positions remain, which in principle could be accounted for, by including further anisotropy terms, however, they could not be modeled properly within statistical significance. The peak intensities are less well simulated at temperatures above 15 K, which indicates the onset of the transitions to and within higher-lying spin multiplets, swamping out magnetic intensity at 28 K. The derived energy spectrum and observed transitions are shown in Figure 3-17 (B).

The D value as determined from INS is slightly smaller than that determined from the magnetic data, but within experimental error. The calculated height of the energy barrier is 54.5 K, which is close to the calculated height of 54.8 K with neglecting the higher-order terms, i.e., these have little effect on the barrier height.

Density Functional Theory

Using first principle methods of electronic structure theory helps in understanding the intricate details of molecular magnetic systems and may provide complementary information on their behavior. The most common theoretical method for prediction of magnetic coupling parameter J is Density Functional Theory (DFT). DFT is the only ab initio method capable of describing large molecules, such as Mn_{12}Ac , Fe_8 , and V_{15} and other molecular magnets.¹⁴³⁻¹⁴⁸ In this method the antiferromagnetic (AF) state is described by the open shell single Slater determinant, where singly occupied magnetic

orbitals are localized on the transition metal atoms (alpha electrons on some, beta electrons on others). Unlike the Slater determinant describing ferromagnetic state (FM), AF determinant is not an eigenfunction of the spin operator (spin symmetry is “broken”). The difference in energy between AM and FM states (spin gap) is then related to J . The pure DFT is known to artificially over delocalize electrons due to the self interaction error. As a result, the band gap and spin gap are strongly underestimated. In order to correct for this error a fraction of Hartree-Fock (HF) exchange often replaces local or semi-local exchange-correlation functional, yielding the so-called hybrid DFT functional. In the HF method the Slater determinant has the physical meaning of the wavefunction of the system, so that broken symmetry indicates the AF determinant is unphysical and does not correctly predict energy for the low-spin system. In a complete analogy, hybrid DFT approaches imply that AF energy needs corrections. Several correction formulas had been developed by Noodleman,¹⁴⁹⁻¹⁵³ Yamaguchi,¹⁵⁴⁻¹⁵⁷ Ruiz,¹⁵⁸ Nishino,¹⁵⁹ and others.¹⁶⁰ While accurate in many cases, this approach tends to err in systems where magnetic orbitals are strongly delocalized (for example binuclear complexes with acetate bridges).^{148,161}

Another way to alleviate the effects of self-interaction error is DFT+U (where the onsite Coulomb repulsion term U is added to the effective Hamiltonian). DFT+U was introduced by Anisimov et al.¹⁶² and simplified by Cococcioni et al.¹⁶³ Recently it was shown^{126,164} that both metal centers and ligand atoms need to be assigned a specific U value in order to accurately describe the J values. The inclusion of a Hubbard- U term for both the M 3d and O 2p electrons greatly enhances the localization, and is essential in order to obtain the correct J value and, in some cases, correct ground state.

Determination of ground spin state of 3-1

The primary goal of the DFT calculation was to predict the correct ground spin arrangement in the molecule. Inelastic Neutron Scattering (INS) data shows the ground spin state has a multiplicity of 22. This value suggests that any two Mn³⁺ atoms in this molecule are aligned as spin down and the other seven possess spin up orientation. Starting from FM optimized geometry, energy for 29 hypothetical spin states were obtained as listed in Table D-1 (atoms are labeled according to Figure 3-18). Since Mn⁺³-Mn⁺³ and Mn⁺²-Mn⁺³ centers have relatively small magnetic exchange constants, small energy gaps between these hypothetical spin states are expected. It can be noted that the lowest energy state corresponds to the minority spin localized on Mn1 and Mn9 atoms, with total multiplicity consistent with the INS observation (Table D-1).

Heisenberg exchange constant in Mn₉ system

The following is the Heisenberg Hamiltonian written with the assumption of neglecting the second and higher neighbor magnetic interactions (equation 3-10):

$$\hat{H} = -J_{13}S_1S_3 - J_{12}S_1S_2 - J_{24}S_2S_4 - J_{35}S_3S_5 - J_{34}S_3S_4 - J_{45}S_4S_5 - J_{23}S_2S_3 - J_{46}S_4S_6 - J_{13}S_9S_7 - J_{12}S_9S_8 - J_{24}S_8S_6 - J_{35}S_7S_5 - J_{34}S_7S_6 - J_{45}S_6S_5 - J_{23}S_8S_7 \quad (3-10)$$

The molecule is composed of two symmetrically equivalent fragments such that Mn1, Mn2, Mn3, Mn4 are equivalent to Mn9, Mn8, Mn7, and Mn6 respectively. The arrangement indicates the presence of eight inequivalent exchange interactions. The J values (apart from J_{46}) were calculated as direct energy differences between the spin states shown in columns 2 and 3 in Table 3-5 by using the equation 3-11.

$$J_{ij} = (E_{SC1} - E_{SC2}) / S_i S_j \quad (3-11)$$

In equation 3-11, E_{SC1} is the energy of (S)_{ij} state from column 2, and is that from the column 3. For example to calculate the exchange constant between Mn1-Mn3, the

energy difference between two hypothetical states have been taken, where in one Mn1 and Mn3 are spin down, and in another Mn1 and Mn7 are spin down. To predict J_{46} the energy difference between two hypothetical spin states is taken where in one Mn2 and Mn4 are spin down, and in the other all Mn atoms are spin up. The energy difference is shown in equation 3-12.

$$\Delta E = - 8J_{12} - 8J_{34} - 10J_{45} - 8J_{23} - 8J_{46} \quad (3-12)$$

The equation 3-12 was solved for J_{46} using J values obtained previously.

Mn₉ topology consists of fused Mn₃ triangles, known to be susceptible for spin frustration, caused by competing exchange pathways. The ground spin state in Table D-1 is characterized by the presence of two AF couplings between Mn1/Mn3 and Mn1/Mn2, while the rest are FM. The calculated J_{12} (Mn1/Mn2) interactions in Table 3-6 are negative (AF) with spin couplings of c.a. -16.87 cm^{-1} , as expected for antiparallel alignments. The rest of the spin couplings (ranging from 1.14 cm^{-1} to 27.32 cm^{-1}) are FM.

Coupling (equation 3-13) for two multi-electron spin centers was expressed by Clark and Davidson as:¹⁶⁵

$$J_{ij} = \frac{1}{2} [S_T(S_T + 1) - S_i(S_i + 1) - S_j(S_j + 1)] \quad (3-13)$$

where S_i and S_j coupled together to give a total spin S_T ($S_T = S_i + S_j$). J predicted by equation 3-13 can be compared for two adjacent spins. For a Mn⁺²/Mn⁺³, and Mn⁺³/Mn⁺³ pairs aligned parallel, the spin couplings from equation 3-13 are 5 and 4, respectively. The calculated J_{13} Mn1/Mn3 interactions in Table 3-6 are positive (ferromagnetic) with spin couplings of 7.48 cm^{-1} . However, the J_{13} (Mn1/Mn3) interactions of the Mn1Mn3, pair in Table 3-6 are ferromagnetic, and yet their spin-

coupling value are very negative (-3.84 cm^{-1}). This means that these ferromagnetic interactions are completely frustrated, and the spins are aligned antiparallel. Hence, the data is rationalized by the ligand induced spin frustration effect that dominates the spin alignment in Mn1, Mn2, Mn3 containing triangle.

Bonding analysis

The Löwdin population analysis is reported in Table 3-7. The oxide dianions serve as pure σ -donors and have spin polarization opposite to that of the nearest Mn ion which is in agreement with the superexchange mechanism. The monodentate azide ion attached to Mn1 is also acting as a pure σ -donor as it known to be a weak field ligand. The azide nitrogen coordinated to Mn1 is showing spin polarization opposite to that of the metal ion. The O atoms of the acetates have the same spin polarization as the nearest Mn cations. This observation contradicts a simple superexchange picture and can be explained with a dative (also known as π -back bonding) mechanism.¹⁶⁶ The acetate has vacant π -orbital extended over three atoms, and can serve as π -acceptor for the d-electrons of the Mn cation. As a result, Anderson's superexchange mechanism, developed for σ -bonding metal-ligand interactions, no longer holds. This is a suggested reason of limitation of hybrid DFT for acetate bridging complex. The chelating edteH₄ is also showing similar Löwdin spin densities as the acetate and making a π -back bond with manganese.

Concluding Remarks

The present work provides a further confirmation of the ability of the edteH₄ ligand to yield interesting complexes. In the present case, it has given a novel, polynuclear, high-spin, half-integer spin Mn₉ SMM which also displays interesting magnetic

properties. The Mn_9 cluster is comprised of a series of edge-sharing triangular units, which is a rare metal topology and allows the presence of six significant Jahn-Teller elongation axes. The anisotropy of the molecule is considerably large with a relatively high energy barrier of 49 K determined from the Arrhenius plot, which is the highest known in a mixed-valent Mn^{III}/Mn^{II} system. The energy spectrum for observed transitions is derived from the INS study. DFT computational analysis calculates all the exchange coupling parameters and rationalizes the spin ground state of Mn_9 SMM. The hysteresis plot reveals plenty of QTM steps, but no step at zero field. This is expected for a half-integer spin SMM but a still rarely observed phenomenon. Further investigations are in progress in order to better understand the physics of this interesting feature.

Table 3-1. Crystallographic data for **3-1**·4MeCN

Parameter	3-1
Formula	C ₆₆ H ₁₂₈ Mn ₉ N ₁₂ O ₃₀
Formula weight, g/mol	2064.26
Crystal system	Monoclinic
Space group	P2 ₁ /n
a, Å	20.965(10)
b, Å	33.819(13)
c, Å	28.485(12)
α, β, γ, °	90, 92.859(8), 90
V, Å ³	20172(15)
Z	8
T, K	100(2)
Radiation, Å ^a	0.71073
ρ, g/cm ³	1.359
μ, mm ⁻¹	1.159
R1 ^{b,c}	0.0886
wR2 ^d	0.1329

^a Graphite monochromator. ^b $I > 2\sigma(I)$. ^c $R1 = \sum(|F_o| - |F_c|) / \sum|F_o|$. ^d $wR2 = [\sum[w(F_o^2 - F_c^2)^2] / \sum[w(F_o^2)^2]]^{1/2}$, $w = 1/[\sigma^2(F_o^2) + [(ap)^2 + bp]$, where $p = [\max(F_o^2, 0) + 2F_c^2]/3$

Table 3-2. BVS calculations for the Mn atoms of complex **3-1**^a

Atom	Mn ²⁺	Mn ³⁺	Mn ⁴⁺
Mn1	3.39	<u>3.16</u>	3.08
Mn2	3.15	<u>2.94</u>	2.87
Mn3	3.41	<u>3.14</u>	3.08
Mn4	3.47	<u>3.20</u>	3.14
Mn5	<u>1.99</u>	1.86	1.81
Mn6	3.45	<u>3.18</u>	3.12
Mn7	3.42	<u>3.15</u>	3.09
Mn8	3.19	<u>2.97</u>	2.89
Mn9	3.41	<u>3.17</u>	3.10

^a The underlined value is the one closest to the charge for which it was calculated. The oxidation state of a particular atom can be taken as the nearest whole number to the underlined value.

Table 3-3. BVS calculations for the O atoms of complex **3-1**^a

Atom	BVS	Assignment	Group
O15	1.86	OR ⁻	edte ⁴⁻
O17	1.99	OR ⁻	edte ⁴⁻
O18	1.89	OR ⁻	edte ⁴⁻
O19	1.98	OR ⁻	edte ⁴⁻
O20	1.86	OR ⁻	edte ⁴⁻
O27	2.07	O ²⁻	OMe ⁻
O29	1.71	O ²⁻	O ²⁻
O28	2.03	O ²⁻	O ²⁻
O30	2.04	O ²⁻	O ²⁻

^aThe BVS values for O atoms of O²⁻, ROH and H₂O groups are typically 1.8 - 2.0, 1.0 - 1.2 and 0.2 - 0.4, respectively, but can be affected somewhat by hydrogen-bonding.

Table 3-4. Fitting parameters for plots of χ' vs. angular frequency and χ'' vs. angular frequency to a single relaxation process and a distribution of single relaxation processes for complex **3-1**

Compound	Single relaxation process	
	χ'	χ''
$\chi_S(\text{cm}^3)$	$1.2808 \cdot 10^{-4}$	0.4996
$\chi_T(\text{cm}^3)$	$9.2070 \cdot 10^{-4}$	0.5004
τ (s)	$4.4867 \cdot 10^{-3}$	$4.2759 \cdot 10^{-3}$
	Distribution of a single relaxation process	
Mn₉(3-1)	χ'	χ''
$\chi_S(\text{cm}^3)$	$8.2713 \cdot 10^{-5}$	12.4997
$\chi_T(\text{cm}^3)$	$9.4188 \cdot 10^{-4}$	12.5003
τ (s)	$4.2237 \cdot 10^{-3}$	$4.1966 \cdot 10^{-3}$
α	0.3287	0.2365

Table 3-5. Computational calculation scheme for seven Heisenberg exchange constants in Mn₉ complex (**3-1**). The symbol 1, 2, 3, 4, 6, 7, 8, 9 are for Mn⁺³ and 5 is for Mn⁺² having four and five unpaired electrons respectively. Here i is presenting spin up and i is showing spin down orientation.

	Spin configuration 1 (<i>SC</i> ₁)	Spin configuration 2 (<i>SC</i> ₂)	$J_{ij} = \frac{E_{SC_1} - E_{SC_2}}{S_i S_j}$ (cm ⁻¹)
<i>J</i> ₁₃			7.48
<i>J</i> ₁₂			-16.87
<i>J</i> ₂₄			1.14
<i>J</i> ₃₅			25.07
<i>J</i> ₃₄			7.92
<i>J</i> ₄₅			3.15
<i>J</i> ₂₃			4.02

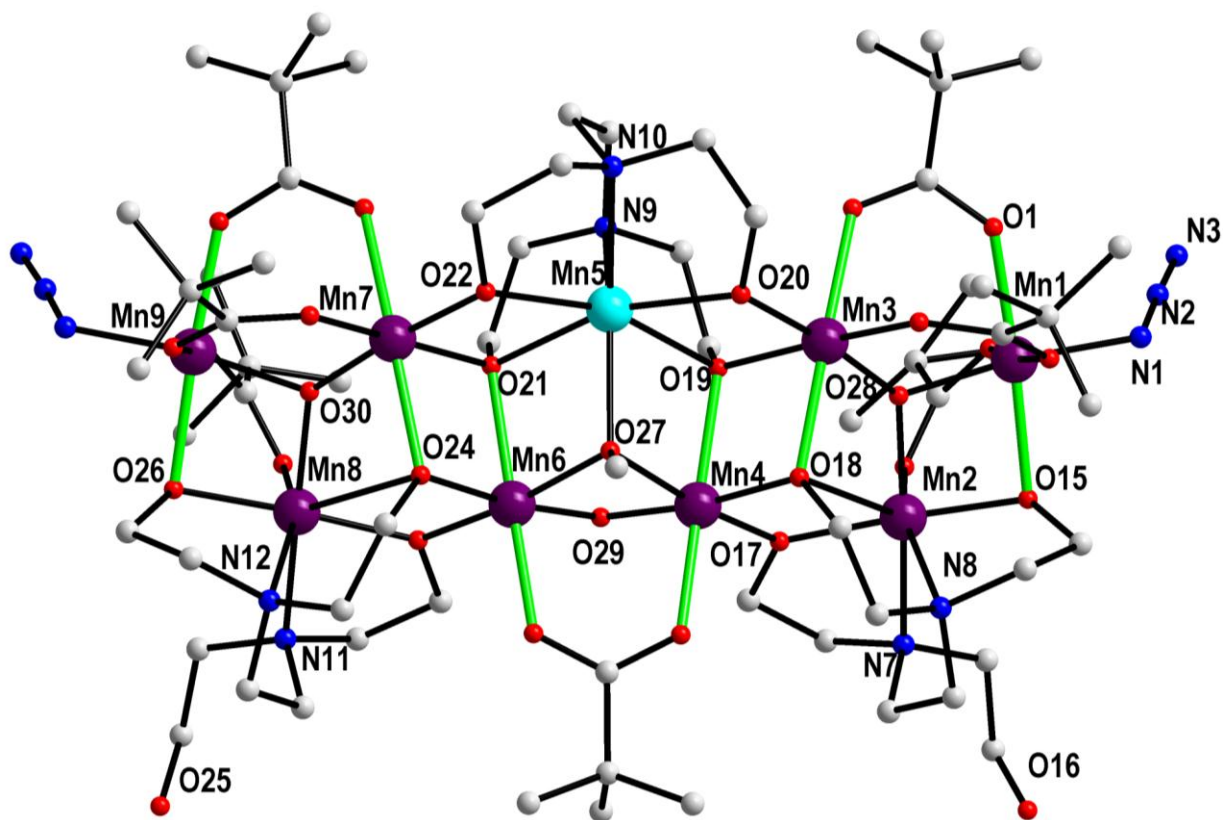
Table 3-6. The distance between Mn_i and Mn_j, Heisenberg exchange constants for two adjacent metal centers and calculated and ideal spin coupling are presented (using equation 3-13)

	Mn _i -Mn _j Å	J cm ⁻¹	$\langle S_i S_j \rangle_{calc}$	$\langle S_i S_j \rangle_{ideal}$
J_{13}	3.35	7.48	-3.84	-4
J_{12}	2.95	-16.87	-3.82	-4
J_{24}	3.43	1.14	3.84	4
J_{35}	3.33	25.07	4.70	5
J_{34}	3.21	7.92	3.82	4
J_{45}	3.38	3.15	3.84	5
J_{23}	3.46	4.02	3.84	4
J_{46}	2.86	27.32	3.82	4

Table 3-7. Löwdin Population analysis for spin densities of complex **3-1** in its ground spin states and the magnetic states having highest possible multiplicity, all Heisenberg exchange constants set as ferromagnetic. The labels of all the indicated atoms refer to Figure 3-1.

	Löwdin Spin Densities	
	IS ₁₉	F
Mn1, Mn9	-3.94	3.94
Mn2, Mn8	3.92	3.92
Mn3, Mn9	3.92	3.92
Mn4, Mn6	3.90	3.90
Mn5	4.83	4.83
N1	-0.03	0.03
N2	0.05	-0.05
N3	0.09	-0.09
N8	-0.04	0.04
N9	0.02	0.02
N10	0.02	0.02
O1	0.02	0.02
O15	-0.05	0.05
O29	-0.07	-0.07
O20	-0.04	0.04
O18	0.02	0.04

A



B

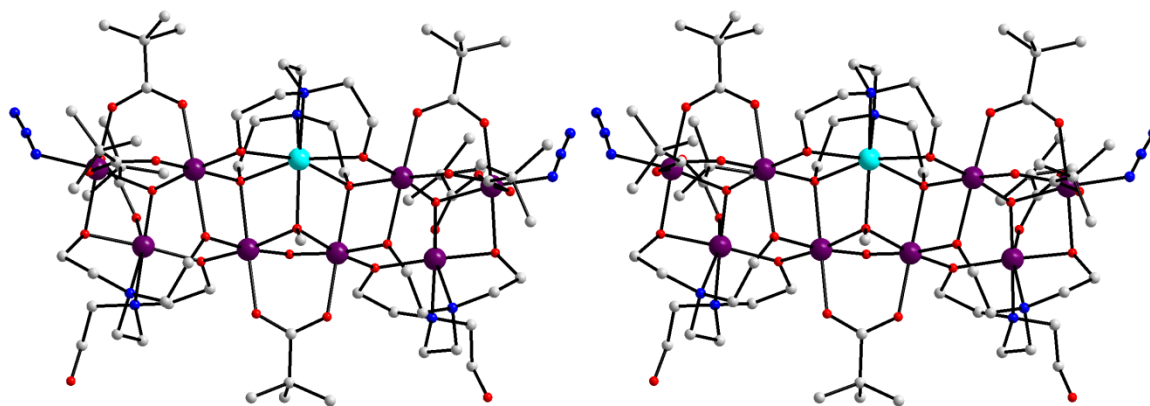
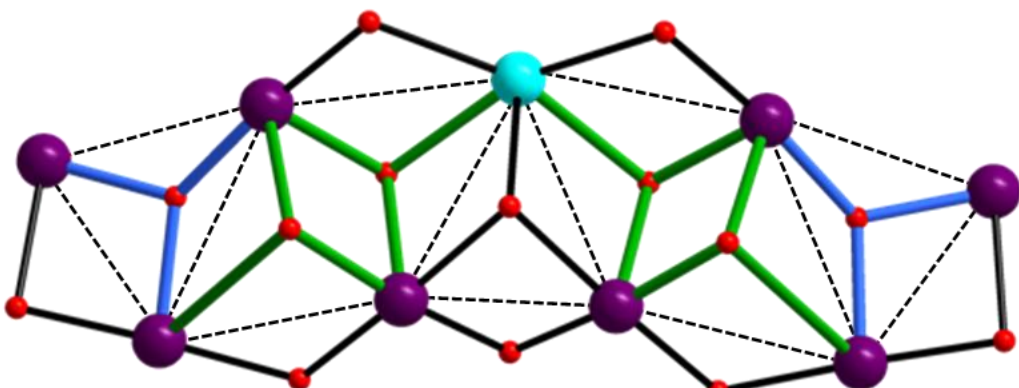


Figure 3-1. A partially labeled representation of complex **3-1** (A, Jahn-Teller axes shown as green thick lines) and a stereopair (B). Hydrogen atoms have been omitted for clarity. Color code: Mn^{3+} , purple; Mn^{2+} , cyan; O, red; N, blue; C, light-grey.

A



B

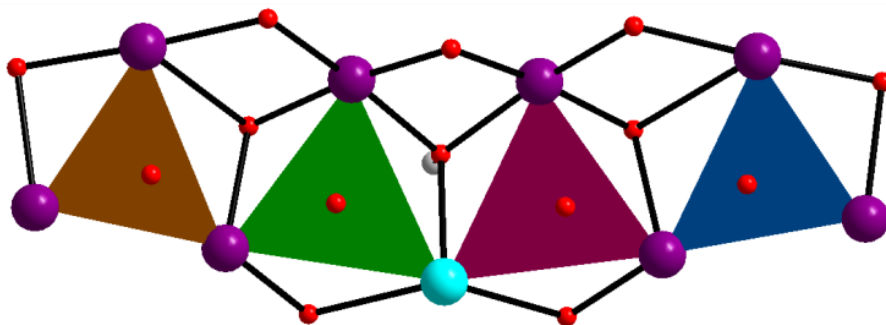


Figure 3-2. The core of complex **3-1** (A) and the core with an emphasis on the triangular sub units (B). Color code: Mn^{3+} , purple; Mn^{2+} , cyan; O, red.

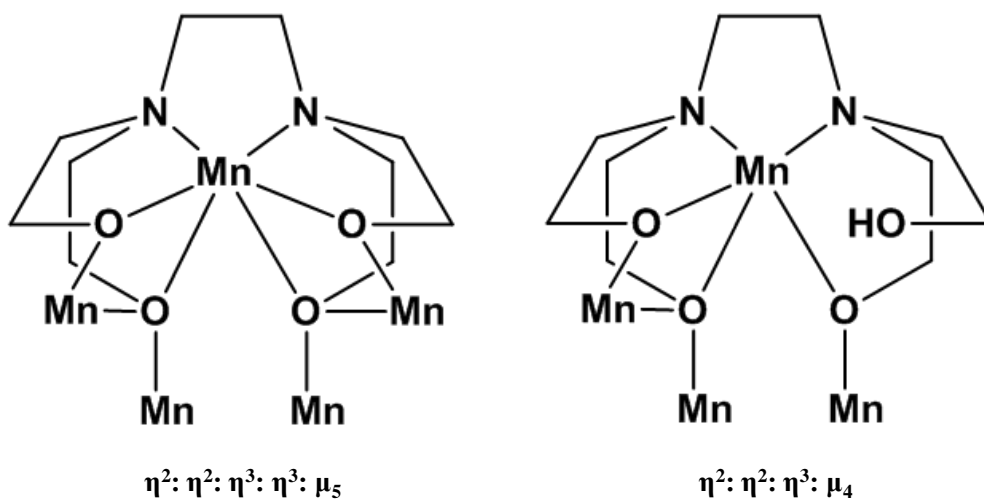


Figure 3-3. The coordination modes of edte^{4-} and edteH^{3-} found in complex **3-1**.

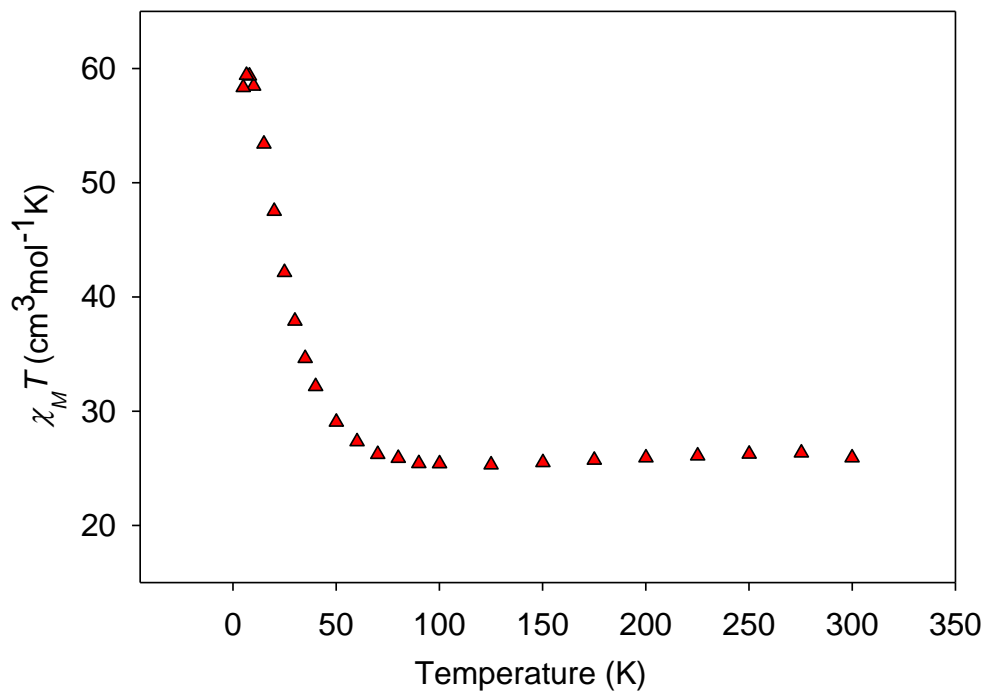


Figure 3-4. Plot of $\chi_M T$ vs. T for complex **3-1**.

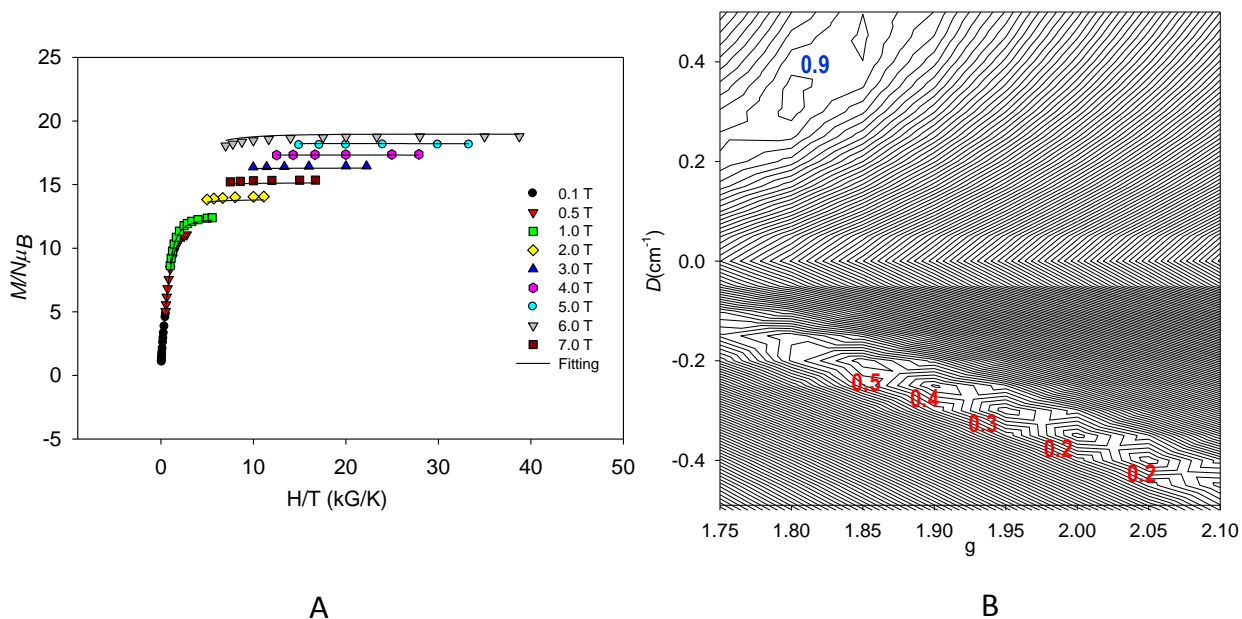


Figure 3-5. Plot of reduced magnetization ($M/N\mu_B$) vs. H/T for complex **3-1** (A) at applied fields of 0.1 - 7.0 T and in the 1.8 - 10 K temperature range. The solid lines are the fit of the data; see the text for the fit parameters. Two-dimensional contour plot for the rms error surface vs. D and g for the reduced magnetization fit for complex **3-1** (B).

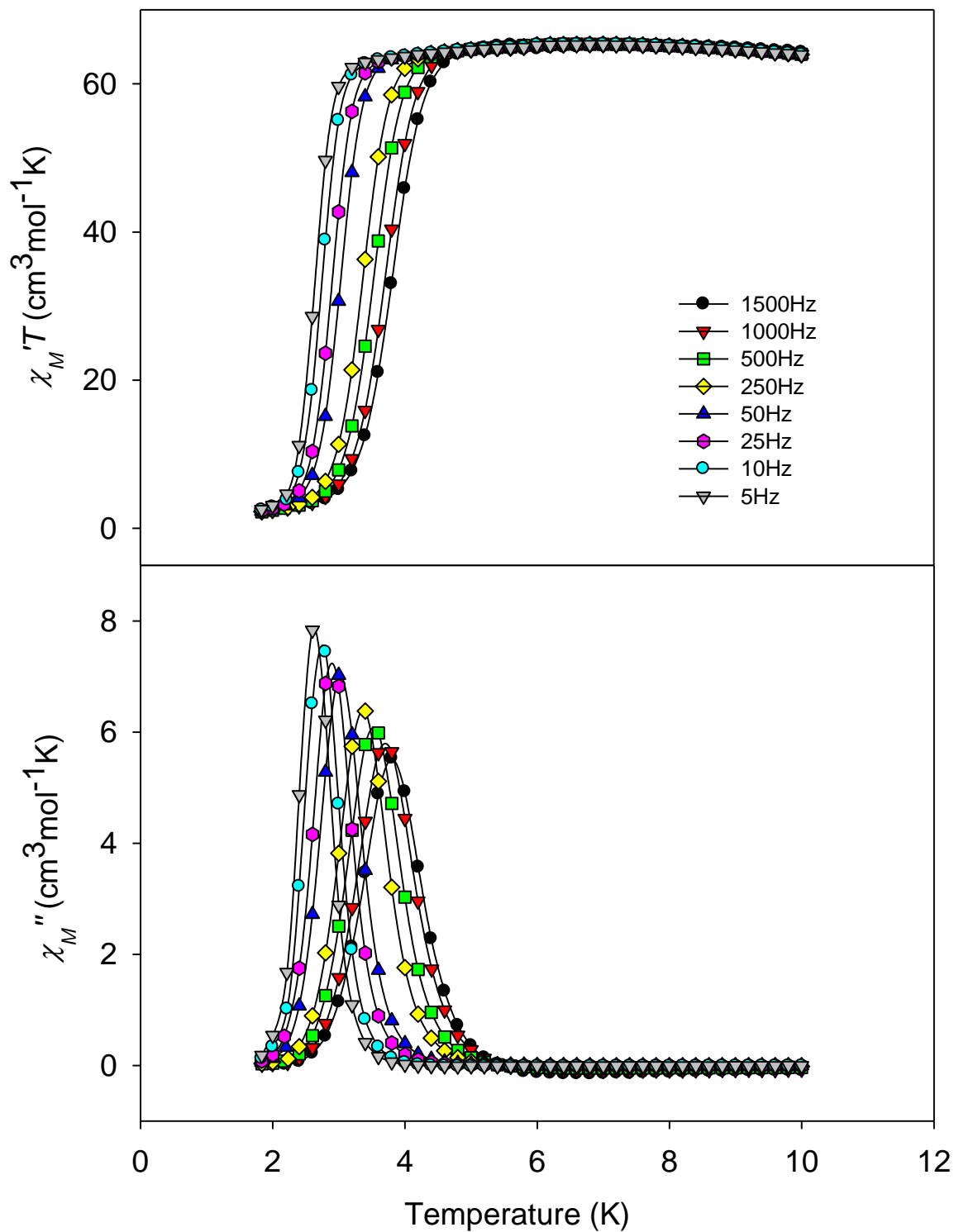
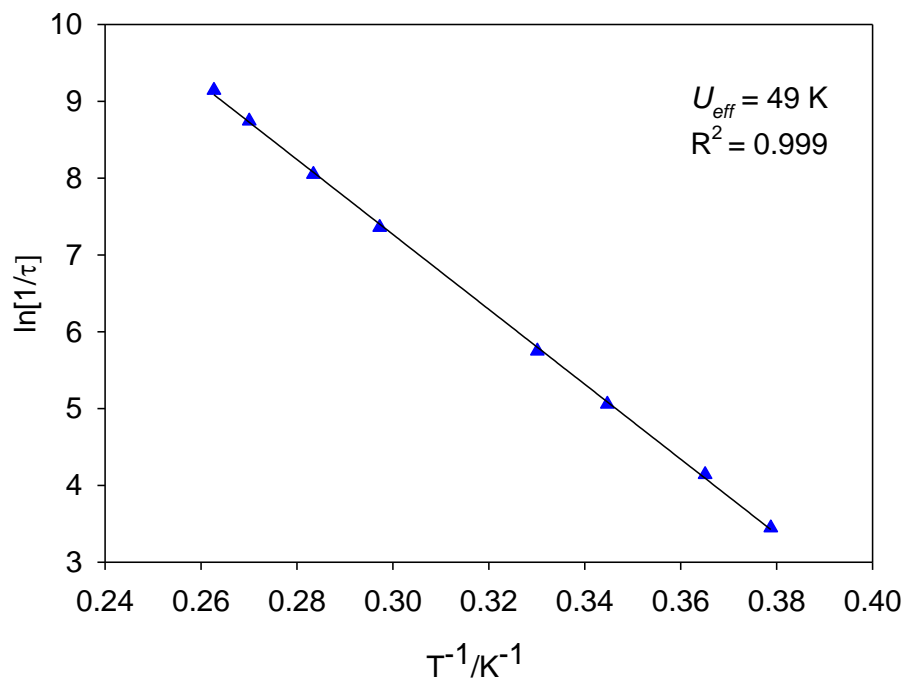


Figure 3-6. Plots of in-phase χ_M' (as $\chi_M'T$) vs. T and out-of-phase χ_M'' vs. T ac signals for complex **3-1** at the indicated frequencies.

A



B

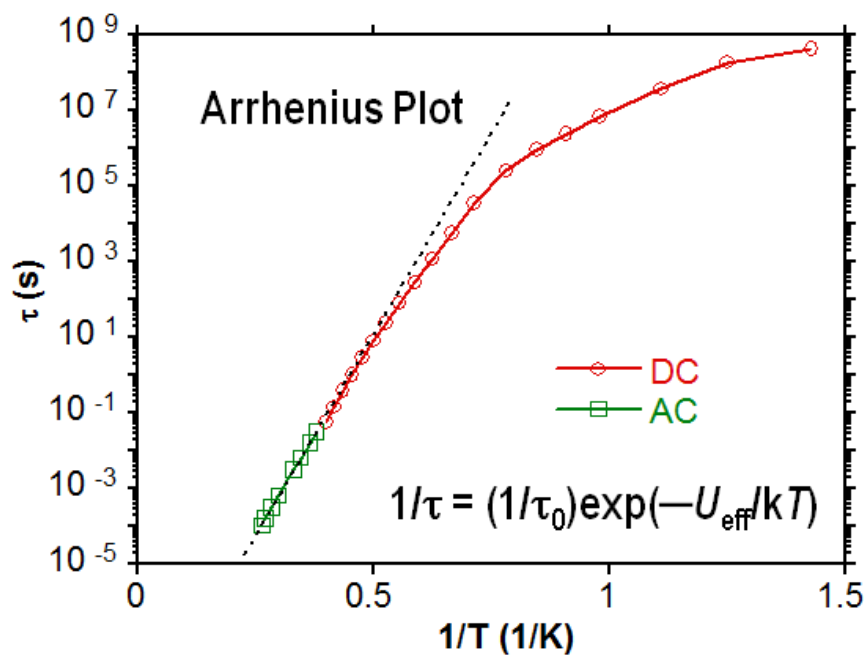
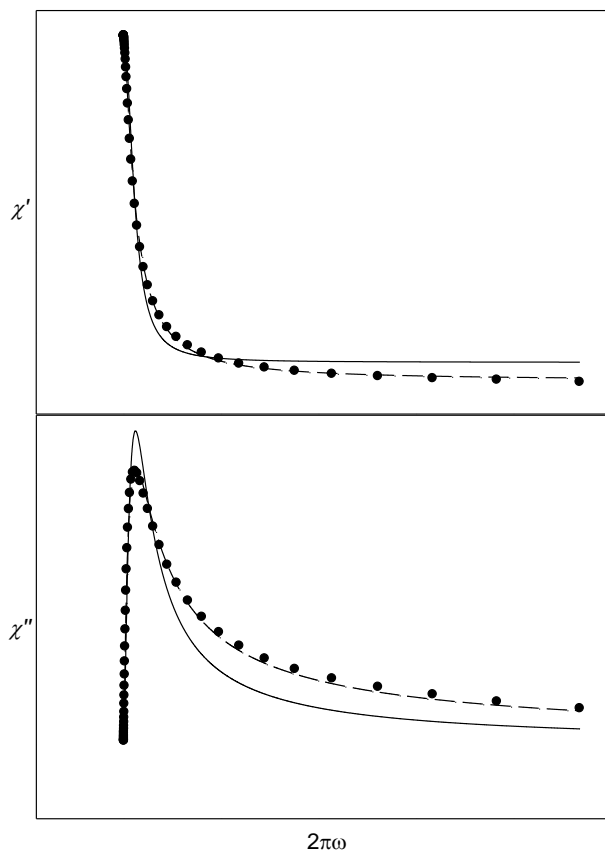


Figure 3-7. Plot of the natural logarithm of relaxation rate $\ln(1/\tau)$, vs. $1/T$ for complex **3-1** using χ_M'' vs. T data at different ac frequencies (A). The solid line is the fitting to the Arrhenius equation. Arrhenius plot obtained from the magnetization vs. time decay study for complex **3-1** (B).

A



B

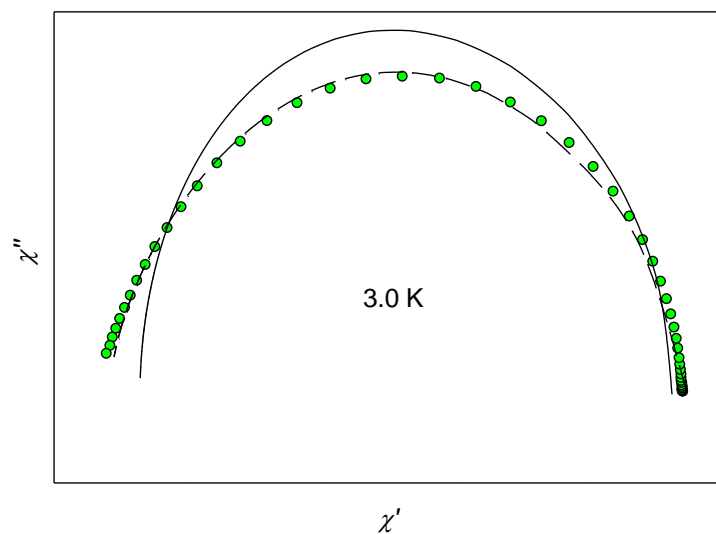
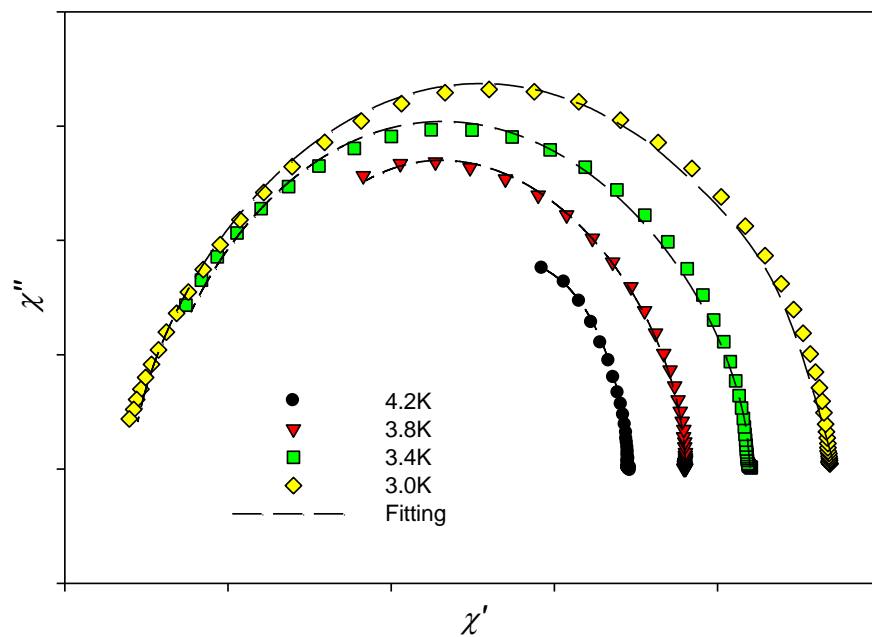


Figure 3-8. Plots of the in-phase (χ') vs. angular frequency (A), out-of-phase (χ'') vs. angular frequency (A) and χ'' vs. χ' (B) at 3.0 K for complex **3-1**. The solid lines are the least-squares fitting of the data to a single relaxation process using equations (3-4) and (3-5). The dashed lines are the least-squares fitting of the data to a distribution of single relaxation processes using equations (3-6) and (3-7). See Table 3-4 for fitting parameters.

A



B

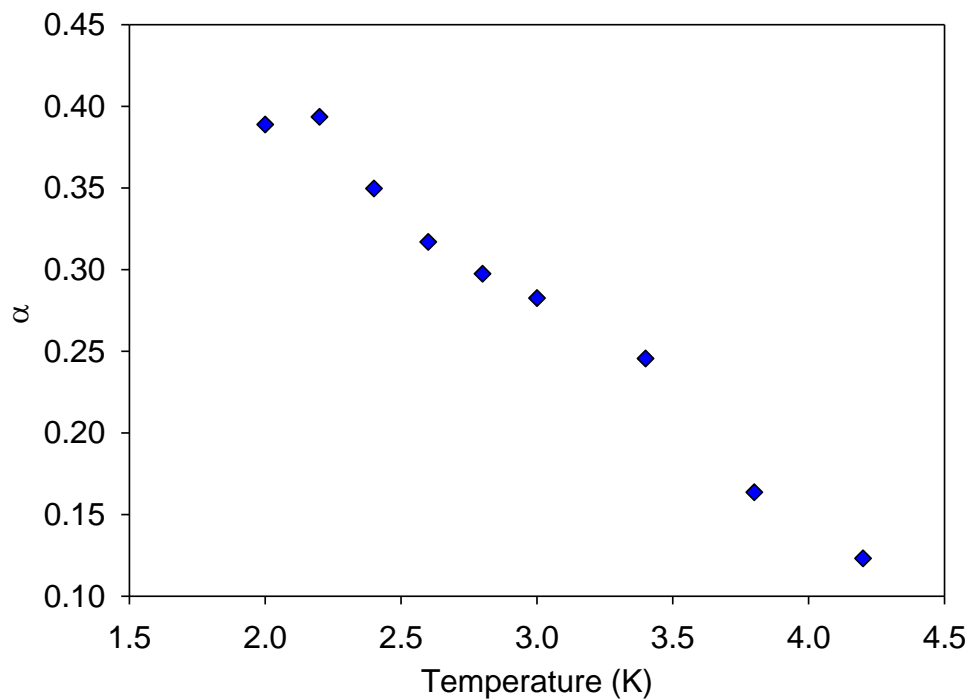
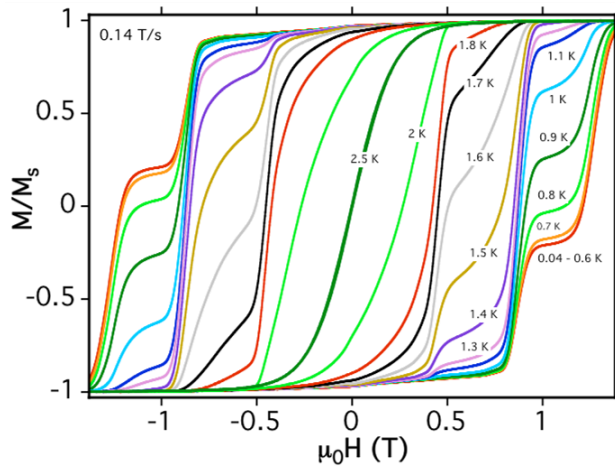
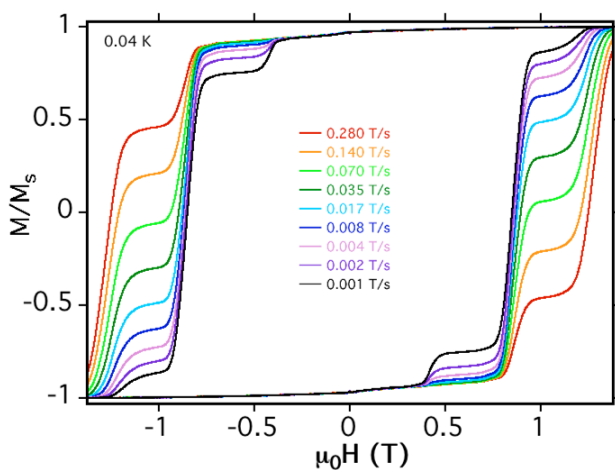


Figure 3-9. Argand plots of χ'' vs. χ' for complex **3-1** at the indicated temperatures (A). The dashed lines are the fit to a distribution of single relaxation processes as described by equations (3-6) and (3-7). The change in α with temperature in the Argand plot for complex **3-1** (B).

A



B



C

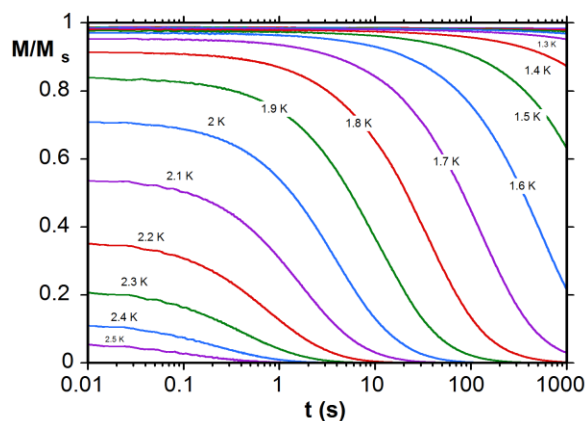
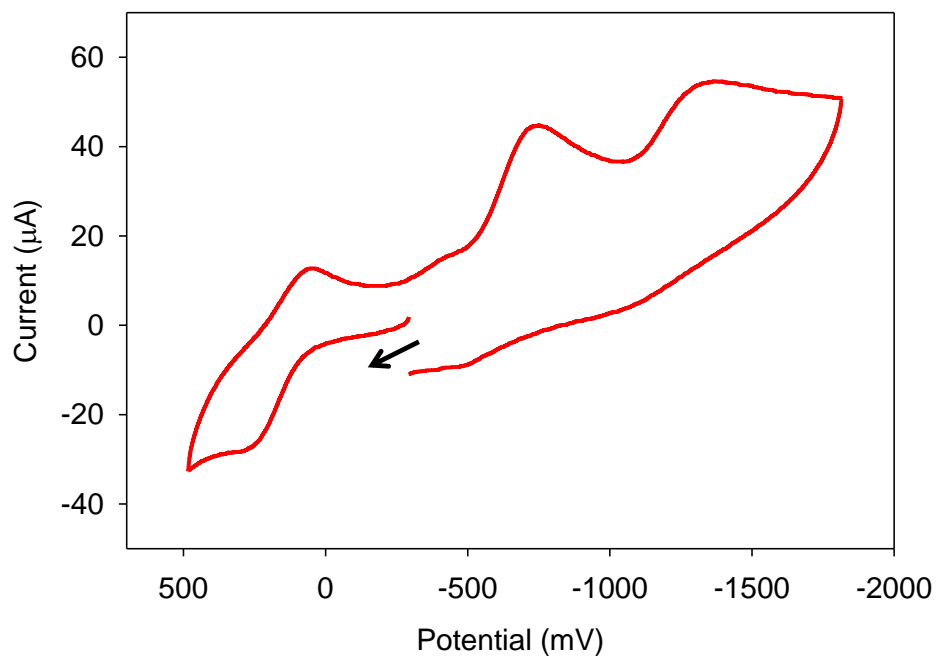


Figure 3-10. Magnetization (M) vs. dc field hysteresis loops for a single crystal of **3-1-4MeCN** at the indicated temperatures (A) and field sweep rates (B). The magnetization is normalized to its saturation value, M_s . Magnetization vs. time decay data for a single crystal of **3-1-4MeCN** at the indicated temperatures (C).

A



B

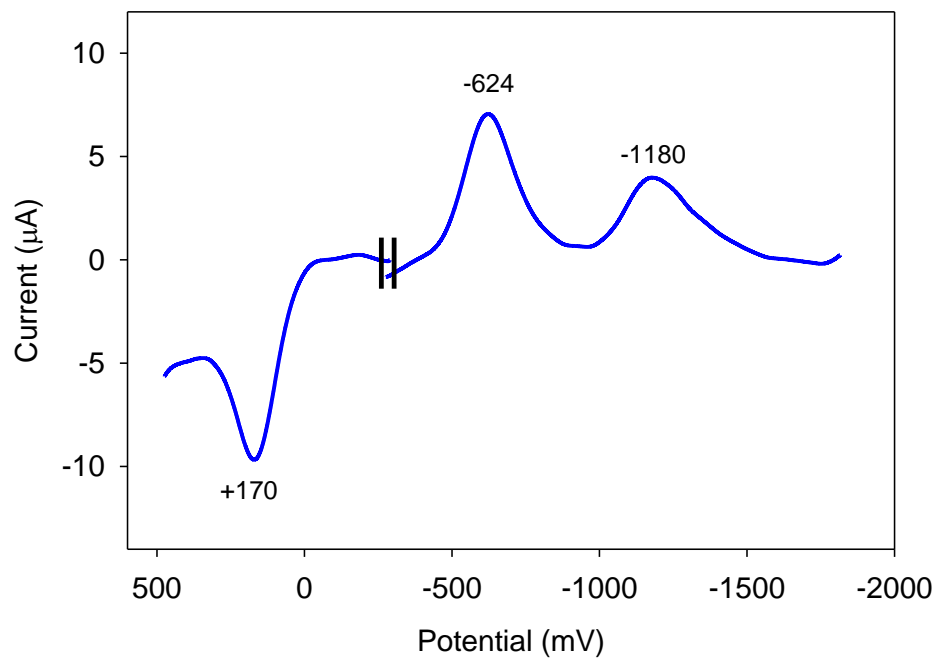
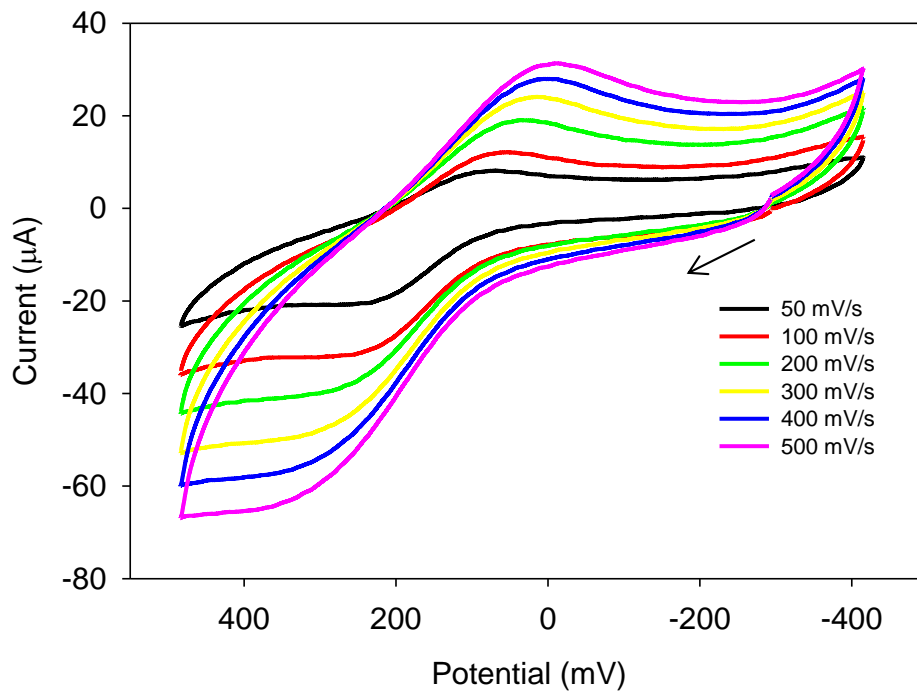


Figure 3-11. A full CV diagram at 100 mV/s (A) and full DPV diagram for complex **3-1** at 20 mV/s (B) in DMF containing 0.1 M NBu_4PF_6 as the supporting electrolyte. The indicated potentials are given vs. ferrocene as an internal standard.

A



B

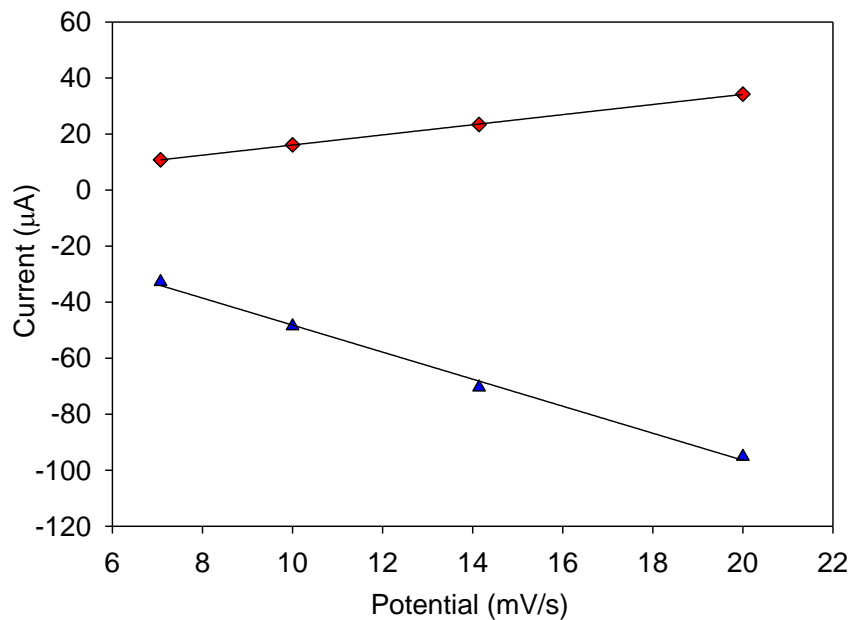


Figure 3-12. The CV diagram at the indicated scan rates, 50 - 500 mV/s (A), for the oxidation wave of **3-1** in DMF containing 0.1 M NBu_4PF_6 as the supporting electrolyte. The indicated potentials are given vs. ferrocene as an internal standard. Plot of cathodic (♦) and anodic (▲) peak current dependence vs. square-root of scan rate ($v^{1/2}$) for 0.14 V oxidation wave (B).

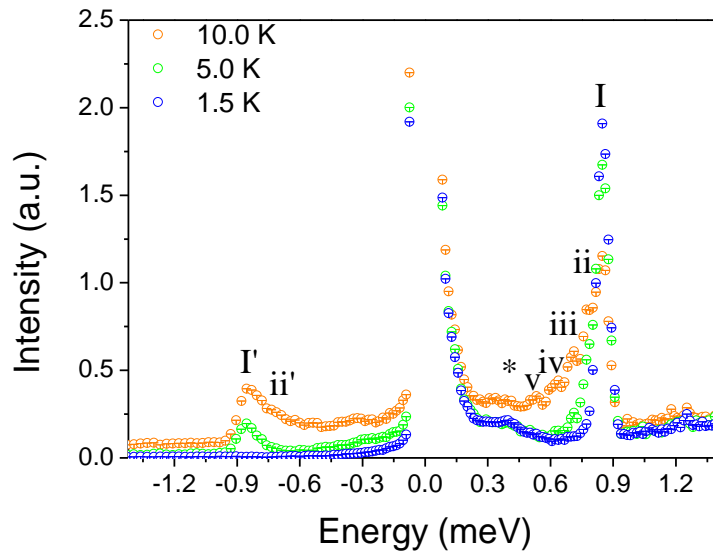


Figure 3-13. INS spectra of **3-1** recorded with an incoming neutron wavelength of 6.5 Å at the indicated temperatures.

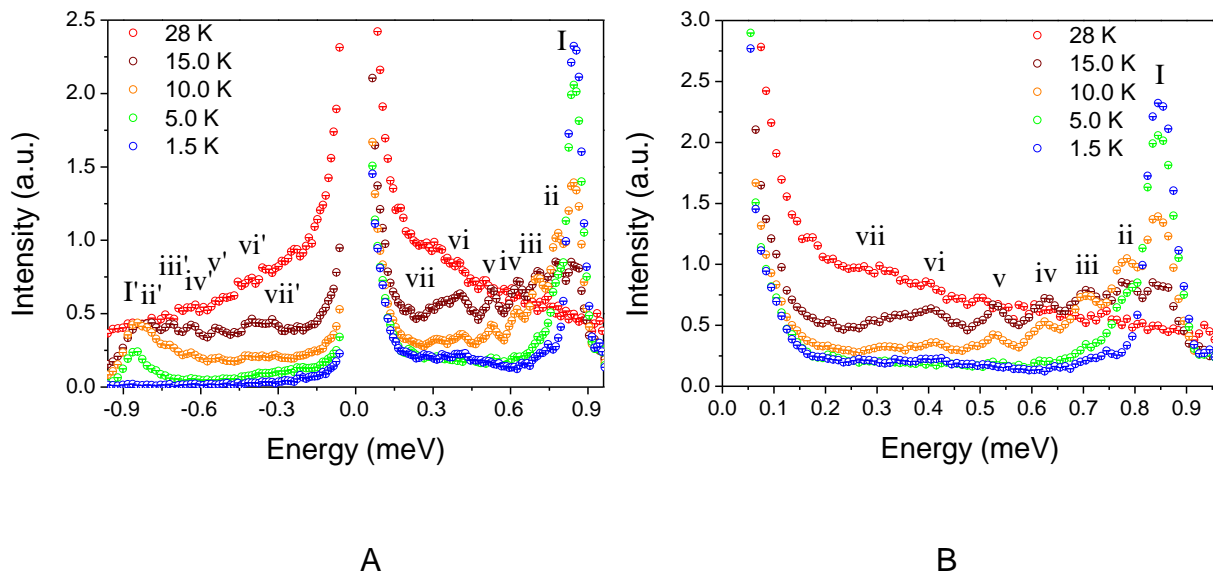


Figure 3-14. INS spectra of **3-1** recorded with wavelength 7.5 Å at the indicated temperatures. Panel (A) shows the energy-gain and loss sides, while (B) shows the energy-loss side of the spectra only.

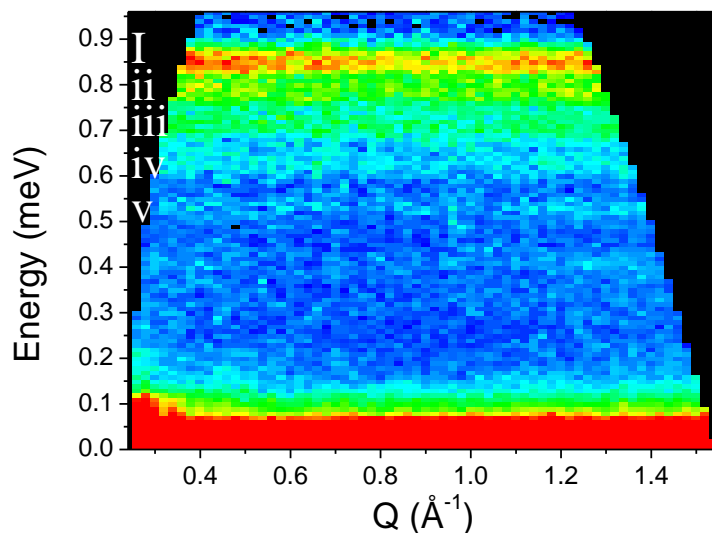


Figure 3-15. $S(Q,E)$ plot of the INS spectrum of **3-1** measured with wavelength 7.5 \AA at a temperature of 10 K . Intensity is color coded from blue (low) to red (high).

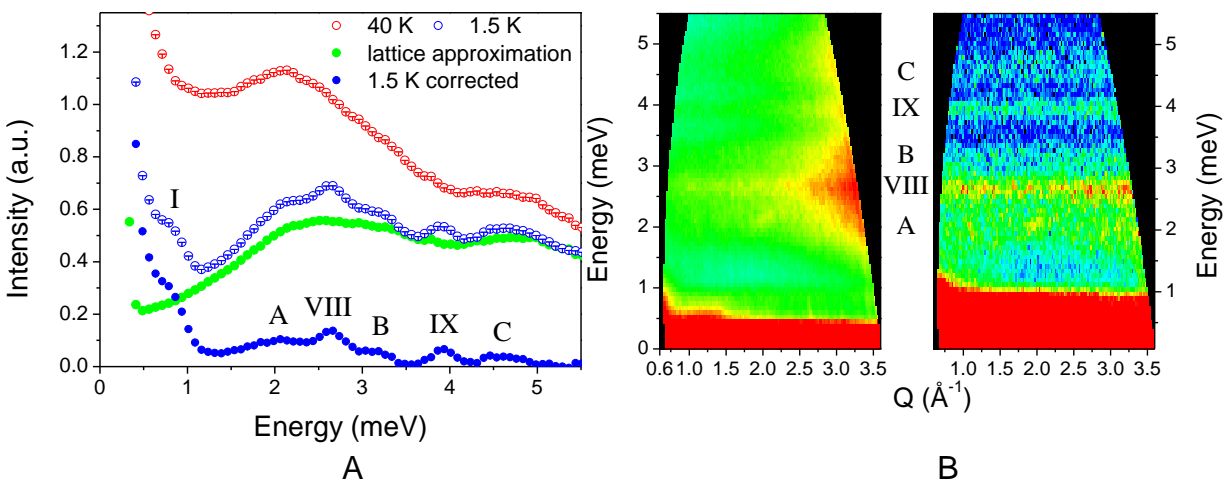
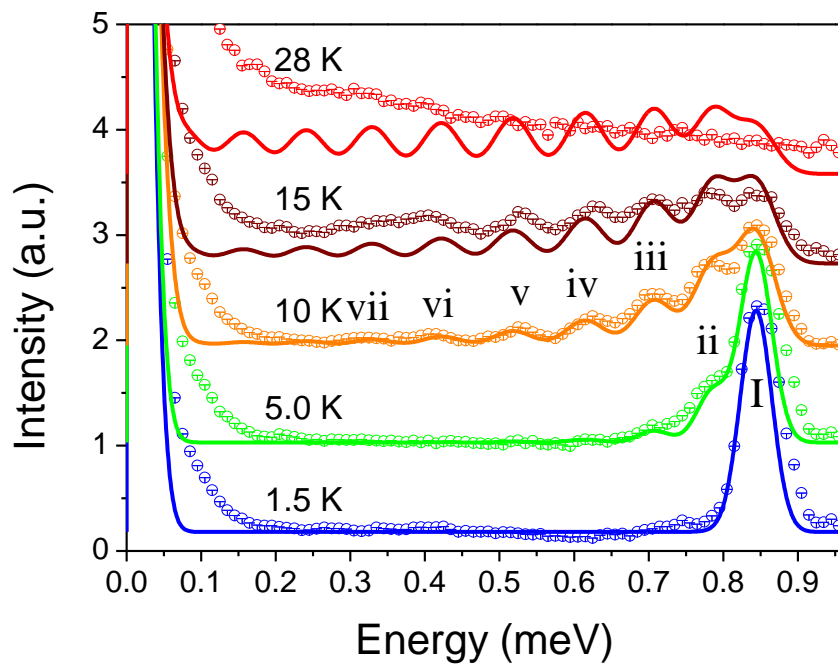


Figure 3-16. INS spectra of **3-1** measured with wavelength 3.2 \AA . (A) Energy-loss sides recorded at 40 K and 1.5 K (open circles). The lattice approximation (green solid circles) was obtained by scaling the 40 K spectrum by the Bose factor. This approximation was then subtracted from 1.5 K spectrum, yielding the corrected 1.5 K spectrum (blue solid circles). (B) $S(Q,E)$ plots at 1.5 K . Intensity is color coded from blue (low) to red (high). The left panel shows the $S(Q,E)$ plot for the uncorrected data and the right one the $S(Q,E)$ plot for the Bose corrected data. The intensity scales are different for the plots.

A



B

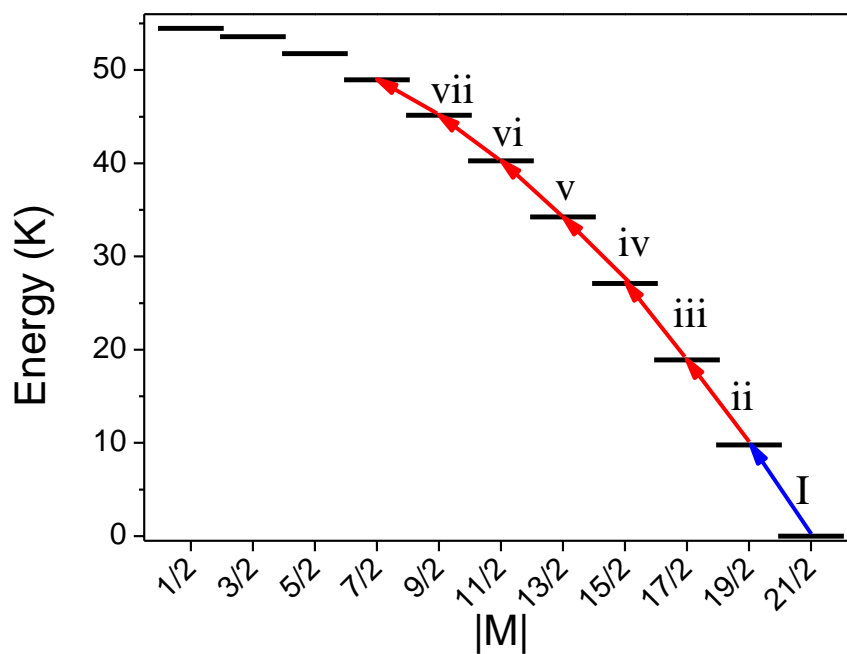


Figure 3-17. (A) Comparison of the experimental (circles) and simulated (lines) INS spectra recorded with wavelength 7.5 Å. The simulated spectra were obtained with the best-fit parameters as given in the text, and using an instrumental resolution of 45 μeV for 1.5 and 5 K and 60 μeV for 10K, 15K and 28K. Data are shown with offsets for clarity. (B) Calculated energy spectrum of **3-1** as a function of the magnitude of the magnetic quantum number M .

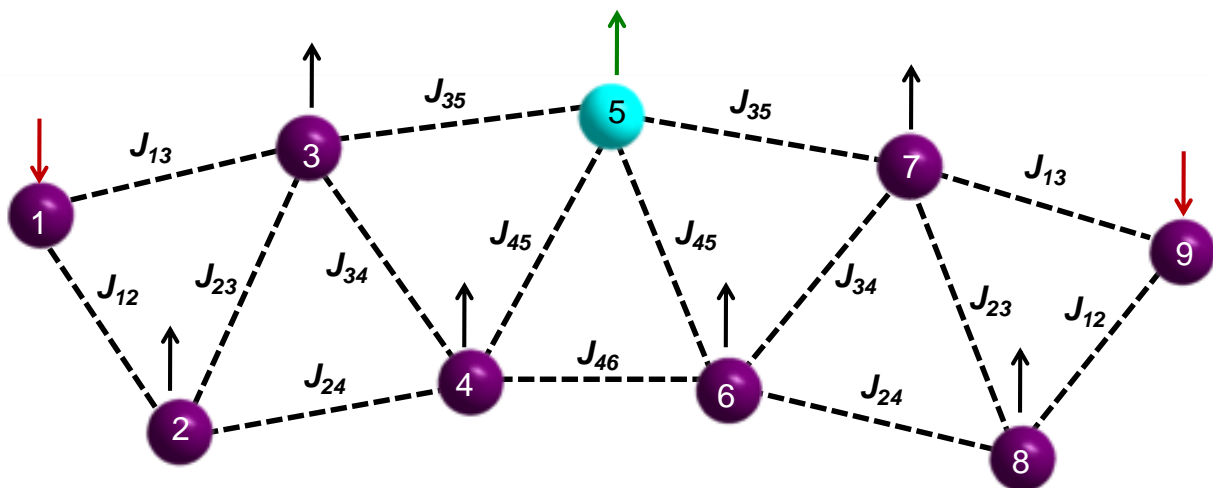


Figure 3-18. Depiction of the spin alignments in the $S = 21/2$ ground state of complex **3-1** as predicted by the DFT calculations, with the Mn1 - Mn9 interaction being antiferromagnetic. The Mn labeling scheme is the same as that in Figure 3-1 (A). Color code: Mn^{3+} , purple; Mn^{2+} , cyan.

CHAPTER 4
A RICHNESS OF NEW MIXED-VALENT Mn AND Mn/Ca CLUSTERS FROM THE USE
OF *N, N, N', N'*-TETRAKIS(2-HYDROXYETHYL)ETHYLENEDIAMINE: Mn₃, Mn₄, Mn₆,
Mn₁₀, Mn₂₀ AND Mn₁₈Ca₂

For the past two decades there has been a growing interest in the field of polynuclear manganese complexes at intermediate oxidation states. For instance, the relevance of Mn carboxylate clusters as active site mimic for various metalloproteins and enzymes is profound. For example synthetic chemists are trying to mimic the active site of the water oxidizing complex (WOC) of photosystem II in green plants and cyanobacteria where the WOC comprises of a mixed-metal, cubane subunit, Mn₄Ca cluster.^{6,7} As the name suggests, WOC catalyses the light-driven oxidation of water to dioxygen. In this regard inorganic Mn/Ca complexes can act as synthetic models of the WOC and they help to understand the magnetic and spectroscopic properties of the native site and the mechanism of its function. On the other hand, the discovery of zero-dimensional nanoscale magnets comprised of Mn clusters, which are better known as SMMs,¹¹ grabs the attention in the field of molecular magnetism. An SMM behaves as a magnet below its blocking temperature (T_B) and exhibits hysteresis in magnetization vs. dc field scans. This behavior requires the combination of a large ground state spin (S) with a large and negative Ising (or easy-axis) type of magnetoanisotropy, as measured by the axial zero-field splitting parameter D . Apart from their bioinorganic relevance and magnetic properties, the intrinsic architectural beauty and the aesthetically pleasing structures of this plethora of polynuclear Mn metal clusters provide another area of research interest in the field of supramolecular chemistry.¹⁶⁷

Various synthetic approaches have been developed in the past, but there is still a continuing search for appropriate ligand precursors to build new polynuclear metal

clusters. As a part of our continuing research on exploring new synthetic schemes, the edteH₄ chelate with carboxylate and azide groups have been used. The edteH₄ chelate is comprised of an ethylenediamine backbone with four hydroxyethyl arms which, upon deprotonation, act as bridging groups to promote formation of high nuclearity clusters. EdteH₄ has already been reported to produce Mn₈, Mn₉, Mn₂₀ and a family of Mn₁₂ complexes with novel metal topologies.⁶⁰ Among these, Mn₉ and one member of the Mn₁₂ family are SMMs, proved by magnetization hysteresis studies.¹⁶⁸ Hence, the initial successful reactions with edteH₄ gave us hope to further scrutinize the bridging capability of the same ligand under various reaction conditions. Herein, we report the synthesis, crystal structures and magnetic properties of an ensemble of mixed-valent Mn_x and Mn/Ca complexes containing edteH₄ ligand where x = 3, 4, 6, 10 and 20.

Experimental Section

Syntheses

All preparations were performed under aerobic conditions using reagents and solvents as received. The syntheses of Mn₁₂O₂(O₂CMe)₁₆(H₂O)₄,^{16,24} [Mn₈O₁₀(O₂CMe)₆(H₂O)₂(bpy)₆](ClO₄)₄,¹⁶⁹ Mn(O₂CBu^t)₂,¹²⁰ and Mn(O₂CEt)₂¹⁷⁰ were carried out as reported in the literature. *Caution! Although no such behavior was observed during the present work, azide salts are potentially explosive; such compounds should be synthesized and used in small quantities, and treated with utmost care at all times.*

[Mn₃(O₂CMe)₂(edteH₂)₂](O₂CMe) (4-1). To a stirred solution of edteH₄ (0.22 g, 0.93 mmol) in MeCN (20 mL) was added Mn₁₂O₂(O₂CMe)₁₆(H₂O)₄ (Mn₁₂Ac, 0.19 g, 0.10 mmol). The resulting dark-brown solution was stirred overnight, filtered and then the solvent was evaporated to dryness. The solid was recrystallized from 15 mL CH₂Cl₂,

layered with Et₂O/C₆H₁₄. X-ray quality reddish-brown cube-like crystals of **4-1**·4CH₂Cl₂ grew over 5 days in a yield of 76 %. The crystals were collected by filtration, washed with Et₂O and C₆H₁₄, and dried under vacuum. Anal. Calc. (found) for **4-1**·H₂O: C, 37.69 (37.96); H, 6.69 (6.90); N, 6.76 (6.38). Selected IR data (cm⁻¹): 2859 (m), 1585 (s), 1413 (s), 1083 (s), 915 (m), 733 (w), 654 (s), 616 (s), 574 (s), 516 (m).

[Mn₃(O₂CMe)₂(edteH₂)₂](ClO₄) (4-2). To a stirred solution of edteH₄ (0.05 g, 0.21 mmol) in MeCN/MeOH (10/1, v/v) was added [Mn₈O₁₀(O₂CMe)₆(H₂O)₂(bpy)₆](ClO₄)₄ (Mn₈Ac, 0.10 g, 0.04 mmol). The resulting dark-brown solution was stirred for six hours, filtered and the filtrate vapor diffused with Et₂O. X-ray quality reddish-brown plate-like crystals of **4-2**·MeCN grew over 12 days in a yield of 51 %. The crystals were collected by filtration, washed with Et₂O, and dried under vacuum. Anal. Calc. (found) for **4-2**·H₂O: C, 32.50 (32.35); H, 6.14 (5.76); N, 6.32 (6.45). Selected IR data (cm⁻¹): 2977 (m), 2857 (m), 1570 (s), 1405 (m), 1094 (vs), 912 (m), 733 (w), 650 (m), 625 (m), 586 (m), 543 (m), 508 (m).

[Mn₄(edteH₂)₂(hmp)₂Cl₂][MnCl₄] (4-3). To a stirred solution of edteH₄ (0.10 g, 0.42 mmol) and Et₃N (0.06 mL, 0.42 mmol) in MeOH (12 mL) was added MnCl₂ (0.17 g, 0.84 mmol). The resulting dark-brown solution was stirred for 30 minutes and then hmpH (0.20 mL, 2.1 mmol) was added and the solution was stirred for a further two hours. The solution was then filtered and layered with Et₂O. X-ray quality, dark-brown hexagonal plate-like crystals of **4-3** grew over 15 days with a yield of 12%. The crystals were collected, washed with Et₂O, and dried under vacuum. Anal. Calc. (found) for **4-3**: C, 32.79(33.24); H, 4.82 (4.88); N, 7.17 (6.87). Selected IR data (cm⁻¹): 2937 (m), 2677

(m), 2492 (m), 1608 (s), 1475 (s), 1439 (s), 1397 (w), 1289 (w), 1171 (w), 1063 (vs), 925 (m), 771 (m), 731 (w), 665 (br), 519 (br).

[Mn₆O₂(O₂CBu^t)₆(edteH)₂(N₃)₂] (4-4). To a stirred solution of edteH₄ (0.20 g, 0.84 mmol) and NEt₃ (0.24 mL, 1.68 mmol) in MeCN (20 mL) was added Mn(O₂CBu^t)₂ (0.60 g, 2.29 mmol). The resulting dark-brown solution was stirred for 15 minutes under mild heating (~60°C) to dissolve all the solids, and then Me₃SiN₃ (0.4 mL, 3.01 mmol) was added and solution was stirred for a further two hours. The solution was then filtered and left undisturbed to slowly evaporate. X-ray quality, dark-brown plate-like crystals of **4-4** grew over 10 days at 4°C in a yield of 24 %. The crystals were collected, washed with Et₂O, and dried under vacuum. Anal. Calc. (found) for **4-4**: C, 39.54 (39.71); H, 6.37 (6.68); N, 9.22 (9.45). Selected IR data (cm⁻¹): 3395 (br), 2957 (vs), 2899 (s), 2863 (s), 2067 (vs), 1586 (vs), 1482 (s), 1415 (s), 1359 (s), 1225 (s), 1086 (vs), 919 (m), 897 (m), 787 (w), 695 (s), 587 (vs), 508 (m), 417 (w).

Na₂[Mn₁₀O₄(OMe)₂(O₂CEt)₆(edte)₂(N₃)₆] (4-5). To a stirred solution of edteH₄ (0.15 g, 0.64 mmol) and LiOH (0.06 g, 0.64 mmol) in MeCN/MeOH (10/5, v/v) was added Mn(O₂CEt)₂ (0.34 g, 1.28 mmol). The resulting dark-brown solution was stirred for an hour and then NaN₃ (0.33 g, 5.12 mmol) was added and the solution was stirred for a further three hours. The solution was then filtered and left undisturbed to slowly evaporate. X-ray quality, dark-brown plate-like crystals of **4-5·2MeCN** grew over 14 days in a yield of 80 %. The crystals were collected by filtration, washed with Et₂O, and dried under vacuum. Anal. Calc. (found) for **4-5·2H₂O**: C, 25.12 (25.05); H, 4.22 (4.06); N, 16.11 (16.14). Selected IR data (cm⁻¹): 2980 (m), 2867 (m), 2050 (vs), 1557 (s), 1412 (m), 1291 (m), 1062 (s), 911 (m), 558 (br).

(NEt₄)₂[Mn₁₀(O)₄(OH)₂(O₂CEt)₆(Edte)₂(N₃)₆] (4-6). To a stirred solution of **4-5** (0.10 g, 0.1 mmol) in 6 mL MeCN was added NEt₄Cl (0.02 g, 0.2 mmol). The resulting dark-brown solution was stirred for an hour and then filtered and the filtrate vapor diffused with Et₂O. X-ray quality, dark-brown, plate-like crystals of **4-6**·2MeCN grew over a few days in a yield of 40 %. The crystals were collected, washed with Et₂O and dried under vacuum. Anal. Calc. (found) for **4-6**·H₂O: C, 31.06 (30.91); H, 5.49 (5.51); N, 16.70 (16.54). Selected IR data (cm⁻¹): 2980 (m), 2062 (s), 1635 (m), 1558 (m), 1396 (m), 1290 (m), 1072 (m), 911 (m), 558 (br).

[Mn₂₀O₈(OH)₆(O₂CEt)₆(edte)₄(edteH)₂](ClO₄)₄ (4-7). To a stirred solution of edteH₄ (0.10 g, 0.42 mmol) and NEt₃ (0.12 mL, 0.84 mmol) in 10 mL EtOH was added Mn(O₂CEt)₂ (0.23 g, 0.84 mmol) and NaClO₄ (0.05 g, 0.42 mmol). The resulting dark-brown solution was stirred for two hours then filtered. X-ray quality brown plate-like crystals of **4-7**·x(Solv) grew from C₆H₁₄ layering over 20 days in a yield of 30 %. The crystallographic sample was kept in contact with mother liquor to prevent damage from exposure to the atmosphere. Otherwise, the crystals were collected by filtration, washed with Et₂O, and dried under vacuum. Anal. Calc. (found) for **4-7**·1.5C₆H₁₄: C, 28.32 (28.41); H, 4.89 (4.81); N, 4.56 (4.78). Selected IR data (cm⁻¹): 2972 (m), 2850 (m), 1567 (s), 1464 (m), 1421 (m), 1295 (m), 1088 (vs), 911 (m), 742 (w), 625 (s), 589 (s), 515 (s).

[Ca₂Mn₁₈O₈(OH)₅(O₂CBu^t)_{4.5}(edte)₅(NO₃)_{3.5}](O₂CBu^t)_{0.5}(NO₃)_{0.5} (4-8). To a stirred solution of edteH₄ (0.10g, 0.42mmol) and NEt₃ (0.16mL, 0.84 mmol) in MeCN/MeOH (10/1, v/v) was added Ca(NO₃)₂ (0.10g, 0.42 mmol) followed by Mn(O₂CBu^t)₂ (0.12g, 0.42 mmol). The resulting dark-brown solution was stirred for 15 minutes under mild

heating (~60°C) to dissolve all solids. Then the solution was stirred for a further two hours at room temperature, filtered, and the filtrate allowed to slowly evaporate undisturbed at ambient temperature. X-ray quality, dark-brown, plate-like crystals of **4-8**·5MeCN slowly grew over several days in a yield of 40 %. The crystals were collected by filtration, washed with Et₂O, and dried in vacuum. Anal. Calc. (found) for **4-8**·3H₂O: C, 30.00 (29.87); H, 5.21 (5.21); N, 6.58 (6.30). Selected IR data (cm⁻¹): 3395 (br, m), 2869 (m), 1605 (w), 1544 (m), 1480 (m), 1383 (s), 1207 (w), 1059 (m), 911 (w), 890 (w), 615 (m), 565 (m).

X-ray Crystallography

Data were collected on a Siemens SMART PLATFORM equipped with a CCD area detector and a graphite monochromator utilizing Mo-K α radiation ($\lambda = 0.71073 \text{ \AA}$). Suitable crystals of **4-1**·4CH₂Cl₂, **4-2**·MeCN, **4-3**, **4-4**, **4-5**·2MeCN, **4-6**·2MeCN, **4-7**·x(Solv) and **4-8**·5MeCN were attached to glass fibers using silicone grease and transferred to a goniostat where they were cooled to 173 K for data collection. Cell parameters were refined using 8192 reflections. A full sphere of data (1850 frames) was collected using the ω -scan method (0.3° frame width). The first 50 frames were re-measured at the end of data collection to monitor instrument and crystal stability (maximum correction on I was < 1 %). Absorption corrections by integration were applied based on measured indexed crystal faces. The structure was solved by direct methods in *SHELXTL6*, and refined on F^2 using full-matrix least squares. The non-H atoms were treated anisotropically, whereas the hydrogen atoms were placed in ideal, calculated positions and were refined as riding on their respective C atoms.

For **4-1**·4CH₂Cl₂, the asymmetric unit consists of two half Mn₃ cluster cations, an acetate anion and four dichloromethane solvent molecules. Three of the solvent

molecules were disordered and could not be modeled properly, thus program SQUEEZE,⁶⁴ a part of the PLATON package of crystallographic software, was used to calculate all of the four solvent molecules disorder area and remove its contribution to the overall intensity data. Four hydroxyl protons, H2, H4, H8 and H10, were obtained from a difference Fourier map and refined freely. A total of 443 parameters were refined in the final cycle of refinement using 6043 reflections with $I > 2\sigma(I)$ to yield R_1 and wR_2 of 6.41 and 16.42 %, respectively.

For **4-2**·MeCN, the asymmetric unit consists of two half timers, a perchlorate anion and an acetonitrile solvent molecule. The latter molecule was disordered and could not be modeled properly, thus program SQUEEZE, a part of the PLATON package of crystallographic software, was used to calculate the solvent disorder area and remove its contribution to the overall intensity data. A total of 16312 parameters were refined in the final cycle of refinement using 4676 reflections with $I > 2\sigma(I)$ to yield R_1 and wR_2 of 3.72 and 9.79 %, respectively.

For **4-3**, the asymmetric unit consists of one Mn_4 cluster cation, and a $MnCl_4^-$ anion. A total of 267 parameters were refined in the final cycle of refinement using 4499 reflections with $I > 2\sigma(I)$ to yield R_1 and wR_2 of 4.19 and 11.44 %, respectively.

For **4-4**, the asymmetric unit consists of a half Mn_6 cluster located on an inversion center. The proton on O11, the uncoordinated hydroxyl group, was located from a difference Fourier map and was held riding on its parent atom. A total of 407 parameters were refined in the final cycle of refinement using 2883 reflections with $I > 2\sigma(I)$ to yield R_1 and wR_2 of 5.30 and 11.24 %, respectively.

For **4-5**·2MeCN, the asymmetric unit consists of a half Mn₁₀ cluster and an acetonitrile solvent molecule. A total of 523 parameters were refined in the final cycle of refinement using 7541 reflections with $I > 2\sigma(I)$ to yield R_1 and wR_2 of 4.17 and 11.07 %, respectively.

For **4-6**·2MeCN, the asymmetric unit consists of two half Mn₁₀ cluster anions, two tetraethylammonium cations and two acetonitrile solvent molecules. Each half cluster has two disorders. One disorder has a hydroxyl ligand disordered against an azide ligand. Another is where the edte⁴⁻ ligand has the CH₂ around N1 and N1' are disordered and were refined in two parts each. A check for higher symmetry was performed but none exists. One acetonitrile molecule is disordered alongside the disorder in the OH⁻/N₃⁻ disorder. A total of 1086 parameters were refined in the final cycle of refinement using 14604 reflections with $I > 2\sigma(I)$ to yield R_1 and wR_2 of 4.03 and 8.96 %, respectively.

For **4-7**·x(Solv), the asymmetric unit consists of a half Mn₂₀ cluster, two perchlorate anions and three ethanol solvent molecules. The solvent molecules were disordered and could not be modeled properly, thus program SQUEEZE, a part of the PLATON package of crystallographic software, was used to calculate the solvent disorder area and remove its contribution to the overall intensity data. Atom Mn10 has disorder between a monodentate propionate and a bidentate propionate ligand. Another disorder is observed in the C13-C14/C13'-C14' unit and in the C19-O15/C19'-O15' unit. The latter hydroxyl group is protonated but the proton was placed in a calculated, idealized position. Similarly, oxygen atoms O1, O3, and O7 are protonated and their protons were placed in calculated, idealized positions. The perchlorate anions are also disordered

and each was refined in two parts; all partial site occupations factors were initially refined to near 50% values and thus were fixed at 50% in the final refinement cycles. A total of 41842 parameters were refined in the final cycle of refinement using 12607 reflections with $I > 2\sigma(I)$ to yield R_1 and wR_2 of 6.2 and 18.67%, respectively.

For **4-8**·5MeCN, the asymmetric unit consists of a $Mn_{18}Ca_2$ cluster cation, half of a nitrate anion, a half $tBuCO_2^-$ anion and five acetonitrile solvent molecules. The solvent molecules were disordered and could not be modeled properly; thus the program SQUEEZE was again used to calculate the solvent disorder area and remove its contribution to the overall intensity data. The cluster exhibits several disordered regions. The tBu group on C1, the methyl groups on C22 and C122 are disordered and each was refined in two parts. N14 of the nitrate anion is disordered and refined in two parts (N14/N14') along with the O atoms. N8 of the nitrate ion is disordered against a $tBuCO_2^-$ ion (on C81). The final two disordered regions are on each Ca center. The edteH₄ ligand acts as a hexadentate ligand half of the time and as a pentadentate ligand in the other half. In the latter case, while one of the branches is not coordinated, an OH⁻ group occupies the bridging coordination position between the Ca and one of the adjacent Mn centers. The same disorder is also seen on the other side of the cluster cation with the second Ca center. This gives rise to a total of one (two half hydroxyl ligands) negative charge in addition to the charges coming from the edteH₄ ligands. The bridging O ligands O14, O16, O32 and O33 are believed to be hydroxyl groups and thus carry a proton each but the H atoms could not be located from difference Fourier maps. The protonation was deduced from the BVS calculations¹⁷¹ which showed those O atoms to be of the hydroxyl type. Considering all of the above,

the cluster carries a +1 charge countered by a half nitrate and a half ${}^t\text{BuCO}_2^-$ anions. In the final cycle of refinement on F^2 , 33638 reflections (of which 10946 are observed with $I > 2\sigma(I)$) were used to refine 1565 parameters and the resulting R1, wR2 and S (goodness of fit) were 7.68%, 20.23% and 0.873, respectively. R1 is calculated to provide a reference to the conventional R value but its function is not minimized. The crystallographic data and structure refinement details for all the eight complexes are listed in Tables 4-1, 4-2 and 4-3, respectively.

Physical Measurements

Infrared spectra were recorded in the solid state (KBr pellets) on a Nicolet Nexus 670 FTIR spectrometer in the 400 - 4000 cm^{-1} range. Elemental analyses (C, H and N) were performed by the in-house facilities of the University of Florida, Chemistry Department. Variable-temperature dc and ac magnetic susceptibility data were collected at the University of Florida using a Quantum Design MPMS-XL SQUID susceptometer equipped with a 7 T magnet and operating in the 1.8 - 300 K range. Samples were embedded in solid eicosane to prevent torquing. Magnetization vs. field and temperature data were fit using the program MAGNET.⁶⁶ Pascal's constants were used to estimate the diamagnetic correction, which was subtracted from the experimental susceptibility to give the molar paramagnetic susceptibility (χ_M).

Result and Discussion

Syntheses

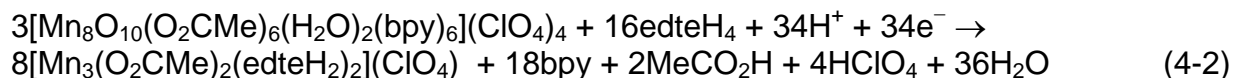
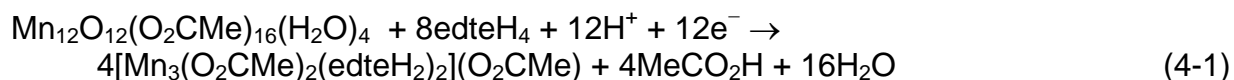
There are two ways to make polynuclear metal clusters with Mn^{3+} ions. One is to start with a preformed higher oxidation state Mn_x cluster^{47,172} and the second is to oxidize simple Mn^{2+} salts in the presence of a chelating ligand.¹¹¹ Both strategies have

been efficiently employed in this chapter to obtain various Mn_x clusters ($x = 3, 4, 6, 10, 20$) with the potentially hexadentate ligand $edteH_4$.

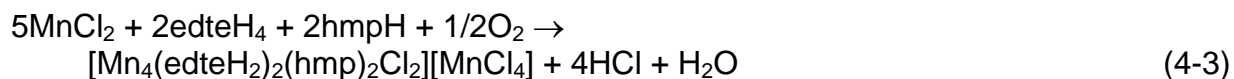
$Mn_{12}Ac$ is a well known SMM with a ground state spin of $S = 10$, which comes from the combination of $8Mn^{III}$ and $4Mn^{IV}$. It also contains $16MeCO_2^-$ and $4H_2O$ molecules. There are many examples in the literature of the acetate groups being replaced partially or completely by other carboxylates *via* ligand substitution reactions.¹¹ The reactivity of $Mn_{12}Ac$ is further verified in presence of $edteH_4$ ligand. There are two possibilities: one is that the $edteH_4$ will replace carboxylate/water by keeping the core intact, and the second is to decompose the $Mn_{12}Ac$ to form a completely new compound. In the reaction, $Mn_{12}Ac$ is decomposed to accommodate the hexadentate ligand $edteH_4$ and $Mn^{3.33+}$ (average oxidation state of Mn in $Mn_{12}Ac$) is being reduced to $Mn^{2.33+}$ (average oxidation state of Mn in **4-1**). The reaction of $Mn_{12}Ac$ with $edteH_4$ in a 1:9 molar ratio led to a $[Mn_3(O_2CMe)_2(edteH_2)_2](O_2CMe)$ complex. The yield of the reaction is as high as 76 %. No crystalline product was obtained by using a lesser quantity of the ligand. Microcrystalline product was obtained from MeCN solvent which did not diffract under X-ray and hence, several other techniques were investigated. After the initial reaction in MeCN, the solvent was evaporated to dryness and the solid product was recrystallized from a mixed-solvent system of $CH_2Cl_2/Et_2O/C_6H_{14}$ to obtain an X-ray quality single crystal of **4-1**. A similar product was also obtained by using another preformed cluster of $[Mn_8O_{10}(O_2CMe)_6(H_2O)_2(bpy)_6](ClO_4)_4$ (Mn_8Ac). The reason for choosing Mn_8Ac as a starting material is its high $Mn^{3.75+}$ average oxidation state, which seemed a good source for making polynuclear cluster containing Mn^{3+} ion. However, the reaction between Mn_8Ac and $edteH_4$ at a 1:5 molar ratio led to the

isolation of a Mn₃ cluster similar to **4-1** with an average Mn oxidation state of +2.33.

These two reactions, yielding Mn₃ clusters are summarized in equation 4-1 and 4-2.

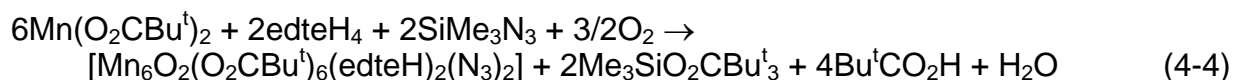


Going from preformed clusters to simple Mn²⁺ salts as starting materials led to a variety of different products. The reaction of edteH₄ with Mn(ClO₄)₂/MnCl₂, NEt₃ and NaN₃ in MeCN/MeOH gave a family of Mn₁₂ clusters. Both end-on azides and N-hydroxymethyl pyridine are known to be ferromagnetic couplers, and have been widely employed in Mn cluster chemistry.^{48,59} The above mentioned scheme is known to give Mn₁₂ clusters incorporating end-on azides. However, the incorporation of the end-on azides did not lead to the desired predominant ferromagnetic interaction in the system. Hence, to tune the magnetic properties of the system hmpH was employed rather than adding NaN₃ in the reaction and this time a Mn₄ cluster was isolated rather than Mn₁₂. The reaction of edteH₄ with MnCl₂, NEt₃ and hmpH in a 2:1:1:5 molar ratio in MeOH afforded a reddish-brown solution from which was subsequently obtained [Mn^{II}₂Mn^{III}(O₂CMe)₂(edteH₂)₂](ClO₄) (**4-3**) in 12 % yield (equation 4-3). Its formation is summarized in equation 4-3 where atmospheric oxygen gas is assumed to provide the oxidizing equivalents and the oxidation is being facilitated in presence of NEt₃.



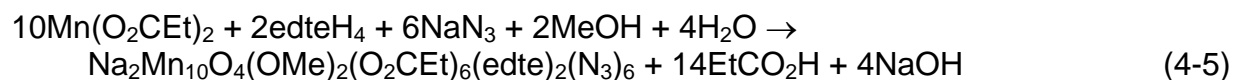
The product can be obtained with a lesser quantity of hmpH; however the excess amount ensures the formation of single-crystals of **4-3**. No other product was isolated using this edteH₄/hmpH, mixed-chelate synthetic scheme.

Modifying the reaction scheme by a bulkier carboxylate containing Mn²⁺ salt gave a very different result. The reaction between Mn(O₂CBu^t)₂, edteH₄, NEt₃ and Me₃SiN₃ in ~ 3:1:2:4 molar ratio results in **4-4** with 24 % yield (equation 4-4). The reagent Me₃SiN₃ serves a dual purpose by delivering azide to the cluster and abstracting carboxylate as Me₃SiO₂CR.¹⁷³ It is interesting to note that the same reaction with NaN₃ as an azide source in MeCN/MeOH leads to a structurally unprecedented Mn₉ SMM.¹⁶⁸



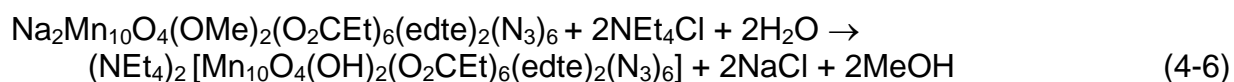
The reaction is solvent specific and single crystals are obtained in MeCN solvent only. Use of other solvents like MeOH or EtOH degrade the crystal quality and remove SiMe₃N₃ as SiMe₃OMe, which hampers the formation of the desired product. The same product was obtained by using MnCl₂, NaO₂CBu^t, edteH₄ and NaN₃ in a 2:4:1:3 molar ratio, but the crystal quality was poor.

The reaction was further explored by switching from a bulkier carboxylate, ^tBuCO₂⁻ to a smaller carboxylate, EtCO₂⁻ and as a result a larger cluster was obtained. The reaction between Mn(O₂CEt)₂, edteH₄, LiOH and NaN₃ in 2:1:1:8 molar ratio in MeCN/MeOH gave the polymer **4-5** in a high yield of 80 % (equation 4-5).

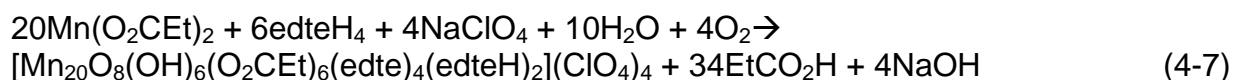


The same product was obtained using NaOH as the base. The use of only MeOH or the combination of MeCN/DMF as the solvent can also give pure single crystals of **4-5**, but the yield was highest from the above reaction. The use of MeOH or DMF along with the main solvent MeCN ensures the solubility of all the components in the reaction mixture. An excess of ligand and NaN₃ helps to give well formed single-crystals. The

compound **4-5** is a $[\text{Na}_2\text{Mn}_{10}]$ is a polymer where Mn_{10} units are connected by end-to-end azide bridges through Na ions. In order to possibly obtain the discrete Mn_{10} unit and assess its intrinsic magnetic properties, Cl^- ions were added to drive the precipitation of Na^+ as NaCl. Hence, one equivalent of $\text{Na}_2\text{Mn}_{10}$ was treated with two equivalents of NEt_4Cl salt in MeCN. NaCl was indeed formed and $(\text{NEt}_4)_2[\text{Mn}_{10}]$ was successfully obtained in discrete form. The reaction is summarized in equation 4-6.

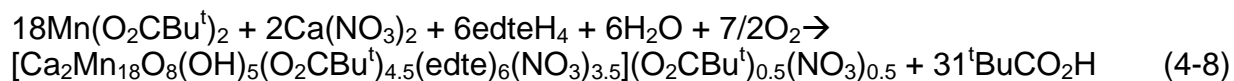


The reaction scheme further explored the effect of EtCO_2^- , edteH_4 and Mn^{2+} in absence of NaN_3 . The 4:2:4:1:2 molar ratio of $\text{Mn}(\text{O}_2\text{CEt})_2$, edteH_4 , NEt_3 and NaClO_4 in EtOH leads to the isolation of a new Mn_{20} cluster where the atmospheric oxygen provided the oxidizing equivalents. The reaction is summarized in equation 4-7.



The absence of azide clearly affects the reaction allowing a different product to be isolated. Changing the carboxylate from propionate to acetate gave another Mn_{20} cluster with a similar metal core.⁶⁰

The final reaction strategy explores the effect of $^t\text{BuCO}_2^-$ in the above reaction scheme. The reaction of $^t\text{BuCO}_2^-$ with edteH_4 and NaN_3 in presence of Mn^{2+} salt led to the isolation of aforementioned Mn_9 ¹⁶⁸ and Mn_6 (**4-4**) clusters. Here, the reaction system is further modified by adding Ca^{2+} salt to the reaction system. The 1:1:1:2 molar ratio of $\text{Mn}(\text{O}_2\text{CBu}^t)_2$, $\text{Ca}(\text{NO}_3)_2$, edteH_4 and NEt_3 in MeCN/MeOH leads to the isolation of a new $[\text{Ca}_2\text{Mn}_{18}\text{O}_8(\text{OH})_5(\text{O}_2\text{CBu}^t)_{4.5}(\text{edte})_6(\text{NO}_3)_{3.5}]^+$ (**4-8**) cluster. The reaction is summarized in equation 4-8.



The product is obtained by using a large excess of the Ca^{2+} salt, whereas no product was isolated by using a 9:1 to 2:1 ratio of Mn^{2+} to Ca^{2+} salt. An analogous $\text{Mn}_{18}\text{Ca}_2$ cluster was isolated by switching tBuCO_2^- to MeCO_2^- as confirmed by IR and elemental analysis. Both reactions involve acid-base (e.g. deprotonation of water) and redox chemistry (oxidation of Mn^{2+} to Mn^{3+}) as well as structural rearrangements. It is clear that the described reactions to complex **4-1** to **4-8** are complicated and they involve acid-base (e.g. deprotonation of water) and redox chemistry (oxidation of Mn^{2+} to Mn^{3+}) as well as structural rearrangements.

Description of Structures

Structure of $[\text{Mn}_3(\text{O}_2\text{CMe})_2(\text{edteH}_2)_2](\text{O}_2\text{CMe})$ (**4-1**)

A partially labeled representation of the $[\text{Mn}_3(\text{O}_2\text{CMe})_2(\text{edteH}_2)_2]^+$ cation of **4-1** is shown in Figure 4-1(A), and selected inter-atomic distances and angles are summarized in Table A-5. Complex **4-1** crystallizes in the triclinic space group $P-1$ and has crystallographic inversion symmetry. The core of the complex is comprised of a linear $[\text{Mn}^{3+}\text{Mn}^{2+}_2(\text{OR})_4]^{3+}$ unit in which the central Mn^{3+} ion (Mn1) is connected to the terminal Mn^{2+} ions (Mn2) by $\eta^1:\eta^1:\mu$ -acetate bridges. The coordination of the two peripheral Mn ions is completed by two edteH_2^{2-} ligands. Each edteH_2^{2-} group is hexadentate-chelating to the terminal Mn2 atom with two of its deprotonated alkoxide arms bridging to the central Mn1 (O1, O3) atom. Thus, the edteH_2^{2-} groups are overall $\eta^1:\eta^1:\eta^2:\eta^2:\mu$ -bridging, as shown in Figure 4-14. The Mn oxidation states were determined by charge considerations and metric parameters, and confirmed by BVS calculations¹⁷¹ which are summarized in Table 4-4. Mn1 and Mn2 are six and seven coordinate, respectively.

Charge balance considerations require 2Mn^{2+} , Mn^{3+} , 2MeCO_2^- , 2edteH_2^{2-} and one additional negative charge comes from the acetate counteranion. Two Mn_3 units are connected through an acetate group with H-bond and hence make a 1D polymeric chain (Figure 4-1, B). The acetate ion is making H-bond ($\text{OH}\cdots\text{O}$) to the protonated OH group (O2) of the edteH_2^{2-} ligand. The bond distance between O2 and the acetate ion (O13) is 2.652 Å. There are two additional H-bonds ($\text{OH}\cdots\text{O}$) between the protonated OH group (O4, O10) of the edteH_2^{2-} ligand in one Mn_3 unit and the acetate ion (O12, O6) of the adjacent Mn_3 unit. The protonation levels of all the O atoms were determined by BVS calculations and the results are listed in Table 4-8. Two of the edteH_2^{2-} O atoms have BVS values of >1.8 , confirming them as deprotonated, whereas the other two have BVS values of around 1.1, confirming them as protonated.

Structure of $[\text{Mn}_3(\text{O}_2\text{CMe})_2(\text{edteH}_2)_2](\text{ClO}_4)$ (4-2)

Complex **4-2** crystallizes in the monoclinic space group $\text{P}2_1/\text{n}$. The structure of **4-2** is very similar to **4-1**. It comprises the same core as $[\text{Mn}_3(\text{O}_2\text{CMe})_2(\text{edteH}_2)_2]^+$ with ClO_4^- as a counterion (Figure 4-2). The selected interatomic distances and angles are summarized in Table A-5. The BVS calculations for the Mn ions and O atoms are shown in Tables 4-4 and Table 4-8, respectively. The linear $\text{Mn}_2^{2+}\text{Mn}^{3+}$ core of complexes **4-1** and **4-2** is quite rare in the literature except for two examples where one is an SMM using tripodal alcohol ligand¹⁷⁴ and other is a trinuclear unit embedded in a macrocycle.¹⁷⁵

There are few other examples of linear Mn_3 complexes known in the literature, which include Mn^{2+}_3 ,¹⁷⁶ Mn^{4+}_3 ,¹⁷⁷ $\text{Mn}^{2+}\text{Mn}^{3+}\text{Mn}^{4+}$,¹⁷⁸ and $\text{Mn}^{3+}_2\text{Mn}^{2+}$ ¹⁷⁹ oxidation levels. Apart from the linear topology, a large family of triangular Mn^{3+}_3 SMMs is also known in the literature.¹⁸⁰

Structure of $[\text{Mn}_4(\text{edteH}_2)_2(\text{hmp})_2\text{Cl}_2][\text{Mn}^{\text{II}}\text{Cl}_4]$ (**4-3**)

A partially labeled representation of the $[\text{Mn}_4(\text{edteH}_2)_2(\text{hmp})_2\text{Cl}_2]^{2+}$ cation of **4-3** is shown in Figure 4-3, and selected interatomic distances and angles are summarized in Table A-6. Complex **4-3** crystallizes in the monoclinic space group C2/c with the cation lying on an inversion center and consisting of a planer Mn_4 rhombus. The Mn_4 comprises of two bridging $\mu_3\text{-O}$ (O5) of hmp^- ligand, above and below the Mn_4 plane. The $[\text{Mn}_4(\mu_3\text{-OR})_2]^{6+}$ unit is commonly known as a 'planer butterfly' unit (Figure 4-4, A). In this case each 'wingtip' Mn1 (Mn^{2+}) is chelated by a hexadentate edteH_2^{2-} ligand and the 'body' is connected by two bridging $\mu_3\text{-O}$ (O5) of hmp^- ligand. The Mn_2 edges of Mn_4 rhombus are comprised of $\mu\text{-O}$ (O2, O4) of $\eta^1: \eta^1: \eta^2: \eta^2: \mu_3\text{-bridging edteH}_2^{2-}$ ligand (Figure 4-14). Mn1 is seven coordinate and Mn2 is six coordinate and their oxidation states were determined by charge considerations and metric parameters, and confirmed by BVS calculations (Table 4-5). Mn2 undergoes Jahn-Teller (JT) axial elongation as expected for near octahedral geometry, with the elongated axes as O5–Mn2–Cl1 (green thick lines in Figure 4-3). The Mn2 is also ligated by a terminal Cl^- ion. Charge balance considerations require 2Mn^{3+} , 2Mn^{2+} , 2edteH_2^{2-} , 2hmp^- , 2Cl^- and $[\text{MnCl}_4]^{2-}$. The protonation levels of all O atoms in **4-3** have been determined by BVS calculations, and the results are listed in Table 4-9. The structure contains intramolecular $\text{OH}\cdots\text{Cl}$ hydrogen-bonds between OH groups of edteH_2^{2-} and MnCl_4^{2-} ($\text{O3}\cdots\text{Cl3} = 3.070\text{\AA}$). These interactions serve to link the neighboring Mn_4 units in the crystal into a 1D polymeric chain (Figure 4-4, B). There are a large number of Mn_4 clusters known in the literature¹⁷⁰⁻¹⁷⁸ and they cover a wide range of metal topologies such as linear units, rectangles, rhombi, cubanes, butterflies, and so on. The $[\text{Mn}_4(\mu_3\text{-OR})_2(\mu\text{-OR})_4]^{4+}$ core

has been seen before,¹⁸¹ but this is the first example with a mixed edteH₂²⁻ and hmp⁻ chelate system.

Structure of [Mn₆O₂(O₂CBu^t)₆(edteH)₂(N₃)₂] (4-4)

The structure (A) and a stereoview (B) of **4-4** are presented in Figure 4-5, and selected interatomic distances and angles are summarized in Table A-6. The complex **4-4** crystallizes in the monoclinic space group C2/c with the Mn₆ cluster located on an inversion center. The core (Figure 4-5, C) comprises two [Mn₃(μ₃-O)]⁷⁺ triangular subunits linked *via* bridging oxygen atoms (O9, O10) of η²: η²: η³: μ₄-edteH³⁻ ligands (Figure 4-14). Mn1 and Mn2 are further bridged by a bridging oxygen atom (O8) from the edteH³⁻ ligand. Coordination of the Mn centers is completed by six bridging ^tBuCO₂⁻ groups and two terminal azide groups. All Mn ions are six coordinate and in the +3 oxidation state, as determined by charge calculations, metric parameters and BVS calculations (presented in Table 4-5). The near-octahedral Mn³⁺ ions undergo JT elongation, and the elongated axes are shown as green thick lines in Figure 4-5 (A). The JT elongated axes at Mn2 and Mn3 are oriented in a near parallel fashion to each other and perpendicular to that of Mn1. The charge balance consideration requires 6Mn³⁺, 2O²⁻, 2edteH³⁻, 6 ^tBuCO₂⁻ and 2N₃⁻; the protonation levels of all O atoms in **4-4** have been confirmed by BVS calculations, and the results are listed in Table 4-9. There are a large number of substituted salicylaldoxime ligand containing Mn₆ clusters (R-saoH₂ family) known in the literature.¹⁸² The complex **4-4** has some structural resemblance with this series, but with an ethylenediamine based alkoxide-containing ligand.

Structure of Na₂[Mn₁₀O₄(OMe)₂(O₂CEt)₆(edte)₂(N₃)₆] (4-5)

A partially labeled representation (A) and a stereoview (B) of **4-5** are presented in Figure 4-6. Selected interatomic distances and angles are listed in Table A-9. Complex **4-5** crystallizes in the triclinic space group P-1 with the Mn₁₀ on an inversion center. The core of **4-5** consists of a central Mn₄ rhombus, fused on each side by two distorted [Mn₄O₂(OR)₂]⁵⁺ cubanes as shown in Figure 4-7 (A). Each distorted cubane is further linked to Na1 by a bridging μ₄-O²⁻ (O14) ion. Each cubane consists of three Mn³⁺ (Mn3, Mn4, Mn5), one Mn²⁺ (Mn1), two bridging μ₄-O²⁻ (O13 & O14), and two oxygen atoms (O2, O4) from a η³: η³: η³: η²: μ₆-edte⁴⁻ ligand (Figure 4-14). The cubane is connected to the central Mn₂ dimer by two oxygens (O1, O3) from η³: η³: η³: η² edte⁴⁻ ligands and one μ-O (O7) from a OMe⁻ group. The coordination sites of the Mn ions are completed by six peripheral EtCO₂⁻ groups and six terminal azide groups. The coordination sites of the Na ions are completed by terminal MeCN, MeOH and end-to-end azide (N7-N8-N9) groups. Each Na ion is connected with the neighboring Na ion by two end-to-end azide bridges (N7-N8-N9), thus making a 1D polymer of Na₂Mn₁₀ (Figure 4-7, B). All Mn ions (Mn2, Mn3, Mn4, Mn5) are six coordinate and are in +3 oxidation state except Mn1 (seven coordinate and in +2 oxidation state) as determined by charge calculations, metric parameters and BVS calculations (Table 4-6). All eight near-octahedral Mn³⁺ ions undergo JT elongation, roughly four parallel and four perpendicular axes where all the elongated axes are shown as green thick lines in the Figure 4-6 (A). Charge balance considerations require 8Mn³⁺, 2Mn²⁺, 2Na⁺, 4O²⁻, 2MeO⁻, 6EtCO₂⁻, 2edte⁴⁻, and 6 N₃⁻. The protonation levels of all O atoms in **4-5** have been determined by BVS calculations, and the results are listed in Table 4-10.

Structure of $(\text{NEt}_4)_2[\text{Mn}_{10}\text{O}_4(\text{OH})_2(\text{O}_2\text{CEt})_6(\text{edte})_2(\text{N}_3)_6]$ (**4-6**)

A partially labeled representation (A) and a stereoview (B) of $[\text{Mn}_{10}(\text{O})_4(\text{OH})_2(\text{O}_2\text{CEt})_6(\text{edte})_2(\text{N}_3)_6]^{2-}$ (**4-6**) are presented in Figure 4-8, and selected interatomic distances and angles are listed in Table A-8. The cores of **4-5** and **4-6** are very similar (as described above). Complex **4-6** is a discrete Mn_{10} cluster with two tetraethylammonium counter cations. These NEt_4^+ cations replace the Na^+ ions of **4-5**, but unlike **4-5** no end-to-end azide bridges, connecting the individual Mn_{10} units exist in **4-6**. The BVS calculations for all the Mn ions and O atoms have been listed in Tables 4-6 and Table 4-10. A number of other Mn_{10} complexes have previously been reported.¹⁸³⁻¹⁸⁸ These possess a variety of metal topologies such as molecular cage, loop, wheel, and rod but none of them have possessed the core of the complex **4-5/4-6**, which is unprecedented in the literature.

Structure of $[\text{Mn}_{20}\text{O}_8(\text{OH})_6(\text{O}_2\text{CEt})_6(\text{edte})_4(\text{edteH})_2](\text{ClO}_4)_4$ (**4-7**)

The structure of the cation of **4-7** (A) and a stereopair (B) is shown in Figure 4-9, and selected inter atomic distances and angles are summarized in Table A-9. Complex **4-7** crystallizes in the monoclinic space group $\text{P}2_1/\text{c}$ where the asymmetric unit consists of a half Mn_{20} cluster and two perchlorate anions. The cation of **4-7** holds a central face-sharing dicubane unit $[\text{Mn}_6\text{O}_2(\text{OR})_4]$ fused with an adjacent edge-sharing distorted dicubane unit on both sides (highlighted by thick pink lines in Figure 4-10). The central dicubane unit comprises of 4Mn^{3+} (Mn1, Mn3), 2Mn^{2+} (Mn2), $2\mu_6\text{-O}^{2-}$ (O2) and two bridging oxygen atoms (O9, O11) from $\eta^3:\eta^3:\eta^3:\eta^3\text{edte}^{4-}$ ligand. Each terminal dicubane unit is further linked with a butterfly unit (highlighted by thick blue lines in Figure 4-10), $\text{Mn}_4(\mu_3\text{-O})_2$ (Mn7, Mn8, Mn9, Mn10) shared by a common Mn^{3+} ion (Mn7). This gives an overall tube-like arrangement of twenty Mn atoms inside of which are two

$\mu_6\text{-O}^{2-}$ (O2) and two $\mu_4\text{-O}^{2-}$ (O6) ions (Figure 4-10). There are four additional $\mu_3\text{-O}^{2-}$ (O4, O5) ions and six $\mu\text{-OH}^-$ (O1, O3, O7) ions helping to maintain this tubular structure. There are three different bridging modes of the ligand in complex **4-7**. All four edte^{4-} groups bind as hexadentate chelates to Mn ions (Mn2, Mn9) and then bridge through its deprotonated alkoxide arms to various Mn atoms. Hence, two edte^{4-} are overall $\eta^3: \eta^3: \eta^3: \eta^3: \mu_7$ -bridging (Figure 4-14) and the other two are $\eta^2: \eta^2: \eta^2: \eta^3: \mu_5$ -bridging (Figure 4-14). The remaining two edteH^{3-} are pentadentate to Mn ions (Mn8) and are overall $\eta^2: \eta^3: \eta^2: \mu_4$ -bridging (Figure 4-14). The remaining ligation of the molecule is provided by six propionate ligands, two of which are $\eta^1: \eta^1: \mu$ -bridging (Mn3, Mn7), two each are η^2 -chelating on Mn10, and η^1 -terminal on Mn6. Charge balance considerations require 14Mn^{3+} , 6Mn^{2+} , 8O^{2-} , 6OH^- , 6EtCO_2^- , 4edte^{4-} , 2edteH^{3-} and 4ClO_4^- . The protonation levels of all Mn and O atoms in **4-7** have been decided by BVS calculations, and the results are listed in Tables 4-7 and 4-11. The oxides, OH^- and edte^{4-} O atoms have BVS values of >1.83 , confirming them as completely deprotonated, as concluded above from their bridging modes. All Mn ions are six-coordinate except, Mn3 (penta-coordinate) and Mn2 (seven-coordinate). The JT elongation axes on six-coordinate Mn^{3+} atoms are shown as thick green bonds in Figure 4-9. It shows the presence of six parallel JT axes countered by six near perpendicular JT axes. There are only two other Mn_{20} clusters available in the literature.^{60,189} Between them one has structural resemblance with complex **4-7**. However, the core of complex **4-7** is different than that of the previously reported Mn_{20} due to the oxidation state of the Mn ions and coordination modes of the surrounding ligands.

Structure of $[\text{Ca}_2\text{Mn}_{18}\text{O}_8(\text{OH})_5(\text{O}_2\text{CBu}^t)_{4.5}(\text{edte})_5(\text{NO}_3)_{3.5}](\text{O}_2\text{CBu}^t)_{0.5}(\text{NO}_3)_{0.5}$ (**4-8**)

The structure of cation of **4-8** (Figure 4-11) and a stereopair (Figure 4-12) are shown, and selected interatomic distances and angles are listed in Table A-10.

Complex **4-7** crystallizes in the monoclinic space group $P2_1/c$ where the asymmetric unit consists of a $\text{Mn}_{18}\text{Ca}_2$ cluster cation, a half nitrate group and a half $^t\text{BuCO}_2^-$ anion. The core of the structure is similar to that of **4-7** which means the cation of **4-8** also possesses a central face-sharing dicubane unit $[\text{Mn}_6\text{O}_2(\text{OR})_4]$ fused with an adjacent edge-sharing distorted dicubane unit on both sides (Figure 4-13, A). The central dicubane unit comprises of 4Mn^{3+} (Mn2, Mn7, Mn12, Mn16), 2Mn^{2+} (Mn3, Mn17), $2\mu_6\text{-O}^{2-}$ (O14, O17) and four bridging oxygen atoms (O5, O6, O51, O52) from the $\eta^3: \eta^3: \eta^3: \eta^3$ edte^{4-} ligand (highlighted by thick pink lines in Figure 4-13, B). The two adjacent distorted dicubane units consist of a set of 4Mn^{3+} (Mn1, Mn2, Mn8, Mn18 and Mn4, Mn13, Mn15, Mn16), 2Mn^{2+} (Mn11, Mn17 and Mn6, Mn3), $\mu_6\text{-O}^{2-}$ (O14 and O17), $\mu_4\text{-O}^{2-}$ (O31 and O37), $2\mu_3\text{-O}^{2-}$ (O1, O2 and O47, O48) and two bridging oxygen atoms (O53, O58 and O7, O8) from the edte^{4-} ligand. These two edte^{4-} groups bind as hexadentate chelates to Mn ions (Mn3, Mn17) and then bridge through their deprotonated alkoxide arms to various Mn atoms. Hence, they are overall $\eta^3: \eta^3: \eta^3: \eta^3: \mu_7$ -bridging (Figure 4-14). The edge of each distorted dicubane unit (Mn1, Mn18 and Mn15, Mn4) further connects to 1Ca^{2+} (Ca1, Ca2) ion and 2Mn^{3+} ions (Mn9, Mn10 and Mn5, Mn14) by two edte^{4-} ligands. For example, Ca1 and Mn1 are connected by two $\mu_3\text{-O}$ atoms (O19, O27) of two edte^{4-} ligands. The total four terminal edte^{4-} ligands are hexadentate chelated to Mn ions (Mn9, Mn10 and Mn5, Mn14) and are overall $\eta^2: \eta^2: \eta^2: \eta^2: \eta^3: \mu_5$ -bridging (Figure 4-14). Mn4 and Mn14 are further connected by a bridging $\mu\text{-OH}^-$ ion (O36'). The remaining ligation of the molecule is provided by four $^t\text{BuCO}_2^-$ ligands

and four nitrate groups. Two of the carboxylate ligands are $\eta^1: \eta^1: \mu$ -bridging (Mn1, Mn2 and Mn15 and Mn16), and two are η^1 -terminal on Mn4 and Mn18 atoms. The four nitrates are η^2 -chelating on Ca1 and Ca2 ions. One of the nitrate groups is disordered with a ${}^t\text{BuCO}_2^-$ group by an occupancy factor of 0.5 at the Ca2 site. Charge balance consideration requires 14Mn^{3+} , 4Mn^{2+} , 8O^{2-} , 5OH^- , $5{}^t\text{BuCO}_2^-$, 6edte^{4-} and 4ClO_4^- . The protonation levels of all Mn and O atoms in **4-7** have been decided by BVS calculations, and the results are listed in Tables 4-7 and 4-12. The oxides, OH^- and edte^{4-} O atoms have BVS values of >1.8 , confirming them as completely deprotonated, as concluded above from their bridging modes. The BVS values for O9 and O31 are ~ 1.6 , little smaller for edte^{4-} O atoms and the reason can be attributed to the presence of H-bonds in the respective O atoms. All Mn ions are six-coordinate except, Mn4, Mn14, M10 and Mn18 (seven-coordinate). The JT elongation axes on six-coordinate Mn^{3+} atoms are shown as thick green bonds in Figure 4-11. Compound **4-8** is the largest Mn-Ca cluster to date with a structurally unprecedented metal topology. There are only very few Mn/Ca complexes known in the literature¹⁹⁰⁻¹⁹² and the field is still in its infancy for mimicking the structural features and various physical properties of WOC in photosystem II.

Magnetochemistry

Dc and ac magnetic susceptibility studies of **4-1** and **4-2**

Solid-state, variable-temperature dc magnetic susceptibility data in a 0.1 T field and in the 5.0 - 300 K range were collected on powdered microcrystalline samples of **4-1**·H₂O and **4-2**·H₂O. The $\chi_M T$ values for complexes **4-1** and **4-2** at 300 K are 9.13 and 10.98 cm³Kmol⁻¹, lower than the spin-only ($g = 2$) value expected for three non-interacting Mn ions (Mn^{3+} and 2Mn^{2+}) which is 11.75 cm³Kmol⁻¹. This is indicative of

antiferromagnetic exchange interactions among the paramagnetic Mn ions in the system. For both complexes, $\chi_M T$ stays fairly constant down to 150 K and decreases smoothly to 5.75 and 5.79 $\text{cm}^3\text{Kmol}^{-1}$ at 5.0 K, which is suggestive of a $S = 3$ ground state. The data for complex **4-1** and **4-2** were fit to the theoretical χ_M vs. T and $\chi_M T$ vs. T expression for a linear $\text{Mn}^{\text{II}}\text{Mn}^{\text{III}}\text{Mn}^{\text{II}}$ core with two exchange coupling parameters, J and J' , representing the $\text{Mn}^{\text{II}}\text{Mn}^{\text{III}}$ and $\text{Mn}^{\text{III}}\text{Mn}^{\text{III}}$ interactions, respectively. The corresponding Heisenberg spin Hamiltonian is given by equation 4-8 (the atom labeling is that of Figure 4-15) and its eigenvalues in equation 4-10, where $\hat{S}_A = \hat{S}_2 + \hat{S}_3$ and $\hat{S}_T = \hat{S}_A + \hat{S}_1$. The corresponding Heisenberg spin Hamiltonian (equation 4-8) can be converted to an equivalent one in equation 4-9 by using the Kambe vector coupling method.¹⁹³

$$\hat{H} = -2J(\hat{S}_1 \cdot \hat{S}_2 + \hat{S}_1 \cdot \hat{S}_3) + -2J'\hat{S}_2 \cdot \hat{S}_3 \quad (4-8)$$

$$\hat{H} = -J(\hat{S}_T^2 - \hat{S}_A^2 - \hat{S}_1^2) - J'(\hat{S}_A^2 - \hat{S}_2^2 - \hat{S}_3^2) \quad (4-9)$$

$$E(S_T, S_A) = -J[S_T(S_T+1) - S_A(S_A+1)] - J'[S_A(S_A+1)] \quad (4-10)$$

There are 24 possible S_T states ranging in value from 0 to 7. The eigenvalue expression and the Van Vleck equation were used to derive the theoretical χ_M vs. T and $\chi_M T$ vs. T expression for complexes **4-1** and **4-2**, and this was used to least-squares-fit the experimental data. The fit for complex **4-1** (solid line in Figure 4-16) gave $J = -2.6(2) \text{ cm}^{-1}$, $J' = 0$, and $g = 1.99(1)$ and the fit for complex **4-2** (solid line in Figure 4-17) gave $J = -1.4(1) \text{ cm}^{-1}$, $J' = 0.3(1) \text{ cm}^{-1}$, and $g = 1.98(1)$. These values identify the $|S_T, S_A\rangle = |3, 5\rangle$ state to be the ground state, as expected. For complex **4-1**, the next excited state, $|2, 4\rangle$ lies 10.60 cm^{-1} above the ground state followed by two degenerate energy states of $|4, 5\rangle$ and $|1, 3\rangle$ separated by 21.20 cm^{-1} from the lowest energy state (Figure 4-18). For complex **4-2**, the next two excited states, $|2, 4\rangle$ and $|4, 5\rangle$ lie 8.6 and 11.3 cm^{-1} above the ground state (Figure 4-19). The type of exchange interactions in both the

molecules is similar however in **4-1** the magnetic interaction between two Mn²⁺ ions is practically zero. The spin configuration of the excited states is also different in both the complexes which show the effect of minor structural change in magnetic properties.

To confirm the above initial estimates of the ground state spin of the compound **4-1** and **4-2**, variable-field (*H*) and -temperature magnetization (*M*) data were collected in the 0.1 - 7 T and 1.8 - 10 K ranges. The resulting data for **4-1** and **4-2** are plotted as reduced magnetization (*M/Nμ_B*) vs. *H/T*, where *N* is Avogadro's number and *μ_B* is the Bohr magneton. The data were fit using the program MAGNET,⁶⁶ by diagonalization of the spin Hamiltonian matrix assuming only the ground state is populated, incorporating axial anisotropy (*DŜ_z²*) and Zeeman terms, and employing a full powder average. The corresponding spin Hamiltonian is given by equation 4-11, where *Ŝ_z* is the easy-axis spin operator, *g* is the Landé *g* factor, and *μ₀* is the vacuum permeability. The last term in equation 4-11 is the Zeeman energy associated with the applied magnetic field.

$$H = D\hat{S}_z^2 + g\mu_B\mu_0\hat{S}\cdot H \quad (4-11)$$

However, for neither **4-1** nor **4-2** were we able to obtain a satisfactory fit. This is not unusual in Mn_x cluster chemistry, and is almost always due to the presence of low-lying excited states because (i) the excited states are close enough to the ground state that they are populated even at very low temperatures, and/or (ii) even higher-lying excited states whose *S* is greater than the ground-state become populated as their larger *M_S* levels rapidly decrease in energy in the applied dc field and approach (or even cross) those of the ground state. Either (or both) of these two effects will lead to poor fits because the fitting program assumes population of only the ground state.⁹⁴⁻⁹⁶ A large density of low-lying excited states is expected for those with a significant content of

Mn²⁺ atoms, which give weak exchange couplings. One likely way to avoid the above mentioned complication is to collect the data at the lower fields. Indeed, a satisfactory fit was achieved using data in fields up to 3 T for **4-2** with fit parameters $S = 3$, $g = 2.03$, and $D = -0.38 \text{ cm}^{-1}$ (Figure 4-20). Alternative fits were also obtained with $S = 2$, $g = 2.93$ and $S = 4$, $g = 1.57$, but were discarded because of the unreasonable g values. The fitting was also good for $S = 3$, $g = 2.02$, and $D = 0.37 \text{ cm}^{-1}$. In order to ensure that the true global minimum had been obtained and to assess the hardness of the fit, a root-mean-square D vs. g error surface for the fit was generated using the program GRID,⁹⁷ which calculates the relative difference between the experimental $M/N\mu_B$ data and those calculated for various combinations of D and g . This is shown as a 2-D contour plot in Figure 4-21. True global minima were observed. The fit uncertainties are quite hard and estimated as $g = 2.03(1)$, $D = -0.38(1) \text{ cm}^{-1}$. The satisfactory fitting was not achieved for **4-1** even at lower fields.

In all the previous chapters, it has been stated that ac magnetic susceptibility studies are a powerful complement to dc studies. This is a useful technique for determining the ground state of a system, since they preclude any complications arising from the presence of a dc field. Hence, ac studies on microcrystalline complex **4-1**·H₂O and **4-2**·H₂O were carried out in the 1.8 - 15 K range using a 3.5 G ac field oscillating at 1000 Hz. Ac study can probe the relaxation of the magnetisation vector. If the magnetisation vector relaxes fast enough to keep in-phase with the oscillating field, then the susceptibility (χ_M) will be equal to the dc susceptibility. However, if the barrier of magnetisation relaxation is significant compared to thermal energy (kT), then the in-phase signal can not keep up with the oscillating field and decreases with the

concomitant rise of the out-of-phase signal. This behavior is suggestive of the superparamagnet-like properties of an SMM. For both complexes, the in-phase $\chi_M T$ signals below 15 K are almost temperature independent (Figure 4-22), and the extrapolation of the plots to 0 K gives values of ~ 5.95 and $5.26 \text{ cm}^3\text{Kmol}^{-1}$ indicating an $S = 3$ ground state and $g \sim 2.0$. The dc magnetization fit for **4-1** gives a g value of $1.99(1)$ which closely agree with the ac data. Both the complexes **4-1** and **4-2** did not exhibit an out-of-phase ac magnetic susceptibility signals above 1.8 K, i.e., they are not SMMs.

Dc and ac magnetic susceptibility studies of **4-3**

Solid-state, variable-temperature dc magnetic susceptibility data in a 0.1 T field and in the 5.0 - 300 K range were collected on powdered microcrystalline samples of **4-3**. The obtained data are plotted as $\chi_M T$ vs. T in Figure 4-23. The $\chi_M T$ value at 300 K is $18.18 \text{ cm}^3\text{Kmol}^{-1}$, a little smaller than that expected for five non-interacting Mn ions ($19.13 \text{ cm}^3\text{Kmol}^{-1}$ for 3Mn^{2+} and 2Mn^{2+} ions). The magnetic susceptibility steadily rises to $41.58 \text{ cm}^3\text{Kmol}^{-1}$ at 6.5K, indicative of dominant ferromagnetic interactions. The $\chi_M T$ value decreases slightly to $41.01 \text{ cm}^3\text{Kmol}^{-1}$ at 5 K, due to some intermolecular interactions. Since **4-3** has a MnCl_4^{2-} as counterion, the spin ground state of the cluster cation was determined after deducting the anion's contribution of $4.375 \text{ cm}^3\text{Kmol}^{-1}$ from the overall $\chi_M T$ value. The resulting value of $37.21 \text{ cm}^3\text{Kmol}^{-1}$ at 6.5 K suggests an $S = 9$ ground state spin for $g < 2$. Further studies were carried out for investigating spin-ground state as before. The $\chi_M T$ vs. T data were least-squares-fit to a theoretical expression derived for a Mn_4 core with two exchange coupling parameters, J_{wb} and J_{bb} (as shown in Figure 4-24).¹⁸¹ The corresponding Heisenberg spin Hamiltonian (equation

4-12) can be converted to an equivalent one in equation 4-13 by using the Kambe vector coupling method¹⁹³ where, $\hat{S}_A = \hat{S}_1 + \hat{S}_3$, $\hat{S}_B = \hat{S}_2 + \hat{S}_4$ and $\hat{S}_T = \hat{S}_A + \hat{S}_B$

$$\hat{H} = -2J_{wb}(\hat{S}_1 \cdot \hat{S}_2 + \hat{S}_1 \cdot \hat{S}_4 + \hat{S}_2 \cdot \hat{S}_3 + \hat{S}_3 \cdot \hat{S}_4) - 2J_{bb}\hat{S}_1 \cdot \hat{S}_3 \quad (4-12)$$

$$\hat{H} = -J_{wb}(\hat{S}_T^2 - \hat{S}_A^2 - \hat{S}_B^2) - J_{bb}(\hat{S}_A^2 - \hat{S}_1^2 - \hat{S}_3^2) \quad (4-13)$$

$$E(S_T, S_A, S_B) = -J_{wb}[S_T(S_T+1) - S_A(S_A+1) - S_B(S_B+1)] - J_{bb}[S_A(S_A+1)] \quad (4-14)$$

There are a total of 110 possible S_T states ranging in value from 0 to 9, where S_T is the total spin of the Mn_4 cluster. This eigenvalue expression (equation 4-14) and the Van Vleck equation were used to derive a theoretical $\chi_M T$ vs. T expression for **4-3**, and this was used to least-squares-fit the experimental data. The fit (solid line in Figure 4-23) gave $J_{bb} = +7.20(3) \text{ cm}^{-1}$, $J_{wb} = +1.34(3) \text{ cm}^{-1}$ and $g = 1.87(2)$ with temperature-independent paramagnetism (TIP) fixed at $6 \times 10^{-4} \text{ cm}^3 \text{ mol}^{-1}$. The spin-ground state is sensitive to the ratio of J_{wb}/J_{bb} and the plots of E/J_{bb} vs. J_{wb}/J_{bb} by using the equation 4-14, truly identify a $|S_T, S_A, S_B\rangle = |9, 4, 5\rangle$ ground-state for **4-3** as shown in Figure 4-25 (A). Since, the J values are positive, the system is not spin-frustrated and the lowest energy state indicates only one spin state, independent of the J_{wb}/J_{bb} ratio. The first two excited states are the $|8, 4, 4\rangle$ and $|7, 4, 3\rangle$ states at 10.72 and 21.44 cm^{-1} above the ground state, respectively (Figure 4-25, B).

The ac susceptibility data were collected on microcrystalline samples in a 3.5 G ac field and these signals for complex **4-3** at 50 and 250 Hz are plotted as $\chi_M' T$ vs. T in Figure 4-26. The $\chi_M' T$ slowly rises from $40.49 \text{ cm}^3 \text{ K mol}^{-1}$ at 15 K to $43.12 \text{ cm}^3 \text{ K mol}^{-1}$ at ~ 7 K and then decreases sharply to $37.98 \text{ cm}^3 \text{ K mol}^{-1}$ at 1.8 K for the complex **4-3**. This decrease at low temperature is not frequency-dependent and can be attributed to intermolecular antiferromagnetic interactions. The behavior indicates that compound **4-3** is not an SMM. Due to the steep downfall of the ac signals, the determination of the

spin-ground state from in-phase ac data is not accurate. There are other examples of Mn_4 clusters with similar butterfly cores of $S = 9$ spin ground state, which all exhibit characteristic properties of SMMs. However, the compound **4-3** does not show any slow relaxation at low temperature and the outcome could be explained by the presence of strong antiferromagnetic interactions between Mn_4 units with $MnCl_4^{2-}$ ions in the cluster which prevails at very low temperature (Figure 4-4, B).

Dc and ac magnetic susceptibility studies of 4-4

Solid-state, variable-temperature dc magnetic susceptibility data in a 0.1 T field and in the 5.0 - 300 K range were collected on powdered microcrystalline samples of **4-4**. The 300 K value, $16.97 \text{ cm}^3\text{Kmol}^{-1}$ is slightly lower than the spin-only ($g = 2$) value of $18.0 \text{ cm}^3\text{Kmol}^{-1}$ for six non-interacting Mn^{3+} ions, indicative of antiferromagnetic interactions in the core. The $\chi_M T$ value smoothly decreases from 300 K down to $7.87 \text{ cm}^3\text{Kmol}^{-1}$ at 15K and then stays fairly constant down to 5K. This results in a plateau, observed at very low temperature, which indicates a stable and well isolated ground-state spin. The $\chi_M T$ at 5 K suggests an $S = 4$ ground state (Figure 4-27). Confirmation of these came from the reduced magnetization fit. For this purpose, variable-field (H) and -temperature magnetization (M) data were collected in the 0.1 - 7 T and 1.8 - 10 K ranges, however, best fit data were obtained at lower fields of 3.0 - 6.0 T. The resulting data are plotted as reduced magnetization ($M/N\mu_B$) vs. H/T and the data were fitted using the program MAGNET⁶⁶ as explained before. A satisfactory fit was obtained with the fit parameters $S = 4$, $D = -1.03 \text{ cm}^{-1}$ and $g = 1.86$ (Figure 4-28). The obtained g value is reasonable for a system containing only Mn^{3+} ions. The fit for an $S = 4$ ground-state spin considering a positive D gave an unreasonable value of $D = +4.85 \text{ cm}^{-1}$ and

was therefore discarded. Alternative fits were also obtained with $S = 3$, $g = 2.48$ and $S = 5$, $g = 1.52$, but were discarded because of the unreasonable g values. In order to ensure that the true global minimum had been obtained and to assess the hardness of the fit, a root-mean-square D vs. g error surface for the fit was generated using the program GRID,⁹⁷ which calculates the relative difference between the experimental $M/N\mu_B$ data and those calculated for various combinations of D and g . This is shown as a 2-D contour plot in Figure 4-29. Five local minima were observed where the values of D are spanning over -0.95 to -1.15 cm^{-1} and the corresponding g varies from 1.83 to 1.90. The fit uncertainties are quite soft and estimated as $g = 1.86 \pm 0.04$, $D = -1.03 \pm 0.10$ cm^{-1} . The large negative D value indicates appreciable anisotropy in the system, which would be consistent with the four nearly parallel JT elongated axes in the complex (Figure 4-5, A).

Ac susceptibility data were collected on a microcrystalline sample of **4-4** in a 3.5 G ac field oscillating at 50 - 1000 Hz. The data are plotted as $\chi_M'T$ vs. T in Figure 4-30. Below 10 K, the $\chi_M'T$ value is almost temperature independent at a value of ~ 8.6 $\text{cm}^3\text{Kmol}^{-1}$, confirming an $S = 4$ ground-state spin for **4-4**. In spite of having significantly high negative D value, no frequency dependent ac signal was observed above 1.8 K. Such a notably high D value has been observed before in a family of substituted salicylaldehyde ligand-containing Mn_6 and Mn_3 clusters.^{180,182} The absence of slow relaxation in **4-4** can be attributed to fast quantum tunneling of magnetization through the spin-reversal barrier.¹⁹⁴ On a separate note, the D could be less than 1 cm^{-1} . The reduced magnetization fit may not provide an accurate estimation of D value e.g., the

magnetization saturation may have been affected by the presence of low-lying excited states.

Dc and ac magnetic susceptibility studies of 4-5 and 4-6

Solid-state, variable-temperature dc magnetic susceptibility data in a 0.1 T field and in the 5.0 - 300 K range were collected on powdered microcrystalline samples of **4-5**·2H₂O and **4-6**·H₂O. The $\chi_M T$ values at 300 K are 29.49 and 30.73 cm³Kmol⁻¹, a little lower than the spin-only ($g = 2$) value of 32.75 cm³Kmol⁻¹ expected for a system containing ten non-interacting Mn ions (8Mn³⁺ and 2Mn²⁺). The behavior is indicative of strong antiferromagnetic interactions among the paramagnetic metal centers within the cluster. For both complexes, $\chi_M T$ decreases smoothly to 9.64 and 12.06 cm³Kmol⁻¹, respectively, at 5.0 K suggesting ground state spin in the $S = 4$ or 5 region (Figure 4-31). The difference in the $\chi_M T$ values at 5 K between the complexes 4-5 and 4-6 could be due to the effect of intermolecular interactions prevails at a low temperature.

Ac data were collected on microcrystalline samples of **4-5**·2H₂O and **4-6**·H₂O in a 3.5 G ac field oscillating at 1000 Hz and are plotted as $\chi_M' T$ vs. T in Figure 4-32. The extrapolation of in-phase ($\chi_M' T$) signal at ~7.4 and 9.8 cm³Kmol⁻¹ confirms the $S = 4$ ground state spin for both complexes. The downward slope of the $\chi_M' T$ plot in both the complexes indicates the presence of several low-lying excited states coming from weak exchange coupling in Mn²⁺ and/or spin-frustration effects. This feature affects the dc reduced magnetization fit where the saturation of the magnetization could not be achieved at low temperature and high field. As a result, for both complexes, attempts to fit the data resulted in poor quality and unreliable fit and the reasons discussed in detail earlier for complexes **4-1** and **4-2**.

Dc and ac magnetic susceptibility studies of 4-7

Solid-state, variable-temperature dc magnetic susceptibility data in a 0.1 T field and in the 5.0 - 300 K range were collected on powdered microcrystalline samples of **4-7**·1.5C₆H₁₄. The obtained data are plotted as $\chi_M T$ vs. T in Figure 4-33 for **4-7**. The 300 K value is lower than the spin-only ($g = 2$) value of 68.25 cm³Kmol⁻¹ indicative of strong antiferromagnetic interaction and the value corresponds to twenty non-interacting Mn ions (14 Mn³⁺ and 6 Mn²⁺). The $\chi_M T$ reaches a plateau at 20 K and the value decreases down to 28.8 cm³Kmol⁻¹ at 5 K suggesting $S = 7$ ground state spin. Further verification of spin-ground state comes from the reduced magnetization fit. Variable-field (H) and -temperature magnetization (M) data were collected in the 0.1 - 0.8 T and 1.8 - 10 K ranges. The resulting data are plotted as reduced magnetization ($M/N\mu_B$) vs. H/T and the data were fitted using the program MAGNET as explained before. The solid lines in Figure 4-34 (A) are a fit of the experimental data, with the fit parameters $S = 7$, $D = -0.09$ cm⁻¹ and $g = 2.00$. Fitting is fairly good for $D = 0.18$ cm⁻¹ and $g = 1.99$. An alternative fit is obtained with $S = 8$ and $g = 1.76$ where g is too small for a Mn²⁺/Mn³⁺ system and hence this possibility is discarded. In order to ensure that the true global minimum had been obtained and to assess the hardness of the fit, a root-mean-square D vs. g error surface for the fit was generated using the program GRID, which calculates the relative difference between the experimental $M/N\mu_B$ data and those calculated for various combinations of D and g . This is shown as a 2-D contour plot in Figure 4-34 (B). Two local minima were observed. The one at $D = 0.18$ cm⁻¹ exhibits the largest error and is hence discarded. A true global minimum was observed and the

parameter set is shallow and the fit uncertainties are thus estimated as $g = 1.98$ (2), $D = -0.08\text{cm}^{-1}$ (2).

For further confirmation of the spin-ground state in the system, ac susceptibility data were collected on a microcrystalline sample of **4-7**·1.5C₆H₁₄ in a 3.5 G ac field oscillating at 50 - 1000 Hz. The data are plotted as $\chi_M'T$ vs. T in Figure 4-35 over a temperature range spanning 1.8 - 15 K. The extrapolation of the in-phase ($\chi_M'T$) signal ($\sim 28\text{ cm}^3\text{Kmol}^{-1}$) to 0 K confirms the $S = 7$ ground state spin for compound **4-7**. Despite the presence of small anisotropy in the molecule, no significant frequency dependent signal is observed in out-of-phase ac study which indicates that compound **4-7** is not an SMM (Figure 4-35).

Dc and ac magnetic susceptibility studies of 4-8

Solid-state, variable-temperature dc magnetic susceptibility data in a 0.1 T field and in the 5.0 - 300 K range were collected on powdered microcrystalline samples of **4-8**·3H₂O. The obtained data are plotted as $\chi_M T$ vs. T in Figure 4-36 (A) for **4-8**. The $\chi_M T$ at 300 K is $39.67\text{ cm}^3\text{Kmol}^{-1}$, significantly lower than the spin-only ($g = 2$) value of $59.50\text{ cm}^3\text{Kmol}^{-1}$ expected for eighteen non-interacting Mn ions (14 Mn³⁺ and 4 Mn²⁺). This behavior indicates the presence of strong antiferromagnetic interactions among the Mn ions at 300 K. The $\chi_M T$ at 5 K for **4-8** is $7.31\text{ cm}^3\text{Kmol}^{-1}$, suggesting an $S = 4$ ground state spin. Compound **4-8** is structurally similar to **4-7** where two terminal Mn²⁺ (Mn10) ions are replaced by two diamagnetic Ca²⁺ ions. This structural difference causes a notable change in the interactions among the remaining Mn²⁺/Mn³⁺, Mn²⁺/Mn²⁺ and Mn³⁺/Mn³⁺ ions reflecting the extent of the antiferromagnetic interactions among the paramagnetic centers along with the change in spin- ground state. For further

verification of the spin ground state variable-field (H) and -temperature magnetization (M) data were collected in the field ranges to both 0.1 - 1 T and 0.1 - 7 T field in the temperature range spanning 1.8 - 10 K. The resulting data were plotted as reduced magnetization ($M/N\mu_B$) vs. H/T and the data were fitted using the program MAGNET as explained before. Both possible solutions are discarded due to unreasonable D values (both positive and negative) assuming either $S = 4$ or $S = 3$ spin ground state. This can be attributed to the presence of low-lying excited states as a result of weak interactions and/or spin frustration effects, which is evident from the in-phase ac study.

For confirmation of spin-ground state, ac susceptibility data were collected on a microcrystalline sample of **4-8**·3H₂O in a 3.5 G ac field oscillating at 50 - 1000 Hz. The data are plotted as $\chi_M'T$ vs. T in Figure 4-36 (B) at the temperature range spanning 1.8 - 15 K. The $\chi_M'T$ value at 15 K is 11.54 cm³Kmol⁻¹ which then decreases sharply down to 5.94 cm³Kmol⁻¹ at 1.8 K which is indicative of the depopulation of excited states of higher spin-ground state values. The feature also suggests the presence of a large number of low-lying excited states close to the ground state. This feature makes it difficult to extrapolate the ac in-phase data to 0 K to rationalize the spin-ground state, however, a reasonable attempt justifies an $S = 4$ spin state for a value of ~ 7.0 cm³Kmol⁻¹ at 0 K.

Concluding Remarks

The present work provides an ensemble of various nuclearity oxide, carboxylate rich Mn_x and Mn/Ca clusters ($x = 3, 4, 6, 10, 20$) containing edteH₄ ligand. The crystal structures, syntheses and magnetic properties of all these complexes have been discussed. This work once again proves the ability of the edteH₄ ligand to bridge to

many metal ions, e.g. one edte⁴⁻ ligand links to six metal ions in **4-5/4-6**. Mn₁₈Ca₂ is the highest nuclearity Mn/Ca cluster known to date and this establishes the gateway of making polynuclear Mn/Ca clusters relevant to WOC in photosystem II in bio-inorganic research. This outcome opens up the possibility of isolating new higher nuclearity Mn clusters in polynuclear metal chemistry, perhaps mixed-metal chemistry and will be explored in the following chapters. The current study shows the possibility of analyzing a new mixed-chelate system using both the edteH₄ and hmpH ligands together for the first time in Mn cluster chemistry.

Table 4-1. Crystallographic data for **4-1**·4CH₂Cl₂, **4-2**·MeCN, and **4-3**

parameter	4-1	4-2	4-3
formula	C ₃₀ H ₆₁ Cl ₈ Mn ₃ N ₄ O ₁₄	C ₂₄ H ₅₀ ClMn ₃ N ₄ O ₁₆	C ₃₂ H ₅₂ Cl ₆ Mn ₅ N ₆ O ₁₀
fw, g/mol	1150.25	850.95	1168.2
crystal system	Triclinic	Monoclinic	Monoclinic
space group	P-1	P2(1)/n	C2/c
a, Å	11.571(2)	15.762(4)	26.757(2)
b, Å	13.783(2)	14.032(4)	10.7825(9)
c, Å	17.330(3)	17.582(5)	15.7930(13)
α, β, γ, °	89.845(3) 88.967(3) 65.826(3)	90 113.187(4) 90	90 91.931(2) 90
V, Å ³	2521.0(8)	3574.7(16)	4553.9(6)
Z	2	4	8
T, K	173(2)	100(2) K	173(2)
radiation, Åa	0.71073	0.71073	0.71073
ρ, g/cm ³	1.515	1.581	1.704
μ, mm ⁻¹	1.222	1.191	1.758
R1b,c	0.0641	0.0372	0.0419
wR2d	0.1642	0.0979	0.1144

^a Graphite monochromator. ^b $I > 2\sigma(I)$. ^c $R1 = \sum(|F_o| - |F_c|) / \sum|F_o|$. ^d $wR2 = [\sum[w(F_o^2 - F_c^2)^2] / \sum[w(F_o^2)^2]]^{1/2}$, $w = 1/[\sigma^2(F_o^2) + [(ap)^2 + bp]$, where $p = [\max(F_o^2, 0) + 2F_c^2]/3$

Table 4-2. Crystallographic data for **4-4**, **4-5·2MeCN** and **4-6·2MeCN**

parameter	4-4	4-5	4-6
Formula	C ₅₀ H ₉₄ Mn ₆ N ₁₀ O ₂₂	C ₅₀ H ₉₄ Mn ₁₀ N ₂₆ Na ₂ O ₂₈	C ₅₈ H _{117.50} Mn ₁₀ N _{27.50} O _{25.50}
fw, g/mol	1517.0	2102.9	2157.70
crystal system	Monoclinic	Triclinic	Triclinic
space group	C2/c	P-1	P-1
a, Å	23.5084(17)	12.682(2)	13.058(3)
b, Å	14.4661(11)	12.716(2)	16.551(3)
c, Å	20.2570(15)	14.595(3)	22.339(5)
α, β, γ, °	90 104.264(5) 90	90.132(4) 96.501(3) 115.491(3)	82.451(4) 82.488(7) 66.784(7)
V, Å ³	6676.5(9)	2107.5(7)	4382.3(16)
Z	8	2	2
T, K	100(2) K	173(2)	100(2) K
radiation, Åa	0.71073	0.71073	0.71073
ρ, g/cm ³	1.509	1.657	1.635
μ, mm ⁻¹	9.620	1.541	1.474
R1b,c	0.0530	0.0417	0.0403
wR2d	0.1124	0.1107	0.0896

^a Graphite monochromator. ^b $I > 2\sigma(I)$. ^c $R1 = \sum(|F_o| - |F_c|) / \sum|F_o|$. ^d $wR2 = [\sum[w(F_o^2 - F_c^2)^2] / \sum[w(F_o^2)^2]]^{1/2}$, $w = 1/[\sigma^2(F_o^2) + [(ap)^2 + bp]$, where $p = [\max(F_o^2, O) + 2F_c^2]/3$

Table 4-3. Crystallographic data for **4-7** and **4-8**

parameter	4-7 ·x(solv)	4-8 ·5MeCN
formula	C ₇₈ H ₁₅₈ Cl ₄ Mn ₂₀ N ₁₂ O ₆₆	C ₈₅ H ₁₇₀ Ca ₂ Mn ₁₈ N ₁₆ O ₅₉
fw, g/mol	3560.76	3429.45
crystal system	monoclinic	monoclinic
space group	P2(1)/c	P2(1)/c
a, Å	17.5303(16)	21.56(2)
b, Å	25.922(2)	26.62(3)
c, Å	16.2321(15)	26.78(3)
α, β, γ, °	90, 103.134(2), 90	90, 107.625(18), 90
V, Å ³	7183.3(11)	14648(26)
Z	4	4
T, K	173(2)	100(2)
radiation, Å ^a	0.71073	0.71073
ρ, g/cm ³	1.646	1.555
μ, mm ⁻¹	1.851	1.645
R1 ^{b,c}	0.0620	0.0768
wR2 ^d	0.1867	0.2023

^a Graphite monochromator. ^b $I > 2\sigma(I)$. ^c $R1 = \sum(|F_o| - |F_c|) / \sum|F_o|$. ^d $wR2 = [\sum[w(F_o^2 - F_c^2)^2] / \sum[w(F_o^2)^2]]^{1/2}$, $w = 1/[\sigma^2(F_o^2) + [(ap)^2 + bp]$, where $p = [\max(F_o^2, 0) + 2F_c^2]/3$

Table 4-4. Bond-valence sums for the Mn atoms of complexes **4-1**, **4-2**^a

Atoms	4-1			4-2		
	Mn ²⁺	Mn ³⁺	Mn ⁴⁺	Mn ²⁺	Mn ³⁺	Mn ⁴⁺
Mn1	3.43	3.16	3.10	1.62	1.51	1.48
Mn2	1.96	1.82	1.78	3.40	3.14	3.08

^a The underlined value is the one closest to the charge for which it was calculated. The oxidation state of a particular atom can be taken as the nearest whole number to the underlined value

Table 4-5. Bond-valence sums for the Mn atoms of complexes **4-3**, **4-4**^a

Atoms	4-3			4-4		
	Mn ²⁺	Mn ³⁺	Mn ⁴⁺	Mn ²⁺	Mn ³⁺	Mn ⁴⁺
Mn1	2.04	1.90	1.91	3.14	2.93	2.86
Mn2	3.33	3.11	3.05	3.44	3.21	3.13
Mn3	2.08	2.14	2.08	3.46	3.19	3.13

^a See the footnotes to Table 4-4Table 4-6. Bond-valence sums for the Mn atoms of complexes **4-5**, **4-6**^a

Atom	4-5			4-6		
	Mn ²⁺	Mn ³⁺	Mn ⁴⁺	Mn ²⁺	Mn ³⁺	Mn ⁴⁺
Mn1	2.03	1.89	1.85	2.02	1.88	1.84
Mn2	3.36	3.09	3.04	3.29	3.09	3.00
Mn3	3.44	3.17	3.11	3.35	3.09	3.03
Mn4	3.36	3.14	3.06	3.31	3.05	2.99
Mn5	3.28	3.09	3.06	3.33	3.10	3.03

^a See the footnotes to Table 4-4Table 4-7. Bond-valence sums for the Mn atoms of complex **4-7** and **4-8**^a

Atom	4-7			4-8		
	Mn ²⁺	Mn ³⁺	Mn ⁴⁺	Mn ²⁺	Mn ³⁺	Mn ⁴⁺
Mn1	3.34	<u>3.09</u>	3.03	3.39	<u>3.13</u>	3.07
Mn2	<u>1.92</u>	1.80	1.75	3.36	<u>3.10</u>	3.04
Mn3	<u>3.24</u>	<u>2.99</u>	2.94	<u>1.99</u>	1.86	1.81
Mn4	3.18	<u>2.93</u>	2.87	3.28	<u>3.15</u>	2.97
Mn5	<u>2.06</u>	1.90	1.86	3.15	<u>2.94</u>	2.87
Mn6	3.37	<u>3.11</u>	3.06	2.81	<u>2.59</u>	2.54
Mn7	3.54	<u>3.10</u>	3.04	3.33	<u>3.07</u>	3.01
Mn8	3.30	<u>3.08</u>	3.00	2.81	<u>2.60</u>	2.54
Mn9	3.14	<u>2.93</u>	2.86	3.20	<u>2.98</u>	2.91
Mn10	<u>2.28</u>	2.11	2.07	3.02	<u>2.82</u>	2.75
Mn11				<u>2.34</u>	2.19	2.15
Mn12				3.32	<u>3.06</u>	3.00
Mn13				<u>2.38</u>	2.19	2.15
Mn14				3.45	<u>2.87</u>	2.80
Mn15				3.28	<u>3.03</u>	2.97
Mn16				3.39	<u>3.13</u>	3.07
Mn17				1.95	1.82	1.79
Mn18				3.16	<u>2.92</u>	2.86

^a See the footnotes to Table 4-4

Table 4-8. Bond-valence sums for the O atoms of complexes **4-1** and **4-2**^a

Compound	Atom	BVS	Assignment	Group
4-1	O1	1.82	OR ⁻	edteH ₂ ²⁻
	O2	1.13	ROH	edteH ₂ ²⁻
	O3	1.97	OR ⁻	edteH ₂ ²⁻
	O4	1.18	ROH	edteH ₂ ²⁻
4-2	O1	1.15	ROH	edteH ₂ ²⁻
	O2	1.12	ROH	edteH ₂ ²⁻
	O3	1.92	OR ⁻	edteH ₂ ²⁻
	O6	1.81	OR ⁻	edteH ₂ ²⁻

^aThe BVS values for O atoms of O²⁻, ROH and H₂O groups are typically 1.8 - 2.0, 1.0 - 1.2 and 0.2 - 0.4, respectively, but can be affected somewhat by hydrogen-bonding.

Table 4-9. Bond-valence sums for the O atoms of complexes **4-3** and **4-4**^a

Compound	Atom	BVS	Assignment	Group
4-3	O1	1.12	ROH	edteH ₂ ²⁻
	O2	1.94	OR ⁻	edteH ₂ ²⁻
	O3	1.19	ROH	edteH ₂ ²⁻
	O4	1.98	OR ⁻	edteH ₂ ²⁻
	O5	1.95	OR ⁻	hmp ⁻
4-4	O1	2.06	O ²⁻	O ²⁻
	O8	1.79	OR ⁻	edteH ³⁻
	O9	1.77	OR ⁻	edteH ³⁻
	O10	2.03	OR ⁻	edteH ³⁻
	O11	0.88	ROH	edteH ³⁻

^a See the footnotes to Table 4-8

Table 4-10. Bond-valence sums for the O atoms of complexes **4-5** and **4-6**^a

Compound	Atom	BVS	Assignment	Group
4-5	O1	2.35	OR ⁻	edte ⁴⁻
	O2	1.93	OR ⁻	edte ⁴⁻
	O3	1.93	OR ⁻	edte ⁴⁻
	O4	1.97	OR ⁻	edte ⁴⁻
	O7	2.05	OR ⁻	OMe ⁻
	O13	1.87	O ²⁻	O ²⁻
4-6	O14	2.13	O ²⁻	O ²⁻
	O1	1.94	OR ⁻	edte ⁴⁻
	O2	1.89	OR ⁻	edte ⁴⁻
	O3	1.93	OR ⁻	edte ⁴⁻
	O10	1.89	OR ⁻	edte ⁴⁻
	O11	1.89	O ²⁻	O ²⁻
	O12	1.92	O ²⁻	O ²⁻
	O13	1.00	OH ⁻	OH ⁻

^a See the footnotes to Table 4-8Table 4-11. Bond-valence sums for the O atoms of complex **4-7**^a

Compound	Atom	BVS	Assignment	Group
4-7	O1	1.13	OH ⁻	OH ⁻
	O2	1.85	O ²⁻	O ²⁻
	O3	1.15	OH ⁻	OH ⁻
	O4	2.16	O ²⁻	O ²⁻
	O5	1.84	O ²⁻	O ²⁻
	O6	1.84	O ²⁻	O ²⁻
	O7	1.11	OH ⁻	OH ⁻
	O8	2.00	OR ⁻	edte ⁴⁻
	O9	1.96	OR ⁻	edte ⁴⁻
	O10	1.91	OR ⁻	edte ⁴⁻
	O11	1.97	OR ⁻	edte ⁴⁻
	O12	1.72	OR ⁻	edteH ³⁻
	O13	1.88	OR ⁻	edteH ³⁻
	O14	1.97	OR ⁻	edteH ³⁻
	O15	0.97	ROH	edteH ³⁻
	O16	1.83	OR ⁻	edte ⁴⁻
	O17	1.91	OR ⁻	edte ⁴⁻
	O18	1.83	OR ⁻	edte ⁴⁻
	O19	1.97	OR ⁻	edte ⁴⁻

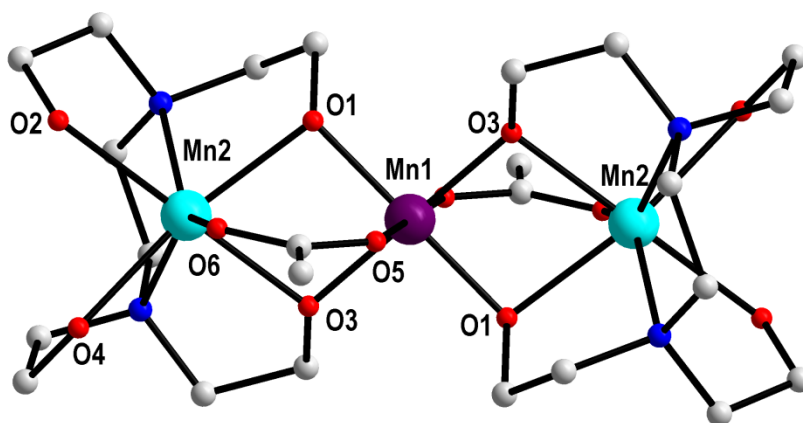
^a See the footnotes to Table 4-8

Table 4-12. Bond-valence sums for the O atoms of complex **4-8**^a

Compound	Atom	BVS	Assignment	Group
4-8	O1	1.85	O ²⁻	O ²⁻
	O2	1.92	O ²⁻	O ²⁻
	O5	1.91	OR ⁻	edte ⁴⁻
	O6	1.91	OR ⁻	edte ⁴⁻
	O7	1.93	OR ⁻	edte ⁴⁻
	O8	1.89	OR ⁻	edte ⁴⁻
	O9	1.50	OR ⁻	edte ⁴⁻
	O12	2.12	OR ⁻	edte ⁴⁻
	O13	1.80	OR ⁻	edte ⁴⁻
	O14	1.18	OH ⁻	OH ⁻
	O15	1.83	O ²⁻	O ²⁻
	O16	1.19	OH ⁻	OH ⁻
	O17	1.81	O ²⁻	O ²⁻
	O31	1.73	O ²⁻	O ²⁻
	O32	1.14	OH ⁻	OH ⁻
	O33	1.17	OH ⁻	OH ⁻
	O34	2.02	OR ⁻	edte ⁴⁻
	O36	1.57	OR ⁻	edte ⁴⁻
	O37	1.79	O ²⁻	O ²⁻
	O38	2.03	OR ⁻	edte ⁴⁻
O45	1.92	OR ⁻	edte ⁴⁻	
O46	1.94	OR ⁻	edte ⁴⁻	
O47	1.83	O ²⁻	O ²⁻	
O48	1.89	O ²⁻	O ²⁻	

^a See the footnotes to Table 4-8

A



B

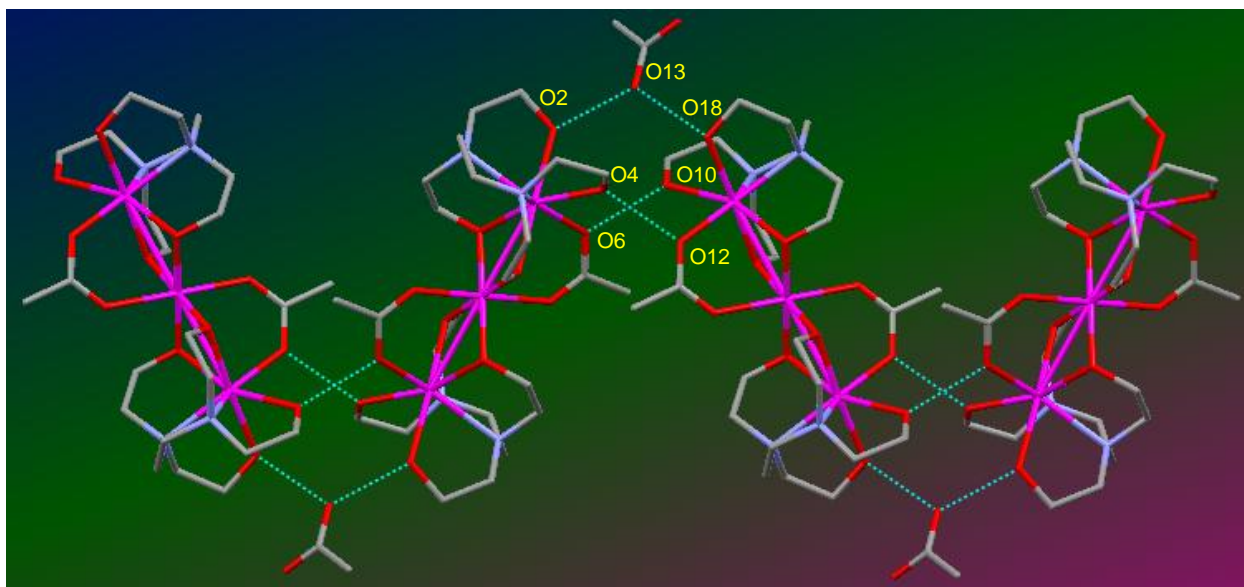


Figure 4-1. Labeled representation of the cation of complex **4-1** (A). Hydrogen atoms have been omitted for clarity. A section of the 1D polymeric chain (B) of complex **4-1** where the two Mn_3 units in a chain are connected through a MeCO_2^- group by H-bonds (shown as dashed lines). Color code: Mn^{3+} , purple; Mn^{2+} , cyan; O, red; N, blue; C, light-grey.

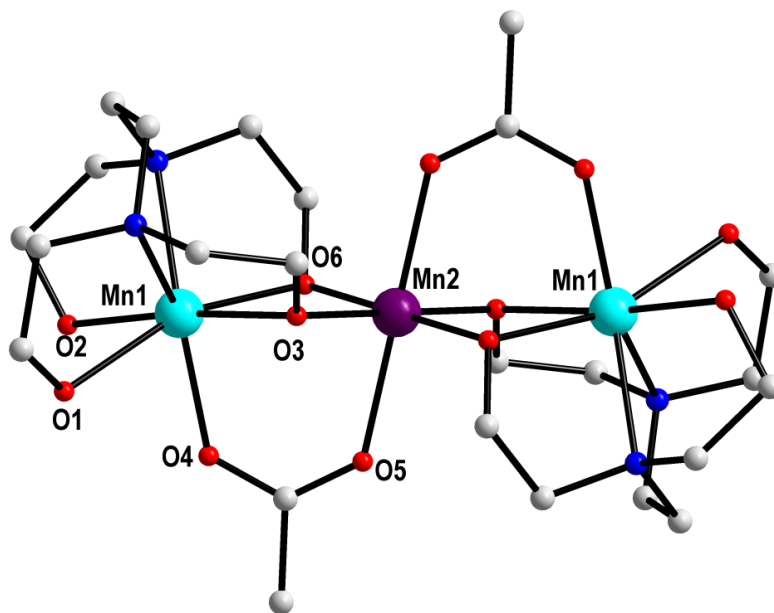


Figure 4-2. Labeled representation of the cation of complex **4-2**. Hydrogen atoms have been omitted for clarity. Color code: Mn^{3+} , purple; Mn^{2+} , cyan; O, red; N, blue; C, light-grey.

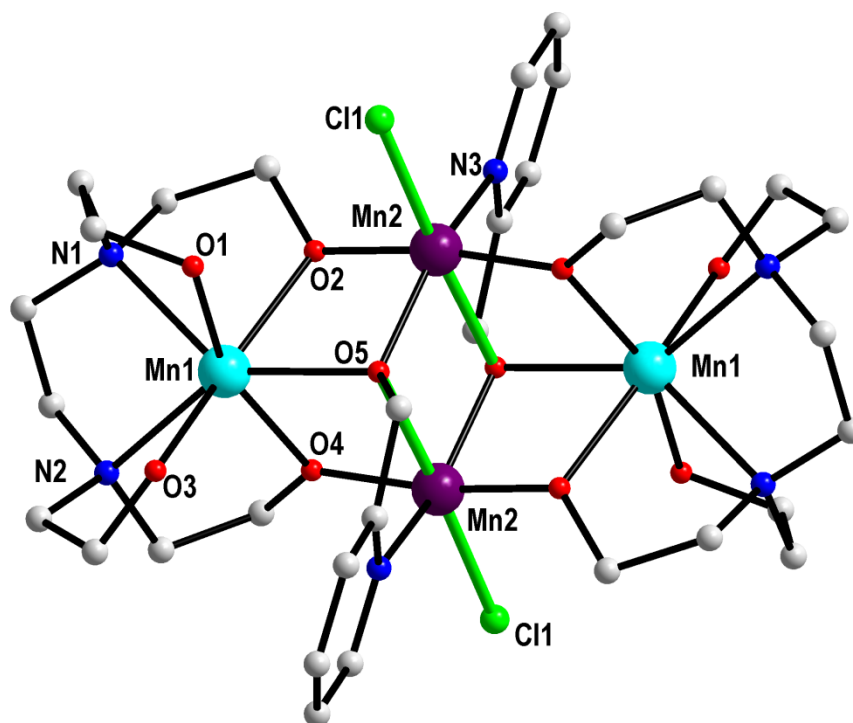
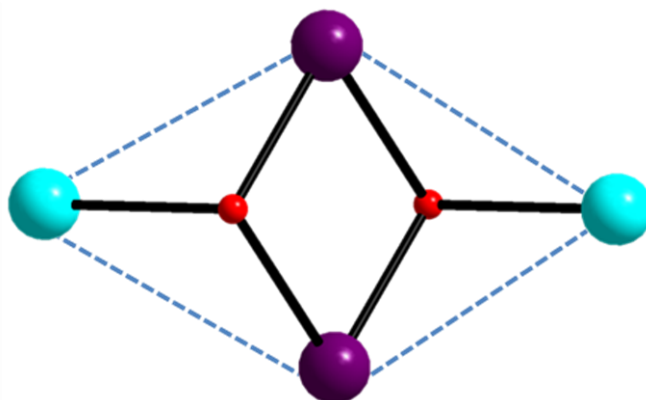


Figure 4-3. Labeled representation of the cation of complex **4-3** with Jahn–Teller elongation axes shown as green thick lines. Hydrogen atoms have been omitted for clarity. Color code: Mn^{3+} , purple; Mn^{2+} , cyan; O, red; N, blue; Cl, green; C, light-grey.

A



B

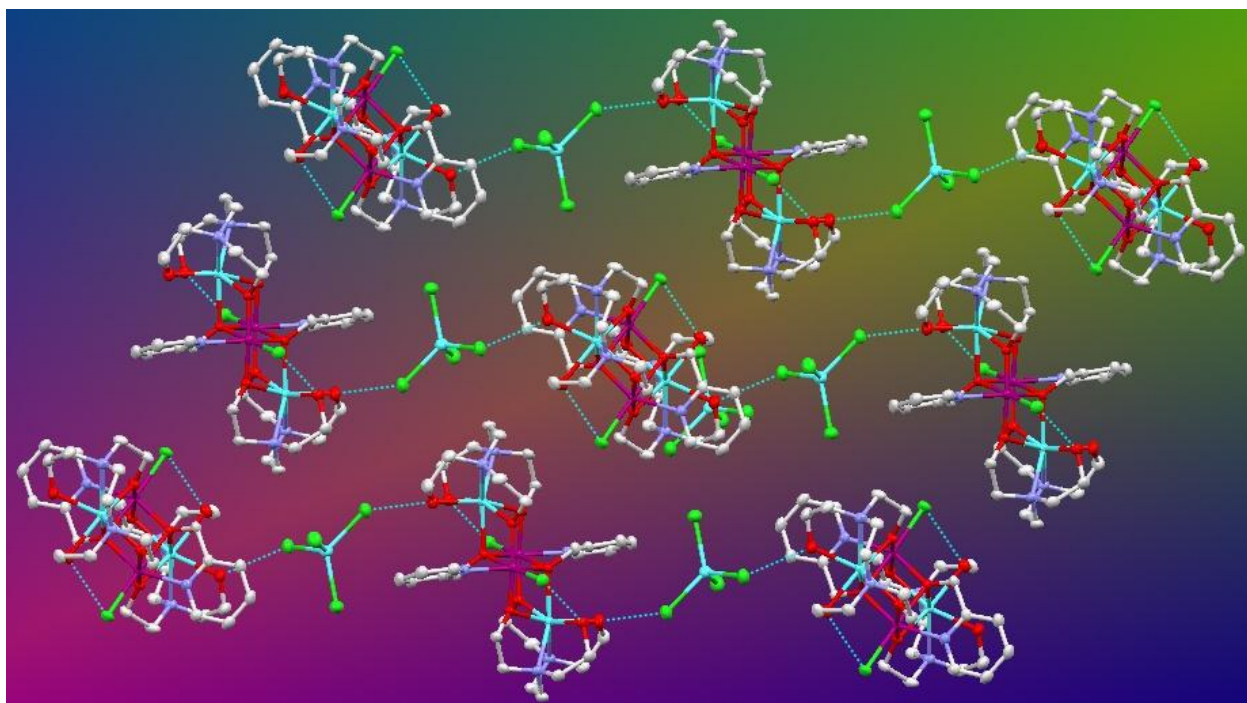
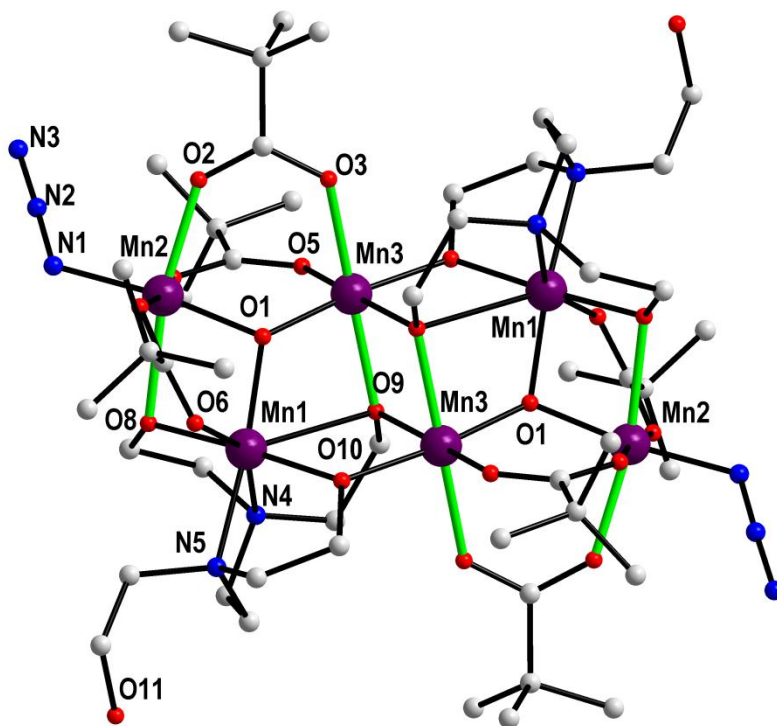
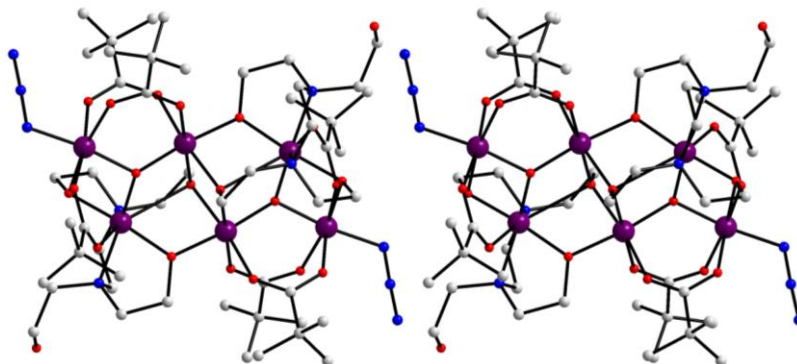


Figure 4-4. The core of complex **4-3** (A). Hydrogen atoms have been omitted for clarity. A section of the 1D polymeric chains of complex **4-3** where the two Mn_4 units in a chain are connected through a MnCl_4^{2-} group via H-bonds (shown as dashed lines) (B). Color code: Mn^{3+} , purple; Mn^{2+} , cyan; O, red; N, blue; Cl, green; C, light-grey.

A



B



C

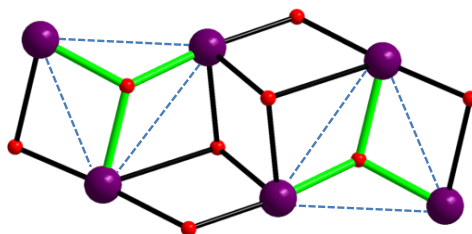
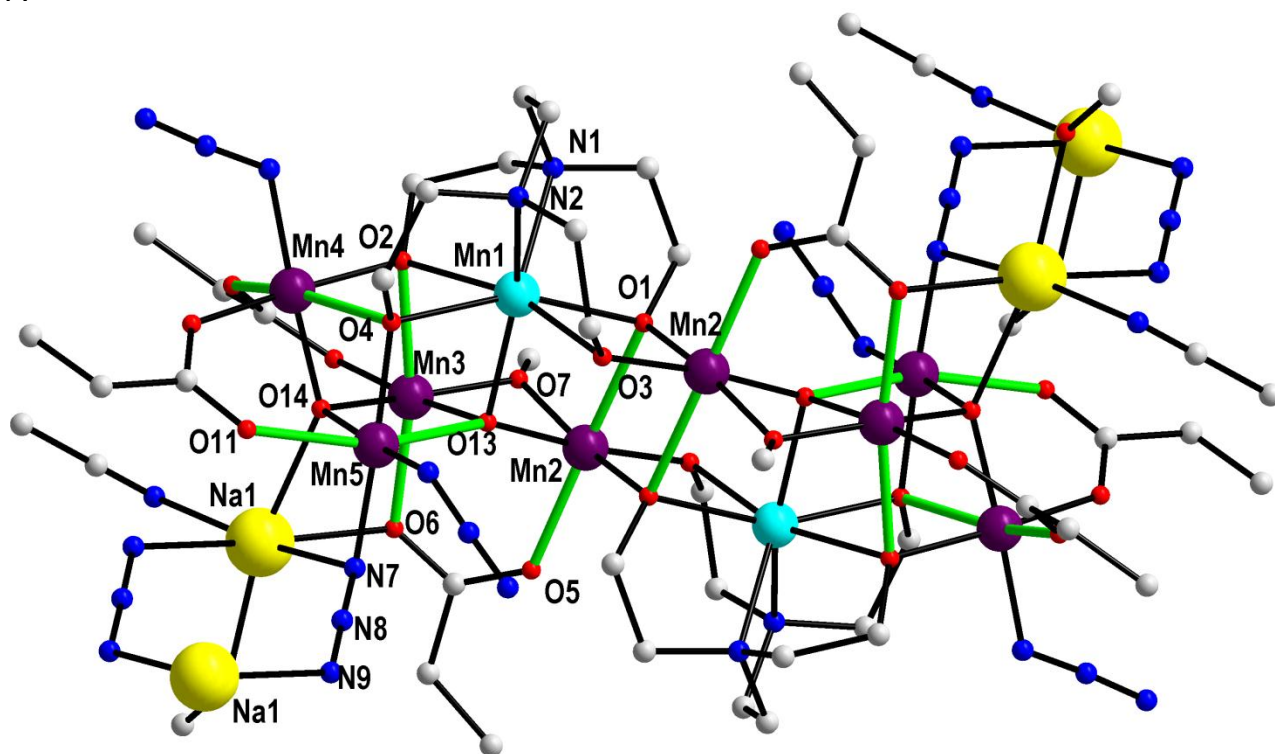


Figure 4-5. The labeled representation of complex **4-4** with Jahn-Teller axes shown as green thick lines (A), a stereoview (B) and the core (C) of complex **4-4**. H atoms have been removed for clarity. Color code: Mn³⁺, purple; O, red; N, blue; C, light-grey.

A



B

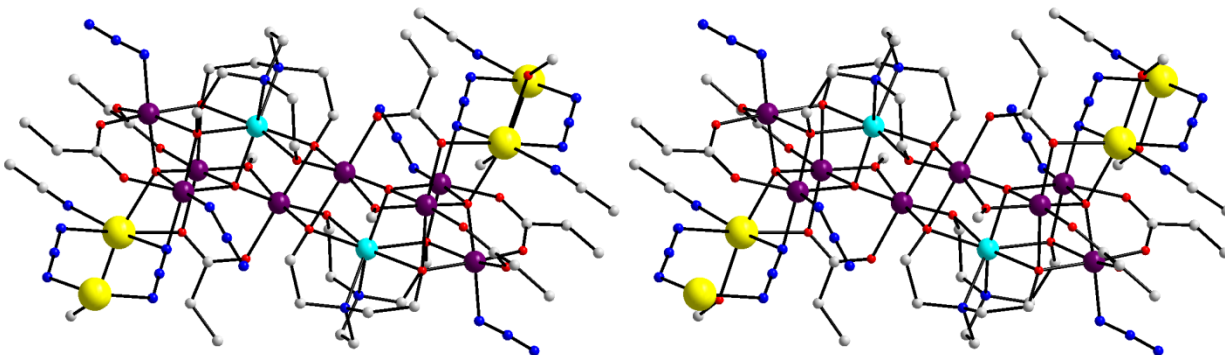
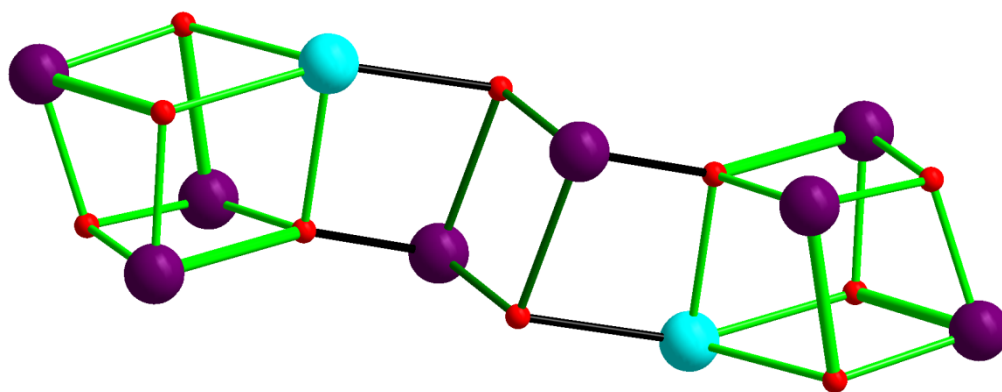


Figure 4-6. Labeled representation of the part of $(\text{Na}_2\text{Mn}_{10})_\infty$ polymer, **4-5** with Jahn–Teller elongation axes as green thick lines (A) and a stereopair (B). Hydrogen atoms have been omitted for clarity. Color code: Mn^{3+} , purple; Mn^{2+} , cyan; Na, yellow; O, red; N, blue; C, light-grey.

A



B

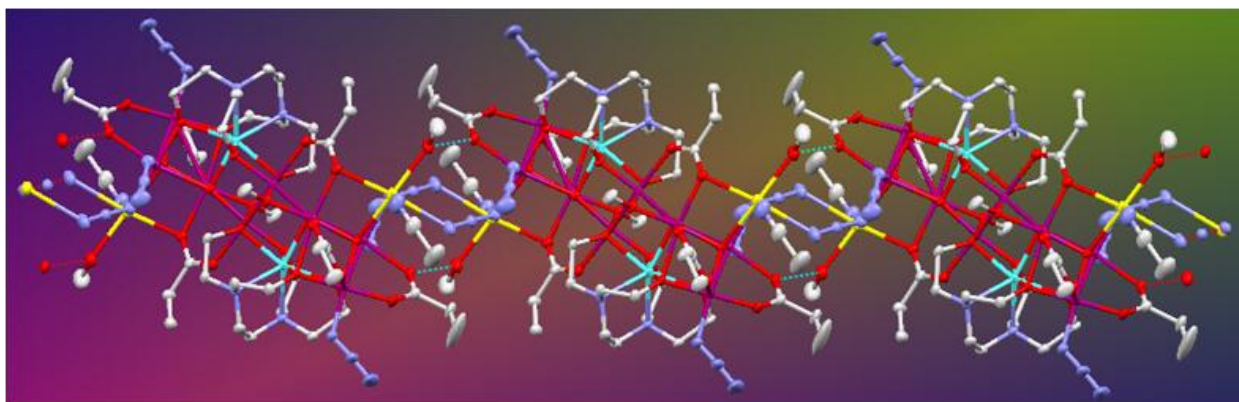
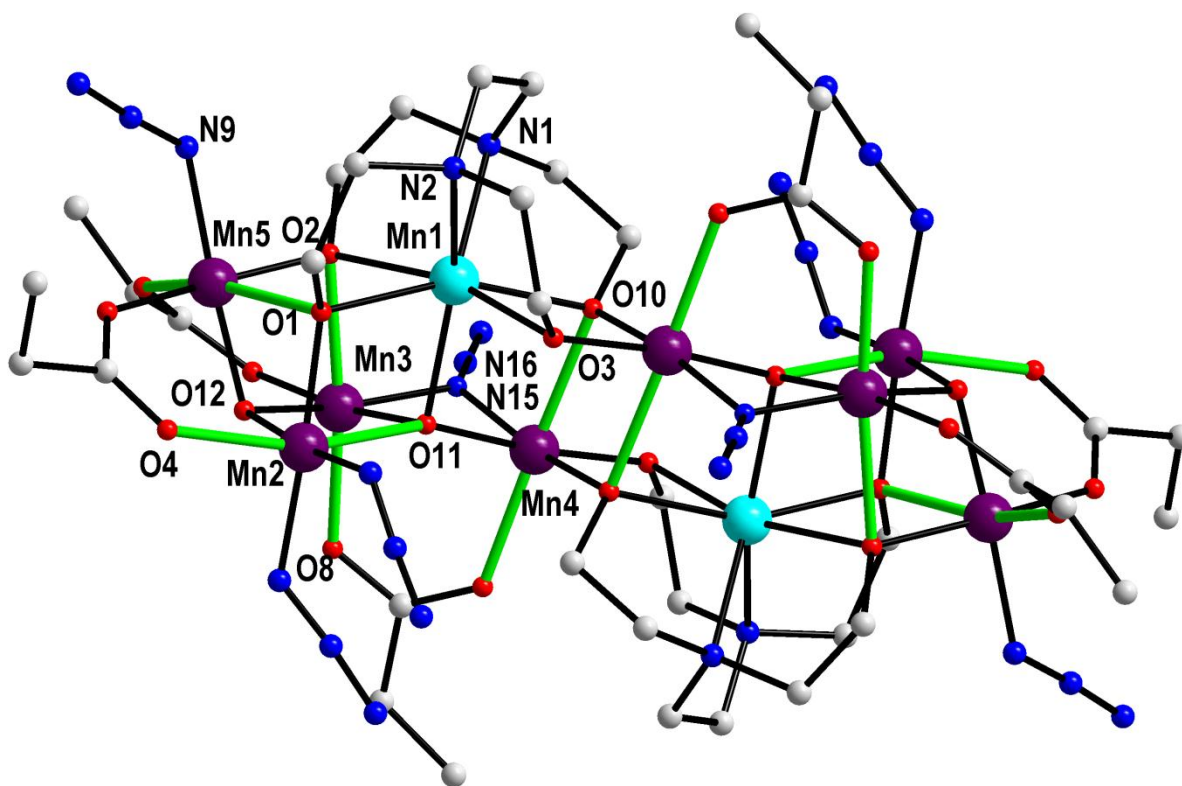


Figure 4-7. The core of complex **4-5** (A) and a section of the 1D polymeric chain of complex **4-5** (B). Color code: Mn^{3+} , purple; Mn^{2+} , cyan; Na, yellow; O, red; N, blue; C, light-grey.

A



B

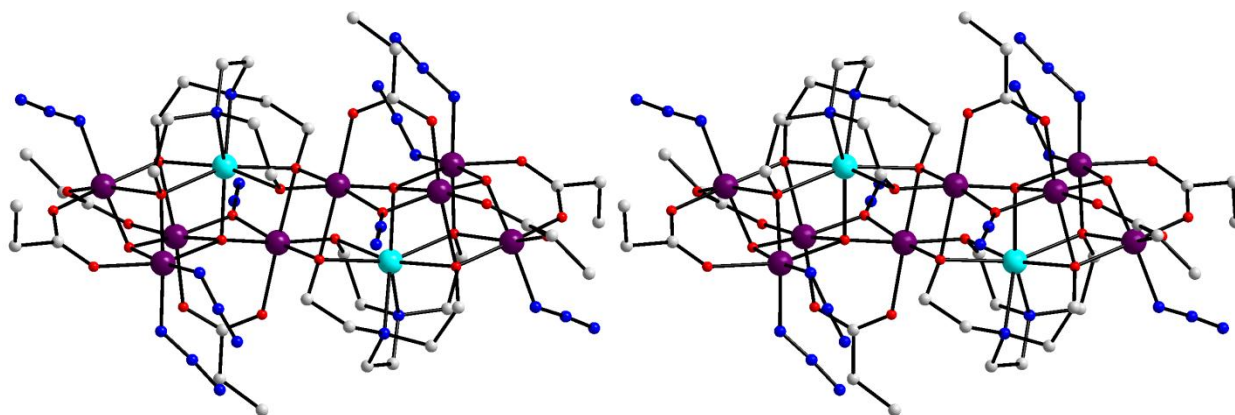


Figure 4-8. Labeled representation of the cation of complex **4-6** with Jahn–Teller elongation axes shown as green thick lines (A) and a stereopair (B). Hydrogen atoms have been omitted for clarity. Color code: Mn^{3+} , purple; Mn^{2+} , cyan; Na, yellow; O, red; N, blue; C, light-grey.

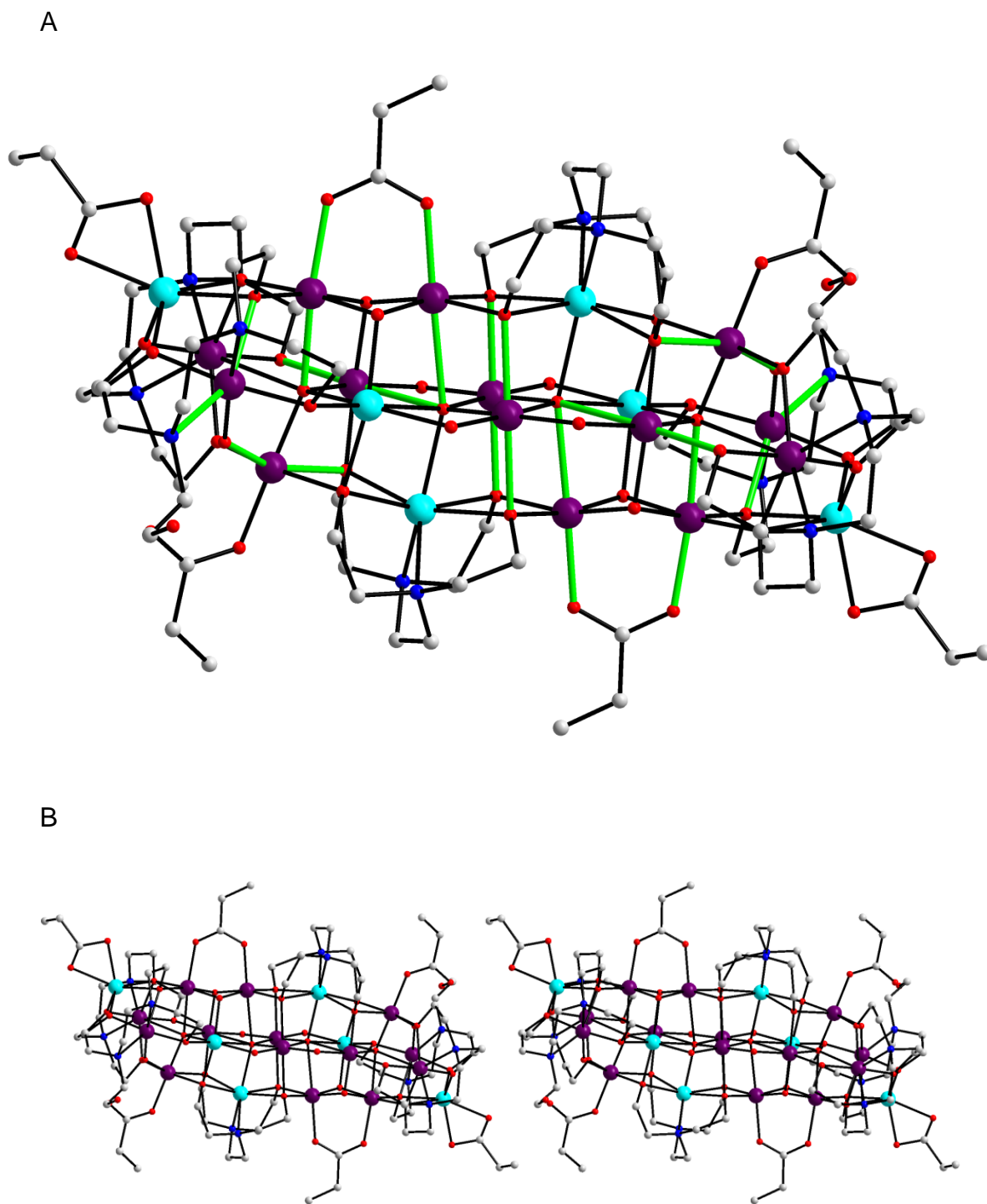


Figure 4-9. Structural representation of the cation of complex **4-7** with Jahn -Teller elongation axes shown as green thick lines (A) and a stereopair (B). Hydrogen atoms have been omitted for clarity. Color code: Mn³⁺, purple; Mn²⁺, cyan; O, red; N, blue; C, light-grey.

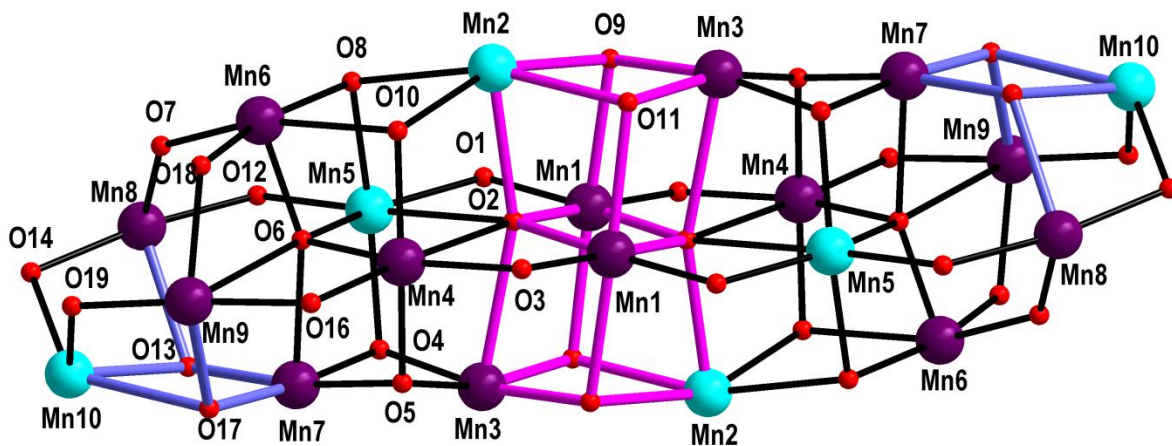


Figure 4-10. Labeled representation of the core of complex 4-7.

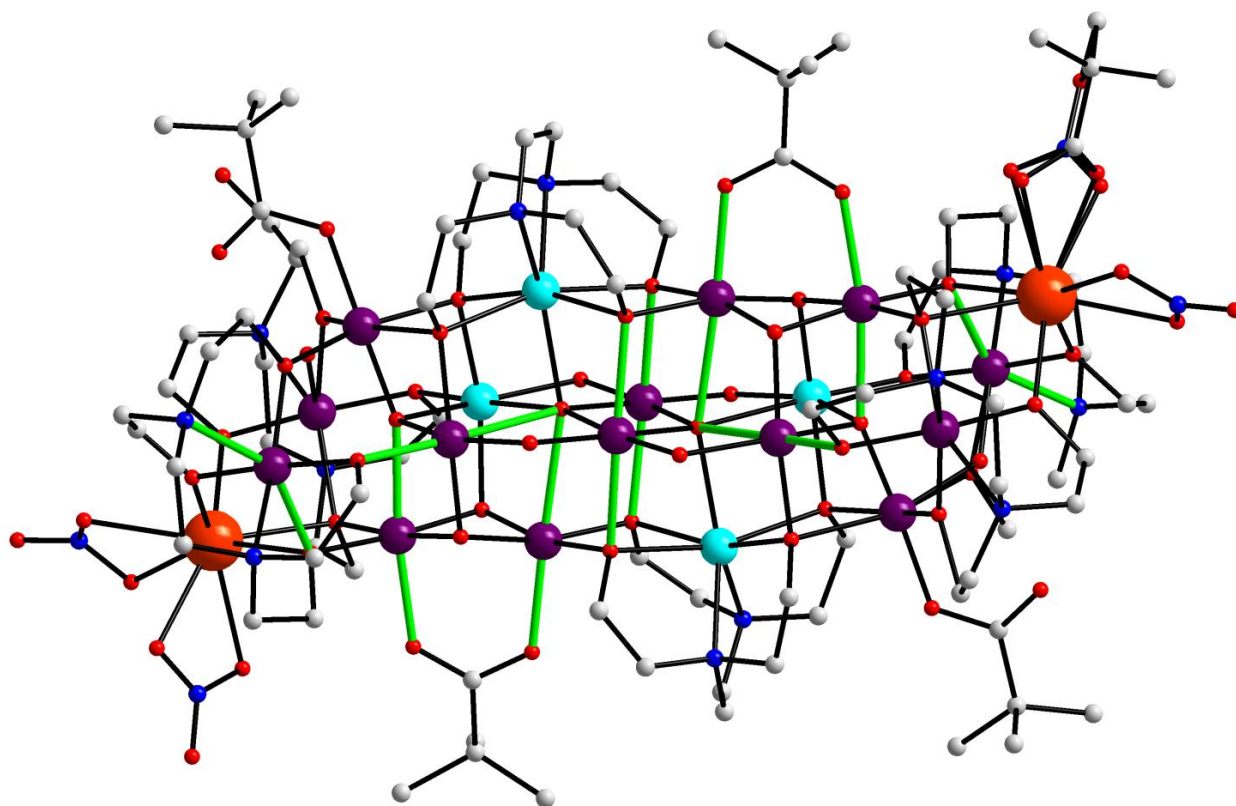


Figure 4-11. Structural representation of the cation of complex 4-8 with Jahn-Teller elongation axes shown as green thick lines. Hydrogen atoms have been omitted for clarity. Color code: Mn^{3+} , purple; Mn^{2+} , cyan; Ca^{2+} , orange; O, red; N, blue; C, light-grey.

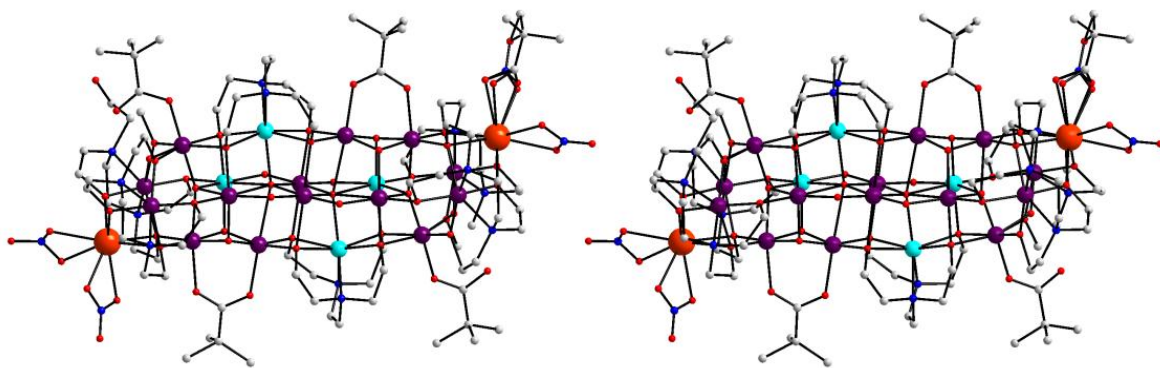


Figure 4-12. Structural representation of the stereopair of complex **4-8**.

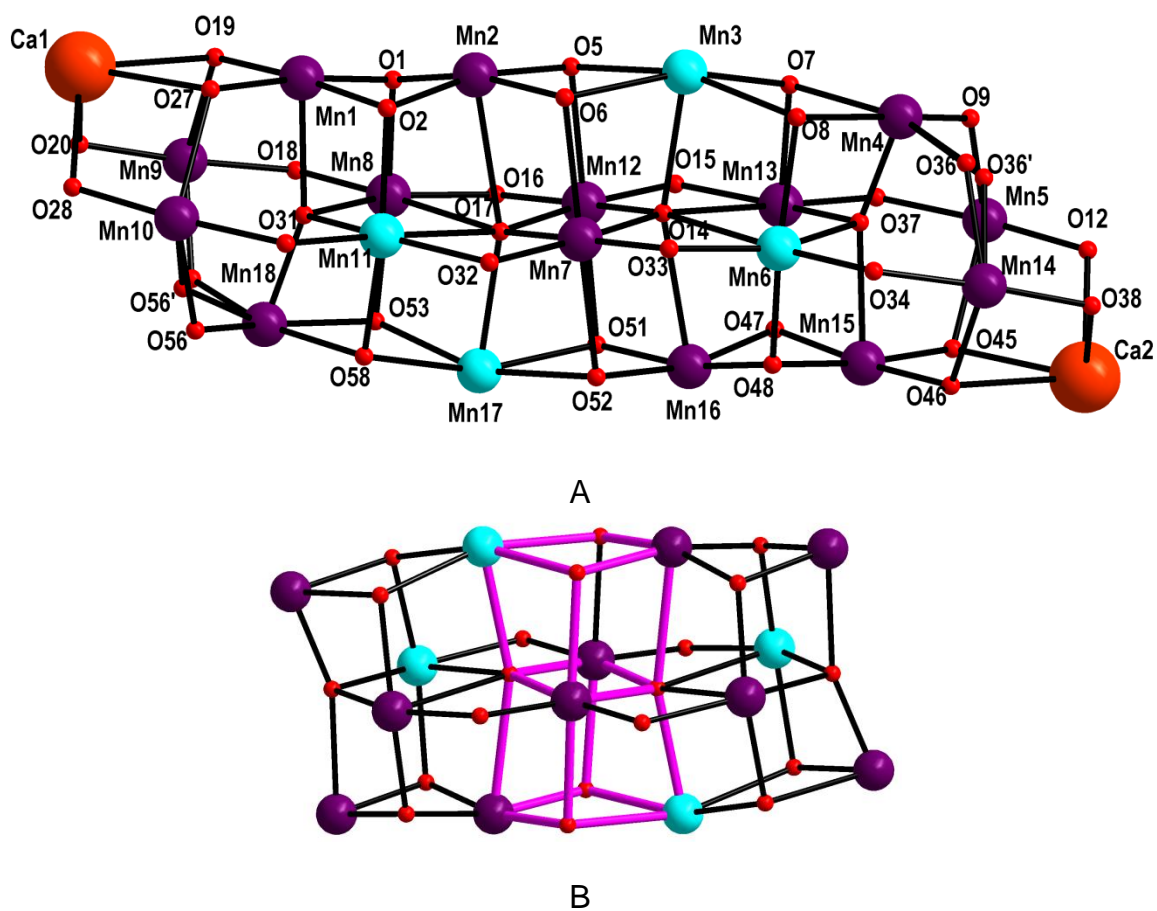


Figure 4-13. Labeled representation of the core of complex **4-8** (A) and a part of the core of complex **4-8** (B).

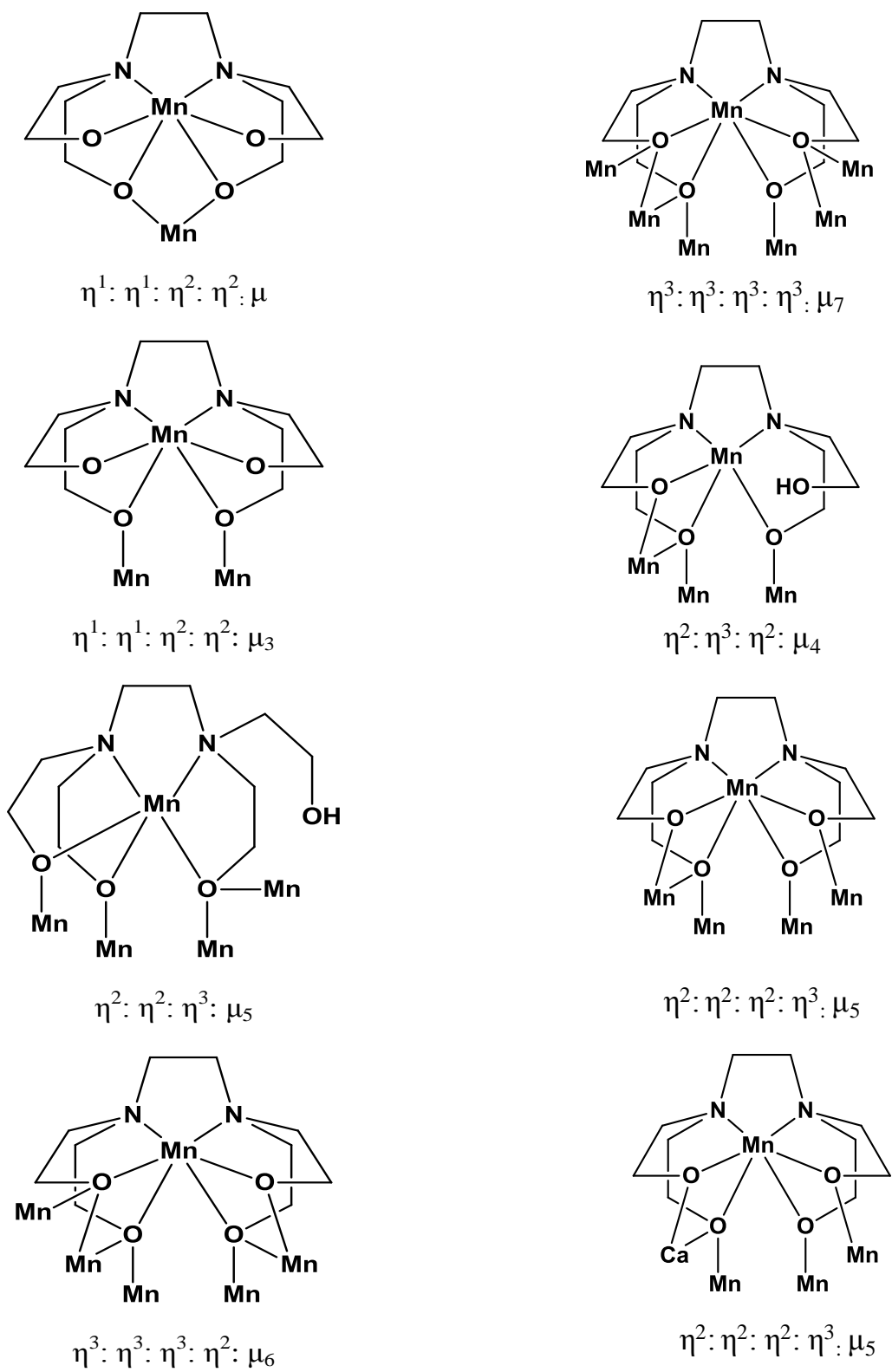


Figure 4-14. Coordination modes of edteH_2^{2-} , edteH^{3-} and edte^{4-} in complexes 4-1 to 4-8.

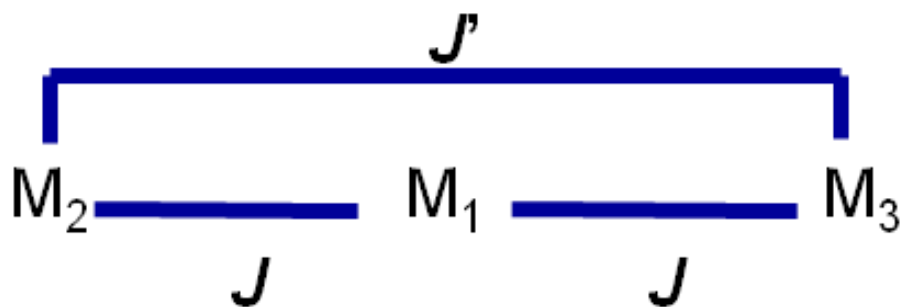


Figure 4-15. Schematic diagram for the linear Mn_3 core for complexes **4-1** and **4-2** with two exchange coupling parameters, J and J'

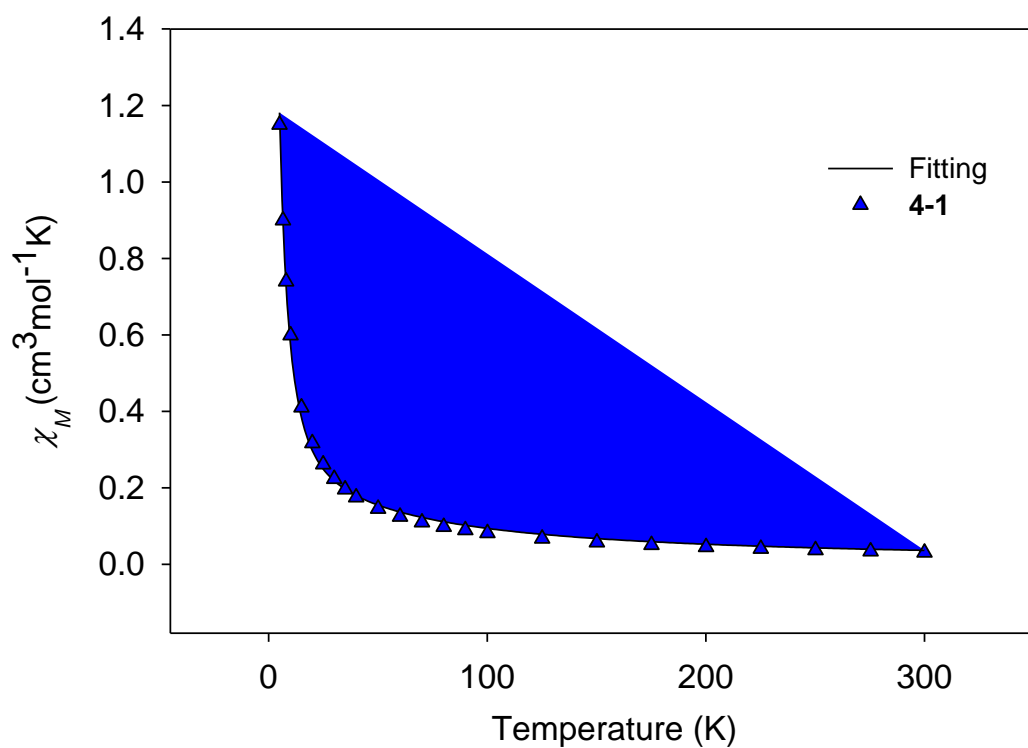


Figure 4-16. Plot of χ_M vs. T for complex **4-1**· H_2O where solid line shows the fit to the experimental data. See the text for the fitting parameters.

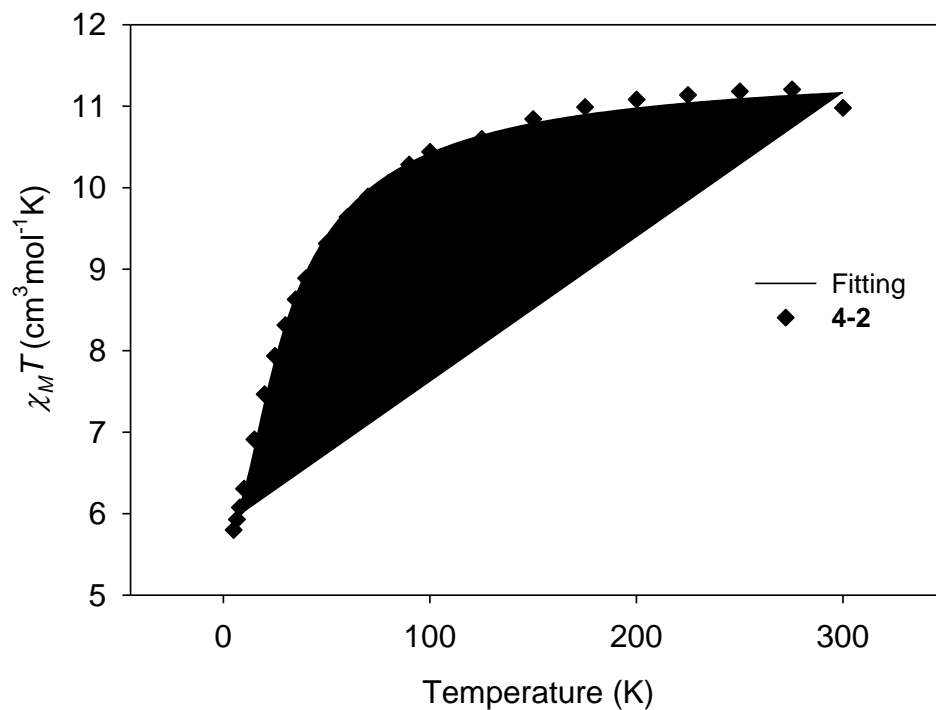


Figure 4-17. Plot of $\chi_M T$ vs. T for complex **4-2**·H₂O where solid line shows the fit to the experimental data. See the text for the fitting parameters.

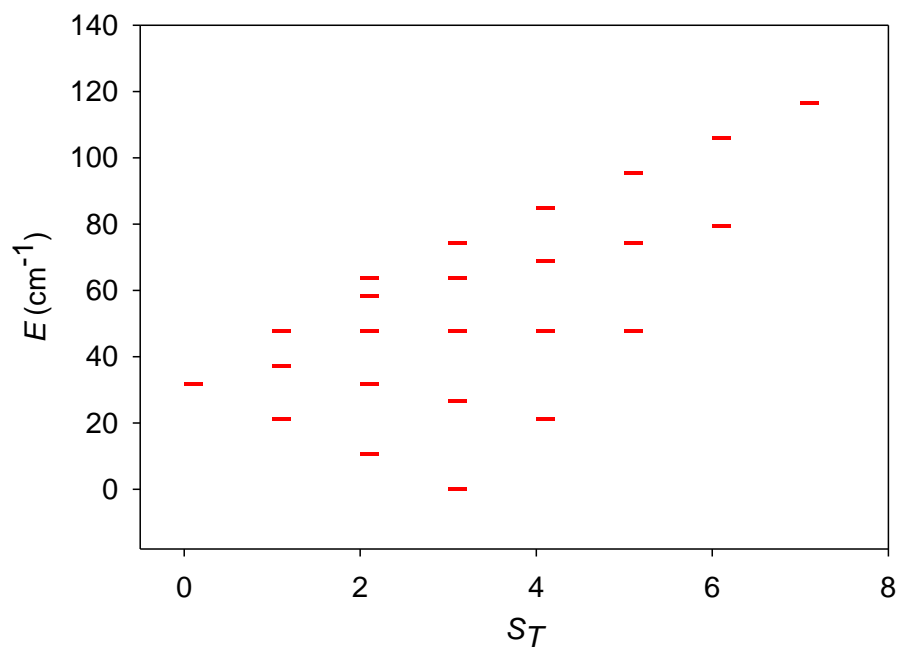


Figure 4-18. Plot of all possible energy states for complex **4-1** using the J value, obtained from the fit to the experimental χ_M data.

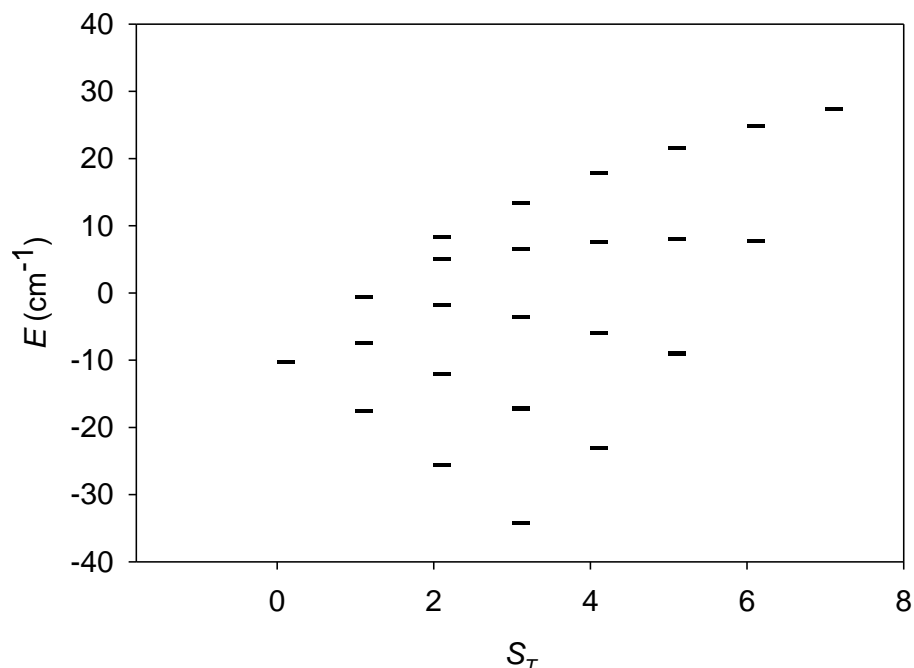


Figure 4-19. Plot of all possible energy states for complex **4-2** using the J values, obtained from the fit to the experimental $\chi_M T$ data.

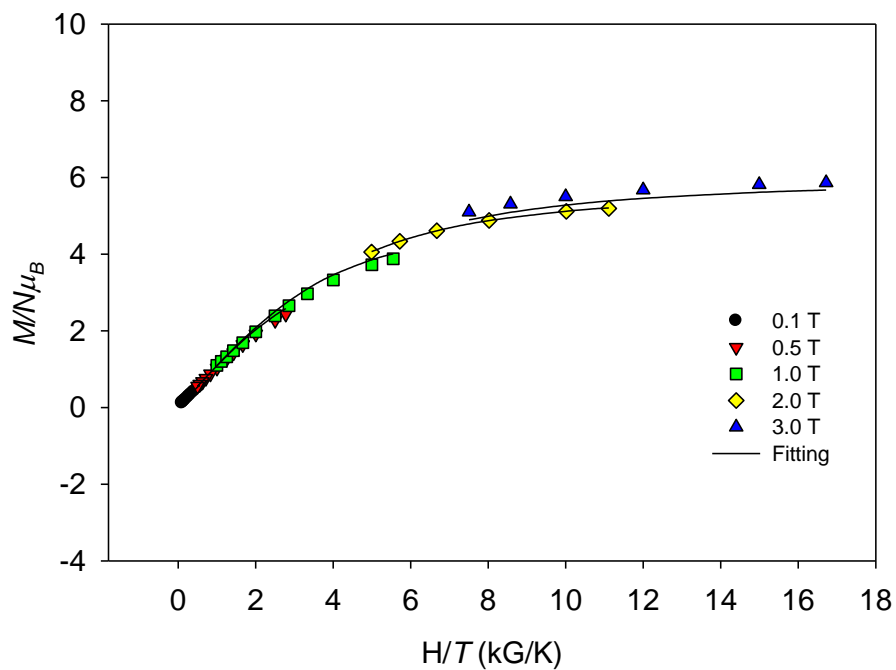


Figure 4-20. Plot of reduced magnetization ($M/N\mu_B$) vs. H/T for complex **4-2**· H_2O at applied fields of 0.1 - 3.0 T and in the 1.8 - 10 K temperature range. The solid lines are the fit to the data; see the text for the fit parameters.

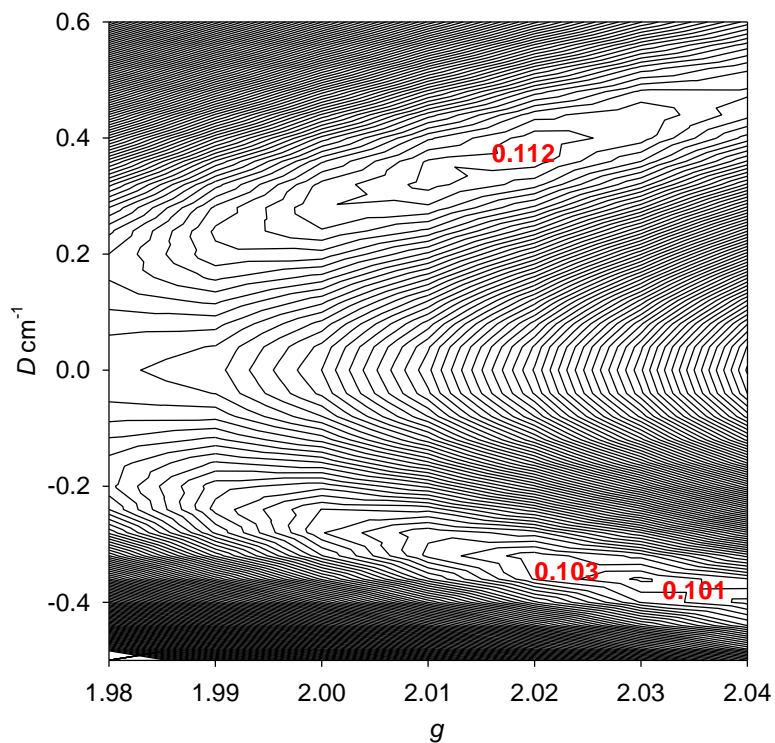


Figure 4-21. Two-dimensional contour plot for the rms error surface vs. D and g for the reduced magnetization fit for complex **4-2**.

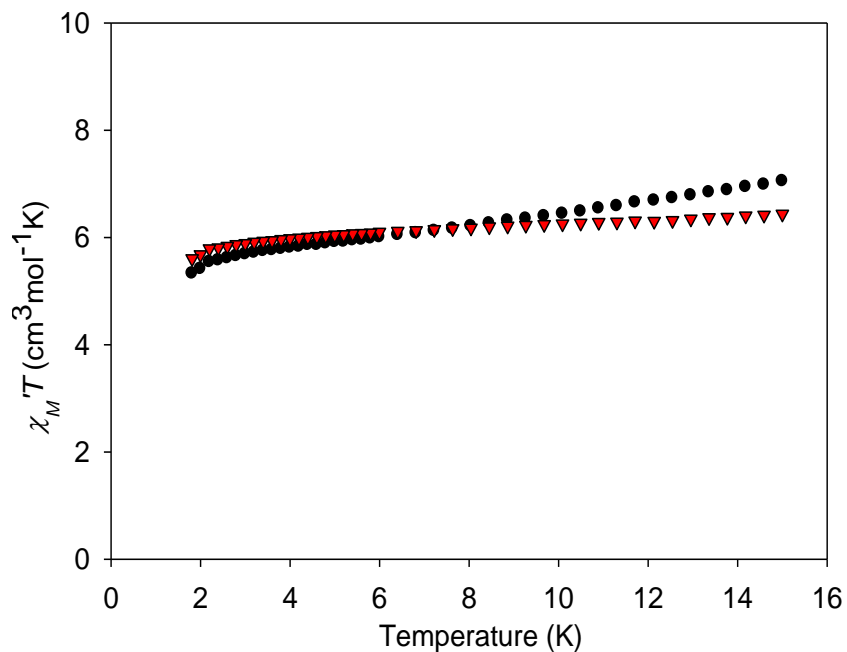


Figure 4-22. Plot of in-phase χ_M' (as $\chi_M'T$) vs. T ac signals at 1000 Hz for complexes **4-1**·H₂O (▼) and **4-2**·H₂O (●).

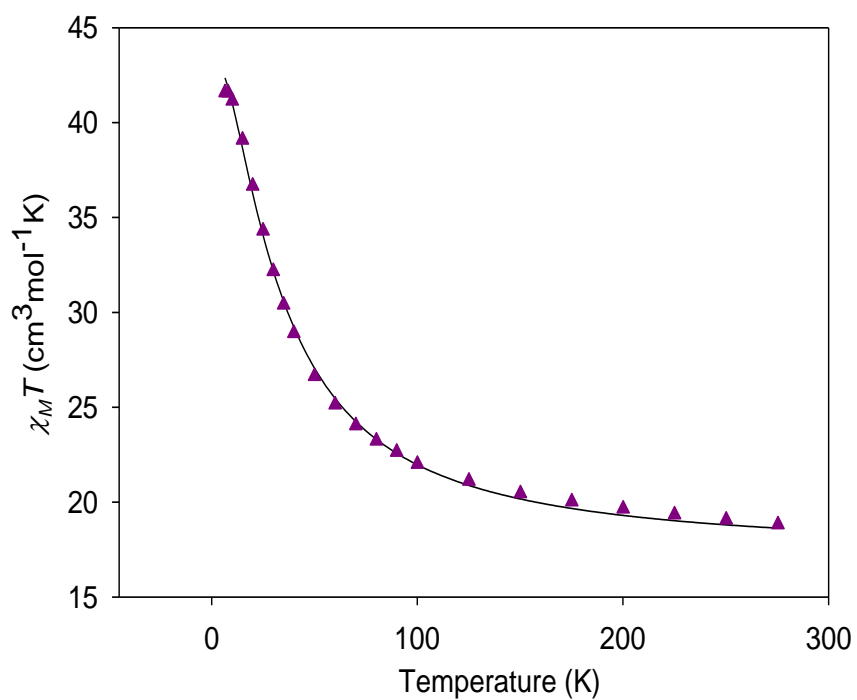


Figure 4-23. Plot of $\chi_M T$ vs. T for complex **4-3** (solid line indicates the fit to the experimental data). See the text for the fitting parameters.

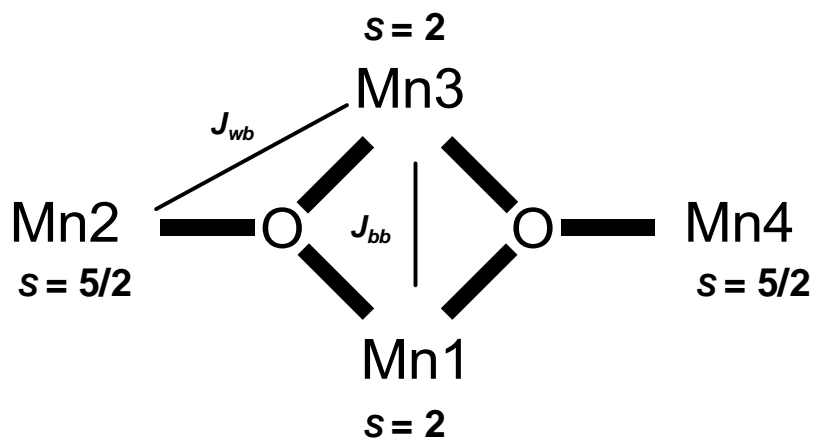
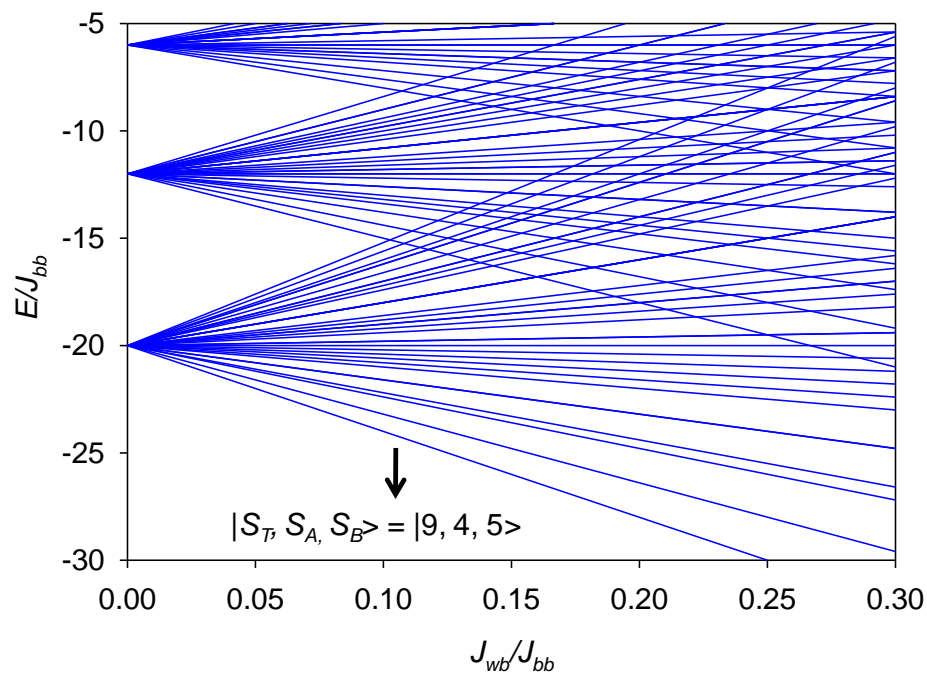


Figure 4-24. Schematic diagram for a Mn_4 core with two exchange coupling parameters, J_{wb} and J_{bb}

A



B

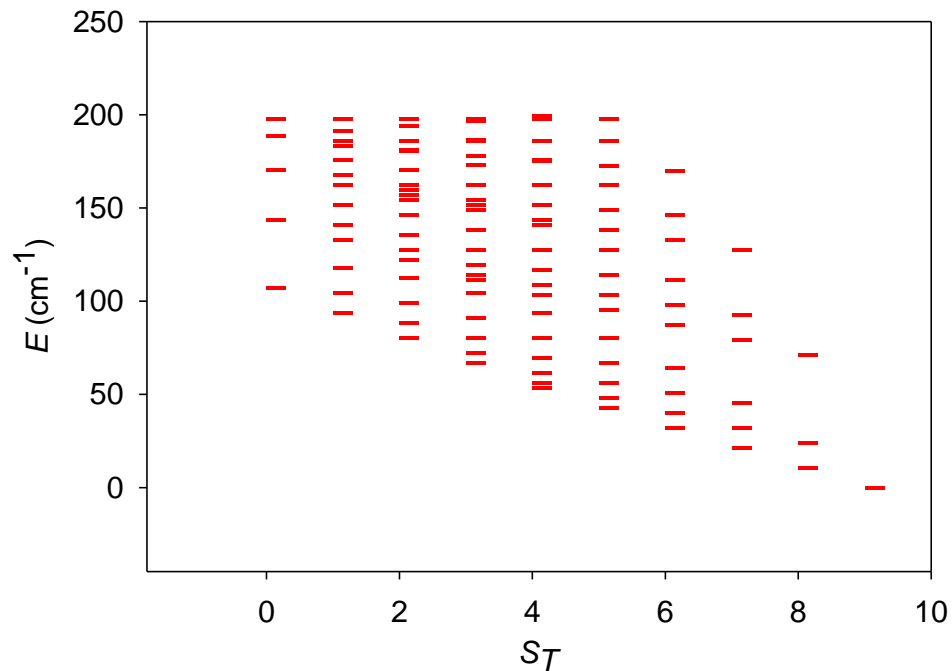


Figure 4-25. (A) Plot of energies of various spin states vs. the ratio of J_{wb}/J_{bb} for complex **4-3**. (B) Plot of all possible energy states for complex **4-3** using the J values, obtained from the fit to the experimental $\chi_M T$ data.

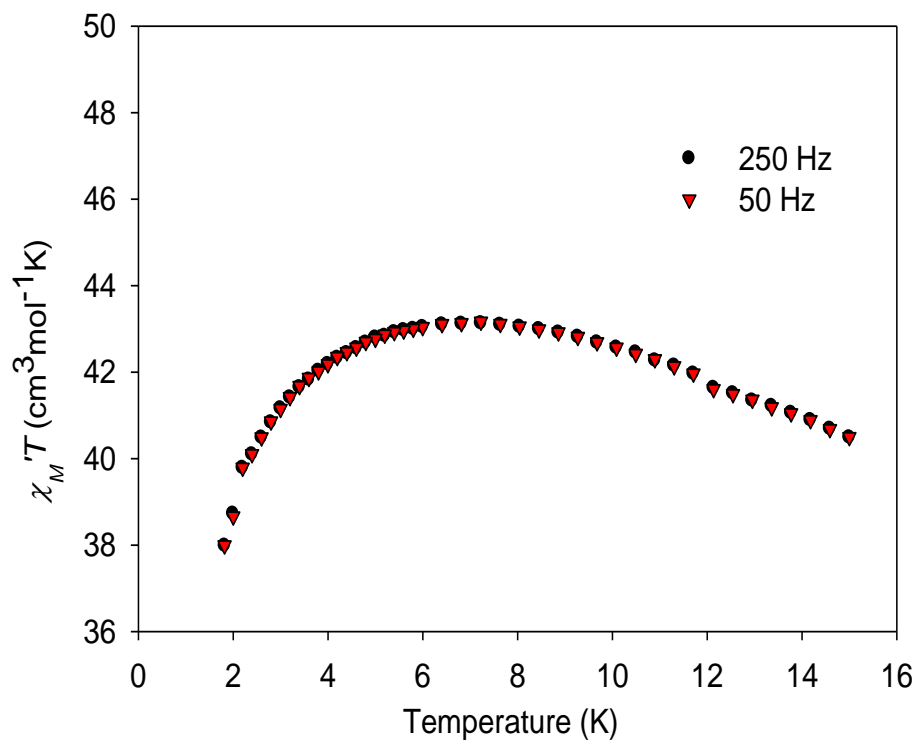


Figure 4-26. The plots of in-phase χ_M' (as $\chi_M' T$) vs. T ac signals for complex **4-3** at the indicated frequencies.

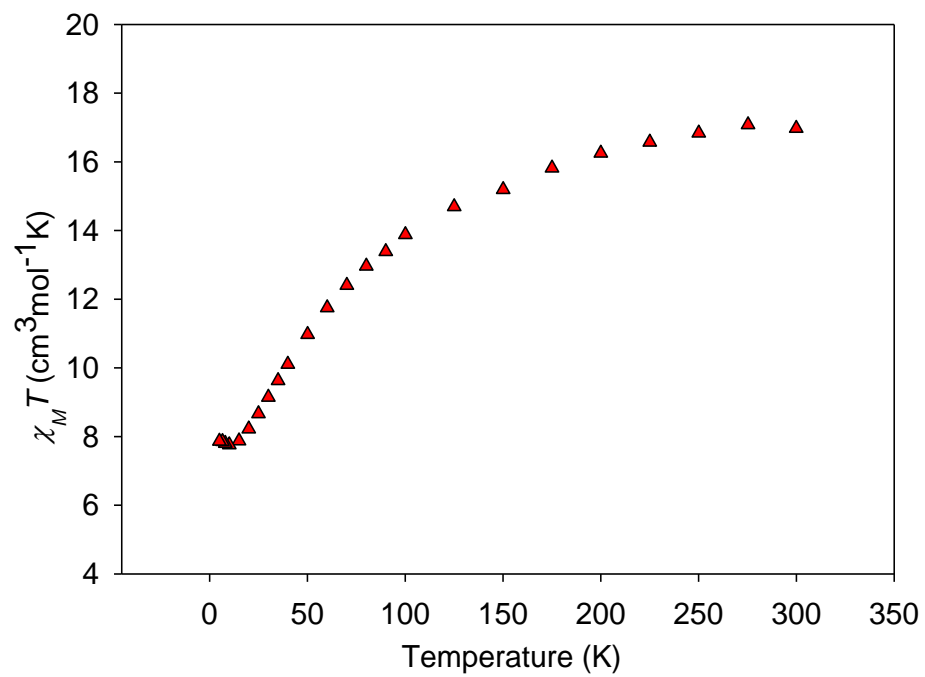


Figure 4-27. Plot of $\chi_M T$ vs. T for complex **4-4**.

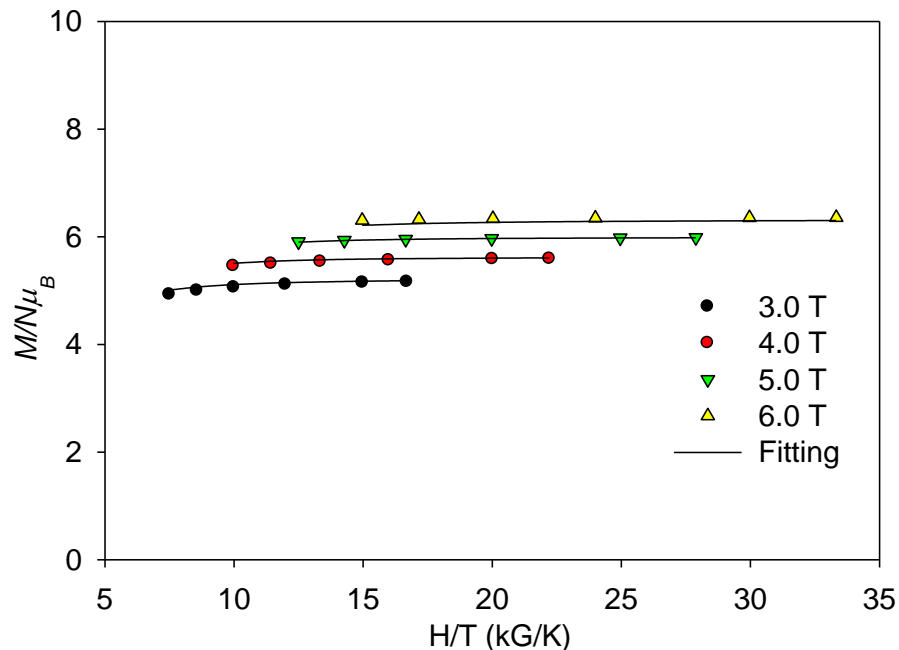


Figure 4-28. Plot of reduced magnetization ($M/N\mu_B$) vs. H/T for complex **4-4** at applied fields of 3.0 - 6.0 T and in the 1.8 - 10 K temperature range. The solid lines are the fit to the data; see the text for the fit parameters.

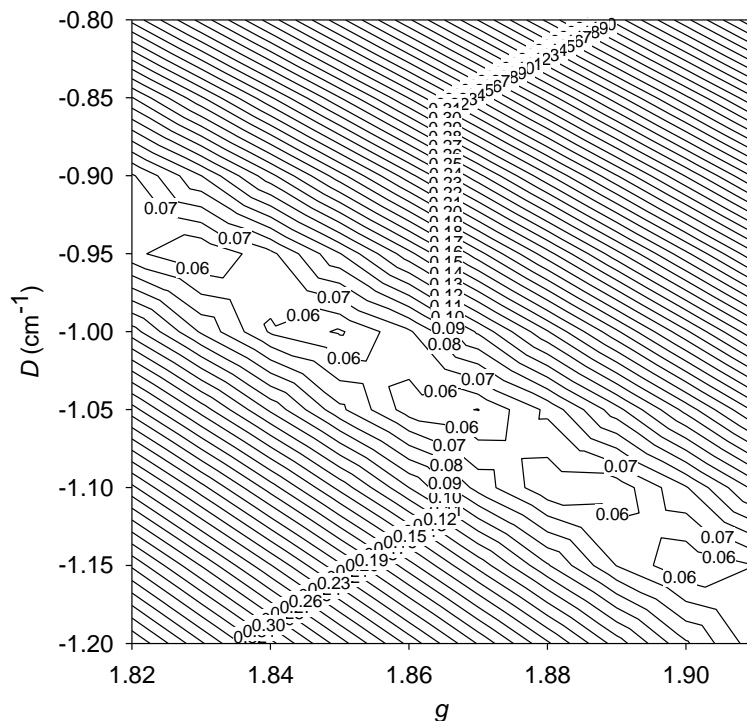


Figure 4-29. Two-dimensional contour plot for the rms error surface vs. D and g for the reduced magnetization fit for complex **4-4**.

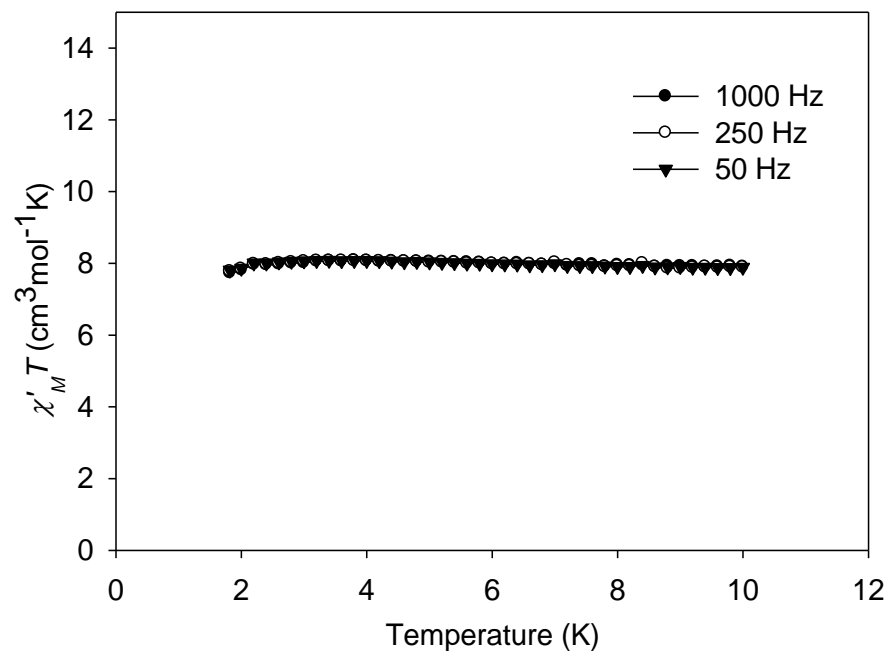


Figure 4-30. Plot of in-phase χ_M' (as $\chi_M' T$) vs. T ac signals for complex **4-4** at the indicated frequencies.

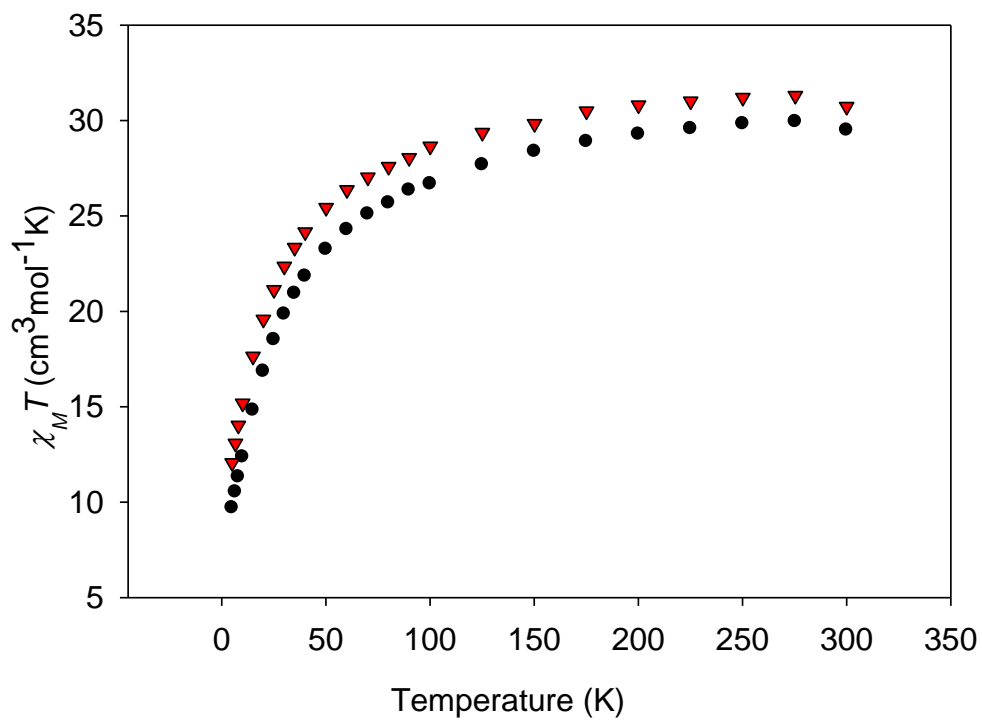


Figure 4-31. Plot of $\chi_M T$ vs. T for complexes **4-5**·2H₂O (●) and **4-6**·H₂O (▼).

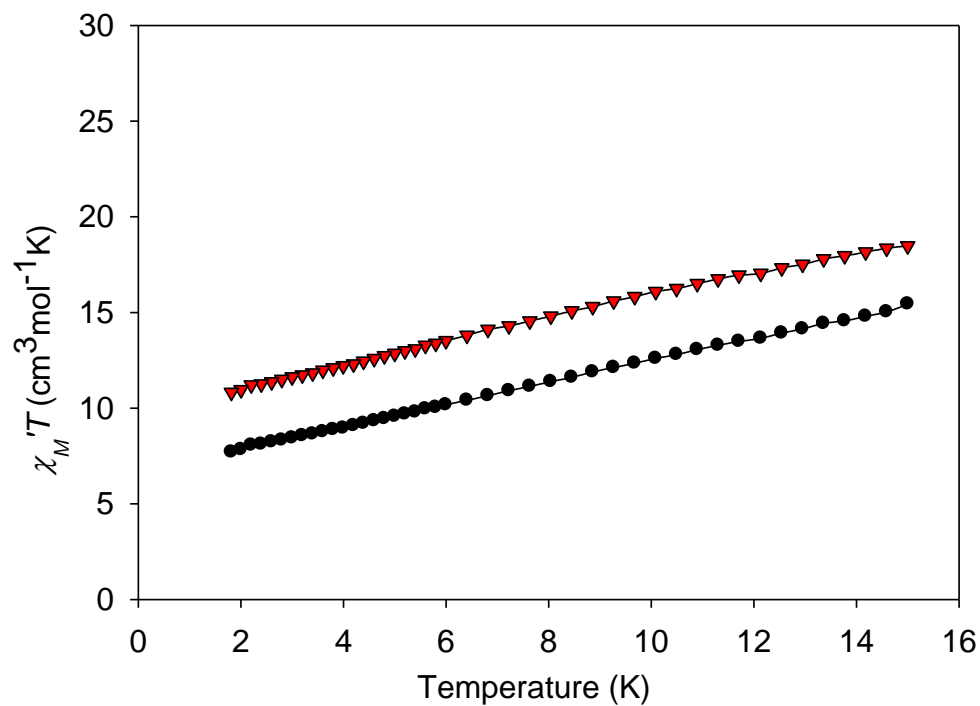


Figure 4-32. Plot of in-phase χ_M' (as $\chi_M'T$) vs. T ac signals for complexes **4-5**·2H₂O (●) and **4-6**·H₂O (▼) at 1000Hz.

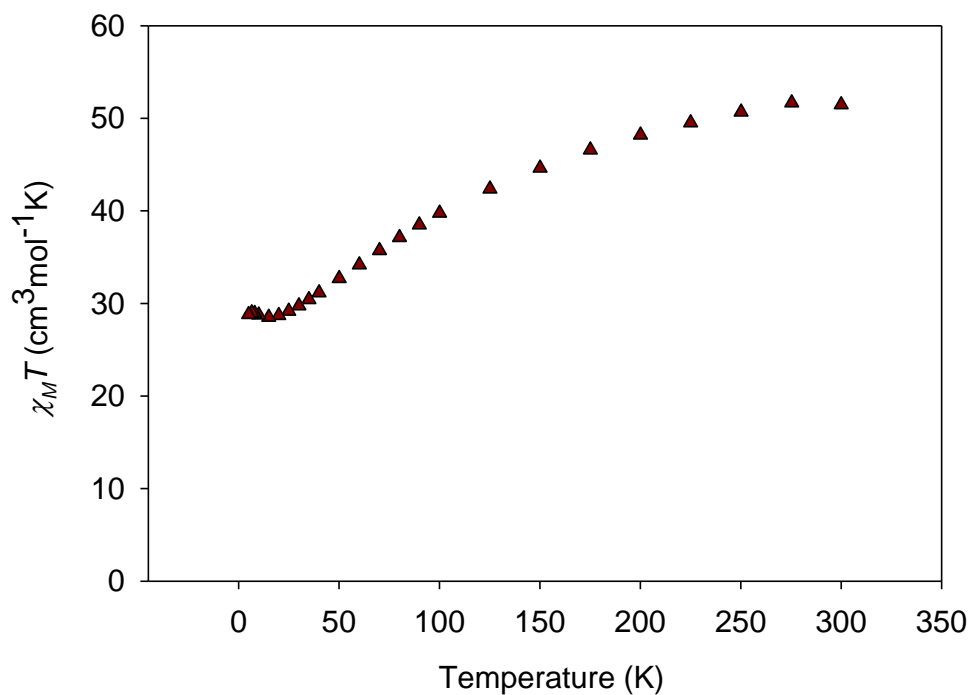
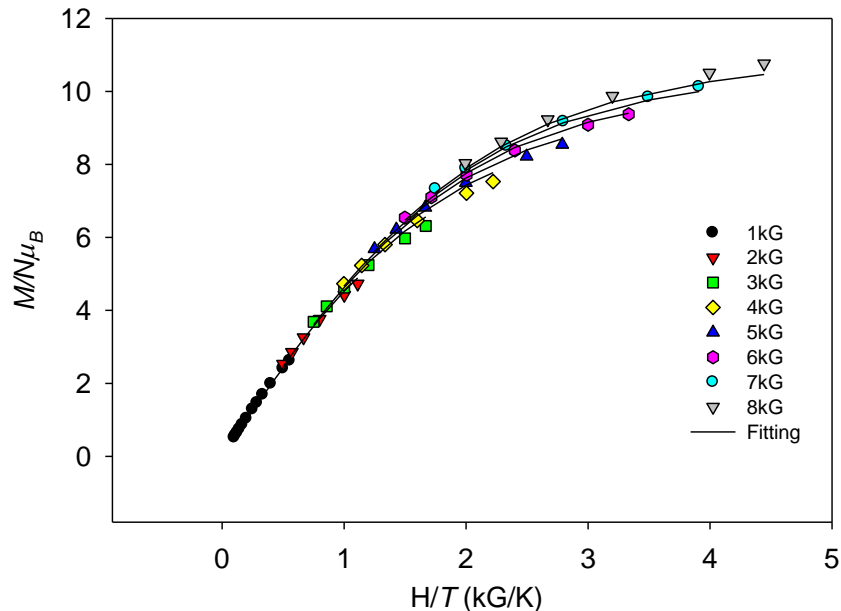


Figure 4-33. Plot of $\chi_M T$ vs. T for complex **4-7**·1.5C₆H₁₄.

A



B

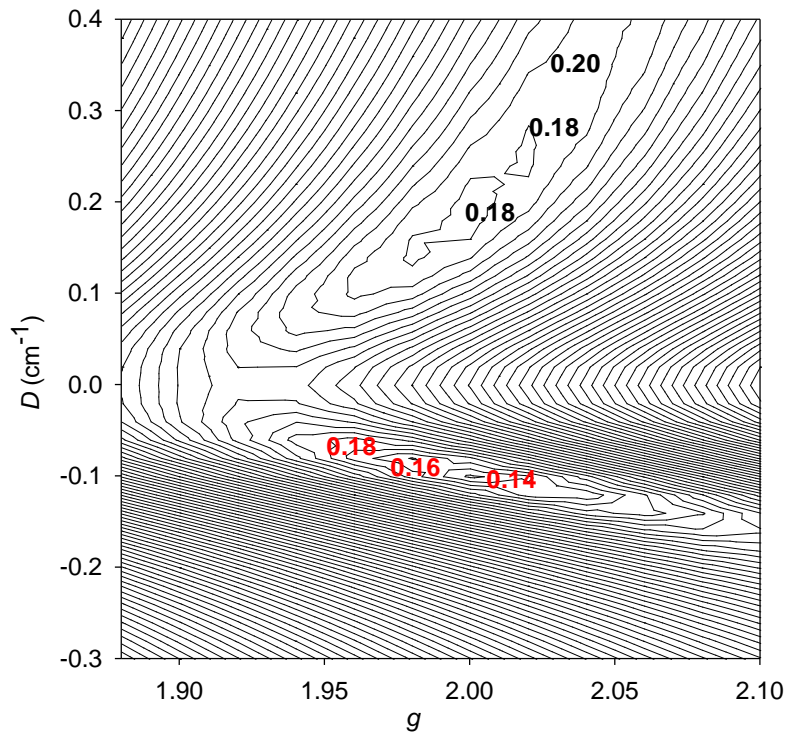


Figure 4-34. Plot of reduced magnetization ($M/N\mu_B$) vs. H/T for complex **4-7**· $1.5\text{C}_6\text{H}_{14}$ at applied fields of 0.1 - 0.8 T and in the 1.8 - 10 K temperature range (A). The solid lines are the fit to the data; see the text for the fit parameters. Two-dimensional contour plot for the rms error surface vs. D and g for the reduced magnetization fit for complex **4-7**· $1.5\text{C}_6\text{H}_{14}$ (B).

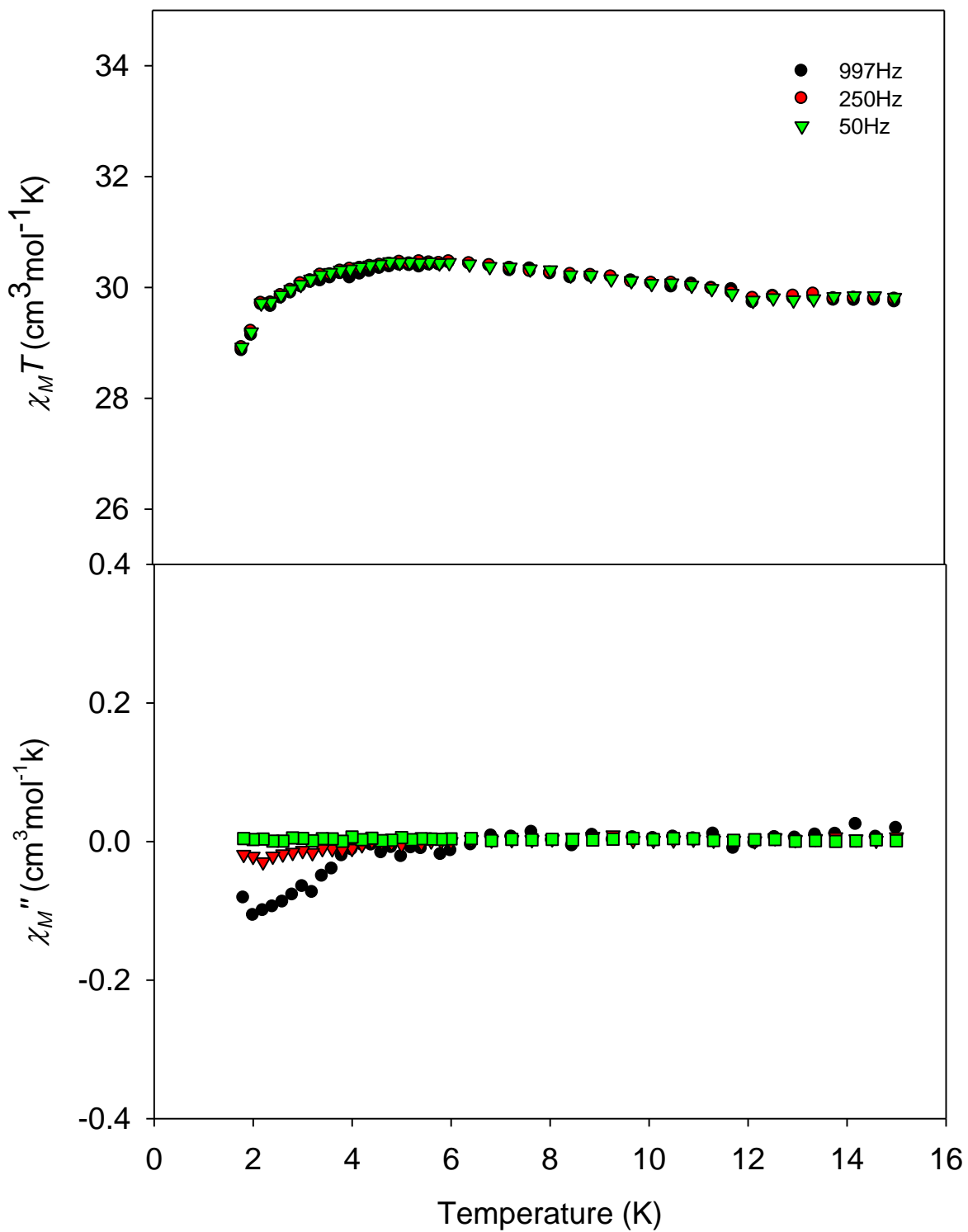
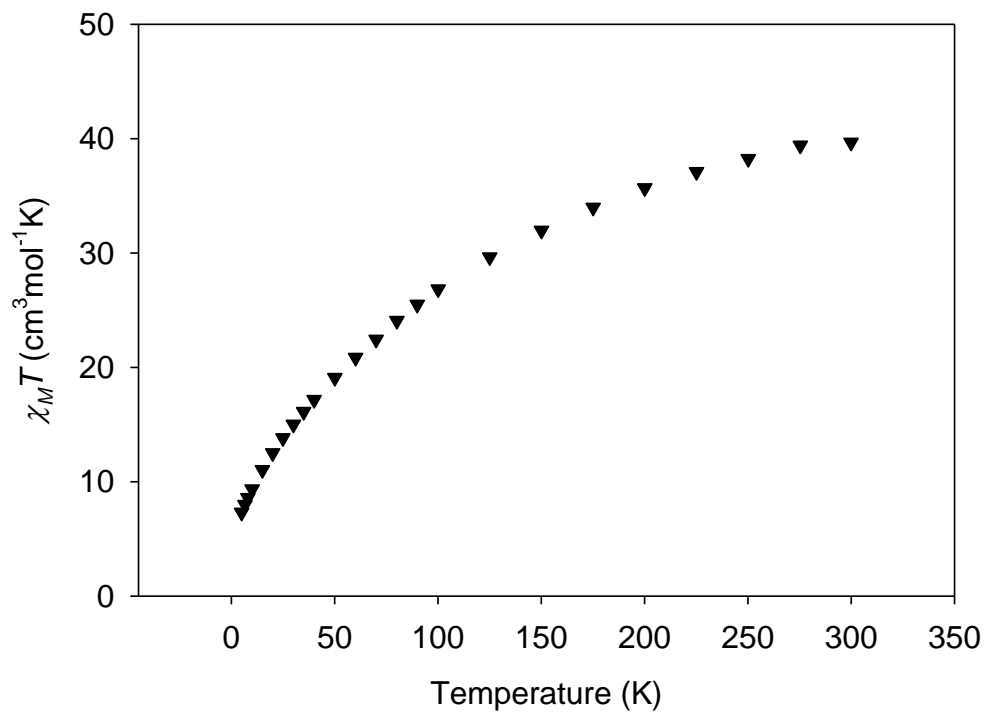


Figure 4-35. Plots of in-phase χ_M' (as $\chi_M'T$) vs. T and out-of-phase χ_M'' vs. T ac signals for complex **4-7**·1.5C₆H₁₄ at the indicated frequencies.

A



B

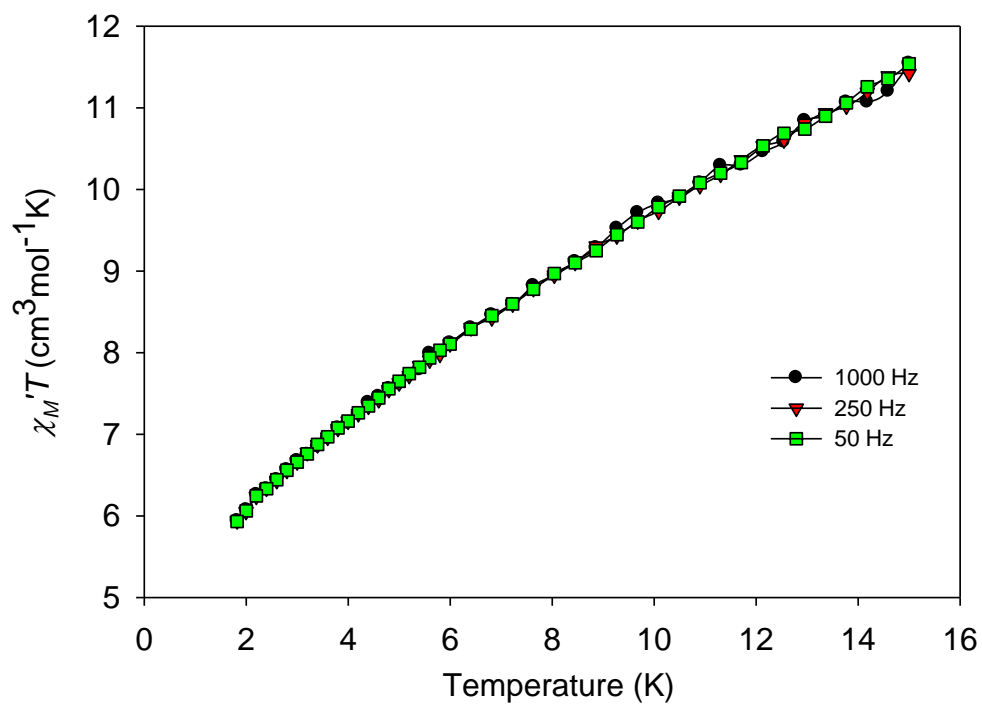


Figure 4-36. Plots of $\chi_M T$ vs. T (A) and in-phase χ_M' (as $\chi_M' T$) vs. T ac signals for complex **4-8**·3H₂O at the indicated frequencies (B).

CHAPTER 5
A FAMILY OF RARE FUSED DOUBLE-CUBANE Mn_4Ln_2 ($Ln = Gd, Tb, Dy, Ho$) AND
 Mn_4Y_2 COMPLEXES CONTAINING SINGLE-MOLECULE MAGNET

Polynuclear mixed-metal oxide clusters are of great importance to chemists and solid-state physicists interested in new metal alloys, intermetallics and perovskite-type metal architectures.¹⁹⁵⁻²⁰⁰ The heterometallic nature of those materials influences many interesting properties such as ferromagnetism and ferroelectricity.²⁰¹⁻²⁰³ In addition, polynuclear 3d/4f complexes have drawn significant interest in the field of molecular magnets, especially single-molecule magnets (SMMs) as promising substitutes to homometallic transition metal complexes.²⁰⁴⁻²¹⁰ SMMs are individual molecules that possess a significant barrier to magnetization relaxation, and thus exhibit the properties of a magnet below their blocking temperature (T_B). These properties result from a combination of a high-spin ground state (S) value (i.e. several unpaired electrons) and easy-axis magnetic anisotropy (negative zero-field parameter, D). SMMs also straddle the classical/quantum interface by displaying not just classical magnetization hysteresis but also quantum tunneling of magnetization (QTM) and quantum phase interference. These properties make SMMs potential candidates to be used as qubits in quantum computation. Besides, SMMs can be used for information storage due to their bulk magnetic properties, and other applications include molecular spintronics and biomedical applications (for example as MRI contrast agents).^{11,13-15,211} Over the past two decades there have been massive amounts of research in this area, and the SMM database has greatly expanded; however, to date manganese has been the transition metal of choice due to its tendencies to give molecules with large S values and significant anisotropy from the presence of Jahn-Teller (JT) distorted Mn^{3+} ions. In the

search for another metal source with large single-ion anisotropy, trivalent lanthanides are wise alternatives. In particular Tb^{3+} or Dy^{3+} ions can provide large spin and high spin-orbit coupling and have participated in making a new class of SMMs.²¹²⁻²²⁰ Additional advantages of mixed-metal clusters come from the often ferromagnetic coupling between 3d and 4f ions resulting in a high spin ground state.²²¹ In the past decade a number of Mn/Ln metal clusters^{118,222-234} have been made, such as Mn_2Ln_2 , Mn_2Ln_3 , Mn_4Ln_4 , Mn_4Ln_3 , Mn_5Ln_4 , Mn_6Dy_6 , Mn_9Dy_8 , $Mn_{10}Ln_2$, $Mn_{11}Dy_4$, $Mn_{11}Gd_2$, $Mn_{12}Gd$, $Mn_{18}Dy$ and $Mn_{21}Dy$. Formation of all these clusters incorporates polydentate chelating ligands,^{223,225,226,233} *N*-substituted diethanolamines^{118,224,227}, carboxylate groups^{222,224,227-232,234} and tripodal ligands.²²² All these ligands feature either alcohol or carboxylate arms which, upon deprotonation, foster formation of high nuclearity products.

Like the previous chapters, edteH₄ is the ligand of choice. The compounds so far obtained with edteH₄ are Mn_x (x = 3, 4, 6, 8, 9, 10, 12, 20), Mn₁₈Ca₂, and Fe_x (x = 5, 6, 12) metal complexes. In the present work for the first time, the reactivity of the edteH₄ group has been explored in the presence of carboxylate as co-ligand in manganese/lanthanide cluster chemistry. Herein, we report the syntheses, crystal structures, and magnetic measurements on a family of 3d/4f, mixed-metal, Mn₄Ln₂ complexes (where Ln = Y (diamagnetic), Gd (isotropic) or Tb, Dy, Ho (anisotropic)) with an unprecedented metal topology. The Tb analogue is a new addition to the SMM family.

Experimental Section

Syntheses

All the preparations were performed under aerobic conditions using reagents and solvents as received. The synthesis of $\text{Mn}(\text{O}_2\text{CBu}^t)_2$ was carried out as reported in the literature.¹²⁰

$\text{Mn}_4\text{Gd}_2\text{O}_2(\text{O}_2\text{CBu}^t)_6(\text{edteH}_2)_2(\text{NO}_3)_2$ (5-1). To a stirred solution of edteH₄ (0.20 g, 0.84 mmol) and NEt₃ (0.25 mL, 1.68 mmol) in MeCN/MeOH (20/1, v/v) was added $\text{Mn}(\text{O}_2\text{CBu}^t)_2$ (0.66 g, 2.52 mmol). The resulting brown solution was stirred for 20 minutes under mild heating and then Gd(NO₃)₃ (0.76 g, 1.68 mmol) was added to the solution and stirred for further 2 hours. The solution was then filtered and left undisturbed. X-ray quality, orange plate-like crystals of **5-1**·3MeCN grew after two days from slow evaporation with a yield of 12 %. The crystals were collected by filtration, washed with Et₂O and dried in vacuum. Anal. Calc. (found) for **5-1** (solvent-free): C: 34.01 (33.73); H: 5.59 (5.56); N: 4.76 (4.67) %. Selected IR data (cm⁻¹): 3405 (br), 2967 (m), 2678 (w), 1566 (s), 1484 (s), 1415 (br, s), 1308 (m), 1228 (s), 1072 (s), 1032 (m), 897 (m), 795 (w), 741(w), 594 (br, s), 530 (w), 454 (m).

$\text{Mn}_4\text{Tb}_2\text{O}_2(\text{O}_2\text{CBu}^t)_6(\text{edteH}_2)_2(\text{NO}_3)_2$ (5-2). The preparation is similar to that above but Tb(NO₃)₃ (0.73 mg, 1.68 mmol) was used as the Ln salt. The yield was 15 %. Anal. Calc. (found) for **5-2** (solvent-free): C: 33.95 (33.78); H: 5.58 (5.58); N: 4.75 (4.71) %. Selected IR data (cm⁻¹): 3393 (br), 2967 (m), 2906 (m), 2679 (w), 1566 (s), 1484 (s), 1416 (br, s), 1309 (m), 1228 (s), 1114 (w), 1072 (s), 1031 (m), 925 (w), 898 (m), 795 (m), 743 (w), 594 (br, s), 531 (w), 454 (m).

$\text{Mn}_4\text{Dy}_2\text{O}_2(\text{O}_2\text{CBu}^t)_6(\text{edteH}_2)_2(\text{NO}_3)_2$ (5-3). The preparation is similar to that above but Dy(NO₃)₃ (0.58 mg, 1.68 mmol) was used as the Ln metal ion. The yield was 15 %.

Anal. Calc. (found) for **5-3** (solvent-free): C: 33.81 (33.61); H: 5.56 (5.58); N: 4.73 (4.98) %. Selected IR data (cm^{-1}): 3392 (br), 2970 (w), 2739 (w), 2677 (w), 1567 (s), 1484 (s), 1412 (br, s), 1311 (m), 1228 (s), 1171 (w), 1072 (s), 1033 (s), 926 (w), 898 (s), 825 (m), 794 (w), 744 (w), 595 (br, s), 533 (w), 455 (m).

$\text{Mn}_4\text{Ho}_2\text{O}_2(\text{O}_2\text{CBu}^t)_6(\text{edteH}_2)_2(\text{NO}_3)_2$ (5-4). The preparation is similar to that above but $\text{Ho}(\text{NO}_3)_3$ (0.74 mg, 1.68 mmol) was used as the Ln salt. The yield was 15 %. Anal. Calc. (found) for **5-4** (solvent-free): C: 33.72 (33.54); H: 5.55 (5.54); N: 4.72 (4.73) %. Selected IR data (cm^{-1}): 3370 (br), 2967 (br), 2678 (w), 1567 (s), 1418 (br, s), 1312 (s), 1227 (s), 1114 (w), 1072 (s), 1031 (s), 897 (s), 820 (w), 795 (w), 746 (w), 595 (br, s), 533 (w), 455 (m).

$\text{Mn}_4\text{Y}_2\text{O}_2(\text{O}_2\text{CBu}^t)_6(\text{edteH}_2)_2(\text{NO}_3)_2$ (5-5). The preparation is similar to that above but $\text{Y}(\text{NO}_3)_3$ (0.58 mg, 1.68 mmol) was used. The yield was 14 %. Anal. Calc. (found) for **5-5** (solvent-free): C: 36.87 (36.58); H: 6.06 (6.01); N: 5.16 (5.18) %. Selected IR data (cm^{-1}): 3396 (br), 2967 (s), 2905 (m), 1567 (s), 1484 (s), 1417 (s), 1374 (m), 1314 (m), 1228 (s), 1072 (vs), 1032 (s), 925 (m), 898 (m), 818 (w), 796 (w), 747 (w), 594 (br, s), 530 (w), 456 (m).

X-ray Crystallography

Data were collected at 100 K on a Bruker DUO system equipped with an APEX II area detector and a graphite monochromator utilizing $\text{MoK}\alpha$ radiation ($\lambda = 0.71073 \text{ \AA}$). Cell parameters were refined using up to 9999 reflections. A hemisphere of data was collected using the ω -scan method (0.5° frame width). Absorption corrections by integration were applied based on measured indexed crystal faces. The structure was solved by direct methods in *SHELXTL6*, and refined on F^2 using full-matrix least

squares. The non-H atoms were treated anisotropically, whereas the hydrogen atoms were calculated in ideal positions and refined as riding on their respective carbon atoms. Crystallographic parameters are listed in Table 5-1.

For **5-1**·3MeCN, the asymmetric unit consists of a half Mn_4Gd_2 cluster (located on an inversion center) and 1.5 acetonitrile solvent molecules (the half molecule is located on a 2-fold rotation axis). Fragment O2-C9-C10 was disordered and refined in two parts. A total of 448 parameters were refined in the final cycle of refinement using 5716 reflections with $I > 2\sigma(I)$ to yield R_1 and wR_2 of 3.68 % and 9.01 %, respectively.

For **5-2**·0.5MeCN, the asymmetric unit consists of a Mn_4Tb_2 cluster and a half acetonitrile solvent molecule. The latter were disordered and could not be modeled properly, thus the program SQUEEZE,⁶⁴ a part of the PLATON package of crystallographic software, was used to calculate the solvent disorder area and remove its contribution to the overall intensity data. There are two disordered regions in the cluster. The C10-O4 group of the edteH₄ ligand is disordered and refined in two parts with their site occupation factors dependently refined. The three methyl groups on atom C22 are disordered and treated in the same manner. In the final cycle of refinement, 8260 reflections (of which 6090 are observed with $I > 2\sigma(I)$) were used to refine 403 parameters and the resulting R_1 , wR_2 and S (goodness of fit) were 3.00%, 6.06% and 0.902, respectively. The refinement was carried out by minimizing the wR_2 function using F^2 rather than F values. R_1 is calculated to provide a reference to the conventional R value but its function is not minimized.

Physical Measurements

Infrared spectra were recorded in the solid state (KBr pellets) on a Nicolet Nexus 670 FTIR spectrometer in the 400 - 4000 cm^{-1} range. Elemental analyses (C, H and N)

were performed by the in-house facilities of the University of Florida, Chemistry Department. Variable-temperature dc and ac magnetic susceptibility data were collected at the University of Florida using a Quantum Design MPMS-XL SQUID susceptometer equipped with a 7 T magnet and operating in the 1.8 - 300 K range. Samples were embedded in solid eicosane to prevent torquing. Magnetization vs. field and temperature data were fit using the program MAGNET.⁶⁶ Pascal's constants were used to estimate the diamagnetic correction, which was subtracted from the experimental susceptibility to give the molar paramagnetic susceptibility (χ_M). Low-temperature (<1.8 K) hysteresis loop and dc relaxation measurements were performed in Grenoble using an array of micro-SQUIDs.⁶⁷ The field can be applied in any direction by separately driving three orthogonal coils. The applied field was aligned parallel to the easy axis (z axis) of the molecules using a published method.¹²¹ The high sensitivity of this magnetometer allows the study of single crystals of the order of 10 to 500 μm .

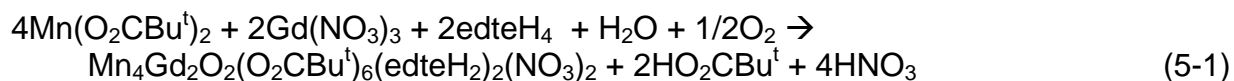
Results and Discussion

Syntheses

In this work, ethylenediamine based alkoxide-containing edteH₄ ligand has been as the main ligand of choice. The edteH₄ ligand has proven to be a good chelating ligand on deprotonation, mainly due to the presence of four flexible alkoxide arms.^{54,60,168} In the previous chapter it has been noted that the reaction between Mn(O₂CBu^t)₂ and edteH₄ gives a high spin, high nuclearity Mn₉ SMM with a high spin barrier. Therefore, it is interesting to further evaluate the synthetic scheme by adding isotropic, anisotropic and diamagnetic lanthanides ions to the system. The new reaction scheme has the potential to give new heterometallic clusters where the magnetism is now governed by both the Ln³⁺ and Mn³⁺ ions. So far there are only few examples of

Mn/Ln metal clusters with *N*-substituted alkoxide ligands in the literature.^{118,224,227} The following scheme will be a new addition to this family. Trivalent lanthanide ions show strong affinity towards oxygen and so the combination of ^tBuCO₂⁻, edteH₄, Mn and Ln ions has been explored in this chapter.

The reaction of edteH₄ with Mn(O₂CBu^t)₂, NEt₃ and Gd(NO₃)₃ in a 1:3:2:2 molar ratio in MeCN/MeOH (10/1, v/v) afforded a reddish-brown solution from which the Mn₂^{III}Mn₂^{II}Gd^{III}₂O₂(O₂CBu^t)₆(edteH₂)₂(NO₃)₂ (**5-1**) was obtained in 12 % yield. Its formation is summarized in equation 5-1. The base NEt₃ facilitates the oxidation of Mn²⁺ to Mn³⁺ by atmospheric oxygen gas and the deprotonation of water to form more O²⁻. Using MeCN only as solvent also leads to the same product, but the use of MeCN/MeOH is imperative to obtain good single-crystals of **5-1** in the highest yield.



The same product is also obtained by using 1:2 ligand-to-metal molar ratio; however, the best yield is obtained from the above reaction. The same product with comparable yield is obtained by using Mn(NO₃)₂, MnCl₂ or Mn(ClO₄)₂ and ^tBuCO₂H in 1:2 molar ratio instead Mn(O₂CBu^t)₂. Interestingly, no product was isolated by switching the ^tBuCO₂⁻ to MeCO₂⁻, EtCO₂⁻ or PhCO₂⁻ groups in the original scheme. However, the reaction of Mn(O₂CMe)₂/Mn(O₂CEt)₂, Gd³⁺, ^tBuCO₂H, edteH₄ and NEt₃ gives the same product with no MeCO₂⁻/EtCO₂⁻ in the final product. Hence, the bulky ^tBuCO₂⁻ plays a crucial role in trapping the Mn₄Gd₂ cluster from the MeCN/MeOH solvent system. This reaction strategy was used to make the other family members of Mn₄Ln₂ (where Ln = Tb, Dy, Ho) and Mn₄Y₂ clusters. The complexes were characterized by IR and elemental analysis.

Description of Structure $\text{Mn}_4\text{Gd}_2\text{O}_2(\text{O}_2\text{CBu}^t)_6(\text{edteH}_2)_2(\text{NO}_3)_2$

The complete structure and a stereoview of **5-1** are presented in Figure 5-1 and 5-2; selected interatomic distances and angles are listed in Table A-11. This complex crystallizes in the monoclinic space group $C2/c$ and has crystallographic inversion symmetry. The centrosymmetric molecule possesses a $[\text{Mn}_4\text{Gd}_2\text{O}_2(\text{OR})_4]^{8+}$ core. The core has a fused, face-sharing double-cubane structure, containing two $\mu_4\text{-O}^{2-}$ (O5) and four $\mu_3\text{-OR}^-$ (O1, O4) bridging to the four Mn and two Gd atoms (Figure 5-3). The coordination of the two peripheral Mn1 atoms is completed by two doubly deprotonated edteH_2^{2-} ligands. Each edteH_2^{2-} group is hexadentate-chelating on to the terminal Mn1 atom with two of its deprotonated alkoxide arms bridging to the two Mn2 atoms and Gd1 atom. Thus, the edteH_2^{2-} groups are overall $\eta^1: \eta^1: \eta^3: \eta^3: \mu_4$ -bridging, as shown in Figure 5-4. The determination of the protonation levels of all the O atoms was accomplished by BVS calculations¹⁷¹ and the results are listed in Table 5-2. Two of the edteH_2^{2-} O atoms have BVS values of >1.9 , confirming them as deprotonated, whereas the other two have BVS values of around 1.3-1.4, confirming them as protonated. Mn1 (Mn^{2+}) is seven-coordinate and Mn2 (Mn^{3+}) is six-coordinate with near-octahedral geometry. The oxidation states were confirmed by charge considerations, metric parameters and BVS calculations (Table 5-3). The two Mn^{3+} atoms display JT axial elongations, defined by the axis O1-Mn2-O4 and shown as green solid lines in Figure 5-5. The JT axes are oriented nearly parallel to each other and the elongated $\text{Mn}^{3+}\text{-O}$ bonds are ~ 0.3 Å longer than the other $\text{Mn}^{3+}\text{-O}$ bonds. The Gd atoms are nine-coordinate with their geometries completed by two bridging ($\eta^1: \eta^1: \mu$) and one chelating ${}^t\text{BuCO}_2^-$ groups and one chelating NO_3^- ion. Hence, the charge balance consideration requires 2Mn^{2+} , 2Mn^{3+} , 2Gd^{3+} , 2O_2^{2-} , ${}^t\text{BuCO}_2^-$, 2edteH_2^{2-} and 2NO_3^- . The structure of **5-2**

(Figure 5-6) is similar to that of **5-1** where Gd^{3+} is replaced by Tb^{3+} . The other family members (**5-3**, **5-4**, **5-5**) are isostructural to $\text{Gd}^{3+}/\text{Tb}^{3+}$ analogues, proved by elemental and IR spectroscopic analyses. This face-sharing double-cubane core is a rare structural type. There is no structural precedence for the fused double-cubane structure in 3d/4f cluster chemistry, but two Mn^{III}_6 fused double-cubane clusters have been reported in the past.^{235,236}

Magnetochemistry

Dc magnetic susceptibility studies

Solid state, variable-temperature magnetic susceptibility measurements were performed on vacuum-dried microcrystalline samples of complexes **5-1** to **5-5**. The dc molar magnetic susceptibility (χ_M) data were collected in the 5.0 - 300 K range in a 0.1 T (1000 Oe) magnetic field, and are shown in Figure 5-7, as $\chi_M T$ versus T plots. At 300 K the experimental $\chi_M T$ are a little smaller than the expected values for the four non-interacting Mn ($S = 2$ for Mn^{3+} , $S = 5/2$ for Mn^{2+} , $g = 2$) and two $\text{Ln}^{3+}/\text{Y}^{3+}$ metal ions (as summarized in Table 5-4). The behavior suggests the presence of antiferromagnetic interaction at room temperature among the adjacent paramagnetic centers. Upon lowering the temperature $\chi_M T$ stays fairly constant down to 50 K (**5-1**), 30 K (**5-2**, **5-3**), 20 K (**5-4**) and then increases markedly to reach a maximal value (Table 5-4). The $\chi_M T$ value ($63.93 \text{ cm}^3 \text{ mol}^{-1} \text{ K}$ at 5 K) for complex **5-1** which contains isotropic Gd^{3+} ion, an ion devoid of any spin-orbit coupling, suggests the spin-ground state as $S = 12$. For compound **5-5** with the diamagnetic Y^{3+} ion, $\chi_M T$ decreases slowly from $11.36 \text{ cm}^3 \text{ mol}^{-1} \text{ K}$ at 300 K to $8.02 \text{ cm}^3 \text{ mol}^{-1} \text{ K}$ at 5 K and the $\chi_M T$ value at 5 K suggests an $S = 4$ ground-state spin. Complex **5-5** contains diamagnetic Y^{3+} ions and hence, the

corresponding magnetic behavior is coming from Mn ions only. To further probe the type of exchange interactions within the paramagnetic Mn ions, the $\chi_M T$ data for complex **5-5** were fit to the theoretical $\chi_M T$ expression for a butterfly core of $\text{Mn}^{\text{II}}_2\text{Mn}^{\text{III}}_2$ with two exchange coupling parameters, J_{wb} and J_{bb} , representing the $\text{Mn}^{\text{II}}\text{Mn}^{\text{III}}$ and $\text{Mn}^{\text{III}}\text{Mn}^{\text{III}}$ interactions, respectively. The corresponding Heisenberg spin Hamiltonian is given by equation 5-2 (the atom labeling is that of Figure 5-8) and its eigenvalues in equation 5-3, where $\hat{S}_A = \hat{S}_1 + \hat{S}_3$, $\hat{S}_B = \hat{S}_2 + \hat{S}_4$, $\hat{S}_T = \hat{S}_A + \hat{S}_B$, and S_T is the total spin of the molecule.

$$\hat{H} = -2J_{wb}(\hat{S}_1 \cdot \hat{S}_2 + \hat{S}_1 \cdot \hat{S}_4 + \hat{S}_2 \cdot \hat{S}_3 + \hat{S}_3 \cdot \hat{S}_4) - 2J_{bb}\hat{S}_1 \cdot \hat{S}_3 \quad (5-2)$$

$$\hat{H} = -J_{wb}(\hat{S}_T^2 - \hat{S}_A^2 - \hat{S}_B^2) - J_{bb}(\hat{S}_A^2 - \hat{S}_1^2 - \hat{S}_3^2) \quad (5-3)$$

$$E(S_T, S_A, S_B) = -J_{wb}[S_T(S_T+1) - S_A(S_A+1) - S_B(S_B+1)] - J_{bb}[S_A(S_A+1)] \quad (5-4)$$

There are total of 110 possible S_T states ranging in values from 0 to 9, where S_T is the total spin of the Mn_4 cluster. This eigenvalue expression (equation 5-4) and the Van Vleck equation were used to derive a theoretical $\chi_M T$ vs. T expression for **5-5**, and this was used to least-squares-fit the experimental data. The fit (solid line in Figure 5-9) gave $J_{bb} = -32.5(4) \text{ cm}^{-1}$, $J_{wb} = +1.0(1) \text{ cm}^{-1}$ and $g = 1.95(1)$ with temperature-independent paramagnetism (TIP) fixed at $4 \times 10^{-4} \text{ cm}^3 \text{ mol}^{-1}$. The energies of all possible spin-states are shown in Figure 5-10 using the J values obtained from the fit. The plot indicates the existence of six degenerate ground states where $|S_T, S_A, S_B\rangle = |0, 0, 0\rangle, |1, 0, 1\rangle, |2, 0, 2\rangle, |3, 0, 3\rangle, |4, 0, 4\rangle, |5, 0, 5\rangle$. The large negative value for J_{bb} makes the spin coupling S_A is zero and hence S_T is equal to S_B . The spin of Mn1 and Mn3 is $S = 5/2$ i.e. the S_B can be of any value from 0 to 5 so as S_T . Considering the weighted average for six possible degenerate spin states, the theoretical $\chi_M T$ value

comes out as $8.32 \text{ cm}^3 \text{ mol}^{-1} \text{ K}$ for $g = 1.95$ which is close to the experimental $\chi_M T$ value at 5 K. The calculation is shown in equation 5-5 considering total 36 m_s states where the spin states vary from 0 to 5.

$$\chi_M T \text{ (theoretical)} = (g^2/8)[1/36 * 0(0+1) + 3/36 * 1(1+2) + 5/36 * 2(2+1) + 7/36 * 3(3+1) + 9/36 * 4(4 + 1) + 11/36 * 5(5+1)] \quad (5-5)$$

To further study the effect of exchange coupling parameters on ground-state spin, energies of all possible spin states are plotted as a function of J_{wb}/J_{bb} (Figure 5-11). The value of the ratio below -0.2 indicates the presence six possible spin states as mentioned before. The ground-state spin starts changing with the decrease in the J_{bb} value as shown in the Figure 5-11. For example, the lowest energy state becomes $|6, 1, 5\rangle$ for changing the ratio from -0.2 up to -0.4. Considering the structural similarities among complexes **5-1** to **5-5**, it is fair to conclude that the interaction between Mn^{3+} - Mn^{3+} is strongly antiferromagnetic and the interaction between Mn^{2+} - Mn^{3+} is weak. Hence, the overall behavior in dc magnetic susceptibility study for complexes **5-1** to **5-4** suggests the presence of predominant ferromagnetic interactions at low temperature coming from the interaction between Mn^{3+} - Ln^{3+} (possibly from μ_3 -O1, μ_3 -O4, μ_4 -O5 and/or η^1 : η^1 : μ carboxylate) and/or Mn^{2+} - Ln^{3+} (possibly from μ_3 -O1, μ_3 -O4, μ_4 -O5) in addition to the intrinsic magnetic properties of Ln^{3+} ions (Figure 5-7).

It is interesting to note that previously reported homometallic, fused double-cubane Mn^{3+}_6 clusters show predominantly antiferromagnetic interaction in dc magnetic susceptibility studies.^{235,236} These findings indicate that the trivalent lanthanide ions play a pivotal role in overall magnetic exchange interactions between the paramagnetic centers in the Mn_4Ln_2 complexes.

To confirm the estimation of the ground state spin of **5-1** and **5-5**, variable-field (H) and temperature magnetization (M) data were collected at various fields up to 7 T and in the 1.8 - 10 K temperature ranges. The resulting data are plotted as reduced magnetization ($M/N\mu_B$) vs. H/T , where N is Avogadro's number and μ_B is the Bohr magneton in Figure 5-12 and 5-13. For Mn_4Gd_2 complex, the saturation value at the highest fields and the lowest temperatures is ~ 24.0 , as expected for an $S = 12$ spin state and g slightly less than 2. The saturation value should be gS in the absence of complications from low-lying excited states or significant anisotropy. The data were fitted using the program MAGNET,⁶⁶ which is based on diagonalizing the giant-spin Hamiltonian given by equation 5-6, which can be assumed to be valid at low temperatures where only the ground state is thermally populated, and employs a full powder average.

$$H = D\hat{S}_z^2 + g\mu_B\mu_0\hat{S}\cdot H \quad (5-6)$$

The best-fit to the data is shown as the solid lines in Figure 5-12 and was obtained with $S = 12$, $D = 0 \text{ cm}^{-1}$, and $g = 1.928 \pm 0.001$ for **5-1**. The fitting is equally good for $S = 11$, $D = 0 \text{ cm}^{-1}$, and $g = 2.098 \pm 0.001$, however, the fit is discarded due to fact that the g value is little higher than 2, is unreasonable for a Mn^{3+}/Gd^{3+} system. The zero field splitting parameter, D is zero which can be rationalized by the super-imposable isofield lines obtained from the reduced magnetization plot. Further confirmation of spin ground state comes from low temperature ac magnetic susceptibility measurements. For Mn_4Y_2 complex, the best-fit data was obtained at the lower fields, 0.1 - 1.0 T (Figure 5-13). This is often a case for polynuclear complexes where fitting is bad at higher fields due to the low-lying excited states as a result of weak interactions and/or spin frustration

effects. An acceptable fit for **5-5** was obtained with $S = 4$, $g = 1.81(1)$ and $D = 0 \text{ cm}^{-1}$ and the fitting is shown as the solid lines in Figure 5-13. The ZFS parameter is zero, same as the case for **5-1**. The g value is little smaller than usual and it indicates the fit is also not the best even with the lower fields. Alternative fits with $S = 3$ or 5 were rejected because they gave unreasonable values of g of 2.34 and 1.48, respectively.

Alternating current (ac) magnetic susceptibility studies

The temperature-dependent ac susceptibilities of all compounds were measured on microcrystalline samples of **5-1** to **5-5** in a 3.5 G ac field. In addition, the in-phase (χ_M') ac susceptibility signal is invaluable for assessing S without any complications from a dc field, and these signals for complexes **5-1** to **5-5** are measured in the 1.8 - 15 K range at 250 Hz (Figure 5-14). A plateau is observed at low temperature and extrapolation of the plot to 0 K, from temperature ~ 2 K, gives a value of $\sim 76 \text{ cm}^3\text{Kmol}^{-1}$ for **5-1** which confirms the presence of $S = 12$ spin-ground state for $g < 2.00$. The in-phase ac signal for **5-5** is nearly constant at low temperature and the extrapolation of the $\chi_M'T$ at 0 K gives a value of $8.2 \text{ cm}^3\text{Kmol}^{-1}$, confirms an $S = 4$ ground state for a g value of ~ 1.8 . The values of S and g compliment the dc magnetization fit data.

Frequency-dependent ac susceptibility measurement is an excellent tool to probe slow relaxation of the magnetization vector at low temperature. Only the Tb^{3+} analogue showed such behavior in the present work and hence, data were collected for **5-2** in the 1.8 - 15 K range at 5 - 1500 Hz. At lower temperature, below 2.5 K, a frequency-dependent decrease in $\chi_M'T$ and the concomitant rise in the out-of-phase χ_M'' signal were seen (Figure 5-15), indicating the slow relaxation of a magnetization vector due to the presence of a spin-barrier. However, in the ac out-of-phase plots, no peaks were

observed; i.e., the peak maxima lie below 1.8 K, the minimum operating temperature of the SQUID magnetometer. Comparing the ac behaviors of the isotropic Gd^{3+} and the anisotropic analogues, it can be concluded that the slow relaxation of magnetization originates from the additional magnetic anisotropy introduced by Tb^{3+} .

Single-crystal hysteresis studies of 5-2 below 1.8 K.

The ac measurements strongly suggest that **5-2** behaves as an SMM, which was confirmed by the observation of hysteresis loops in magnetization vs. dc field scans, measured on a single crystal of **5-2** using the micro-SQUID apparatus. The temperature-dependence at 0.035 T s^{-1} and the scan-rate dependence at 0.04 K of the hysteresis loops are shown in Figure 5-16. The coercivities clearly increase with decreasing temperature and increasing scan rate, as expected for the superparamagnet-like behavior of SMMs.¹⁹ The data thus confirm that complex **5-2** is a new addition to the family of 3d/4f SMMs, with a blocking temperature (T_B) of 0.9 K. Another interesting feature of the loops is to show steps at periodic values of applied field positions. These steps are diagnostic of resonant QTM in several classes of SMMs in 3d family^{14,76,83,237-239} and only one in 3d/4f complexes. The first step in sweeping the field in Figure 5-16 occurs at the zero field, where the double-well potential energy curve is symmetric and M_s levels on one side of the barrier are in resonance with those on the other, allowing tunneling to occur through the barrier. Additional steps are also observed at the periodic fields when the M_s levels are once again brought into resonance. The field separation, ΔH between the steps is proportional to D and is given by equation 5-7.

$$\Delta H = |D|/g\mu_B \quad (5-7)$$

Measurement of the step positions in Figure 5-16 gave an average ΔH of 0.1 T and a resulting $|D|/g\mu_B$ value of 0.046 cm^{-1} (where $D \approx 0.09 \text{ cm}^{-1}$, for $g \approx 2.0$).

Concluding Remarks

Five Mn_4Ln_2 complexes of rare, fused double-cubane metal topology containing isotropic, anisotropic and diamagnetic lanthanides have been reported with thorough syntheses, crystal structures and magnetic analyses. All five complexes follow a similar reaction scheme with a comparable yield. The Gd^{3+} and Tb^{3+} analogues were structurally characterized by X-Ray crystallography and the rest of the family members were characterized by IR and elemental analysis. Spin-orbit coupling is much larger for trivalent lanthanides than for a 3d metal ion, which complicates the magnetic investigation of the heterometallic complexes. In this regard, the isotropic Gd^{3+} and diamagnetic Y^{3+} analogues of the Mn_4Ln_2 complexes help to understand the magnetic properties of the clusters in detail. The use of the diamagnetic Y^{3+} analogue helps to nail down the type of exchange interactions between Mn and Ln metal ions in the core. The Tb^{3+} analogue is a new member in the wide family of 3d/4f, heterometallic SMMs proved by single-crystal hysteresis study.

Table 5-1. Crystallographic data for **5-1**·3MeCN and **5-2**·0.5MeCN

parameter	5-1	5-2
Formula	C ₅₆ H ₁₀₃ Gd ₂ Mn ₄ N ₉ O ₂₈	C ₅₂ H ₉₇ Mn ₄ N ₇ O ₂₈ Tb ₂
fw, g/mol	1884.73	1805.97
crystal system	Monoclinic	Monoclinic
space group	C2/c	C2/c
a, Å	24.733(4)	24.2909(15)
b, Å	13.810(2)	14.4236(9)
c, Å	22.262(4)	21.8221(13)
α, β, γ, °	90, 104.651(9), 90	90, 109.987(1), 90
V, Å ³	7357(2)	7185.1(8)
Z	4	4
T,K	100(2)	100(2)
Radiation, Åa	0.71073	0.71073
ρ, g/cm ³	1.702	1.669
μ, mm ⁻¹	2.527	2.705
R1b,c	0.0368	0.0300
wR2d	0.0901	0.0606

^a Graphite monochromator. ^b $I > 2\sigma(I)$. ^c $R1 = \sum(|F_o| - |F_c|) / \sum|F_o|$. ^d $wR2 = [\sum[w(F_o^2 - F_c^2)^2] / \sum[w(F_o^2)^2]]^{1/2}$, $w = 1/[\sigma^2(F_o^2) + [(ap)^2 + bp]$, where $p = [\max(F_o^2, 0) + 2F_c^2]/3$

Table 5-2. Bond-valence sums for the O atoms of complex **5-1**^a

Atom	BVS	Assignment	Group
O1	2.05	RO ⁻	edteH ₂ ²⁻
O2	1.45	ROH	edteH ₂ ²⁻
O3	1.29	ROH	edteH ₂ ²⁻
O4	1.99	RO ⁻	edteH ₂ ²⁻
O5	1.96	O ²⁻	O ²⁻

^aThe BVS values for O atoms of O²⁻ (RO⁻), ROH and H₂O groups are typically 1.8 - 2.0, 1.0 - 1.2 and 0.2 - 0.4, respectively, but can be affected somewhat by hydrogen-bonding.

Table 5-3. Bond-valence sums for the Mn atoms of complex **5-1** and **5-2**^a

Atom	5-1			5-2		
	Mn ²⁺	Mn ³⁺	Mn ⁴⁺	Mn ²⁺	Mn ³⁺	Mn ⁴⁺
Mn1	<u>2.24</u>	2.09	2.04	3.35	<u>3.09</u>	3.04
Mn1	3.39	<u>3.13</u>	3.07	<u>2.23</u>	2.13	2.07

^a The underlined value is the one closest to the charge for which it was calculated. The oxidation state of a particular atom can be taken as the nearest whole number to the underlined value.

Table 5-4. Magnetic data summarized from the dc measurements

Compounds	Ground state of the Ln ³⁺ ion	$\chi_M T$ (cm ³ mol ⁻¹ K) expected for non-interacting ions per complex	$\chi_M T$ (cm ³ mol ⁻¹ K) measured at 300K per complex	$\chi_M T$ (cm ³ mol ⁻¹ K) measured at 5K per complex
Mn ₄ Gd ₂ (5-1)	⁸ S _{7/2}	30.51	27.71	63.93
Mn ₄ Tb ₂ (5-2)	⁷ F ₆	38.39	35.57	70.39
Mn ₄ Dy ₂ (5-3)	⁶ H _{15/2}	43.09	37.42	59.24
Mn ₄ Ho ₂ (5-4)	⁵ I ₈	42.89	39.52	48.76
Mn ₄ Y ₂ (5-5)	¹ S ₀	14.75	11.36	8.02

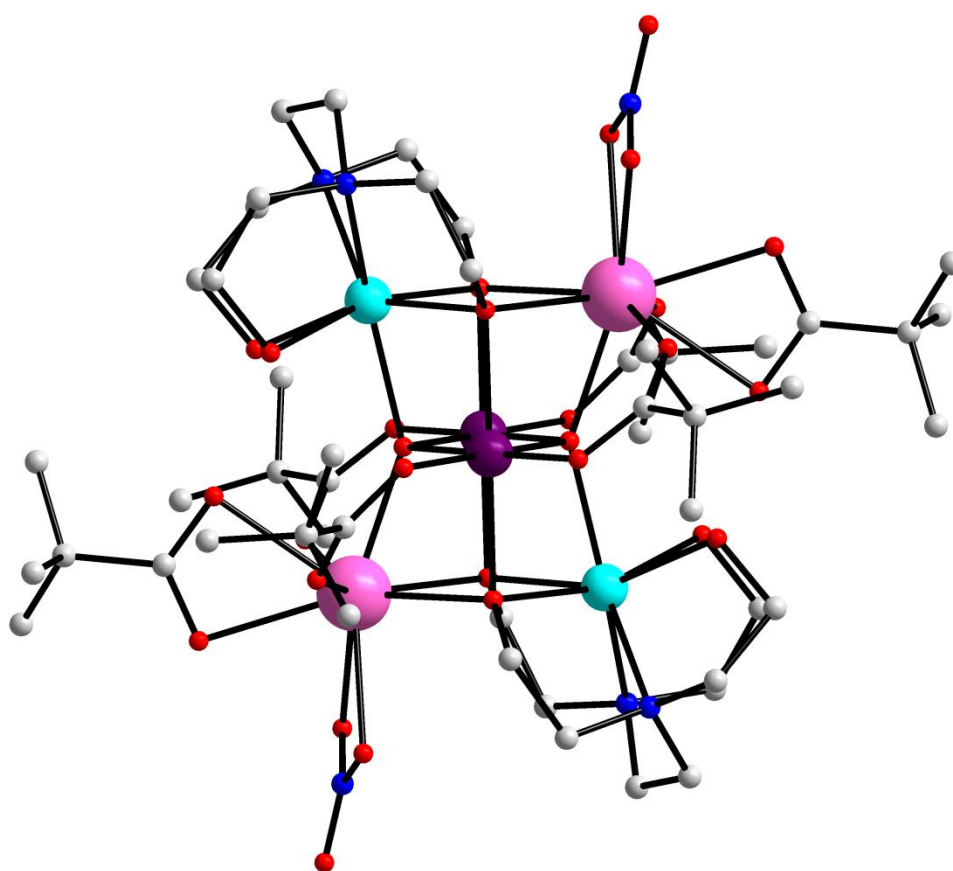


Figure 5-1. The structure of **5-1**. Hydrogen atoms have been omitted for clarity. Color code: Mn³⁺, purple; Mn²⁺, cyan; Gd³⁺, pink; O, red; N, blue; C, light-grey

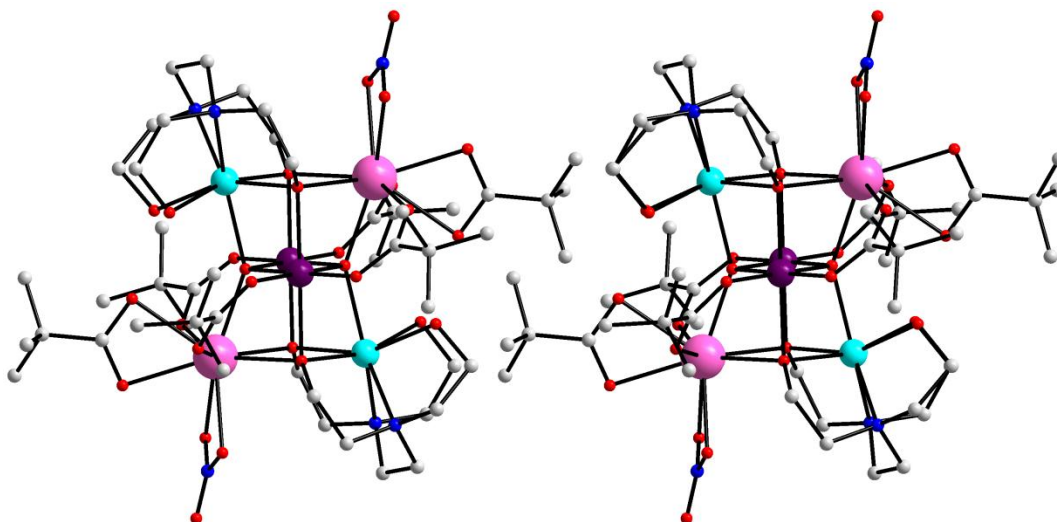


Figure 5-2. The stereopair of **5-1**. Hydrogen atoms have been omitted for clarity. Color code: Mn³⁺, purple; Mn²⁺, cyan; Gd³⁺, pink; O, red; N, blue; C, light-grey

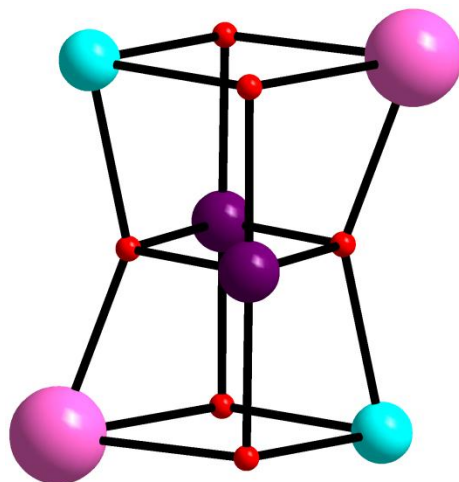


Figure 5-3. The core of **5-1**. Hydrogen atoms have been omitted for clarity. Color code: Mn³⁺, purple; Mn²⁺, cyan; Gd³⁺, pink; O, red.

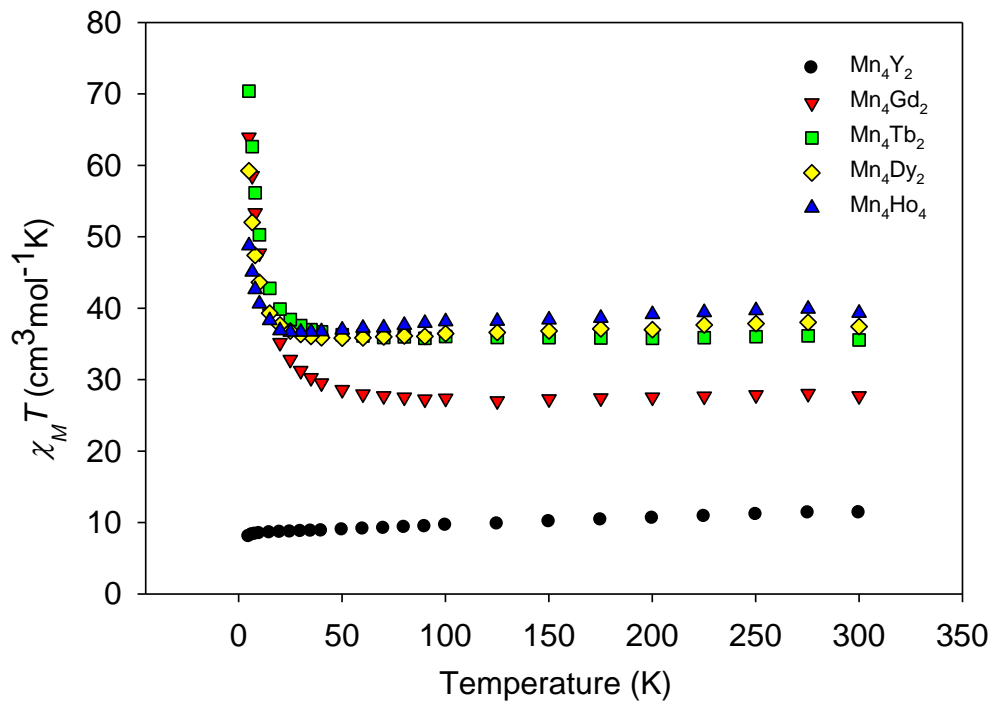


Figure 5-7. Plot of $\chi_M T$ vs. T for complexes 5-1 to 5-5

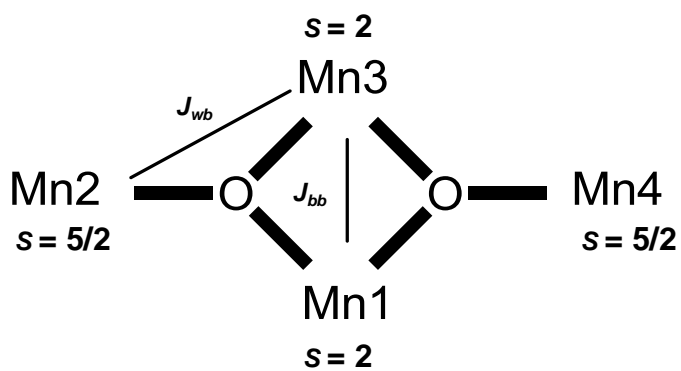


Figure 5-8. Schematic diagram for Mn₄ core with two exchange coupling parameters, J_{wb} and J_{bb}

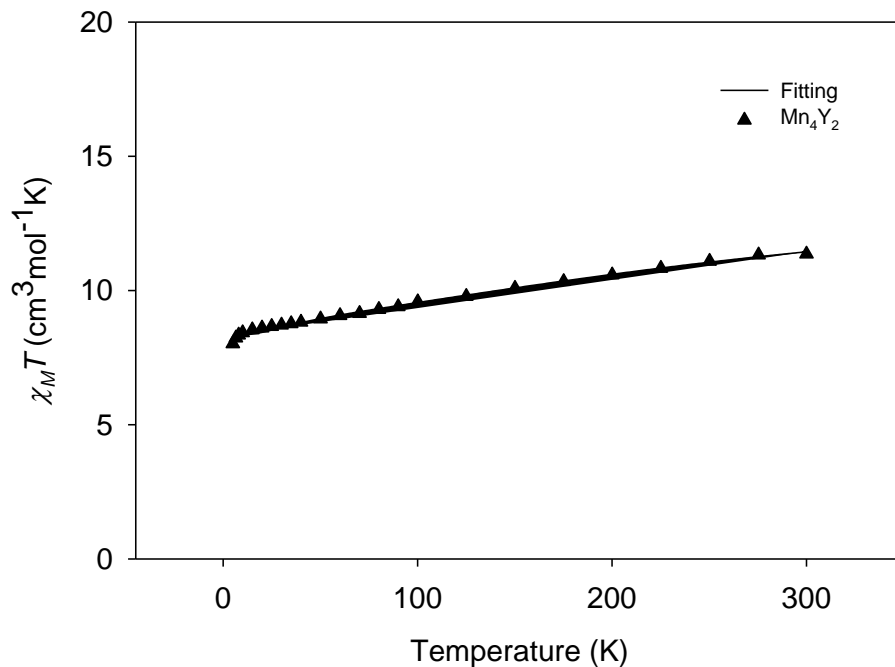


Figure 5-9. Plot of $\chi_M T$ vs. T for complex **5-5** where the solid line shows the fit of the experimental data. See the text for the fit parameters.

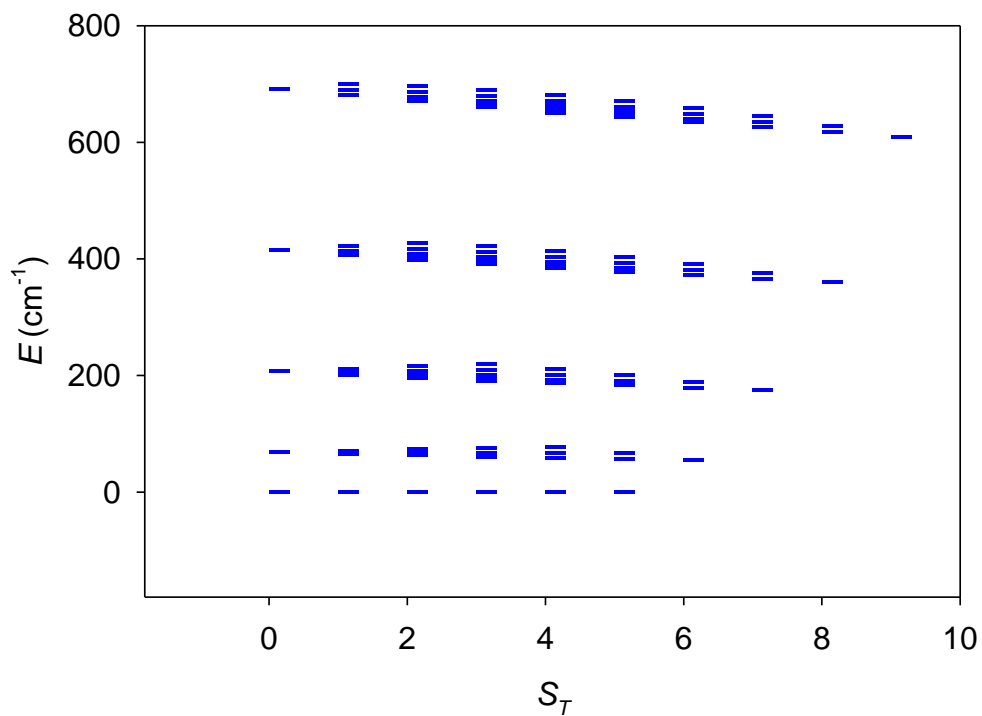


Figure 5-10. Plot of all possible energy states for complex **5-5** using the J values, obtained from the fit to the experimental $\chi_M T$ data.

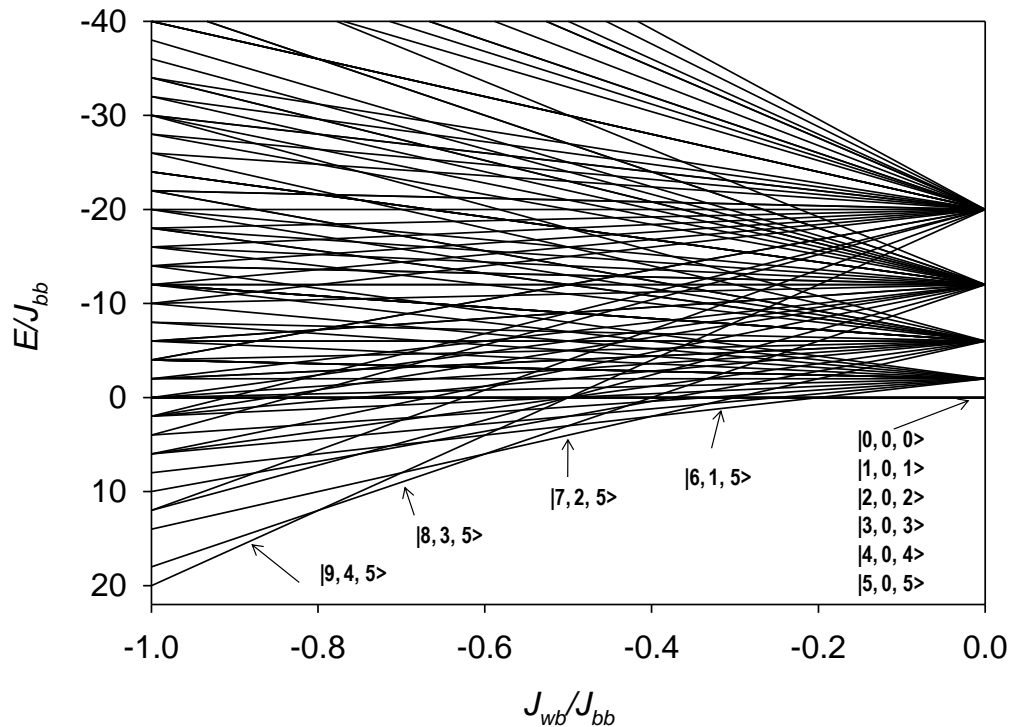


Figure 5-11. Plot of energies of various spin states vs. the ratio of J_{wb}/J_{bb} .

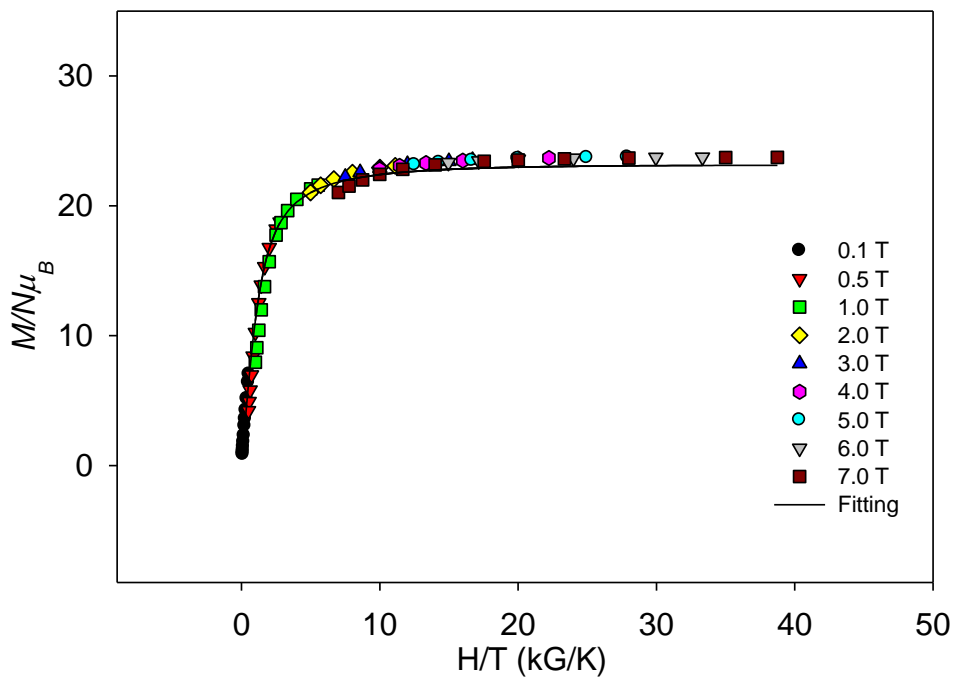


Figure 5-12. Plot of reduced magnetization ($M/N\mu_B$) vs. H/T for complex **5-1** at applied fields of 0.1 - 7.0 T in the 1.8 - 10 K temperature range. The solid lines are the fit of the data; see the text for the fit parameters.

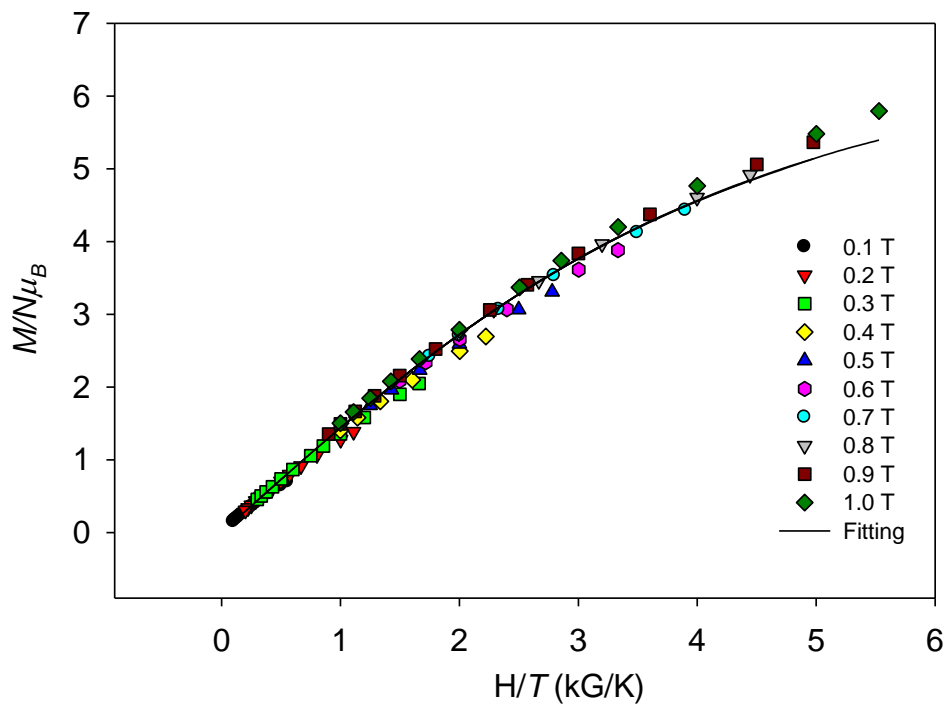


Figure 5-13. Plots of reduced magnetization ($M/N\mu_B$) vs. H/T for complex **5-5** at the applied fields of 0.1 – 1.0 T, in the 1.8 - 10 K temperature range. The solid lines are the fit of the data; see the text for the fit parameters.

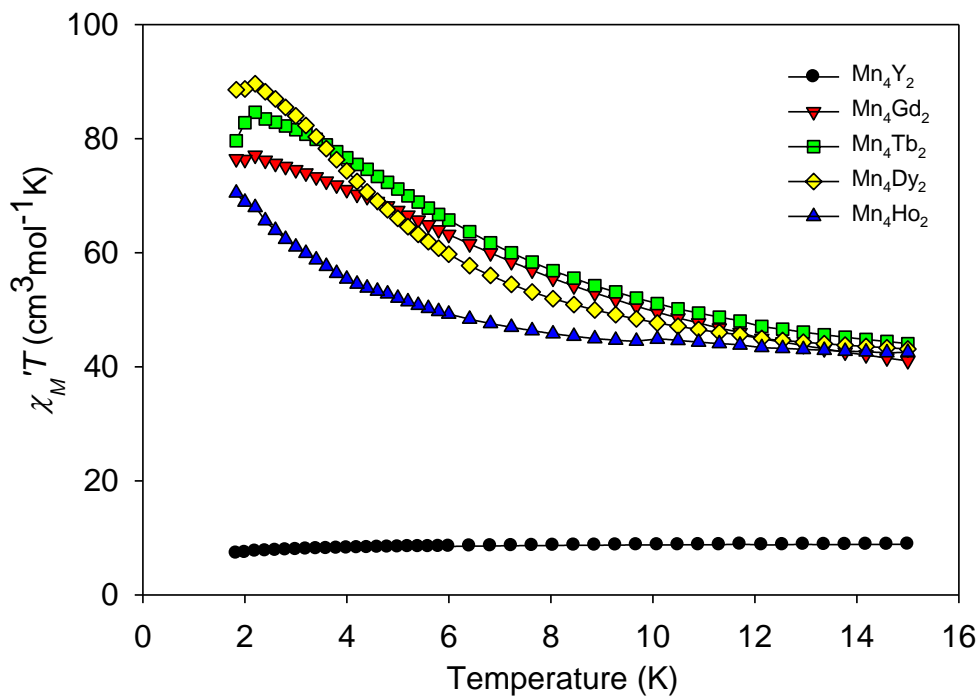


Figure 5-14. Plot of in-phase χ_M' (as $\chi_M'T$) vs. T ac signals at 250 Hz for complexes **5-1** to **5-5**

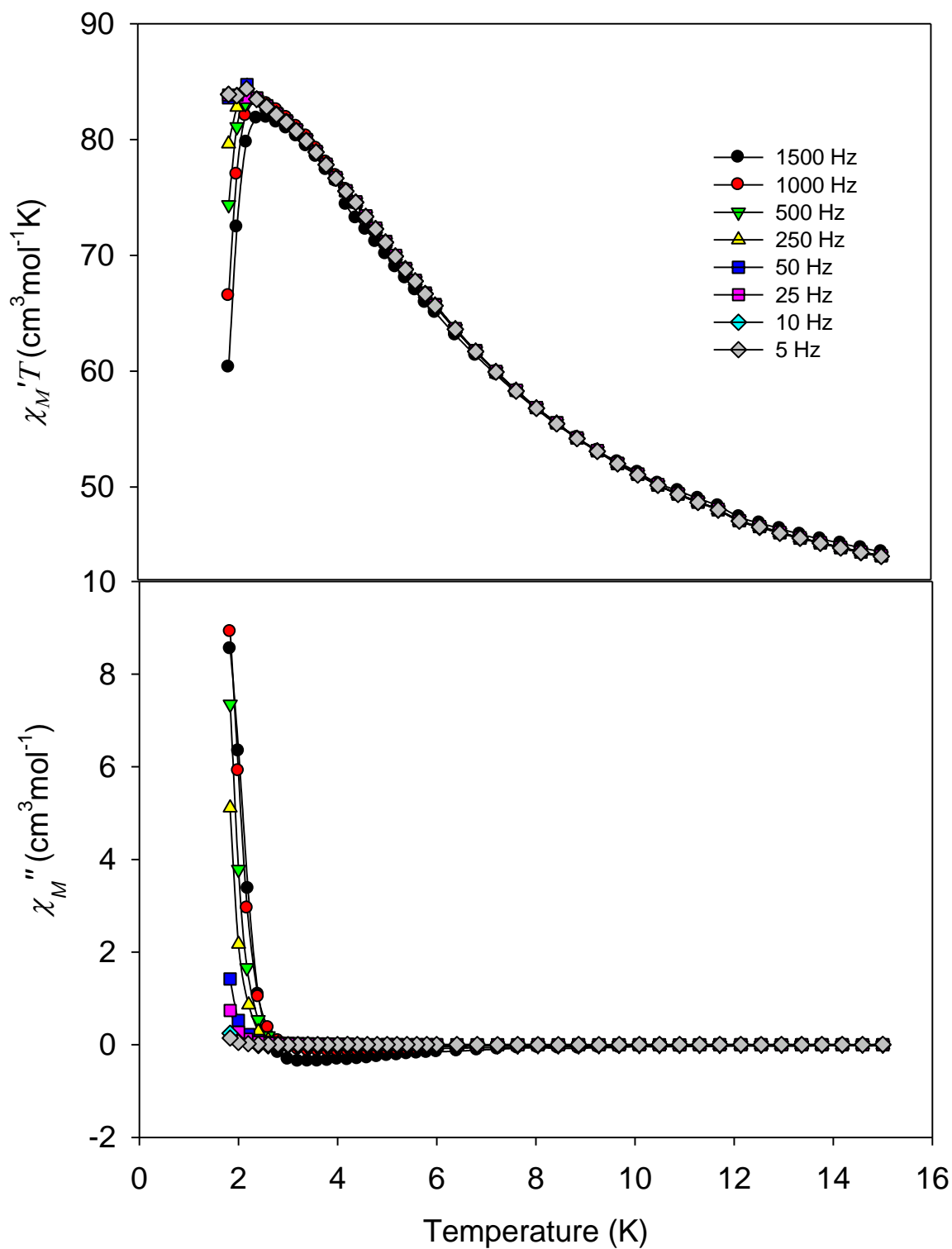
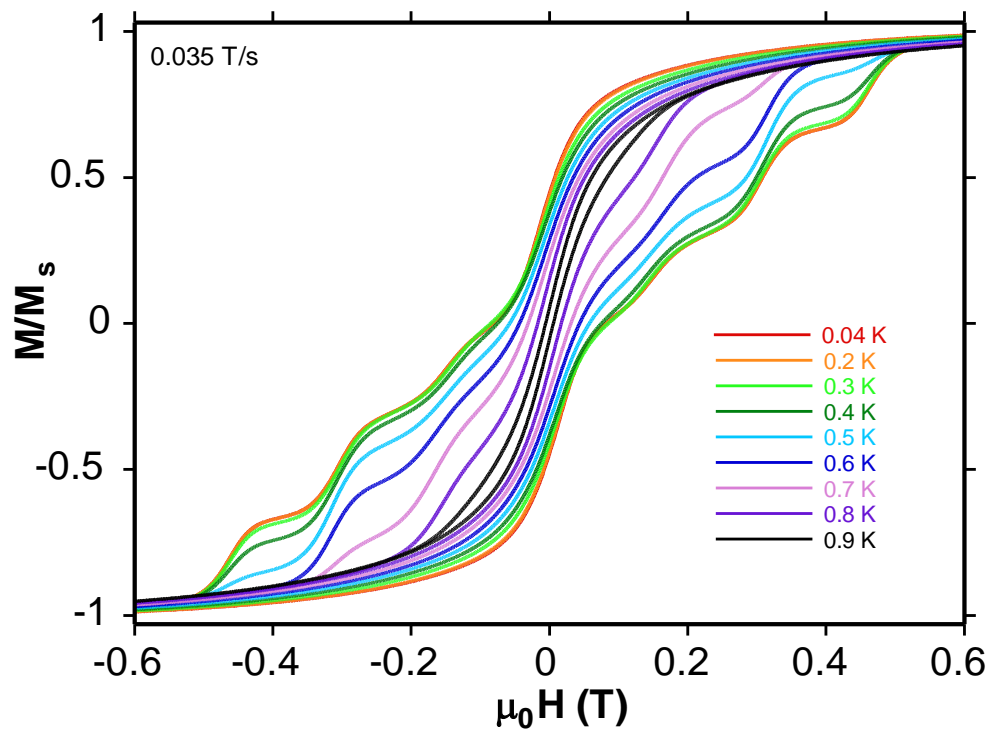


Figure 5-15. Plots of in-phase χ_M' (as $\chi_M' T$) vs. T and out-of-phase χ_M'' vs. T ac signals for complex **5-2** at the indicated frequencies

A



B

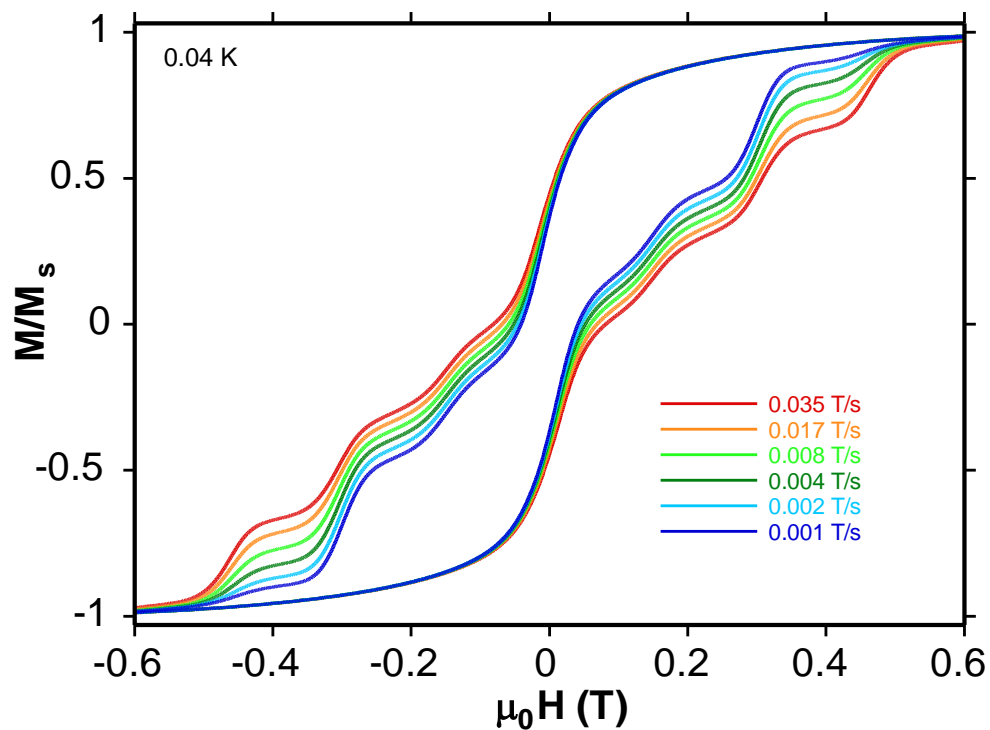


Figure 5-16. Magnetization (M) vs. dc field hysteresis loops for a single crystal of **5-2** at the indicated temperature (A) and the field sweep rate (B). The magnetization is normalized to its saturation value, M_S .

APPENDIX A
BOND DISTANCES AND ANGLES

Table A-1. Selected interatomic distances (Å) and angles (deg) for **2-1•MeCN**

2-1•MeCN			
Mn1...Mn2	3.191(1)	Mn3-O2	2.124(4)
Mn1...Mn3	3.224(1)	Mn3-O1	2.227(4)
Mn2...Mn3	3.199(1)	Mn3-N1	2.257(5)
Mn1-O1'	1.880(3)	Mn3-O4	2.264(4)
Mn1-O2	1.896(4)	Mn3-N2	2.280(5)
Mn1-O1	2.039(4)	Mn2-O1-Mn1	104.1(2)
Mn1-O4'	2.059(4)	Mn2-O1-Mn3	97.9(1)
Mn1-O6	2.084(3)	Mn1-O1-Mn3	98.1(2)
Mn2-O1	2.010(4)	Mn1-O2-Mn3	106.5(2)
Mn2-O3	2.069(4)	Mn3-O3-Mn2	107.4(2)
Mn2-O5'	2.078(4)	Mn2'-O4-Mn3	96.5(2)
Mn2-O4'	2.209(4)	Mn3-O5-Mn2'	114.6(2)
Mn3-O5	1.886(4)	Mn1''-O6-Mn1	128.8(3)
Mn3-O3	1.898(4)		

^a unprimed, primed, and double-primed atoms are related by the symmetry.

Table A-2. Selected interatomic distances (Å) and angles (deg) for **2-2•3MeCN**

2-2•3MeCN			
Mn1...Mn3	3.196(1)	Mn7...Mn9	3.193(2)
Mn1...Mn2	3.239(2)	Mn7...Mn8	3.224(2)
Mn2...Mn12	3.153(1)	Mn9...Mn11	3.149(1)
Mn3...Mn5	3.129(2)	Mn10...Mn12	3.223(1)
Mn4...Mn6	3.236(2)	Mn10...Mn11	3.231(1)
Mn5...Mn6	3.122(2)	Mn11...Mn12	3.132(1)
Mn6...Mn8	3.166(1)	Mn2-O17	2.128(4)
Mn1-O1	1.885(4)	Mn3-O17	2.098(4)
Mn2-O1	2.148(5)	Mn12-O17	1.840(4)
Mn1-O2	2.397(5)	Mn3-O18	1.980(4)
Mn11-O2	2.111(5)	Mn9-O18	2.001(4)
Mn12-O2	2.107(5)	Mn6-N30	2.183(6)
Mn1-O3	2.137(4)	Mn12-N30	2.119(6)
Mn3-O3	1.881(4)	Mn2-N12	2.244(6)
Mn1-O4	1.890(4)	Mn12-N12	2.082(6)
Mn11-O4	2.120(5)	Mn1-N2	2.259(6)
Mn1-O17	2.109(4)	Mn1-N1	2.289(6)
Mn1-O1-Mn2	106.7(2)	Mn3-O17-Mn1	98.9(2)

Mn1-O2-Mn11	96.3(2)	Mn12-O17-Mn2	105.0(2)
Mn1-O3-Mn3	105.2(2)	Mn3-O17-Mn2	102.6(2)
Mn1-O4-Mn11	113.9(2)	Mn1-O17-Mn2	99.8(2)
Mn12-O17-Mn3	134.7(2)	Mn3-O18-Mn9	130.2(2)
Mn12-O17-Mn1	110.8(2)	Mn2-N12-Mn12	93.5(2)

Table A-3. Selected interatomic distances (Å) and angles (deg) for **2-3**·MeCN

2-3 ·MeCN			
Mn1...Mn2'	3.127(1)	Mn2...Mn3	3.196(2)
Mn1...Mn2	3.197(2)	Mn2...Mn1''	3.127(1)
Mn1...Mn3	3.224(1)	Mn3-O5	1.900(6)
Mn1-O1	2.037(5)	Mn2-O5'	2.059(6)
Mn2-O1	2.009(5)	Mn1-O6	2.049(9)
Mn3-O1	2.202(5)	Mn1-N6	2.151(15)
Mn1-O2	1.901(5)	Mn1-N3	2.174(8)
Mn3-O2	2.130(5)	Mn2-N3'	2.185(8)
Mn2-O3	2.075(6)	Mn3-N1	2.245(7)
Mn3-O3	1.884(5)	Mn3-N2	2.274(7)
Mn3-O4	2.254(5)	Mn1-O2-Mn3	106.1(2)
Mn1-O4'	2.061(5)	Mn3-O3-Mn2	107.5(2)
Mn2-O4'	2.220(5)	Mn1'-O4-Mn2'	96.6(2)
Mn1'-O1-Mn2	106.4(3)	Mn1'-O4-Mn3	98.5(2)
Mn1'-O1-Mn1	136.7(3)	Mn2'-O4-Mn3	96.5(2)
Mn2-O1-Mn1	104.4(2)	Mn3-O5-Mn2'	114.9(3)
Mn1'-O1-Mn3	105.7(2)	Mn1''-O6-Mn1	132.7(11)
Mn2-O1-Mn3	98.6(2)		

Table A-4. Selected interatomic distances (Å) and angles (deg) for **3-1**·4MeCN

3-1 ·4MeCN			
Mn(1)...Mn(2)	2.928(1)	Mn(1)...Mn(3)	3.301(1)
Mn(3)...Mn(4)	3.183(1)	Mn(2)...Mn(3)	3.443(1)
Mn(4)...Mn(6)	2.825(1)	Mn(2)...Mn(4)	3.416(1)
Mn(4)...Mn(5)	3.339(1)	Mn(3)...Mn(5)	3.316(1)
Mn(6)...Mn(5)	3.349(1)	Mn3-O18	2.183(2)
Mn1-O28	1.871(2)	Mn3-O19	1.977(2)
Mn1-N1	1.987(3)	Mn3-O20	1.905(2)
Mn2-O15	1.913(3)	Mn3-O28	1.879(2)
Mn2-O17	1.917(2)	Mn4-O17	2.004(2)

Mn2-O28	1.923(2)	Mn4-O18	1.911(2)
Mn2-N7	2.144(3)	Mn4-O19	2.188(2)
Mn2-N8	2.371(3)	Mn4-O27	2.050(2)
Mn6-O21	2.191(2)	Mn4-O29	1.807(2)
Mn6-O23	2.008(2)	Mn5-O20	2.222(2)
Mn6-O24	1.914(2)	Mn5-O27	2.230(2)
Mn6-O27	2.045(2)	Mn5-O22	2.246(2)
Mn6-O29	1.813(2)	Mn5-O21	2.269(2)
Mn5-N10	2.304(3)	Mn5-O19	2.285(2)
Mn5-N9	2.361(3)	Mn6-O21-Mn5	97.30(9)
Mn2-O15-Mn1	92.84(10)	Mn6-O27-Mn4	87.22(10)
Mn2-O17-Mn4	121.20(12)	Mn6-O27-Mn5	103.03(9)
Mn4-O18-Mn3	101.89(10)	Mn4-O27-Mn5	102.45(9)
Mn3-O19-Mn4	99.54(10)	Mn1-O28-Mn3	123.36(13)
Mn3-O19-Mn5	101.92(10)	Mn1-O28-Mn2	101.04(11)
Mn4-O19-Mn5	96.52(9)	Mn3-O28-Mn2	129.80(12)
Mn3-O20-Mn5	106.70(11)	Mn4-O29-Mn6	102.59(12)

Table A-5. Selected interatomic distances (Å) and angles (deg) for **4-1**·4CH₂Cl₂ and **4-2**·MeCN,

4-1 ·4CH ₂ Cl ₂		4-2 ·MeCN	
Mn(1)...Mn(2)	3.131(1)	Mn(1)...Mn(2)	3.144(1)
Mn(1)-O(3)	1.902(3)	Mn(1)-O(3)	2.163(2)
Mn(1)-O(1)	1.933(3)	Mn(1)-O(6)	2.235(2)
Mn(2)-O(3)	2.177(3)	Mn(1)-O(1)	2.334(2)
Mn(2)-O(1)	2.213(3)	Mn(1)-O(2)	2.308(3)
Mn(2)-O(4)	2.275(3)	Mn(1)-O(4)	2.160(2)
Mn(2)-O(2)	2.297(3)	Mn(1)-N(1)	2.374(3)
Mn(2)-N(2)	2.379(4)	Mn(1)-N(2)	2.386(3)
Mn(2)-N(1)	2.427(3)	Mn(2)-O(3)	1.907(2)
Mn(1)-O(1)-Mn(2)	97.98(12)	Mn(2)-O(6)	1.931(2)
Mn(1)-O(3)-Mn(2)	100.21(12)	Mn(2)-O(5)	2.250(2)
Mn(1)-O(3)-Mn(2)	100.95(10)	Mn(1)-O(6)-Mn(2)	97.73(9)

Table A-6. Selected interatomic distances (Å) and angles (deg) for **4-3** and **4-4**

4-3		4-4	
Mn1...Mn2	3.275(1)	Mn(1)...Mn(2)	3.014(1)
Mn(1)-O(1)	2.311(2)	Mn(2)...Mn(3)	3.267(1)
Mn(1)-O(2)	2.188(2)	Mn(1)...Mn(3)	3.320(1)

Mn(1)-O(3)	2.224(2)	Mn(1)-O(1)	1.948(3)
Mn(1)-O(4)	2.174(2)	Mn(1)-O(9)	2.671(4)
Mn(1)-O(5)	2.261(2)	Mn(1)-O(8)	1.901(4)
Mn(1)-N(1)	2.335(2)	Mn(1)-O(10)	1.953(4)
Mn(1)-N(2)	2.378(2)	Mn(2)-O(1)	1.869(3)
Mn(2)-O(4)	1.863(2)	Mn(2)-O(8)	2.239(4)
Mn(2)-O(5)	2.281(2)	Mn(3)-O(9)	2.111(4)
Mn(2)-N(3)	2.093(2)	Mn(1)-O(1)-Mn(2)	104.31(15)
Mn(2)-Cl(1)	2.449(1)	Mn(2)-O(1)-Mn(3)	123.07(19)
Mn(2)-O(4)-Mn(1)	110.19(9)	Mn(3)-O(1)-Mn(1)	122.03(18)
Mn(1)-O(5)-Mn(2)	93.77(7)	Mn(1)-O(8)-Mn(2)	93.09(15)
Mn(1)-O(2)-Mn(2')	107.24(9)	Mn(3)-O(9)-Mn(3')	102.24(15)
		Mn(3')-O(10)-Mn(1)	118.69(18)

Table A-7. Selected interatomic distances (Å) and angles (deg) for **4-5·2MeCN**

4-5·2MeCN			
Mn(1)...Mn(2')	3.218(1)	Mn(3)...Mn(5)	3.089(1)
Mn(1)...Mn(2)	3.245(1)	Mn(3)...Na(1)	3.276(1)
Mn(1)...Mn(3)	3.224(1)	Mn(3)...Mn(4)	2.955(1)
Mn(1)...Mn(4)	3.541(1)	Mn(4)...Mn(5)	3.023(1)
Mn(2)...Mn(3)	2.843(1)	Mn(5)...Na(1)	3.438(1)
Mn(2)...Mn(2')	3.311(1)	Mn(5)...Mn(1)	3.269(1)
Mn(1)-O(3)	2.205(2)	Mn(3)-O(7)	1.943(2)
Mn(1)-O(1)	2.237(2)	Mn(3)-O(13)	1.873(2)
Mn(1)-O(4)	2.243(2)	Mn(3)-O(14)	1.916(2)
Mn(1)-O(2)	2.364(2)	Mn(4)-O(2')	1.950(2)
Mn(1)-O(13)	2.214(2)	Mn(4)-O(4')	2.318(2)
Mn(2)-O(1)	1.938(2)	Mn(4)-O(14)	1.909(3)
Mn(2)-O(7)	1.963(2)	Mn(5)-O(13)	2.345(2)
Mn(2)-O(13)	1.902(2)	Mn(5)-O(14)	1.939(2)
Mn(3)-O(2)	2.254(2)	Mn(5)-O(4')	1.953(2)
Mn(2)-O(1)-Mn(1)	100.65(8)	Mn(3)-O(13)-Mn(2)	97.75(9)
Mn(2)-O(1)-Mn(2')	101.06(8)	Mn(3)-O(13)-Mn(1)	103.83(8)
Mn(1)-O(1)-Mn(2')	90.29(7)	Mn(2)-O(13)-Mn(1)	103.77(9)
Mn(4)-O(2)-Mn(1)	109.99(8)	Mn(3)-O(13)-Mn(5)	93.51(8)
Mn(3)-O(2)-Mn(1)	88.53(6)	Mn(2)-O(13)-Mn(5)	158.11(10)
Mn(2)-O(3)-Mn(1)	103.41(9)	Mn(4)-O(14)-Mn(3)	101.16(9)
Mn(5)-O(4)-Mn(1)	102.14(8)	Mn(4)-O(14)-Mn(5)	103.54(9)
Mn(5)-O(4)-Mn(4)	89.68(8)	Mn(3)-O(14)-Mn(5)	106.54(9)
Mn(1)-O(4)-Mn(4)	101.86(8)	Mn(4)-O(14)-Na(1)	141.69(10)

Mn(3)-O(7)-Mn(2)	93.46(8)	Mn(3)-O(14)-Na(1)	97.05(8)
Mn(1)-O(13)-Mn(5)	91.58(7)	Mn(5)-O(14)-Na(1)	103.11(8)

Table A-8. Selected interatomic distances (Å) and angles (deg) for **4-6**·2MeCN

4-6 ·2MeCN			
Mn(1)...Mn(2')	3.283(1)	Mn(3)...Mn(4)	2.861(1)
Mn(1)...Mn(4)	3.242(1)	Mn(3)...Mn(5)	2.986(1)
Mn(2)...Mn(3)	3.079(1)	Mn(4)...Mn(1')	3.225(1)
Mn(5)...Mn(2)	3.014(1)	Mn(1)...Mn(4')	3.225(1)
Mn(5)...Mn(3)	2.986(1)	Mn(3)...Mn(1)	3.254(1)
Mn(1)-O(3)	2.190(2)	Mn(3)-O(12)	1.907(2)
Mn(1)-O(11)	2.213(2)	Mn(3)-O(13)	1.995(2)
Mn(1)-O(1)	2.237(2)	Mn(4)-O(3')	1.886(2)
Mn(1)-O(10)	2.251(2)	Mn(4)-O(11)	1.892(2)
Mn(1)-O(2)	2.350(2)	Mn(4)-O(10')	1.956(2)
Mn(2)-O(1)	1.978(2)	Mn(4)-O(13)	1.993(2)
Mn(2)-O(11)	2.356(2)	Mn(4)-O(10)	2.315(2)
Mn(2)-O(12)	1.923(2)	Mn(5)-O(12)	1.897(2)
Mn(3)-O(11)	1.872(2)	Mn(5)-O(2)	1.958(2)
Mn(2)-O(1)-Mn(1)	102.16(8)	Mn(5)-O(1)	2.297(2)
Mn(2)-O(1)-Mn(5)	89.33(8)	Mn(3)-O(11)-Mn(4)	98.95(9)
Mn(1)-O(1)-Mn(5)	101.06(8)	Mn(3)-O(11)-Mn(1)	105.29(9)
Mn(5)-O(2)-Mn(3)	88.84(7)	Mn(4)-O(11)-Mn(1)	104.06(9)
Mn(5)-O(2)-Mn(1)	108.39(9)	Mn(3)-O(11)-Mn(2)	92.77(8)
Mn(3)-O(2)-Mn(1)	88.95(7)	Mn(4)-O(11)-Mn(2)	156.88(11)
Mn(4')-O(3)-Mn(1)	104.38(9)	Mn(1)-O(11)-Mn(2)	91.83(7)
Mn(4')-O(10)-Mn(1)	99.87(8)	Mn(5)-O(12)-Mn(3)	103.44(9)
Mn(4)-O(13)-Mn(3)	91.69(9)	Mn(5)-O(12)-Mn(2)	104.16(10)
Mn(1)-O(10)-Mn(4)	90.48(7)	Mn(3)-O(12)-Mn(2)	107.01(9)

Table A-9. Selected interatomic distances (Å) and angles (deg) for **4-7**·x(Solv)

4-7 ·x(Solv)			
Mn(1)...Mn(1')	2.8792(17)	Mn(3)...Mn(7)	2.7524(11)
Mn(1)...Mn(4)	3.1234(10)	Mn(3)...Mn(4)	3.1561(11)
Mn(1)...Mn(5')	3.2149(10)	Mn(4)...Mn(7)	3.0442(11)
Mn(1)...Mn(3)	3.2225(10)	Mn(4)...Mn(6)	3.0613(13)
Mn(1)...Mn(3')	3.2366(12)	Mn(5)...Mn(7)	3.0895(13)
Mn(1)...Mn(2)	3.2988(12)	Mn(5)...Mn(6)	3.1213(12)
Mn(2)...Mn(3')	3.2171 (10)	Mn(5)...Mn(1')	3.2149(10)
Mn(3)...Mn(5)	3.2186(13)	Mn(8)...Mn(10)	3.2311(15)

Mn(3)...Mn(1')	3.2367(12)	Mn(9)...Mn(10)	103.3222(12)
Mn(1)-O(1')	1.897(4)	Mn(1')-O(1)-Mn(5)	109.0(2)
Mn(1)-O(3)	1.929(4)	Mn(1')-O(2)-Mn(1)	96.30(15)
Mn(1)-O(2')	1.932(4)	Mn(1')-O(2)-Mn(2)	99.12(16)
Mn(1)-O(2)	1.933(4)	Mn(1)-O(2)-Mn(2)	101.20(14)
Mn(1)-O(11)	2.257(4)	Mn(1')-O(2)-Mn(4)	168.99(18)
Mn(1)-O(9')	2.285(4)	Mn(1)-O(2)-Mn(4)	89.30(14)
Mn(2)-O(10)	2.240(4)	Mn(2)-O(2)-Mn(4)	89.03(12)
Mn(2)-O(9)	2.258(3)	Mn(1')-O(2)-Mn(3)	92.12(13)
Mn(2)-O(11)	2.284(4)	Mn(1)-O(2)-Mn(3)	91.56(15)
Mn(2)-O(8)	2.317(4)	Mn(2)-O(2)-Mn(3)	161.88(15)
Mn(2)-O(2)	2.324(4)	Mn(4)-O(2)-Mn(3)	78.22(11)
Mn(3)-O(4)	1.862(4)	Mn(1)-O(3)-Mn(4)	106.76(18)
Mn(3)-O(5)	1.907(4)	Mn(3)-O(4)-Mn(7)	94.50(19)
Mn(3)-O(9')	1.937(4)	Mn(3)-O(4)-Mn(5)	110.44(17)
Mn(3)-O(11')	1.959(4)	Mn(7)-O(4)-Mn(5)	103.20(17)
Mn(3)-O(20)	2.142(4)	Mn(3)-O(5)-Mn(7)	91.73(17)
Mn(3)-O(2)	2.526(4)	Mn(3)-O(5)-Mn(4)	110.38(19)
Mn(4)-O(6)	1.915(4)	Mn(7)-O(5)-Mn(4)	103.94(19)
Mn(4)-O(5)	1.937(4)	Mn(6)-O(6)-Mn(4)	107.95(19)
Mn(4)-O(10)	1.942(4)	Mn(6)-O(6)-Mn(7)	157.1(2)
Mn(4)-O(3)	1.963(4)	Mn(4)-O(6)-Mn(7)	93.77(18)
Mn(4)-O(16)	2.186(4)	Mn(6)-O(6)-Mn(5)	95.7(2)
Mn(4)-O(2)	2.477(4)	Mn(4)-O(6)-Mn(5)	104.98(17)
Mn(5)-O(1)	2.051(4)	Mn(7)-O(6)-Mn(5)	85.21(14)
Mn(5)-O(4)	2.054(4)	Mn(8)-O(7)-Mn(6)	138.3(2)
Mn(5)-O(12)	2.099(4)	Mn(6)-O(8)-Mn(5)	98.37(18)
Mn(5)-O(8)	2.131(4)	Mn(6)-O(8)-Mn(2)	108.36(19)
Mn(5)-O(6)	2.319(5)	Mn(5)-O(8)-Mn(2)	100.07(17)
Mn(6)-O(6)	1.870(4)	Mn(3')-O(9)-Mn(2)	104.71(16)
Mn(6)-O(22)	1.935(4)	Mn(3')-O(9)-Mn(1')	99.17(17)
Mn(6)-O(18)	1.955(4)	Mn(2)-O(9)-Mn(1')	91.32(13)
Mn(6)-O(8)	1.991(4)	Mn(4)-O(10)-Mn(2)	107.05(16)
Mn(6)-O(7)	2.085(4)	Mn(4)-O(10)-Mn(6)	90.86(15)
Mn(6)-O(10)	2.338(4)	Mn(2)-O(10)-Mn(6)	99.64(17)
Mn(7)-O(4)	1.886(4)	Mn(3')-O(11)-Mn(1)	100.06(15)
Mn(7)-O(5)	1.928(4)	Mn(3')-O(11)-Mn(2)	103.03(16)
Mn(7)-O(17)	1.971(4)	Mn(1)-O(11)-Mn(2)	93.18(13)
Mn(7)-O(13)	1.975(4)	Mn(7)-O(13)-Mn(10)	103.83(18)
Mn(7)-O(21)	2.138(4)	Mn(7)-O(13)-Mn(8)	122.69(18)
Mn(7)-O(6)	2.244(4)	Mn(10)-O(13)-Mn(8)	90.85(14)
Mn(8)-O(7)	1.869(4)	Mn(8)-O(14)-Mn(10)	106.30(19)
Mn(8)-O(12)	1.904(4)	Mn(9)-O(16)-Mn(4)	107.75(18)
Mn(8)-O(14)	1.909(4)	Mn(7)-O(17)-Mn(9)	116.98(19)
Mn(8)-O(13)	2.285(5)	Mn(7)-O(17)-Mn(10)	98.01(17)
Mn(9)-O(19)	1.879(4)	Mn(9)-O(17)-Mn(10)	93.34(15)

Mn(9)-O(16)	1.901(4)	Mn(6)-O(18)-Mn(9)	118.8(2)
Mn(9)-O(18)	2.012(5)	Mn(9)-O(19)-Mn(10)	113.22(19)
Mn(9)-O(17)	2.134(4)	Mn(10)-(O24')	2.213(10)
Mn(10)-O(19)	2.098(4)	Mn(10)-O(13)	2.251(4)
Mn(10)-O(14)	2.125(5)	Mn(10)-O(24)	2.263(14)
Mn(10)-O(25)	2.150(7)	Mn(10)-O(170)	2.425(4)

Table A-10. Selected interatomic distances (Å) and angles (deg) for **4-8·5MeCN**

4-8·5MeCN			
Mn(1)...Mn(2)	2.756(3)	Mn(7)...Mn(12)	2.901(3)
Mn(1)...Mn(8)	3.071(3)	Mn(7)...Mn(8)	3.120(3)
Mn(1)...Mn(11)	3.090(3)	Mn(7)...Mn(16)	3.213(3)
Mn(2)...Mn(11)	3.177(3)	Mn(8)...Mn(18)	3.088(3)
Mn(2)...Mn(8)	3.178(3)	Mn(11)...Mn(18)	3.138(3)
Mn(4)...Mn(6)	3.102(3)	Mn(11)...Mn(12)	3.155(3)
Mn(4)...Mn(13)	3.118(3)	Mn(12)...Mn(13)	3.166(3)
Mn(6)...Mn(15)	3.058(3)	Mn(13)...Mn(15)	3.103(3)
Mn(6)...Mn(7)	3.128(3)	Mn(13)...Mn(16)	3.191(3)
Mn(6)...Mn(16)	3.161(4)	Mn(15)...Mn(16)	2.758(3)
Ca(2)-O(45)	2.555(6)	Ca(1)-O(19)	2.552(6)
Ca(2)-O(46)	2.507(6)	Ca(1)-O(20)	2.345(6)
Ca(2)-O(38)	2.384(7)	Ca(1)-O(27)	2.477(5)
Ca(2)-O(12)	2.338(6)	Ca(1)-O(28)	2.357(6)
Mn(2)-O(1)	1.895(5)	Mn(2)-O(5)	1.960(5)
Mn(1)-O(1)	1.917(5)	Mn(3)-O(5)	2.251(5)
Mn(8)-O(1)	1.986(5)	Mn(7)-O(5)	2.267(5)
Mn(1)-O(2)	1.887(5)	Mn(2)-O(6)	1.947(5)
Mn(2)-O(2)	1.861(5)	Mn(3)-O(6)	2.271(5)
Mn(11)-O(2)	2.022(5)	Mn(12)-O(6)	2.276(5)
Mn(7)-O(17)	1.960(5)	Mn(3)-O(7)	2.224(6)
Mn(12)-O(17)	1.948(5)	Mn(4)-O(7)	2.253(6)
Mn(17)-O(17)	2.280(5)	Mn(6)-O(7)	2.037(5)
Mn(1)-O(31)	2.223(6)	Mn(3)-O(8)	2.248(6)
Mn(8)-O(31)	2.058(7)	Mn(4)-O(8)	2.105(7)
Mn(11)-O(31)	2.197(7)	Mn(13)-O(8)	2.095(6)
Mn(18)-O(31)	1.870(6)	Mn(4)-O(9)	1.988(6)
Mn(6)-O(14)	1.976(5)	Mn(5)-O(9)	1.990(8)
Mn(7)-O(14)	1.902(5)	Mn(5)-O(13)	1.909(5)
Mn(7)-O(16)	1.901(5)	Mn(6)-O(13)	2.145(5)
Mn(8)-O(16)	1.973(5)	Mn(5)-O(12)	1.876(6)
Mn(11)-O(32)	2.026(5)	Mn(5)-O(45)	2.180(6)
Mn(12)-O(33)	1.903(5)	Mn(15)-O(45)	1.976(5)
Mn(12)-O(32)	1.907(5)	Mn(13)-O(34)	2.107(5)
Mn(13)-O(33)	2.012(5)	Mn(14)-O(34)	1.903(6)
Mn(4)-O(36')	1.998(9)	Mn(14)-O(38)	1.882(6)

Mn(4)-O(36)	2.097(13)	Mn(15)-O(45)	1.976(5)
Mn(14)-O(36')	1.930(9)	Mn(5)-O(45)	2.180(6)
Mn(14)-O(36)	2.001(13)	Mn(1)-O(19)-Mn(9)	117.8(3)
Mn(2)-O(1)-Mn(1)	92.6(2)	Mn(1)-O(19)-Ca(1)	101.0(2)
Mn(2)-O(1)-Mn(8)	109.9(2)	Mn(9)-O(19)-Ca(1)	96.7(2)
Mn(1)-O(1)-Mn(8)	103.8(2)	Mn(9)-O(20)-Ca(1)	114.7(3)
Mn(2)-O(2)-Mn(1)	94.7(2)	Mn(1)-O(27)-Mn(10)	119.1(2)
Mn(2)-O(2)-Mn(11)	109.7(2)	Mn(1)-O(27)-Ca(1)	104.1(2)
Mn(1)-O(2)-Mn(11)	104.4(2)	Mn(10)-O(27)-Ca(1)	96.38(18)
Mn(2)-O(5)-Mn(3)	104.2(2)	Mn(10)-O(28)-Ca(1)	112.8(2)
Mn(2)-O(5)-Mn(7)	100.2(2)	Mn(10)-O(30)-Mn(11)	112.6(3)
Mn(3)-O(5)-Mn(7)	93.00(17)	Mn(18)-O(31)-Mn(8)	103.5(3)
Mn(2)-O(6)-Mn(3)	103.9(2)	Mn(18)-O(31)-Mn(11)	100.7(3)
Mn(2)-O(6)-Mn(12)	100.3(2)	Mn(8)-O(31)-Mn(11)	105.3(2)
Mn(3)-O(6)-Mn(12)	91.18(19)	Mn(18)-O(31)-Mn(1)	159.3(3)
Mn(6)-O(7)-Mn(3)	104.9(2)	Mn(8)-O(31)-Mn(1)	91.6(3)
Mn(6)-O(7)-Mn(4)	92.5(2)	Mn(11)-O(31)-Mn(1)	88.7(2)
Mn(3)-O(7)-Mn(4)	102.5(2)	Mn(12)-O(32)-Mn(11)	106.7(2)
Mn(13)-O(8)-Mn(4)	95.9(3)	Mn(12)-O(33)-Mn(13)	107.9(2)
Mn(13)-O(8)-Mn(3)	101.7(2)	Mn(14)-O(34)-Mn(13)	115.4(3)
Mn(4)-O(8)-Mn(3)	106.7(2)	Mn(4)-O(37)-Mn(6)	106.9(3)
Mn(4)-O(9)-Mn(5)	123.5(4)	Mn(4)-O(37)-Mn(13)	99.6(3)
Mn(5)-O(12)-Ca(2)	114.6(3)	Mn(6)-O(37)-Mn(13)	106.2(2)
Mn(5)-O(13)-Mn(6)	110.6(2)	Mn(4)-O(37)-Mn(15)	157.4(3)
Mn(7)-O(14)-Mn(6)	107.5(2)	Mn(6)-O(37)-Mn(15)	91.2(2)
Mn(12)-O(15)-Mn(7)	96.8(2)	Mn(13)-O(37)-Mn(15)	87.6(2)
Mn(12)-O(15)-Mn(3)	99.4(2)	Mn(14)-O(38)-Ca(2)	112.4(3)
Mn(7)-O(15)-Mn(3)	100.48(19)	Mn(15)-O(45)-Mn(5)	117.7(3)
Mn(12)-O(15)-Mn(13)	89.50(18)	Mn(15)-O(45)-Ca(2)	101.5(2)
Mn(7)-O(15)-Mn(13)	168.1(2)	Mn(5)-O(45)-Ca(2)	96.99(19)
Mn(3)-O(15)-Mn(13)	88.37(15)	Mn(15)-O(46)-Mn(14)	120.0(3)
Mn(12)-O(15)-Mn(6)	169.6(2)	Mn(15)-O(46)-Ca(2)	103.2(2)
Mn(7)-O(15)-Mn(6)	87.97(18)	Mn(14)-O(46)-Ca(2)	96.7(2)
Mn(3)-O(15)-Mn(6)	88.72(17)	Mn(16)-O(47)-Mn(15)	92.8(2)
Mn(13)-O(15)-Mn(6)	84.28(15)	Mn(16)-O(47)-Mn(6)	109.8(3)
Mn(12)-O(15)-Mn(16)	93.03(19)	Mn(15)-O(47)-Mn(6)	103.7(2)
Mn(7)-O(15)-Mn(16)	91.07(18)	Mn(16)-O(48)-Mn(15)	94.4(2)
Mn(3)-O(15)-Mn(16)	161.8(2)	Mn(16)-O(48)-Mn(13)	110.4(2)
Mn(13)-O(15)-Mn(16)	78.48(14)	Mn(15)-O(48)-Mn(13)	103.6(2)
Mn(6)-O(15)-Mn(16)	77.61(15)	Mn(16)-O(51)-Mn(7)	98.6(2)
Mn(7)-O(16)-Mn(8)	107.3(2)	Mn(16)-O(51)-Mn(17)	103.5(2)
Mn(12)-O(17)-Mn(7)	95.84(19)	Mn(7)-O(51)-Mn(17)	91.81(19)
Mn(12)-O(17)-Mn(17)	100.8(2)	Mn(16)-O(52)-Mn(17)	104.3(2)
Mn(7)-O(17)-Mn(17)	99.9(2)	Mn(16)-O(52)-Mn(12)	100.5(2)
Mn(12)-O(17)-Mn(8)	168.7(2)	Mn(17)-O(52)-Mn(12)	91.59(17)
Mn(7)-O(17)-Mn(8)	88.03(17)	Mn(8)-O(53)-Mn(18)	93.9(2)

Mn(17)-O(17)-Mn(8)	88.90(15)	Mn(8)-O(53)-Mn(17)	103.6(3)
Mn(12)-O(17)-Mn(11)	89.20(18)	Mn(18)-O(53)-Mn(17)	102.6(3)
Mn(7)-O(17)-Mn(11)	167.8(2)	Mn(9)-O(57)-Mn(18)	124.7(3)
Mn(17)-O(17)-Mn(11)	89.94(17)	Mn(18)-O(58)-Mn(11)	96.9(3)
Mn(8)-O(17)-Mn(11)	85.05(15)	Mn(18)-O(58)-Mn(17)	106.4(3)
Mn(9)-O(18)-Mn(8)	113.7(3)	Mn(11)-O(58)-Mn(17)	102.2(2)

Table A-11. Selected interatomic distances (Å) and angles (deg) for **5-1·3MeCN**

5-1·3MeCN			
Mn(2)...Mn(2')	2.8813(14)	Mn(1)...Mn(2')	3.1442(9)
Mn(2)...Mn(1')	3.1442(9)	Mn(1)...Mn(2)	3.1673(11)
Mn(2)...Gd(1')	3.3195(8)	Gd(1)...Mn(2')	3.3195(8)
Gd(1)-O(5)	2.331(3)	Mn(1)-O(5')	2.275(3)
Gd(1)-O(6)	2.364(3)	Mn(1)-O(2)	2.296(9)
Gd(1)-O(10)	2.415(3)	Mn(1)-N(2)	2.335(5)
Gd(1)-O(4)	2.442(3)	Mn(1)-O(3)	2.344(4)
Gd(1)-O(9)	2.445(4)	Mn(1)-N(1)	2.379(3)
Gd(1)-O(1)	2.470(3)	Mn(2)-O(5')	1.902(3)
Gd(1)-O(12)	2.495(3)	Mn(2)-O(5)	1.916(3)
Gd(1)-O(13)	2.498(4)	Mn(2)-O(11')	1.954(4)
Gd(1)-O(8)	2.586(3)	Mn(2)-O(7)	1.964(4)
Mn(1)-O(4)	2.176(3)	Mn(2)-O(1)	2.163(3)
Mn(1)-O(1)	2.192(3)	Mn(2)-O(4')	2.221(3)
Mn(2)-O(1)-Gd(1)	92.26(10)	Mn(2')-O(5)-Mn(1')	98.24(12)
Mn(1)-O(1)-Gd(1)	107.89(12)	Mn(2)-O(5)-Mn(1')	6.88(15)
Mn(1)-O(4)-Mn(2')	91.30(14)	Mn(2')-O(5)-Gd(1)	102.83(15)
Mn(1)-O(4)-Gd(1)	109.42(13)	Mn(2)-O(5)-Gd(1)	103.61(11)
Mn(2')-O(4)-Gd(1)	90.65(11)	Mn(1')-O(5)-Gd(1)	148.03(16)
Mn(2')-O(5)-Mn(2)	98.01(16)	Mn(2)-O(1)-Mn(1)	93.31(12)

Table A-12. Selected interatomic distances (Å) and angles (deg) for **5-2·0.5MeCN**

5-2·0.5MeCN			
Mn(1)...Mn(1')	2.8964(10)	Mn(1)...Mn(2')	3.1609(7)
Mn(2)...Mn(1')	3.1609(7)	Mn(1)...Mn(2)	3.1767(7)
Mn(1)...Tb(1')	3.3210(5)	Tb(1)...Mn(1')	3.1609(7)
Tb(1)-O(7)	2.318(2)	Mn(1)-O(2')	2.213(2)
Tb(1)-O(6)	2.325(2)	Mn(1)-Mn(1')	2.8964(10)
Tb(1)-O(10)	2.367(2)	Mn(1)-Mn(2')	3.1609(7)
Tb(1)-O(8)	2.437(2)	Mn(1)-Mn(2)	3.1767(7)
Tb(1)-O(2)	2.459(2)	Mn(1)-Tb(1')	3.3210(5)

Tb (1)-O(1)	2.460(2)	Mn(2)-O(2)	2.168(2)
Tb 1)-O(12)	2.475(2)	Mn(2)-O(4')	2.198(6)
Tb (1)-O(13)	2.475(2)	Mn(2)-O(1)	2.203(2)
Tb (1)-O(9)	2.616(2)	Mn(2)-O(7')	2.291(2)
Mn(1)-O(7')	1.897(2)	Mn(2)-O(4)	2.330(6)
Mn(1)-O(7)	1.918(2)	Mn(2)-O(3)	2.342(3)
Mn(1)-O(5)	1.967(2)	Mn(2)-N(1)	2.343(3)
Mn(1)-O(11')	1.973(2)	Mn(2)-N(2)	2.389(3)
Mn(1)-O(1)	2.176(2)	Mn(1')-O(7)-Mn(1)	98.8(1)
Mn(1)-O(1)-Mn(2)	93.01(8)	Mn(1')-O(7)-Mn(2')	98.21(9)
Mn(1)-O(1)-Tb(1)	92.04(8)	Mn(1)-O(7)-Mn(2')	96.95(9)
Mn(2)-O(1)-Tb(1)	108.61(9)	Mn(1')-O(7)-Tb(1)	103.54(9)
Mn(2)-O(2)-Mn(1')	92.37(8)	Mn(1)-O(7)-Tb(1)	103.82(9)
Mn(2)-O(2)-Tb(1)	109.85(9)	Mn(2')-O(7)-Tb(1)	146.99(10)
Mn(1')-O(2)-Tb(1)	90.46(7)		

APPENDIX B
LIST OF COMPOUNDS

- [Mn₁₂O₄(OMe)₂(edte)₄(N₃)₈](ClO₄)(N₃) **(2-1)**
- [Mn₁₂O₄(OH)(edte)₄(N₃)₉] **(2-2)**
- [Mn₁₂O₄(OH)(edte)₄(N₃)₉](ClO₄)(N₃) **(2-3)**
- [Mn₉O₃(OMe)(O₂CBu^t)₇(edte)(edteH)₂(N₃)₂] **(3-1)**
- [Mn₃(O₂CMe)₂(edteH₂)₂](O₂CMe) **(4-1)**
- [Mn₃(O₂CMe)₂(edteH₂)₂](ClO₄) **(4-2)**
- [Mn₄(edteH₂)₂(hmp)₂Cl₂][MnCl₄] **(4-3)**
- [Mn₆O₂(O₂CBu^t)₆(edteH)₂(N₃)₂] **(4-4)**
- Na₂[Mn₁₀O₄(OMe)₂(O₂CEt)₆(edte)₂(N₃)₆] **(4-5)**
- (NEt₄)₂[Mn₁₀O₄(OH)₂(O₂CEt)₆(Edte)₂(N₃)₆] **(4-6)**
- [Mn₂₀O₈(OH)₆(O₂CEt)₆(edte)₄(edteH)₂](ClO₄)₄ **(4-7)**
- [Ca₂Mn₁₈O₈(OH)₅(O₂CBu^t)_{4.5}(edte)₅(NO₃)_{3.5}](O₂CBu^t)_{0.5}(NO₃)_{0.5} **(4-8)**.
- Mn₄Gd₂O₂(O₂CBu^t)₆(edteH₂)₂(NO₃)₂ **(5-1)**.
- Mn₄Tb₂O₂(O₂CBu^t)₆(edteH₂)₂(NO₃)₂ **(5-2)**
- Mn₄Dy₂O₂(O₂CBu^t)₆(edteH₂)₂(NO₃)₂ **(5-3)**
- Mn₄Ho₂O₂(O₂CBu^t)₆(edteH₂)₂(NO₃)₂ **(5-4)**
- Mn₄Y₂O₂(O₂CBu^t)₆(edteH₂)₂(NO₃)₂ **(5-5)**

APPENDIX C ELECTROCHEMICAL REVERSIBLE PROCESSES

Cyclic voltammetry is a simple, rapid and powerful method for characterizing the electrochemical behavior of analytes that can be electrochemically oxidized or reduced. The reversibility of such processes can be determined by studying the voltammogram of the compound. The important accessible parameters from a CV are the magnitude of the anodic current (i_p^{ox}), the cathodic peak current (i_p^{red}), the anodic peak potential (E_p^{ox}), and the cathodic peak potential (E_p^{red}). The study is performed by sweeping the potential of the working electrode at a specific sweep rate (in volts/second) and by measuring the resulting current vs. time curve. Usually the sweep is reversed at a specific switching potential, hence the method is cyclic voltammetry. The standard protocol is to record current vs. applied potential. A typical cyclic voltammogram obtained for a reversible one-electron reduction process is shown in Figure C-1.

The formal reduction potential (E^0) for a reversible couple is centered between E_p^{ox} and E_p^{red} .

$$E^0 = (E_p^{ox} + E_p^{red})/2 \quad (C-1)$$

The peak current for a reversible system is described by the Randles-Sevcik equation for the forward sweep of the first cycle:

$$i_p = (2.69 \times 10^5) n^{3/2} A D^{1/2} \nu^{1/2} C \quad (C-2)$$

where, i_p = peak current, amperes
 n = electron stoichiometry, eq/mol
 A = electrode area, cm^2
 C = analyte concentration, mol/cm^3
 ν = scan rate, volts/second

According to the equation C-2, i_p increases with $v^{1/2}$ and is directly proportional to analyte concentration.

Following properties are true for a reversible couple:

- a) i_p^{ox} is approximately equal to i_p^{red} i.e. $i_p^{ox}/i_p^{red} \approx 1$
- b) E_p is independent of the scan rate, $\Delta E_p = 59/n$ mV at 25° C
- c) $i_p \propto v^{1/2}$ (diffusion controlled)

For a quasi-reversible couple,

- a) $\Delta E_p > 59$ mV and ΔE_p increases with v
- b) $i_p \propto v^{1/2}$ (diffusion controlled)

For an irreversible couple,

- a) chemically – no return wave in CV

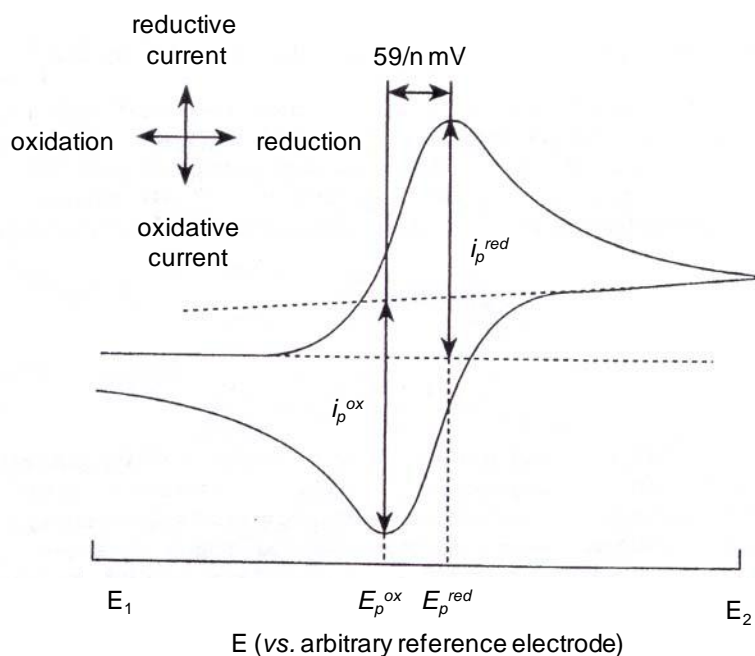


Figure C-1. A typical cyclic voltammogram obtained for a reversible one-electron reduction process.

APPENDIX D
DFT CALCULATIONS

Table D-1. Spin of nine Mn atoms are shown in column S1 to S9 indicating different spin orientations and the labels refer to Figure 3-18. The multiplicity is shown in column M and energy difference as ΔE in kcal/mol. The HS is designated where all the orientations are ferromagnetic. IS is designated for the intermediate multiplicity of 28, 22, 20, 12. LS is designated for lowest multiplicity of 6. The suffix(s) are indicating the index of Mn according to Figure 3-18

	S1	S2	S3	S4	S5	S6	S7	S8	S9	M	ΔE
IS ₁₉	-2	2	2	2	2.5	2	2	2	-2	22	0.000
IS ₂₉	2	-2	2	2	2.5	2	2	2	-2	22	0.069
IS ₁₈	-2	2	2	2	2.5	2	2	-2	2	22	0.139
HS	2	2	2	2	2.5	2	2	2	2	38	0.188
IS ₂₈	2	-2	2	2	2.5	2	2	-2	2	22	0.215
LS ₂₄₆₈	2	-2	2	-2	2.5	-2	2	-2	2	6	0.696
IS ₄₆	2	2	2	-2	2.5	-2	2	2	2	22	0.891
IS ₁₂	-2	-2	2	2	2.5	2	2	2	2	22	0.912
IS ₁₃	-2	2	-2	2	2.5	2	2	2	2	22	1.128
IS ₂₃	2	-2	-2	2	2.5	2	2	2	2	22	1.373
LS ₁₂₈₉	-2	-2	2	2	2.5	2	2	-2	-2	6	1.428
IS ₃₉	2	2	-2	2	2.5	2	2	2	-2	22	1.448
IS ₁₇	-2	2	2	2	2.5	2	-2	2	2	22	1.471
IS ₂₄	2	-2	2	-2	2.5	2	2	2	2	22	1.544
IS ₁₆	-2	2	2	2	2.5	-2	2	2	2	22	1.552
LS ₂₃₄₆	2	-2	-2	-2	2.5	-2	2	2	2	6	1.554
IS ₂₇	2	-2	2	2	2.5	2	-2	2	2	22	1.557
IS ₂₆	2	-2	2	2	2.5	-2	2	2	2	22	1.596
IS ₂₅	2	-2	2	2	-2.5	2	2	-2	2	20	1.720
IS ₁₅	-2	2	2	2	-2.5	2	2	2	-2	20	1.762
IS ₅	2	2	2	2	-2.5	2	2	2	2	28	1.885
IS ₃₅	2	2	-2	2	-2.5	2	2	2	2	20	1.941
IS ₃₅₇	2	2	-2	2	-2.5	2	-2	2	2	12	1.983
IS ₄₅₆	2	2	2	-2	-2.5	-2	2	2	2	12	2.020
IS ₄₅₉	2	2	2	-2	-2.5	2	2	2	-2	12	2.578
IS ₃₄	2	2	-2	-2	2.5	2	2	2	2	22	2.658
IS ₁₅₆	-2	2	2	2	-2.5	-2	2	2	2	12	2.987
IS ₃₇	2	2	-2	2	2.5	2	-2	2	2	22	3.019
IS ₃₆	2	2	-2	2	2.5	-2	2	2	2	22	3.020

APPENDIX E
VAN VLECK EQUATIONS

$$c = N\mu_B^2/3K$$

N = Avogadro's number

g = Lande's factor

k = Boltzmann constant

T = Temperature

TIP = Temperature independent paramagnetism

E-1 $[\text{Mn}_2^{\text{II}}\text{Mn}^{\text{III}}(\text{O}_2\text{CMe})_2(\text{edteH}_2)_2](\text{O}_2\text{CMe})$ (**4-1**) (see Figure 4-15)

$$m = J/k/T$$

$$n = J'/k/T$$

$$\begin{aligned} \text{Num} = & + 30.0000 * \exp(6.0000 * m + 0.0000 * n) \\ & + 6.0000 * \exp(0.0000 * m + 2.0000 * n) \\ & + 30.0000 * \exp(4.0000 * m + 2.0000 * n) \\ & + 84.0000 * \exp(10.0000 * m + 2.0000 * n) \\ & + 0.0000 * \exp(-6.0000 * m + 6.0000 * n) \\ & + 6.0000 * \exp(-4.0000 * m + 6.0000 * n) \\ & + 30.0000 * \exp(0.0000 * m + 6.0000 * n) \\ & + 84.0000 * \exp(6.0000 * m + 6.0000 * n) \\ & + 180.0000 * \exp(14.0000 * m + 6.0000 * n) \\ & + 6.0000 * \exp(-10.0000 * m + 12.0000 * n) \\ & + 30.0000 * \exp(-6.0000 * m + 12.0000 * n) \\ & + 84.0000 * \exp(0.0000 * m + 12.0000 * n) \\ & + 180.0000 * \exp(8.0000 * m + 12.0000 * n) \\ & + 330.0000 * \exp(18.0000 * m + 12.0000 * n) \\ & + 30.0000 * \exp(-14.0000 * m + 20.0000 * n) \\ & + 84.0000 * \exp(-8.0000 * m + 20.0000 * n) \\ & + 180.0000 * \exp(0.0000 * m + 20.0000 * n) \\ & + 330.0000 * \exp(10.0000 * m + 20.0000 * n) \\ & + 546.0000 * \exp(22.0000 * m + 20.0000 * n) \\ & + 84.0000 * \exp(-18.0000 * m + 30.0000 * n) \\ & + 180.0000 * \exp(-10.0000 * m + 30.0000 * n) \\ & + 330.0000 * \exp(0.0000 * m + 30.0000 * n) \\ & + 546.0000 * \exp(12.0000 * m + 30.0000 * n) \\ & + 840.0000 * \exp(26.0000 * m + 30.0000 * n) \end{aligned}$$

$$\begin{aligned}
\text{Den} = & + 5.0000 * \exp(6.0000 * m + 0.0000 * n) \\
& + 3.0000 * \exp(0.0000 * m + 2.0000 * n) \\
& + 5.0000 * \exp(4.0000 * m + 2.0000 * n) \\
& + 7.0000 * \exp(10.0000 * m + 2.0000 * n) \\
& + 1.0000 * \exp(-6.0000 * m + 6.0000 * n) \\
& + 3.0000 * \exp(-4.0000 * m + 6.0000 * n) \\
& + 5.0000 * \exp(0.0000 * m + 6.0000 * n) \\
& + 7.0000 * \exp(6.0000 * m + 6.0000 * n) \\
& + 9.0000 * \exp(14.0000 * m + 6.0000 * n) \\
& + 3.0000 * \exp(-10.0000 * m + 12.0000 * n) \\
& + 5.0000 * \exp(-6.0000 * m + 12.0000 * n) \\
& + 7.0000 * \exp(0.0000 * m + 12.0000 * n) \\
& + 9.0000 * \exp(8.0000 * m + 12.0000 * n) \\
& + 11.0000 * \exp(18.0000 * m + 12.0000 * n) \\
& + 5.0000 * \exp(-14.0000 * m + 20.0000 * n) \\
& + 7.0000 * \exp(-8.0000 * m + 20.0000 * n) \\
& + 9.0000 * \exp(0.0000 * m + 20.0000 * n) \\
& + 11.0000 * \exp(10.0000 * m + 20.0000 * n) \\
& + 13.0000 * \exp(22.0000 * m + 20.0000 * n) \\
& + 7.0000 * \exp(-18.0000 * m + 30.0000 * n) \\
& + 9.0000 * \exp(-10.0000 * m + 30.0000 * n) \\
& + 11.0000 * \exp(0.0000 * m + 30.0000 * n) \\
& + 13.0000 * \exp(12.0000 * m + 30.0000 * n) \\
& + 15.0000 * \exp(26.0000 * m + 30.0000 * n)
\end{aligned}$$

Fitting equation:

$$\chi_M = (cg^2/T)(\text{Num}/\text{Den})$$

Fitting parameters:

$$J = -2.6(2)$$

$$J' = 0$$

$$g = 1.99(1)$$

E-2 [Mn^{II}Mn^{III}(O₂CMe)₂(edteH₂)₂](ClO₄) (**4-2**) (see Figure 4-15)

$$m = J/k/T$$

$$n = J'/k/T$$

$$\begin{aligned}
\text{Num} = & +30.0000 * \exp(6.0000 * m + 0.0000 * n) \\
& +6.0000 * \exp(0.0000 * m + 2.0000 * n) \\
& +30.0000 * \exp(4.0000 * m + 2.0000 * n)
\end{aligned}$$

$+84.0000 \cdot \exp(10.0000 \cdot m + 2.0000 \cdot n)$
 $+0.0000 \cdot \exp(-6.0000 \cdot m + 6.0000 \cdot n)$
 $+6.0000 \cdot \exp(-4.0000 \cdot m + 6.0000 \cdot n)$
 $+30.0000 \cdot \exp(0.0000 \cdot m + 6.0000 \cdot n)$
 $+84.0000 \cdot \exp(6.0000 \cdot m + 6.0000 \cdot n)$
 $+180.0000 \cdot \exp(14.0000 \cdot m + 6.0000 \cdot n)$
 $+6.0000 \cdot \exp(-10.0000 \cdot m + 12.0000 \cdot n)$
 $+30.0000 \cdot \exp(-6.0000 \cdot m + 12.0000 \cdot n)$
 $+84.0000 \cdot \exp(0.0000 \cdot m + 12.0000 \cdot n)$
 $+180.0000 \cdot \exp(8.0000 \cdot m + 12.0000 \cdot n)$
 $+330.0000 \cdot \exp(18.0000 \cdot m + 12.0000 \cdot n)$
 $+30.0000 \cdot \exp(-14.0000 \cdot m + 20.0000 \cdot n)$
 $+84.0000 \cdot \exp(-8.0000 \cdot m + 20.0000 \cdot n)$
 $+180.0000 \cdot \exp(0.0000 \cdot m + 20.0000 \cdot n)$
 $+330.0000 \cdot \exp(10.0000 \cdot m + 20.0000 \cdot n)$
 $+546.0000 \cdot \exp(22.0000 \cdot m + 20.0000 \cdot n)$
 $+84.0000 \cdot \exp(-18.0000 \cdot m + 30.0000 \cdot n)$
 $+180.0000 \cdot \exp(-10.0000 \cdot m + 30.0000 \cdot n)$
 $+330.0000 \cdot \exp(0.0000 \cdot m + 30.0000 \cdot n)$
 $+546.0000 \cdot \exp(12.0000 \cdot m + 30.0000 \cdot n)$
 $+840.0000 \cdot \exp(26.0000 \cdot m + 30.0000 \cdot n)$

Den = $+5.0000 \cdot \exp(6.0000 \cdot m + 0.0000 \cdot n)$
 $+3.0000 \cdot \exp(0.0000 \cdot m + 2.0000 \cdot n)$
 $+5.0000 \cdot \exp(4.0000 \cdot m + 2.0000 \cdot n)$
 $+7.0000 \cdot \exp(10.0000 \cdot m + 2.0000 \cdot n)$
 $+1.0000 \cdot \exp(-6.0000 \cdot m + 6.0000 \cdot n)$
 $+3.0000 \cdot \exp(-4.0000 \cdot m + 6.0000 \cdot n)$
 $+5.0000 \cdot \exp(0.0000 \cdot m + 6.0000 \cdot n)$
 $+7.0000 \cdot \exp(6.0000 \cdot m + 6.0000 \cdot n)$
 $+9.0000 \cdot \exp(14.0000 \cdot m + 6.0000 \cdot n)$
 $+3.0000 \cdot \exp(-10.0000 \cdot m + 12.0000 \cdot n)$
 $+5.0000 \cdot \exp(-6.0000 \cdot m + 12.0000 \cdot n)$
 $+7.0000 \cdot \exp(0.0000 \cdot m + 12.0000 \cdot n)$
 $+9.0000 \cdot \exp(8.0000 \cdot m + 12.0000 \cdot n)$
 $+11.0000 \cdot \exp(18.0000 \cdot m + 12.0000 \cdot n)$
 $+5.0000 \cdot \exp(-14.0000 \cdot m + 20.0000 \cdot n)$
 $+7.0000 \cdot \exp(-8.0000 \cdot m + 20.0000 \cdot n)$
 $+9.0000 \cdot \exp(0.0000 \cdot m + 20.0000 \cdot n)$
 $+11.0000 \cdot \exp(10.0000 \cdot m + 20.0000 \cdot n)$
 $+13.0000 \cdot \exp(22.0000 \cdot m + 20.0000 \cdot n)$
 $+7.0000 \cdot \exp(-18.0000 \cdot m + 30.0000 \cdot n)$
 $+9.0000 \cdot \exp(-10.0000 \cdot m + 30.0000 \cdot n)$
 $+11.0000 \cdot \exp(0.0000 \cdot m + 30.0000 \cdot n)$
 $+13.0000 \cdot \exp(12.0000 \cdot m + 30.0000 \cdot n)$
 $+15.0000 \cdot \exp(26.0000 \cdot m + 30.0000 \cdot n)$

Fitting equation:

$$f = (cg^2/T)*\text{Num}/\text{Den}$$

Fitting parameters:

$$J = -1.4(1)$$

$$J' = 0.3(1)$$

$$g = 1.98(1)$$

E-3 $[\text{Mn}^{\text{II}}_2\text{Mn}^{\text{III}}_2(\text{edteH}_2)_2(\text{hmp})_2\text{Cl}_2][\text{Mn}^{\text{II}}\text{Cl}_4]$ (4-3) (see Figure 4-24)

$$l = J_{bb}/k/T$$

$$m = J_{wb}/k/T$$

$$\text{TIP} = 600*10^{-6}$$

$$\begin{aligned} \text{Num} = & +630.0000*\exp(0.0000*l+0.0000*m) \\ & +6.0000*\exp(2.0000*l+0.0000*m) \\ & +0.0000*\exp(2.0000*l+-4.0000*m) \\ & +630.0000*\exp(2.0000*l+-2.0000*m) \\ & +30.0000*\exp(2.0000*l+2.0000*m) \\ & +6.0000*\exp(2.0000*l+-6.0000*m) \\ & +84.0000*\exp(2.0000*l+4.0000*m) \\ & +30.0000*\exp(2.0000*l+-8.0000*m) \\ & +180.0000*\exp(2.0000*l+6.0000*m) \\ & +84.0000*\exp(2.0000*l+-10.0000*m) \\ & +330.0000*\exp(2.0000*l+8.0000*m) \\ & +180.0000*\exp(2.0000*l+-12.0000*m) \\ & +546.0000*\exp(2.0000*l+10.0000*m) \\ & +114.0000*\exp(6.0000*l+0.0000*m) \\ & +630.0000*\exp(6.0000*l+-6.0000*m) \\ & +30.0000*\exp(6.0000*l+-2.0000*m) \\ & +414.0000*\exp(6.0000*l+4.0000*m) \\ & +30.0000*\exp(6.0000*l+-12.0000*m) \\ & +6.0000*\exp(6.0000*l+-10.0000*m) \\ & +180.0000*\exp(6.0000*l+8.0000*m) \\ & +186.0000*\exp(6.0000*l+-16.0000*m) \\ & +180.0000*\exp(6.0000*l+2.0000*m) \\ & +330.0000*\exp(6.0000*l+12.0000*m) \\ & +30.0000*\exp(6.0000*l+-20.0000*m) \\ & +84.0000*\exp(6.0000*l+-14.0000*m) \\ & +546.0000*\exp(6.0000*l+16.0000*m) \end{aligned}$$

+84.0000*exp(6.0000*I+-24.0000*m)
+546.0000*exp(6.0000*I+6.0000*m)
+840.0000*exp(6.0000*I+20.0000*m)
+630.0000*exp(12.0000*I+0.0000*m)
+30.0000*exp(12.0000*I+-8.0000*m)
+414.0000*exp(12.0000*I+-2.0000*m)
+510.0000*exp(12.0000*I+6.0000*m)
+6.0000*exp(12.0000*I+-16.0000*m)
+624.0000*exp(12.0000*I+-12.0000*m)
+84.0000*exp(12.0000*I+-6.0000*m)
+180.0000*exp(12.0000*I+2.0000*m)
+330.0000*exp(12.0000*I+12.0000*m)
+0.0000*exp(12.0000*I+-24.0000*m)
+186.0000*exp(12.0000*I+-22.0000*m)
+30.0000*exp(12.0000*I+-18.0000*m)
+180.0000*exp(12.0000*I+-4.0000*m)
+546.0000*exp(12.0000*I+18.0000*m)
+90.0000*exp(12.0000*I+-30.0000*m)
+30.0000*exp(12.0000*I+-26.0000*m)
+84.0000*exp(12.0000*I+-20.0000*m)
+546.0000*exp(12.0000*I+10.0000*m)
+840.0000*exp(12.0000*I+24.0000*m)
+30.0000*exp(12.0000*I+-36.0000*m)
+840.0000*exp(12.0000*I+14.0000*m)
+1224.0000*exp(12.0000*I+30.0000*m)
+180.0000*exp(20.0000*I+0.0000*m)
+414.0000*exp(20.0000*I+-10.0000*m)
+510.0000*exp(20.0000*I+-2.0000*m)
+330.0000*exp(20.0000*I+8.0000*m)
+624.0000*exp(20.0000*I+-20.0000*m)
+84.0000*exp(20.0000*I+-14.0000*m)
+180.0000*exp(20.0000*I+-6.0000*m)
+330.0000*exp(20.0000*I+4.0000*m)
+1386.0000*exp(20.0000*I+16.0000*m)
+186.0000*exp(20.0000*I+-30.0000*m)
+30.0000*exp(20.0000*I+-26.0000*m)
+180.0000*exp(20.0000*I+-12.0000*m)
+546.0000*exp(20.0000*I+10.0000*m)
+840.0000*exp(20.0000*I+24.0000*m)
+0.0000*exp(20.0000*I+-40.0000*m)
+90.0000*exp(20.0000*I+-38.0000*m)
+30.0000*exp(20.0000*I+-34.0000*m)
+84.0000*exp(20.0000*I+-28.0000*m)
+546.0000*exp(20.0000*I+2.0000*m)
+1224.0000*exp(20.0000*I+32.0000*m)
+6.0000*exp(20.0000*I+-48.0000*m)

+30.0000*exp(20.0000*l+-44.0000*m)
+546.0000*exp(20.0000*l+-8.0000*m)
+840.0000*exp(20.0000*l+6.0000*m)
+1224.0000*exp(20.0000*l+22.0000*m)
+1710.0000*exp(20.0000*l+40.0000*m)

Den = +36.0000*exp(0.0000*l+0.0000*m)
+3.0000*exp(2.0000*l+0.0000*m)
+1.0000*exp(2.0000*l+-4.0000*m)
+35.0000*exp(2.0000*l+-2.0000*m)
+5.0000*exp(2.0000*l+2.0000*m)
+3.0000*exp(2.0000*l+-6.0000*m)
+7.0000*exp(2.0000*l+4.0000*m)
+5.0000*exp(2.0000*l+-8.0000*m)
+9.0000*exp(2.0000*l+6.0000*m)
+7.0000*exp(2.0000*l+-10.0000*m)
+11.0000*exp(2.0000*l+8.0000*m)
+9.0000*exp(2.0000*l+-12.0000*m)
+13.0000*exp(2.0000*l+10.0000*m)
+12.0000*exp(6.0000*l+0.0000*m)
+35.0000*exp(6.0000*l+-6.0000*m)
+5.0000*exp(6.0000*l+-2.0000*m)
+18.0000*exp(6.0000*l+4.0000*m)
+6.0000*exp(6.0000*l+-12.0000*m)
+3.0000*exp(6.0000*l+-10.0000*m)
+9.0000*exp(6.0000*l+8.0000*m)
+12.0000*exp(6.0000*l+-16.0000*m)
+9.0000*exp(6.0000*l+2.0000*m)
+11.0000*exp(6.0000*l+12.0000*m)
+5.0000*exp(6.0000*l+-20.0000*m)
+7.0000*exp(6.0000*l+-14.0000*m)
+13.0000*exp(6.0000*l+16.0000*m)
+7.0000*exp(6.0000*l+-24.0000*m)
+13.0000*exp(6.0000*l+6.0000*m)
+15.0000*exp(6.0000*l+20.0000*m)
+20.0000*exp(12.0000*l+0.0000*m)
+5.0000*exp(12.0000*l+-8.0000*m)
+18.0000*exp(12.0000*l+-2.0000*m)
+20.0000*exp(12.0000*l+6.0000*m)
+3.0000*exp(12.0000*l+-16.0000*m)
+32.0000*exp(12.0000*l+-12.0000*m)
+7.0000*exp(12.0000*l+-6.0000*m)
+9.0000*exp(12.0000*l+2.0000*m)
+11.0000*exp(12.0000*l+12.0000*m)
+1.0000*exp(12.0000*l+-24.0000*m)
+12.0000*exp(12.0000*l+-22.0000*m)

+5.0000*exp(12.0000*I+-18.0000*m)
 +9.0000*exp(12.0000*I+-4.0000*m)
 +13.0000*exp(12.0000*I+18.0000*m)
 +10.0000*exp(12.0000*I+-30.0000*m)
 +5.0000*exp(12.0000*I+-26.0000*m)
 +7.0000*exp(12.0000*I+-20.0000*m)
 +13.0000*exp(12.0000*I+10.0000*m)
 +15.0000*exp(12.0000*I+24.0000*m)
 +5.0000*exp(12.0000*I+-36.0000*m)
 +15.0000*exp(12.0000*I+14.0000*m)
 +17.0000*exp(12.0000*I+30.0000*m)
 +9.0000*exp(20.0000*I+0.0000*m)
 +18.0000*exp(20.0000*I+-10.0000*m)
 +20.0000*exp(20.0000*I+-2.0000*m)
 +11.0000*exp(20.0000*I+8.0000*m)
 +32.0000*exp(20.0000*I+-20.0000*m)
 +7.0000*exp(20.0000*I+-14.0000*m)
 +9.0000*exp(20.0000*I+-6.0000*m)
 +11.0000*exp(20.0000*I+4.0000*m)
 +28.0000*exp(20.0000*I+16.0000*m)
 +12.0000*exp(20.0000*I+-30.0000*m)
 +5.0000*exp(20.0000*I+-26.0000*m)
 +9.0000*exp(20.0000*I+-12.0000*m)
 +13.0000*exp(20.0000*I+10.0000*m)
 +15.0000*exp(20.0000*I+24.0000*m)
 +1.0000*exp(20.0000*I+-40.0000*m)
 +10.0000*exp(20.0000*I+-38.0000*m)
 +5.0000*exp(20.0000*I+-34.0000*m)
 +7.0000*exp(20.0000*I+-28.0000*m)
 +13.0000*exp(20.0000*I+2.0000*m)
 +17.0000*exp(20.0000*I+32.0000*m)
 +3.0000*exp(20.0000*I+-48.0000*m)
 +5.0000*exp(20.0000*I+-44.0000*m)
 +13.0000*exp(20.0000*I+-8.0000*m)
 +15.0000*exp(20.0000*I+6.0000*m)
 +17.0000*exp(20.0000*I+22.0000*m)
 +19.0000*exp(20.0000*I+40.0000*m)

Fitting equation:

$$\chi_M = (cg^2/T)\text{Num/Den} + (cg^2/T)8.75 + \text{TIP}$$

Fitting parameters:

$$J_{bb} = +7.20(3)$$

$$J_{wb} = +1.34(3)$$

$$g = 1.87(2)$$

E-4 $\text{Mn}^{\text{II}}_2\text{Mn}^{\text{III}}_2\text{Y}_2\text{O}_2(\text{O}_2\text{CBu}^\dagger)_6(\text{edteH}_2)_2(\text{NO}_3)_2$ (5-5) (See Figure 5-8)

$$l = J_{bb}/k/T$$

$$m = J_{wb}/k/T$$

$$\text{TIP} = 400 \cdot 10^{-6}$$

$$\begin{aligned} \text{Num} = & +630.0000 \cdot \exp(0.0000 \cdot l + 0.0000 \cdot m) \\ & +6.0000 \cdot \exp(2.0000 \cdot l + 0.0000 \cdot m) \\ & +0.0000 \cdot \exp(2.0000 \cdot l - 4.0000 \cdot m) \\ & +630.0000 \cdot \exp(2.0000 \cdot l - 2.0000 \cdot m) \\ & +30.0000 \cdot \exp(2.0000 \cdot l + 2.0000 \cdot m) \\ & +6.0000 \cdot \exp(2.0000 \cdot l - 6.0000 \cdot m) \\ & +84.0000 \cdot \exp(2.0000 \cdot l + 4.0000 \cdot m) \\ & +30.0000 \cdot \exp(2.0000 \cdot l - 8.0000 \cdot m) \\ & +180.0000 \cdot \exp(2.0000 \cdot l + 6.0000 \cdot m) \\ & +84.0000 \cdot \exp(2.0000 \cdot l - 10.0000 \cdot m) \\ & +330.0000 \cdot \exp(2.0000 \cdot l + 8.0000 \cdot m) \\ & +180.0000 \cdot \exp(2.0000 \cdot l - 12.0000 \cdot m) \\ & +546.0000 \cdot \exp(2.0000 \cdot l + 10.0000 \cdot m) \\ & +114.0000 \cdot \exp(6.0000 \cdot l + 0.0000 \cdot m) \\ & +630.0000 \cdot \exp(6.0000 \cdot l - 6.0000 \cdot m) \\ & +30.0000 \cdot \exp(6.0000 \cdot l - 2.0000 \cdot m) \\ & +414.0000 \cdot \exp(6.0000 \cdot l + 4.0000 \cdot m) \\ & +30.0000 \cdot \exp(6.0000 \cdot l - 12.0000 \cdot m) \\ & +6.0000 \cdot \exp(6.0000 \cdot l - 10.0000 \cdot m) \\ & +180.0000 \cdot \exp(6.0000 \cdot l + 8.0000 \cdot m) \\ & +186.0000 \cdot \exp(6.0000 \cdot l - 16.0000 \cdot m) \\ & +180.0000 \cdot \exp(6.0000 \cdot l + 2.0000 \cdot m) \\ & +330.0000 \cdot \exp(6.0000 \cdot l + 12.0000 \cdot m) \\ & +30.0000 \cdot \exp(6.0000 \cdot l - 20.0000 \cdot m) \\ & +84.0000 \cdot \exp(6.0000 \cdot l - 14.0000 \cdot m) \\ & +546.0000 \cdot \exp(6.0000 \cdot l + 16.0000 \cdot m) \\ & +84.0000 \cdot \exp(6.0000 \cdot l - 24.0000 \cdot m) \\ & +546.0000 \cdot \exp(6.0000 \cdot l + 6.0000 \cdot m) \\ & +840.0000 \cdot \exp(6.0000 \cdot l + 20.0000 \cdot m) \\ & +630.0000 \cdot \exp(12.0000 \cdot l + 0.0000 \cdot m) \end{aligned}$$

+30.0000*exp(12.0000*I+-8.0000*m)
+414.0000*exp(12.0000*I+-2.0000*m)
+510.0000*exp(12.0000*I+6.0000*m)
+6.0000*exp(12.0000*I+-16.0000*m)
+624.0000*exp(12.0000*I+-12.0000*m)
+84.0000*exp(12.0000*I+-6.0000*m)
+180.0000*exp(12.0000*I+2.0000*m)
+330.0000*exp(12.0000*I+12.0000*m)
+0.0000*exp(12.0000*I+-24.0000*m)
+186.0000*exp(12.0000*I+-22.0000*m)
+30.0000*exp(12.0000*I+-18.0000*m)
+180.0000*exp(12.0000*I+-4.0000*m)
+546.0000*exp(12.0000*I+18.0000*m)
+90.0000*exp(12.0000*I+-30.0000*m)
+30.0000*exp(12.0000*I+-26.0000*m)
+84.0000*exp(12.0000*I+-20.0000*m)
+546.0000*exp(12.0000*I+10.0000*m)
+840.0000*exp(12.0000*I+24.0000*m)
+30.0000*exp(12.0000*I+-36.0000*m)
+840.0000*exp(12.0000*I+14.0000*m)
+1224.0000*exp(12.0000*I+30.0000*m)
+180.0000*exp(20.0000*I+0.0000*m)
+414.0000*exp(20.0000*I+-10.0000*m)
+510.0000*exp(20.0000*I+-2.0000*m)
+330.0000*exp(20.0000*I+8.0000*m)
+624.0000*exp(20.0000*I+-20.0000*m)
+84.0000*exp(20.0000*I+-14.0000*m)
+180.0000*exp(20.0000*I+-6.0000*m)
+330.0000*exp(20.0000*I+4.0000*m)
+1386.0000*exp(20.0000*I+16.0000*m)
+186.0000*exp(20.0000*I+-30.0000*m)
+30.0000*exp(20.0000*I+-26.0000*m)
+180.0000*exp(20.0000*I+-12.0000*m)
+546.0000*exp(20.0000*I+10.0000*m)
+840.0000*exp(20.0000*I+24.0000*m)
+0.0000*exp(20.0000*I+-40.0000*m)
+90.0000*exp(20.0000*I+-38.0000*m)
+30.0000*exp(20.0000*I+-34.0000*m)
+84.0000*exp(20.0000*I+-28.0000*m)
+546.0000*exp(20.0000*I+2.0000*m)
+1224.0000*exp(20.0000*I+32.0000*m)
+6.0000*exp(20.0000*I+-48.0000*m)
+30.0000*exp(20.0000*I+-44.0000*m)
+546.0000*exp(20.0000*I+-8.0000*m)
+840.0000*exp(20.0000*I+6.0000*m)
+1224.0000*exp(20.0000*I+22.0000*m)

$$+1710.0000*\exp(20.0000*l+40.0000*m)$$

$$\begin{aligned} \text{Den} = & +36.0000*\exp(0.0000*l+0.0000*m) \\ & +3.0000*\exp(2.0000*l+0.0000*m) \\ & +1.0000*\exp(2.0000*l+-4.0000*m) \\ & +35.0000*\exp(2.0000*l+-2.0000*m) \\ & +5.0000*\exp(2.0000*l+2.0000*m) \\ & +3.0000*\exp(2.0000*l+-6.0000*m) \\ & +7.0000*\exp(2.0000*l+4.0000*m) \\ & +5.0000*\exp(2.0000*l+-8.0000*m) \\ & +9.0000*\exp(2.0000*l+6.0000*m) \\ & +7.0000*\exp(2.0000*l+-10.0000*m) \\ & +11.0000*\exp(2.0000*l+8.0000*m) \\ & +9.0000*\exp(2.0000*l+-12.0000*m) \\ & +13.0000*\exp(2.0000*l+10.0000*m) \\ & +12.0000*\exp(6.0000*l+0.0000*m) \\ & +35.0000*\exp(6.0000*l+-6.0000*m) \\ & +5.0000*\exp(6.0000*l+-2.0000*m) \\ & +18.0000*\exp(6.0000*l+4.0000*m) \\ & +6.0000*\exp(6.0000*l+-12.0000*m) \\ & +3.0000*\exp(6.0000*l+-10.0000*m) \\ & +9.0000*\exp(6.0000*l+8.0000*m) \\ & +12.0000*\exp(6.0000*l+-16.0000*m) \\ & +9.0000*\exp(6.0000*l+2.0000*m) \\ & +11.0000*\exp(6.0000*l+12.0000*m) \\ & +5.0000*\exp(6.0000*l+-20.0000*m) \\ & +7.0000*\exp(6.0000*l+-14.0000*m) \\ & +13.0000*\exp(6.0000*l+16.0000*m) \\ & +7.0000*\exp(6.0000*l+-24.0000*m) \\ & +13.0000*\exp(6.0000*l+6.0000*m) \\ & +15.0000*\exp(6.0000*l+20.0000*m) \\ & +20.0000*\exp(12.0000*l+0.0000*m) \\ & +5.0000*\exp(12.0000*l+-8.0000*m) \\ & +18.0000*\exp(12.0000*l+-2.0000*m) \\ & +20.0000*\exp(12.0000*l+6.0000*m) \\ & +3.0000*\exp(12.0000*l+-16.0000*m) \\ & +32.0000*\exp(12.0000*l+-12.0000*m) \\ & +7.0000*\exp(12.0000*l+-6.0000*m) \\ & +9.0000*\exp(12.0000*l+2.0000*m) \\ & +11.0000*\exp(12.0000*l+12.0000*m) \\ & +1.0000*\exp(12.0000*l+-24.0000*m) \\ & +12.0000*\exp(12.0000*l+-22.0000*m) \\ & +5.0000*\exp(12.0000*l+-18.0000*m) \\ & +9.0000*\exp(12.0000*l+-4.0000*m) \\ & +13.0000*\exp(12.0000*l+18.0000*m) \\ & +10.0000*\exp(12.0000*l+-30.0000*m) \end{aligned}$$

+5.0000*exp(12.0000*I+-26.0000*m)
 +7.0000*exp(12.0000*I+-20.0000*m)
 +13.0000*exp(12.0000*I+10.0000*m)
 +15.0000*exp(12.0000*I+24.0000*m)
 +5.0000*exp(12.0000*I+-36.0000*m)
 +15.0000*exp(12.0000*I+14.0000*m)
 +17.0000*exp(12.0000*I+30.0000*m)
 +9.0000*exp(20.0000*I+0.0000*m)
 +18.0000*exp(20.0000*I+-10.0000*m)
 +20.0000*exp(20.0000*I+-2.0000*m)
 +11.0000*exp(20.0000*I+8.0000*m)
 +32.0000*exp(20.0000*I+-20.0000*m)
 +7.0000*exp(20.0000*I+-14.0000*m)
 +9.0000*exp(20.0000*I+-6.0000*m)
 +11.0000*exp(20.0000*I+4.0000*m)
 +28.0000*exp(20.0000*I+16.0000*m)
 +12.0000*exp(20.0000*I+-30.0000*m)
 +5.0000*exp(20.0000*I+-26.0000*m)
 +9.0000*exp(20.0000*I+-12.0000*m)
 +13.0000*exp(20.0000*I+10.0000*m)
 +15.0000*exp(20.0000*I+24.0000*m)
 +1.0000*exp(20.0000*I+-40.0000*m)
 +10.0000*exp(20.0000*I+-38.0000*m)
 +5.0000*exp(20.0000*I+-34.0000*m)
 +7.0000*exp(20.0000*I+-28.0000*m)
 +13.0000*exp(20.0000*I+2.0000*m)
 +17.0000*exp(20.0000*I+32.0000*m)
 +3.0000*exp(20.0000*I+-48.0000*m)
 +5.0000*exp(20.0000*I+-44.0000*m)
 +13.0000*exp(20.0000*I+-8.0000*m)
 +15.0000*exp(20.0000*I+6.0000*m)
 +17.0000*exp(20.0000*I+22.0000*m)
 +19.0000*exp(20.0000*I+40.0000*m)

Fitting equation:

$$f = (cg^2/T)*\text{Num/Den} + \text{TIP}$$

Fitting parameters:

$$J_{bb} = -32.5(4)$$

$$J_{wb} = 1.0(1)$$

$$g = 1.95(1)$$

LIST OF REFERENCES

- (1) Stock, A. *Suom. Kemistil. B* **1943**, 16A, 75.
- (2) Stock, A. *Naturwissenschaften* **1937**, 25, 417.
- (3) Stock, A. *Z. Elektrochem. Angew. Phys. Chem.* **1926**, 32, 341.
- (4) Werner, A. *Z. anorg. Ch.* **1897**, 14, 21.
- (5) Bradley, D. C. *Chem. Rev.* **1989**, 89, 1317.
- (6) Yano, J.; Kern, J.; Sauer, K.; Latimer, M. J.; Pushkar, Y.; Biesiadka, J.; Loll, B.; Saenger, W.; Messinger, J.; Zouni, A.; Yachandra, V. K. *Science* **2006**, 314, 821.
- (7) Ferreira, K. N.; Iverson, T. M.; Maghlaoui, K.; Barber, J.; Iwata, S. *Science* **2004**, 303, 1831.
- (8) Grant, R. A.; Filman, D. J.; Finkel, S. E.; Kolter, R.; Hogle, J. M. *Nat. Struct. Biol.* **1998**, 5, 294.
- (9) Theil, E. C.; Matzapetakis, M.; Liu, X. *J. Biol. Inorg. Chem.* **2006**, 11, 803.
- (10) Ako, A. M.; Hewitt, I. J.; Mereacre, V.; Clerac, R.; Wernsdorfer, W.; Anson, C. E.; Powell, A. K. *Angew. Chem., Int. Ed.* **2006**, 45, 4926.
- (11) Bagai, R.; Christou, G. *Chem. Soc. Rev.* **2009**, 38, 1011.
- (12) Christou, G.; Gatteschi, D.; Hendrickson, D. N.; Sessoli, R. *MRS Bull.* **2000**, 25, 66.
- (13) Aromi, G.; Brechin, E. K. *Struct. Bonding (Berlin, Ger.)* **2006**, 122, 1.
- (14) Gatteschi, D.; Sessoli, R. *Angew. Chem., Int. Ed.* **2003**, 42, 268.
- (15) Bircher, R.; Chaboussant, G.; Dobe, C.; Gudel, H. U.; Ochsenein, S. T.; Sieber, A.; Waldmann, O. *Adv. Funct. Mater.* **2006**, 16, 209.
- (16) Sessoli, R.; Tsai, H. L.; Schake, A. R.; Wang, S.; Vincent, J. B.; Folting, K.; Gatteschi, D.; Christou, G.; Hendrickson, D. N. *J. Am. Chem. Soc.* **1993**, 115, 1804.
- (17) Stohr, J. S., H. C. *Magnetism: From Fundamentals to Nanoscale Dynamics*; Springer, 2006; Vol. 152.
- (18) Jiles, D. *Introduction to Magnetism and Magnetic Materials*; Chapman & Hall; New York, 1991.

- (19) Kahn, O. *Molecular Magnetism*; VCH: Weinheim, Germany, 1993.
- (20) Smart, L. M., E. *Solid State Chemistry*, Chapman & Hall: New York, 1993.
- (21) Janutka, A. *J. Phys.: Condens. Matter* **2003**, *15*, 8561.
- (22) Epstein, A. J. *MRS Bull.* **2000**, *25*, 33.
- (23) Miller, J. S.; Epstein, A. J. *MRS Bull.* **2000**, *25*, 21.
- (24) Lis, T. *Acta Crystallogr., Sect. B: Struct. Sci.* **1980**, *36*, 2042.
- (25) Sessoli, R.; Gatteschi, D.; Caneschi, A.; Novak, M. A. *Nature (London)* **1993**, *365*, 141.
- (26) Gatteschi, D.; Sessoli, R.; Cornia, A. *Chem. Commun. (Cambridge)* **2000**, 725.
- (27) Leuenberger, M. N.; Loss, D. *Nature (London, U. K.)* **2001**, *410*, 789.
- (28) Knill, E. *Nature (London, U. K.)* **2010**, *463*, 441.
- (29) Stamp, P. C. E.; Gaita-Arino, A. *J. Mater. Chem.* **2009**, *19*, 1718.
- (30) Winpenny, R. E. P. *Angew. Chem., Int. Ed.* **2008**, *47*, 7992.
- (31) Hill, S.; Edwards, R. S.; Aliaga-Alcalde, N.; Christou, G. *Science* **2003**, *302*, 1015.
- (32) Meier, F.; Levy, J.; Loss, D. *Phys. Rev. B: Condens. Matter Mater. Phys.* **2003**, *68*, 134417/1.
- (33) Christou, G. *Polyhedron* **2005**, *24*, 2065.
- (34) Brechin, E. K. *Chem. Commun. (Cambridge, U. K.)* **2005**, 5141.
- (35) Aubin, S. M. J.; Wemple, M. W.; Adams, D. M.; Tsai, H.-L.; Christou, G.; Hendrickson, D. N. *J. Am. Chem. Soc.* **1996**, *118*, 7746.
- (36) Dendrinou-Samara, C.; Alexiou, M.; Zaleski, C. M.; Kampf, J. W.; Kirk, M. L.; Kessissoglou, D. P.; Pecoraro, V. L. *Angew. Chem., Int. Ed.* **2003**, *42*, 3763.
- (37) Miyasaka, H.; Clerac, R.; Wernsdorfer, W.; Lecren, L.; Bonhomme, C.; Sugiura, K.-i.; Yamashita, M. *Angew. Chem., Int. Ed.* **2004**, *43*, 2801.
- (38) Boudalis, A. K.; Donnadieu, B.; Nastopoulos, V.; Clemente-Juan, J. M.; Mari, A.; Sanakis, Y.; Tuchagues, J.-P.; Perlepes, S. P. *Angew. Chem., Int. Ed.* **2004**, *43*, 2266.

- (39) Oshio, H.; Hoshino, N.; Ito, T.; Nakano, M. *J. Am. Chem. Soc.* **2004**, *126*, 8805.
- (40) Stamatatos, T. C.; Abboud, K. A.; Wernsdorfer, W.; Christou, G. *Angew. Chem., Int. Ed.* **2006**, *45*, 4134.
- (41) Stamatatos, T.; Abboud, K. A.; Wernsdorfer, W.; Christou, G. *Angew. Chem., Int. Ed.* **2007**, *46*, 884.
- (42) Milios, C. J.; Vinslava, A.; Wernsdorfer, W.; Moggach, S.; Parsons, S.; Perlepes, S. P.; Christou, G.; Brechin, E. K. *J. Am. Chem. Soc.* **2007**, *129*, 2754.
- (43) Murugesu, M.; Habrych, M.; Wernsdorfer, W.; Abboud, K. A.; Christou, G. *J. Am. Chem. Soc.* **2004**, *126*, 4766.
- (44) Stamatatos, T. C.; Foguet-Albiol, D.; Stoumpos, C. C.; Raptopoulou, C. P.; Terzis, A.; Wernsdorfer, W.; Perlepes, S. P.; Christou, G. *Polyhedron* **2007**, *26*, 2165.
- (45) Stamatatos, T. C.; Abboud, K. A.; Wernsdorfer, W.; Christou, G. *Polyhedron* **2007**, *26*, 2095.
- (46) Foguet-Albiol, D.; O'Brien, T. A.; Wernsdorfer, W.; Moulton, B.; Zaworotko, M. J.; Abboud, K. A.; Christou, G. *Angew. Chem., Int. Ed.* **2005**, *44*, 897.
- (47) Murugesu, M.; Wernsdorfer, W.; Abboud, K. A.; Christou, G. *Angew. Chem., Int. Ed.* **2005**, *44*, 892.
- (48) Taguchi, T.; Wernsdorfer, W.; Abboud, K. A.; Christou, G. *Inorg. Chem.* **2010**, *49*, 10579.
- (49) Nayak, S.; Beltran, L. M. C.; Lan, Y.; Clerac, R.; Hearn, N. G. R.; Wernsdorfer, W.; Anson, C. E.; Powell, A. K. *Dalton Trans.* **2009**, 1901.
- (50) Nayak, S.; Lan, Y.; Clerac, R.; Anson, C. E.; Powell, A. K. *Chem. Commun. (Cambridge, U. K.)* **2008**, 5698.
- (51) Saalfrank, R. W.; Scheurer, A.; Prakash, R.; Heinemann, F. W.; Nakajima, T.; Hampel, F.; Leppin, R.; Pilawa, B.; Rupp, H.; Mueller, P. *Inorg. Chem.* **2007**, *46*, 1586.
- (52) Saalfrank, R. W.; Nakajima, T.; Mooren, N.; Scheurer, A.; Maid, H.; Hampel, F.; Trieflinger, C.; Daub, J. *Eur. J. Inorg. Chem.* **2005**, 1149.
- (53) Stamatatos, T. C.; Efthymiou, C. G.; Stoumpos, C. C.; Perlepes, S. P. *Eur. J. Inorg. Chem.* **2009**, 3361.
- (54) Bagai, R.; Daniels, M. R.; Abboud, K. A.; Christou, G. *Inorg. Chem.* **2008**, *47*, 3318.

- (55) Sun, Z.; Hendrickson, D. N.; Grant, C. M.; Castro, S. L.; Christou, G. *Chem. Commun. (Cambridge)* **1998**, 721.
- (56) Yang, E.-C.; Hendrickson, D. N.; Wernsdorfer, W.; Nakano, M.; Zakharov, L. N.; Sommer, R. D.; Rheingold, A. L.; Ledezma-Gairaud, M.; Christou, G. *J. Appl. Phys.* **2002**, *91*, 7382.
- (57) Andres, H.; Basler, R.; Blake, A. J.; Cadiou, C.; Chaboussant, G.; Grant, C. M.; Gudel, H.-U.; Murrie, M.; Parsons, S.; Paulsen, C.; Semadini, F.; Villar, V.; Wernsdorfer, W.; Winpenny, R. E. P. *Chem.--Eur. J.* **2002**, *8*, 4867.
- (58) Murugesu, M.; Mishra, A.; Wernsdorfer, W.; Abboud, K. A.; Christou, G. *Polyhedron* **2006**, *25*, 613.
- (59) Stamatatos, T. C.; Christou, G. *Inorg. Chem.* **2009**, *48*, 3308.
- (60) Bagai, R.; Abboud, K. A.; Christou, G. *Inorg. Chem.* **2008**, *47*, 621.
- (61) Hundal, G.; Hundal, M. S.; Obrai, S.; Poonia, N. S.; Kumar, S. *Inorg. Chem.* **2002**, *41*, 2077.
- (62) Plass, W. *Eur. J. Inorg. Chem.* **1998**, 799.
- (63) Zhou, A.-J.; Qin, L.-J.; Beedle, C. C.; Ding, S.; Nakano, M.; Leng, J.-D.; Tong, M.-L.; Hendrickson, D. N. *Inorg. Chem.* **2007**, *46*, 8111.
- (64) Vandersluis, P. S., A. L. *Acta Crystallogr.; Sect. A* **1990**, *46*, 194.
- (65) Gagne, R. R.; Koval, C. A.; Lisensky, G. C. *Inorg. Chem.* **1980**, *19*, 2854.
- (66) Davidson, E. R.; MAGNET; Indiana University: Bloomington, I., Ed. 1999.
- (67) Wernsdorfer, W. *Adv. Chem. Phys.* **2001**, *118*, 99.
- (68) Liu, W.; Thorp, H. H. *Inorg. Chem.* **1993**, *32*, 4102.
- (69) Palenik, G. J. *Inorg. Chem.* **1997**, *36*, 4888.
- (70) Brown, I. D. W., K. K. *Acta Crystallogr., Sect. B: Struct. Sci.* **1976**, *32*, 1957.
- (71) Murugesu, M.; Takahashi, S.; Wilson, A.; Abboud, K. A.; Wernsdorfer, W.; Hill, S.; Christou, G. *Inorg. Chem.* **2008**, *47*, 9459.
- (72) Stamatatos, T. C.; Abboud, K. A.; Wernsdorfer, W.; Christou, G. *Inorg. Chem.* **2009**, *48*, 807.

- (73) Cheng, B.; Fries, P. H.; Marchon, J.-C.; Scheidt, W. R. *Inorg. Chem.* **1996**, *35*, 1024.
- (74) Eppley, H. J.; Tsai, H.-L.; de, V. N.; Folting, K.; Christou, G.; Hendrickson, D. N. *J. Am. Chem. Soc.* **1995**, *117*, 301.
- (75) Soler, M.; Wernsdorfer, W.; Abboud, K. A.; Huffman, J. C.; Davidson, E. R.; Hendrickson, D. N.; Christou, G. *J. Am. Chem. Soc.* **2003**, *125*, 3576.
- (76) Chakov, N. E.; Soler, M.; Wernsdorfer, W.; Abboud, K. A.; Christou, G. *Inorg. Chem.* **2005**, *44*, 5304.
- (77) Bian, G.-Q.; Kuroda-Sowa, T.; Konaka, H.; Hatano, M.; Maekawa, M.; Munakata, M.; Miyasaka, H.; Yamashita, M. *Inorg. Chem.* **2004**, *43*, 4790.
- (78) Zhao, H.; Berlinguette, C. P.; Bacsá, J.; Prosvirin, A. V.; Bera, J. K.; Tichy, S. E.; Schelter, E. J.; Dunbar, K. R. *Inorg. Chem.* **2004**, *43*, 1359.
- (79) Coronado, E.; Forment-Aliaga, A.; Alejandro, G.-A.; Gimenez-Saiz, C.; Romero, F. M.; Wernsdorfer, W. *Angew. Chem., Int. Ed.* **2004**, *43*, 6152.
- (80) Soler, M.; Wernsdorfer, W.; Abboud, K. A.; Hendrickson, D. N.; Christou, G. *Polyhedron* **2003**, *22*, 1777.
- (81) Tasiopoulos, A. J.; Wernsdorfer, W.; Abboud, K. A.; Christou, G. *Inorg. Chem.* **2005**, *44*, 6324.
- (82) King, P.; Wernsdorfer, W.; Abboud, K. A.; Christou, G. *Inorg. Chem.* **2005**, *44*, 8659.
- (83) Rajaraman, G.; Murugesu, M.; Sanudo, E. C.; Soler, M.; Wernsdorfer, W.; Helliwell, M.; Murn, C.; Raftery, J.; Teat, S. J.; Christou, G.; Brechin, E. K. *J. Am. Chem. Soc.* **2004**, *126*, 15445.
- (84) Murugesu, M.; Wernsdorfer, W.; Abboud, K. A.; Brechin, E. K.; Christou, G. *Dalton Trans.* **2006**, 2285.
- (85) Li, Y.; Wernsdorfer, W.; Clerac, R.; Hewitt, I. J.; Anson, C. E.; Powell, A. K. *Inorg. Chem.* **2006**, *45*, 2376.
- (86) Boskovic, C.; Brechin, E. K.; Streib, W. E.; Folting, K.; Christou, G.; Hendrickson, D. N. *Chem. Commun. (Cambridge, U. K.)* **2001**, 467.
- (87) Boskovic, C.; Brechin, E. K.; Streib, W. E.; Folting, K.; Bollinger, J. C.; Hendrickson, D. N.; Christou, G. *J. Am. Chem. Soc.* **2002**, *124*, 3725.

- (88) Rumberger, E. M.; Shah, S. J.; Beedle, C. C.; Zakharov, L. N.; Rheingold, A. L.; Hendrickson, D. N. *Inorg. Chem.* **2005**, *44*, 2742.
- (89) Yao, H.-C.; Li, Y.-Z.; Song, Y.; Ma, Y.-S.; Zheng, L.-M.; Xin, X.-Q. *Inorg. Chem.* **2006**, *45*, 59.
- (90) Dendrinou-Samara, C.; Zaleski, C. M.; Evagorou, A.; Kampf, J. W.; Pecoraro, V. L.; Kessissoglou, D. P. *Chem. Commun. (Cambridge, U. K.)* **2003**, 2668.
- (91) Shah, S. J.; Ramsey, C. M.; Heroux, K. J.; DiPasquale, A. G.; Dalal, N. S.; Rheingold, A. L.; del, B. E.; Hendrickson, D. N. *Inorg. Chem.* **2008**, *47*, 9569.
- (92) Liu, X.; Liu, W.; Lee, K.; Park, M.; Ri, H.-C.; Kim, G. H.; Lah, M. S. *Dalton Trans.* **2008**, 6579.
- (93) Wang, S.; Wemple, M. S.; Yoo, J.; Folting, K.; Huffman, J. C.; Hagen, K. S.; Hendrickson, D. N.; Christou, G. *Inorg. Chem.* **2000**, *39*, 1501.
- (94) Murugesu, M.; Raftery, J.; Wernsdorfer, W.; Christou, G.; Brechin, E. K. *Inorg. Chem.* **2004**, *43*, 4203.
- (95) Scott, R. T. W.; Parsons, S.; Murugesu, M.; Wernsdorfer, W.; Christou, G.; Brechin, E. K. *Angew. Chem., Int. Ed.* **2005**, *44*, 6540.
- (96) Milios, C. J.; Manoli, M.; Rajaraman, G.; Mishra, A.; Budd, L. E.; White, F.; Parsons, S.; Wernsdorfer, W.; Christou, G.; Brechin, E. K. *Inorg. Chem.* **2006**, *45*, 6782.
- (97) Davidson, E. R.; GRID; Indiana University: Bloomington, I., Ed. 1999.
- (98) Tasiopoulos, A. J.; Vinslava, A.; Wernsdorfer, W.; Abboud, K. A.; Christou, G. *Angew. Chem., Int. Ed.* **2004**, *43*, 2117.
- (99) Brechin, E. K.; Boskovic, C.; Wernsdorfer, W.; Yoo, J.; Yamaguchi, A.; Sanudo, E. C.; Concolino, T. R.; Rheingold, A. L.; Ishimoto, H.; Hendrickson, D. N.; Christou, G. *J. Am. Chem. Soc.* **2002**, *124*, 9710.
- (100) Soler, M.; Wernsdorfer, W.; Folting, K.; Pink, M.; Christou, G. *J. Am. Chem. Soc.* **2004**, *126*, 2156.
- (101) Soler, M.; Rumberger, E.; Folting, K.; Hendrickson, D. N.; Christou, G. *Polyhedron* **2001**, *20*, 1365.
- (102) Aubin, S. M. J.; Sun, Z.; Eppley, H. J.; Rumberger, E. M.; Guzei, I. A.; Folting, K.; Gantzel, P. K.; Rheingold, A. L.; Christou, G.; Hendrickson, D. N. *Inorg. Chem.* **2001**, *40*, 2127.

- (103) Soler, M.; Artus, P.; Folting, K.; Huffman, J. C.; Hendrickson, D. N.; Christou, G. *Inorg. Chem.* **2001**, *40*, 4902.
- (104) Soler, M.; Wernsdorfer, W.; Sun, Z.; Ruiz, D.; Huffman, J. C.; Hendrickson, D. N.; Christou, G. *Polyhedron* **2003**, *22*, 1783.
- (105) Lampropoulos, C.; Redler, G.; Data, S.; Abboud, K. A.; Hill, S.; Christou, G. *Inorg. Chem.* **2010**, *49*, 1325.
- (106) Harter, A. G.; Chakov, N. E.; Achey, R.; Reyes, A.; Kuhns, P.; Christou, G.; Dalal, N. S. *Polyhedron* **2005**, *24*, 2346.
- (107) Bagai, R.; Christou, G. *Inorg. Chem.* **2007**, *46*, 10810.
- (108) Forment-Aliaga, A.; Coronado, E.; Feliz, M.; Gaita-Arino, A.; Llusar, R.; Romero, F. M. *Inorg. Chem.* **2003**, *42*, 8019.
- (109) Kuroda-Sowa, T.; Lam, M.; Rheingold, A. L.; Frommen, C.; Reiff, W. M.; Nakano, M.; Yoo, J.; Maniero, A. L.; Brunel, L.-C.; Christou, G.; Hendrickson, D. N. *Inorg. Chem.* **2001**, *40*, 6469.
- (110) Clemente-Juan, J. M.; Coronado, E.; Forment-Aliaga, A.; Gaita-Arino, A.; Gimenez-Saiz, C.; Romero, F. M.; Wernsdorfer, W.; Biagi, R.; Corradini, V. *Inorg. Chem.* **2010**, *49*, 386.
- (111) Taguchi, T.; Wernsdorfer, W.; Abboud, K. A.; Christou, G. *Inorg. Chem.* **2010**, *49*, 199.
- (112) Waldmann, O. *Inorg. Chem. (Washington, DC, U. S.)* **2007**, *46*, 10035.
- (113) Ruiz, E.; Cirera, J.; Cano, J.; Alvarez, S.; Loose, C.; Kortus, J. *Chem. Commun. (Cambridge, U. K.)* **2008**, 52.
- (114) Wernsdorfer, W.; Sessoli, R. *Science (Washington, D. C.)* **1999**, *284*, 133.
- (115) Wernsdorfer, W.; Aliaga-Alcalde, N.; Hendrickson, D. N.; Christou, G. *Nature (London, U. K.)* **2002**, *416*, 406.
- (116) Friedman, J. r.; Sarachik, M. P.; Tejada, J.; Ziolo, R. *Phys. Rev. Lett.* **1996**, *76*, 3830.
- (117) Thomas, L.; Lioni, F.; Ballou, R.; Gatteschi, D.; Sessoli, R.; Barbara, B. *Nature (London)* **1996**, 383, 145.
- (118) Langley, S. K.; Moubaraki, B.; Murray, K. S. *Dalton Trans.* **2010**, 39, 5066.

- (119) de, S. A. S.; Fernandes, M. A. *Polyhedron* **2002**, *21*, 1883.
- (120) Yu, S. B.; Lippard, S. J.; Shweky, I.; Bino, A. *Inorg. Chem.* **1992**, *31*, 3502.
- (121) Wernsdorfer, W.; Chakov, N. E.; Christou, G. *Phys. Rev. B: Condens. Matter Mater. Phys.* **2004**, *70*, 132413/1.
- (122) Baroni, S. D. C., A.; de Gironcoli, S.; Giannozzi, P.; Cavazzoni, C.; Ballabio, G.; Scandolo, S.; Chiarotti, G.; Focher, P.; Pasquarello, A. In Code available from <http://www.quantum-espresso.org>.
- (123) Vanderbilt, D. *Physical Review B* **1990**, *41*.
- (124) Marzari, N.; Vanderbilt, D.; De, V. A.; Payne, M. C. *Phys. Rev. Lett.* **1999**, *82*, 3296.
- (125) Cococcioni, M. d. G., S. *Physical Review B* **2005**, *71*.
- (126) Gangopadhyay, S.; Masunov, A. E.; Poalelungi, E.; Leuenberger, M. N. *J. Chem. Phys.* **2010**, *132*, 244104/1.
- (127) Koumoussi, E. S.; Manos, M. J.; Lampropoulos, C.; Tasiopoulos, A. J.; Wernsdorfer, W.; Christou, G.; Stamatatos, T. C. *Inorg. Chem. (Washington, DC, U. S.)* **2010**, *49*, 3077.
- (128) Lampropoulos, C.; Stamatatos, T. C.; Abboud, K. A.; Christou, G. *Polyhedron* **2009**, *28*, 1958.
- (129) Piligkos, S.; Rajaraman, G.; Soler, M.; Kirchner, N.; van, S. J.; Bircher, R.; Parsons, S.; Guedel, H.-U.; Kortus, J.; Wernsdorfer, W.; Christou, G.; Brechin, E. K. *J. Am. Chem. Soc.* **2005**, *127*, 5572.
- (130) Chakov, N. E.; Zakharov, L. N.; Rheingold, A. L.; Abboud, K. A.; Christou, G. *Inorg. Chem.* **2005**, *44*, 4555.
- (131) Brechin, E. K.; Christou, G.; Soler, M.; Helliwell, M.; Teat, S. J. *Dalton Trans.* **2003**, 513.
- (132) Eppley, H. J.; deVries, N.; Wang, S.; Aubin, S. M.; Tsai, H.-L.; Folting, K.; Hendrickson, D. N.; Christou, G. *Inorg. Chim. Acta* **1997**, *263*, 323.
- (133) Wu, D.; Guo, D.; Song, Y.; Huang, W.; Duan, C.; Meng, Q.; Sato, O. *Inorg. Chem.* **2009**, *48*, 854.

- (134) Marshall, W., Lovesey, S. W. *Theory of Thermal Neutron Scattering*; Oxford Clarendon Press, 1971.
- (135) Furrer, A.; Guedel, H. U. *Phys. Rev. Lett.* **1977**, *39*, 657.
- (136) Waldmann, O. *Phys. Rev. B: Condens. Matter Mater. Phys.* **2003**, *68*, 174406/1.
- (137) Ochsenbein, S. T.; Tuna, F.; Rancan, M.; Davies, R. S. G.; Muryn, C. A.; Waldmann, O.; Bircher, R.; Sieber, A.; Carver, G.; Mutka, H.; Fernandez-Alonso, F.; Podlesnyak, A.; Engelhardt, L. P.; Timco, G. A.; Guedel, H. U.; Winpenny, R. E. P. *Chem.--Eur. J.* **2008**, *14*, 5144.
- (138) Dreiser, J.; Waldmann, O.; Dobe, C.; Carver, G.; Ochsenbein, S. T.; Sieber, A.; Guedel, H. U.; van, D. J.; Taylor, J.; Podlesnyak, A. *Phys. Rev. B: Condens. Matter Mater. Phys.* **2010**, *81*, 024408/1.
- (139) Stuibler, S., Wu, G. Nehr Korn, J., Dreiser, J., Lan, Y. Novitchi, G., Anson, C. E., Unruh, T., Powell, A. K., Waldmann, O *Chem. Eur. J.* **in press**.
- (140) Pieper, O.; Guidi, T.; Carretta, S.; van, S. J.; El, H. F.; Lake, B.; Santini, P.; Amoretti, G.; Mutka, H.; Koza, M.; Russina, M.; Schnegg, A.; Milios, C. J.; Brechin, E. K.; Julia, A.; Tejada, J. *Phys. Rev. B: Condens. Matter Mater. Phys.* **2010**, *81*, 174420/1.
- (141) Gatteschi D., S. R., Villain, J. *Molecular Nanomagnets*; Oxford University Press: Oxford, 2006.
- (142) Rudowicz, C.; Chung, C. Y. *J. Phys.: Condens. Matter* **2004**, *16*, 5825.
- (143) Andrei, V. P. J., K.; Mark, R. P. *Physica Status Solidi (b)* **2006**, *243*, 2533.
- (144) Kortus, J.; Pederson, M. R.; Hellberg, C. S.; Khanna, S. N. *Eur. Phys. J. D* **2001**, *16*, 177.
- (145) Michalak, L.; Canali, C. M.; Pederson, M. R.; Paulsson, M.; Benza, V. G. *Phys. Rev. Lett.* **2010**, *104*, 017202/1.
- (146) Park, K. B., T.; Pederson, M. R. *Abstracts of Papers of the American Chemical Society* **2004**, *228*, 436.
- (147) Ribas-Arino, J.; Baruah, T.; Pederson, M. R. *J. Am. Chem. Soc.* **2006**, *128*, 9497.
- (148) Zhang, J. R. H., L. H.; Cao, H. B.; Wang, F. W.; Zhang, P. L. *J. Chem. Phys.* **2008**, *128*.
- (149) Noodleman, L. *J. Chem. Phys.* **1981**, *74*, 5737.

- (150) Noodleman, L.; Case, D. A. *Adv. Inorg. Chem.* **1992**, 38, 423.
- (151) Noodleman, L.; Han, W.-G. *JBIC, J. Biol. Inorg. Chem.* **2006**, 11, 674.
- (152) Noodleman, L. D., E. R. *Chemical Physics* **1986**, 109, 131.
- (153) Rudberg, E.; Salek, P.; Rinkevicius, Z.; Aagren, H. *J. Chem. Theory Comput.* **2006**, 2, 981.
- (154) Shoji, M.; Hamamoto, T.; Koizumi, K.; Isobe, H.; Kitagawa, Y.; Takano, Y.; Yamanaka, S.; Okumura, M.; Yamaguchi, K. *Polyhedron* **2005**, 24, 2701.
- (155) Shoji, M.; Isobe, H.; Saito, T.; Yabushita, H.; Koizumi, K.; Kitagawa, Y.; Yamanaka, S.; Kawakami, T.; Okumura, M.; Hagiwara, M.; Yamaguchi, K. *Int. J. Quantum Chem.* **2007**, 108, 631.
- (156) Shoji, M.; Koizumi, K.; Taniguchi, T.; Kitagawa, Y.; Yamanaka, S.; Okumura, M.; Yamaguchi, K. *Int. J. Quantum Chem.* **2006**, 107, 116.
- (157) Shoji, M.; Nishiyama, Y.; Maruno, Y.; Koizumi, K.; Kitagawa, Y.; Yamanaka, S.; Kawakami, T.; Okumura, M.; Yamaguchi, K. *Int. J. Quantum Chem.* **2004**, 100, 887.
- (158) Ruiz, E.; Cano, J.; Alvarez, S.; Alemany, P. *J. Comput. Chem.* **1999**, 20, 1391.
- (159) Nishino, M.; Yamanaka, S.; Yoshioka, Y.; Yamaguchi, K. *J. Phys. Chem. A* **1997**, 101, 705.
- (160) Goel, S. M., A. E. *Lecture Notes in Computer Science LNCS*, 2009; Vol. 5545
- (161) Zhao, X. G. R., W. H.; Chen, J. L.; Li, J.; Noodleman, L.; Tsai, H. L.; Hendrickson, D. N. *Inorg Chem* **1997**, 36, 1198.
- (162) Anisimov, V. I.; Zaanen, J.; Andersen, O. K. *Phys. Rev. B: Condens. Matter* **1991**, 44, 943.
- (163) Cococcioni, M. d. G., S. *Physical Review B* **2005**, 71, 035105.
- (164) Gangopadhyay, S. M., A.; Poalelungi, E.; Leuenberger, M. . *In Computational Science – ICCS 2009*; Springer Berlin / Heidelberg, 2009; Vol. 5545.
- (165) Clark, A. E.; Davidson, E. R. *J. Chem. Phys.* **2001**, 115, 7382.
- (166) Gultneh, Y.; Tesema, Y. T.; Yisgedu, T. B.; Butcher, R. J.; Wang, G.; Yee, G. T. *Inorg. Chem.* **2006**, 45, 3023.

- (167) Wang, X.-J.; Langetepe, T.; Persau, C.; Kang, B.-S.; Sheldrick, G. M.; Fenske, D. *Angew. Chem., Int. Ed.* **2002**, *41*, 3818.
- (168) Saha, A. G., S.; Abboud, K.A.; Wernsdorfer, W.; Nehrkorn, J.; Milazzo, R.; Mutka, H.; Waldmann, O.; Masunov, A. E.; Christou, G. *About to be submitted*.
- (169) Tasiopoulos, A. J.; Abboud, K. A.; Christou, G. *Chem. Commun. (Cambridge, U. K.)* **2003**, 580.
- (170) Lis, T. *Acta Crystallogr B* **1977**, *33*, 2964.
- (171) Brese, N. E. O. k., M. *Acta Cryst.* **1991**, *B47*, 192.
- (172) Canada-Vilalta, C.; Pink, M.; Christou, G. *Dalton Trans.* **2003**, 1121.
- (173) Stamatatos, T. C.; Vinslava, A.; Abboud, K. A.; Christou, G. *Chem. Commun. (Cambridge, U. K.)* **2009**, 2839.
- (174) Prescimone, A.; Wolowska, J.; Rajaraman, G.; Parsons, S.; Wernsdorfer, W.; Murugesu, M.; Christou, G.; Piligkos, S.; McInnes, E. J. L.; Brechin, E. K. *Dalton Trans.* **2007**, 5282.
- (175) Yoshino, A.; Miyagi, T.; Asato, E.; Mikuriya, M.; Sakata, Y.; Sugiura, K.-i.; Iwasaki, K.; Hino, S. *Chem. Commun. (Cambridge)* **2000**, 1475.
- (176) Higgs, T. C.; Spartalian, K.; O'Connor, C. J.; Matzanke, B.; Carrano, C. J. *Inorg. Chem.* **1998**, *37*, 2263.
- (177) Bhaduri, S.; Pink, M.; Christou, G. *Chem. Commun. (Cambridge, U. K.)* **2002**, 2352.
- (178) Mukherjee, C.; Weyhermueller, T.; Wiegardt, K.; Chaudhuri, P. *Dalton Trans.* **2006**, 2169.
- (179) Hureau, C.; Anxolabehere-Mallart, E.; Blondin, G.; Riviere, E.; Nierlich, M. *Eur. J. Inorg. Chem.* **2005**, 4808.
- (180) Inglis, R.; Taylor, S. M.; Jones, L. F.; Papaefstathiou, G. S.; Perlepes, S. P.; Datta, S.; Hill, S.; Wernsdorfer, W.; Brechin, E. K. *Dalton Trans.* **2009**, 9157.
- (181) Yang, E.-C.; Harden, N.; Wernsdorfer, W.; Zakharov, L.; Brechin, E. K.; Rheingold, A. L.; Christou, G.; Hendrickson, D. N. *Polyhedron* **2003**, *22*, 1857.
- (182) Inglis, R.; Dalgarno, S. J.; Brechin, E. K. *Dalton Trans.* **2010**, *39*, 4826.

- (183) Stamatatos, T. C.; Poole, K. M.; Abboud, K. A.; Wernsdorfer, W.; O'Brien, T. A.; Christou, G. *Inorg. Chem.* **2008**, *47*, 5006.
- (184) Langley, S. K.; Moubaraki, B.; Berry, K. J.; Murray, K. S. *Dalton Trans.* **2010**, *39*, 4848.
- (185) Moushi, E. E.; Lampropoulos, C.; Wernsdorfer, W.; Nastopoulos, V.; Christou, G.; Tasiopoulos, A. J. *Inorg. Chem.* **2007**, *46*, 3795.
- (186) Papatriantafyllopoulou, C.; Raptopoulou, C. P.; Escuer, A.; Milios, C. J. *Inorg. Chim. Acta* **2007**, *360*, 61.
- (187) Dou, J.; Liu, M.; Li, D.; Wang, D. *Eur. J. Inorg. Chem.* **2006**, 4866.
- (188) Goldberg, D. P.; Caneschi, A.; Delfs, C. D.; Sessoli, R.; Lippard, S. J. *J. Am. Chem. Soc.* **1995**, *117*, 5789.
- (189) Maheswaran, S.; Chastanet, G.; Teat, S. J.; Mallah, T.; Sessoli, R.; Wernsdorfer, W.; Winpenny, R. E. P. *Angew. Chem., Int. Ed.* **2005**, *44*, 5044.
- (190) Mishra, A.; Abboud, K. A.; Christou, G.; *Chem. Comm.* **2005**, 2086.
- (191) Nayak, S.; Nayek, H. P.; Dehnen, S.; Powell, A. K.; Reedijk, J. *Dalton Trans.* **2011**, *40*, 2699.
- (192) Hewitt, I. J.; Tang, J.-K.; Madhu, N. T.; Clerac, R.; Buth, G.; Anson, C. E.; Powell, A. K. *Chem. Commun. (Cambridge, U. K.)* **2006**, 2650.
- (193) Kambe, K. *J. Phys. Soc. Jpn.* **1950**, *5*, 48.
- (194) Freedman, D. E.; Harman, W. H.; Harris, T. D.; Long, G. J.; Chang, C. J.; Long, J. R. *J. Am. Chem. Soc.* **2010**, *132*, 1224.
- (195) Sieve, B.; Chen, X.; Cowen, J.; Larson, P.; Mahanti, S. D.; Kanatzidis, M. G. *Chem. Mater.* **1999**, *11*, 2451.
- (196) Lattner, S. E.; Bilc, D.; Mahanti, S. D.; Kanatzidis, M. G. *Chem. Mater.* **2002**, *14*, 1695.
- (197) Zhuravleva, M. A.; Salvador, J.; Bilc, D.; Mahanti, S. D.; Ireland, J.; Kannewurf, C. R.; Kanatzidis, M. G. *Chem.--Eur. J.* **2004**, *10*, 3197.
- (198) Kanatzidis, M. G.; Pottgen, R.; Jeitschko, W. *Angew. Chem., Int. Ed.* **2005**, *44*, 6996.
- (199) Wu, X. *Intermetallics* **2006**, *14*, 1114.

- (200) Habermeier, H.-U. *Mater. Today (Oxford, U. K.)* **2007**, *10*, 34.
- (201) Ramesh, R.; Spaldin, N. A. *Nat. Mater.* **2007**, *6*, 21.
- (202) Kan, E.; Xiang, H.; Lee, C.; Wu, F.; Yang, J.; Whangbo, M.-H. *Angew. Chem., Int. Ed.* **2010**, *49*, 1603.
- (203) Schmid, H. *Ferroelectrics* **1994**, *162*, 665.
- (204) Andruh, M.; Costes, J.-P.; Diaz, C.; Gao, S. *Inorg. Chem.* **2009**, *48*, 3342.
- (205) Long, J.; Chamoreau, L.-M.; Marvaud, V. *Dalton Trans.* **2010**, *39*, 2188.
- (206) Zhao, X.-Q.; Lan, Y.; Zhao, B.; Cheng, P.; Anson, C. E.; Powell, A. K. *Dalton Trans.* **2010**, *39*, 4911.
- (207) Baskar, V.; Gopal, K.; Helliwell, M.; Tuna, F.; Wernsdorfer, W.; Winpenny, R. E. P. *Dalton Trans.* **2010**, *39*, 4747.
- (208) Pasatoiu, T. D.; Etienne, M.; Madalan, A. M.; Andruh, M.; Sessoli, R. *Dalton Trans.* **2010**, *39*, 4802.
- (209) Benelli, C.; Gatteschi, D. *Chem. Rev.* **2002**, *102*, 2369.
- (210) Winpenny, R. E. P. *Chem. Soc. Rev.* **1998**, *27*, 447.
- (211) Bogani, L.; Wernsdorfer, W. *Nat. Mater.* **2008**, *7*, 179.
- (212) Sessoli, R.; Powell, A. K. *Coord. Chem. Rev.* **2009**, *253*, 2328.
- (213) Ishikawa, N.; Sugita, M.; Ishikawa, T.; Koshihara, S.-Y.; Kaizu, Y. *J. Am. Chem. Soc.* **2003**, *125*, 8694.
- (214) Ke, H.; Xu, G.-F.; Guo, Y.-N.; Gamez, P.; Beavers, C. M.; Teat, S. J.; Tang, J. *Chem. Commun. (Cambridge, U. K.)* **2010**, *46*, 6057.
- (215) Jiang, S.-D.; Wang, B.-W.; Su, G.; Wang, Z.-M.; Gao, S. *Angew. Chem., Int. Ed.* **2010**, *49*, 7448.
- (216) Ma, Y.; Xu, G.-F.; Yang, X.; Li, L.-C.; Tang, J.; Yan, S.-P.; Cheng, P.; Liao, D.-Z. *Chem. Commun. (Cambridge, U. K.)* **2010**, *46*, 8264.
- (217) Lin, P.-H.; Burchell, T. J.; Clerac, R.; Murugesu, M. *Angew. Chem., Int. Ed.* **2008**, *47*, 8848.

- (218) Guo, F.-S.; Liu, J.-L.; Leng, J.-D.; Meng, Z.-S.; Lin, Z.-J.; Tong, M.-L.; Gao, S.; Ungur, L.; Chibotaru, L. F. *Chem.--Eur. J.* **2011**, *17*, 2458.
- (219) Abbas, G.; Lan, Y.; Kostakis, G. E.; Wernsdorfer, W.; Anson, C. E.; Powell, A. K. *Inorg. Chem.* **2010**, *49*, 8067.
- (220) Kong, X.-J.; Wu, Y.; Long, L.-S.; Zheng, L.-S.; Zheng, Z. *J. Am. Chem. Soc.* **2009**, *131*, 6918.
- (221) Bencini, A.; Benelli, C.; Caneschi, A.; Carlin, R. L.; Dei, A.; Gatteschi, D. *J. Am. Chem. Soc.* **1985**, *107*, 8128.
- (222) Mishra, A.; Wernsdorfer, W.; Parsons, S.; Christou, G.; Brechin, E. K. *Chem. Commun. (Cambridge, U. K.)* **2005**, 2086.
- (223) Mereacre, V.; Lan, Y.; Clerac, R.; Ako, A. M.; Hewitt, I. J.; Wernsdorfer, W.; Buth, G.; Anson, C. E.; Powell, A. K. *Inorg. Chem.* **2010**, *49*, 5293.
- (224) Akhtar, M. N.; Zheng, Y.-Z.; Lan, Y.; Mereacre, V.; Anson, C. E.; Powell, A. K. *Inorg. Chem.* **2009**, *48*, 3502.
- (225) Karotsis, G.; Kennedy, S.; Teat, S. J.; Beavers, C. M.; Fowler, D. A.; Morales, J. J.; Evangelisti, M.; Dalgarno, S. J.; Brechin, E. K. *J. Am. Chem. Soc.* **2010**, *132*, 12983.
- (226) Liu, C.-M.; Zhang, D.-Q.; Zhu, D.-B. *Dalton Trans.* **2010**, *39*, 11325.
- (227) Mereacre, V.; Ako, A. M.; Clerac, R.; Wernsdorfer, W.; Hewitt, I. J.; Anson, C. E.; Powell, A. K. *Chem.--Eur. J.* **2008**, *14*, 3577.
- (228) Zaleski, C. M.; Depperman, E. C.; Kampf, J. W.; Kirk, M. L.; Pecoraro, V. L. *Angew. Chem., Int. Ed.* **2004**, *43*, 3912.
- (229) Mereacre, V.; Prodius, D.; Ako, A. M.; Kaur, N.; Lipkowski, J.; Simmons, C.; Dalal, N.; Geru, I.; Anson, C. E.; Powell, A. K.; Turta, C. *Polyhedron* **2008**, *27*, 2459.
- (230) Mishra, A.; Wernsdorfer, W.; Abboud, K. A.; Christou, G. *J. Am. Chem. Soc.* **2004**, *126*, 15648.
- (231) Mereacre, V. M.; Ako, A. M.; Clerac, R.; Wernsdorfer, W.; Filoti, G.; Bartolome, J.; Anson, C. E.; Powell, A. K. *J. Am. Chem. Soc.* **2007**, *129*, 9248.
- (232) Stamatatos, T. C.; Teat, S. J.; Wernsdorfer, W.; Christou, G. *Angew. Chem., Int. Ed.* **2009**, *48*, 521.
- (233) Ako, A. M.; Mereacre, V.; Clerac, R.; Wernsdorfer, W.; Hewitt, I. J.; Anson, C. E.; Powell, A. K. *Chem. Commun. (Cambridge, U. K.)* **2009**, 544.

- (234) Papatriantafyllopoulou, C.; Wernsdorfer, W.; Abboud, K. A.; Christou, G. *Inorg. Chem.* **2011**, *50*, 421.
- (235) Godbole, M. D.; Roubau, O.; Mills, A. M.; Kooijman, H.; Spek, A. L.; Bouwman, E. *Inorg. Chem.* **2006**, *45*, 6713.
- (236) Taguchi, T.; Daniels, M. R.; Abboud, K. A.; Christou, G. *Inorg. Chem.* **2009**, *48*, 9325.
- (237) Leuenberger, M. N.; Mucciolo, E. R. *Phys. Rev. Lett.* **2006**, *97*, 126601/1.
- (238) Wernsdorfer, W.; Caneschi, A.; Sessoli, R.; Gatteschi, D.; Cornia, A.; Villar, V.; Paulsen, C. *Phys. Rev. Lett.* **2000**, *84*, 2965.
- (239) Yang, E.-C.; Wernsdorfer, W.; Hill, S.; Edwards, R. S.; Nakano, M.; Maccagnano, S.; Zakharov, L. N.; Rheingold, A. L.; Christou, G.; Hendrickson, D. N. *Polyhedron* **2003**, *22*, 1727.

BIOGRAPHICAL SKETCH

Arpita Saha was born in West Bengal, India. She is the younger daughter of Mr. Supriya Kumar Saha and Mrs. Kalyani Saha. She did her undergraduate studies from Presidency College, Kolkata and received a Bachelor of Science degree in 2002. She successfully qualified the Joint Admission test for M.Sc. (JAM) and pursued a master's degree from the Indian Institute of Technology, Kanpur. During her master's study she joined the research group of Dr. Sabyasachi Sarakar and worked on the synthesis and characterization of carbon nanotubes. She studied the transport of water through the channel of water soluble carbon nanotubes and its interaction with amino acids and DNA. In 2003 she did a summer internship from Indian Institute of Science, Bangalore under the supervision of Dr. A. R. Chakravarty and investigated the modeling of the trinuclear active site of Ascorbate Oxidase (AO) with spectral and analytical characterization of three trinuclear copper complexes. Then she came to United States of America for higher studies. She started her graduate career in 2005 in University of Florida where she met a gator Subhrajit K. Saha and got married in 2006. She joined the research group of Dr. George Christou in the Department of Chemistry at UF. Her doctoral research primarily focuses on the synthesis, structure, electrochemical, magnetochemical and spectroscopic properties of several transition metals and lanthanide containing nano-materials using various alcohol-based ligands. She received her Ph.D. from the University of Florida in the summer of 2011.